

Space Technology Library

Frederick A. Leve
Brian J. Hamilton
Mason A. Peck



Spacecraft Momentum Control Systems



Space
Technology
Library



Springer

Spacecraft Momentum Control Systems

SPACE TECHNOLOGY LIBRARY

Published jointly by Microcosm Press and Springer

The Space Technology Library Editorial Board

Managing Editor: **James R. Wertz** (Microcosm, Inc., El Segundo, CA)

Editorial Board: **Roland Doré** (Professor and Director International Space University, Strasbourg)

Tom Logsdon (Senior member of Technical Staff, Space Division, Rockwell International)

F. Landis Markley (NASA, Goddard Space Flight Center)

Robert G. Melton (Professor of Aerospace Engineering, Pennsylvania State University)

Keiken Ninomiya (Professor, Institute of Space & Astronautical Science)

Jehangir J. Pocha (Letchworth, Herts.)

Rex W. Ridenoure (CEO and Co-founder at Ecliptic Enterprises Corporation)

Gael Squibb (Jet Propulsion Laboratory, California Institute of Technology)

Martin Sweeting (Professor of Satellite Engineering, University of Surrey)

David A. Vallado (Senior Research Astrodynamist, CSSI/AGI)

Richard Van Allen (Vice President and Director, Space Systems Division, Microcosm, Inc.)

More information about this series at <http://www.springer.com/series/6575>

Frederick A. Leve • Brian J. Hamilton
Mason A. Peck

Spacecraft Momentum Control Systems



Springer

Frederick A. Leve
Space Vehicles Directorate
Air Force Research Laboratory
Kirtland A.F.B., NM, USA

Brian J. Hamilton
Honeywell
Glendale, AZ, USA

Mason A. Peck
Cornell University
Ithaca, NY, USA

Space Technology Library
ISBN 978-3-319-22562-3 ISBN 978-3-319-22563-0 (eBook)
DOI 10.1007/978-3-319-22563-0

Library of Congress Control Number: 2015947342

Springer Cham Heidelberg New York Dordrecht London
© Springer International Publishing Switzerland 2015

This work is subject to copyright. All rights are reserved by the Publisher, whether the whole or part of the material is concerned, specifically the rights of translation, reprinting, reuse of illustrations, recitation, broadcasting, reproduction on microfilms or in any other physical way, and transmission or information storage and retrieval, electronic adaptation, computer software, or by similar or dissimilar methodology now known or hereafter developed.

The use of general descriptive names, registered names, trademarks, service marks, etc. in this publication does not imply, even in the absence of a specific statement, that such names are exempt from the relevant protective laws and regulations and therefore free for general use.

The publisher, the authors and the editors are safe to assume that the advice and information in this book are believed to be true and accurate at the date of publication. Neither the publisher nor the authors or the editors give a warranty, express or implied, with respect to the material contained herein or for any errors or omissions that may have been made.

Printed on acid-free paper

Springer International Publishing AG Switzerland is part of Springer Science+Business Media (www.springer.com)

Preface

It's remarkable how often we, the authors, have had a similar experience. At a conference, or during a break at a technical meeting, someone asks "can you recommend a good book about CMGs and reaction wheels?"

The answer is always about the same: "Well, there's this spacecraft dynamics book and that spacecraft design book, and the new edition of that old reference book we all use, but none of them really talk about momentum control in any depth. You probably already know as much as you'll find there." Then there's a pause. "Not that those books are bad; I'm not saying that. They're a decent start for a certain audience, such as students who have never worked on a flight program."

"How about academic articles?"

"Sure, there are a few helpful survey papers and some useful older stuff—especially from the '70s. For some reason they really seemed to know what they were doing back then." Another awkward pause. "I don't really want to go digging into all that." Then, inevitably, "maybe you should just write a book."

So that's what we did.

The reader will find that this book differs from other books on spacecraft dynamics and control. Others provide a broad overview of actuators, sensors, and feedback-control architectures without ever going into these important matters of implementation. And while there exist whole books on propulsive actuators, offering useful depth in the design and operation of rocket engines such as those used for reaction control, there is nothing analogous for momentum actuators. But omitting momentum actuators from a treatment of spacecraft design is like explaining all about automobiles, except for the engine and the transmission. So, finally, there's a book that addresses the crucial matters of what kind and how many momentum devices to implement, how they should be sized, and how to control the array of them.

This book is an effort to offer a complete picture of momentum actuators—spinning rotors and gimbaled devices—for use in attitude control of spacecraft. It's a picture that combines our diverse experience in government space systems (satellites for the Air Force, Navy, and NASA) as well as in the commercial space industry and academia. The scope of this book extends from electromechanical

details of individual actuators to space-system architecture issues of interest in spacecraft concept development. We discuss the foundational rigid- and flexible-body dynamics, the subtle mathematics of steering multiple devices within an array, and the applications of these technologies.

These momentum actuators are at the heart of contemporary spacecraft that perform Earth imaging. The rapid growth of commercial success in this application area since the beginning of the twenty-first century is ultimately due to the technological capabilities that these actuators offer. In the decades to come, our industry is likely to see new applications: asteroid mining, in-orbit servicing and repair of satellites, and new human-space missions, all of which will require high torque and momentum storage. Small spacecraft, now the most commonly launched type of satellite, are only just beginning to incorporate sophisticated momentum control, thanks to entrepreneurial investment and a new generation of passionate spacecraft technologists. The momentum devices described in this book enable contemporary spacecraft and will make the future possible.

The authors hope that the breadth of information offered here, most of which has never been collected in one place, will serve the needs of this new generation of spacecraft engineers. And, at least as important, we'll have an answer to that perennial question, "can you recommend a book about this stuff?"

Kirtland A.F.B., NM, USA
Glendale, AZ, USA
Ithaca, NY, USA

Frederick A. Leve
Brian J. Hamilton
Mason A. Peck

Contents

1	Introduction	1
1.1	Spacecraft Design, Commercial Space, and Angular Momentum	1
1.2	Momentum Control Devices and Attitude Control Systems	5
1.3	A Brief History of Spin	8
1.4	The Proliferation of Momentum Control	11
1.5	About This Book	13
References		14
2	Applications	15
2.1	Spacecraft Applications	15
2.1.1	GEO Communications Spacecraft	15
2.1.2	Agile Spacecraft Missions and ConOps	18
2.1.3	Space Stations	19
2.1.4	Small Spacecraft	21
2.1.5	Satellite Servicing	24
2.1.6	Asteroid Grappling	27
2.1.7	Space Robotics	27
2.2	Terrestrial Applications	28
2.2.1	Brennan's Monorail	30
2.2.2	Wolseley's Two-Wheeled Wonder Car	30
2.2.3	Lit Motors	31
2.2.4	Nautical Roll and Pitch Stabilization	31
2.3	Chapter Summary	32
References		34
3	Requirements Development for Momentum Control Systems	35
3.1	Quantifying Agility Requirements	35
3.1.1	Slew Angle vs. Time	36
3.1.2	Performance Ratios: Vehicle	39
3.1.3	Performance Ratios: Momentum System	40
3.1.4	Vehicle Velocity	41
3.1.5	Summary	42

3.2 Momentum Device Technology	42
3.2.1 Torque, Momentum, and De-mystifying Precession.....	42
3.2.2 The Reaction Wheel	44
3.2.3 The Double-Gimbal Control Moment Gyroscope (DGCMG).....	45
3.2.4 The Single-Gimbal Control Moment Gyroscope (SGCMG)	46
3.2.5 Vehicle Rate and the SGCMG Gimbal Torquer.....	47
3.2.6 Torque-Amplification Revisited	48
3.3 Momentum Device Technology Tradeoffs	49
3.3.1 Momentum and Torque.....	49
3.3.2 Power.....	50
3.3.3 Vibration	51
3.3.4 Torque Accuracy.....	53
3.3.5 Array Control	54
3.4 Guidelines for Selecting Momentum Device Technology	54
3.5 Chapter Summary	54
References.....	55
4 Dynamics of Momentum-Control Systems	57
4.1 Notation.....	57
4.2 Spacecraft Attitude and Momentum-Device Kinematics.....	61
4.3 Equations of Motion for a Gyrostat with Balanced Rotors	65
4.4 Relative Equilibria and Stability of Gyrostats	67
4.4.1 RWA Spacecraft	71
4.4.2 CMG Spacecraft	72
4.4.3 Large-Angle Slews	73
4.5 Control-Moment Gyroscopes	77
4.6 Actuator Jacobians	82
4.7 Rotor and Gimbal Structural Dynamics	84
4.8 Effects of Scaling CMG Actuators	90
4.8.1 Torque Amplification Degradation with Scaling	92
4.9 Chapter Summary	93
References.....	93
5 Singularities of Control Moment Gyroscopes	95
5.1 Singular Values	95
5.2 Coordinate Singularities Versus Geometric Singularities	96
5.2.1 Coordinate Singularities.....	96
5.2.2 Singularities Associated with Geometric Constraints.....	99
5.3 Control Moment Gyroscope Singularities	101
5.3.1 The Concept of CMG Singularity	102
5.4 Double-Gimbal Control Moment Gyroscope Singularities	104
5.4.1 DGCMG Gimbal Lock	105
5.5 Single-Gimbal Control Moment Gyroscope Singularities	105
5.5.1 SGCMG Gimbal Lock	106

5.6	Classification of Singularities	106
5.7	Singularity Conditions Defined Mathematically	108
5.7.1	Determination of Singularity Degeneracy	111
5.8	Hyperbolic Singularities	112
5.8.1	Non-degenerate Hyperbolic Singularities	112
5.8.2	Degenerate Hyperbolic Singularities	114
5.9	Elliptic Singularities	115
5.9.1	External Elliptic Singularities	115
5.9.2	Internal Elliptic singularities	117
5.10	Passability and Impassability of Singular Points	118
5.10.1	Impassable Singular Points	119
5.10.2	Passable Singular Points	121
5.11	Singular Surfaces for SGCMG	122
5.12	Characteristics of Singular Surfaces	125
5.13	Numerical Sensitivity in the Vicinity of a Singularity	126
5.14	Variable-Speed Control Moment Gyroscope Singularities	127
5.15	Zero-Momentum Spin Up	128
5.15.1	RWA Zero-Momentum Spin-Up	129
5.15.2	Four-CMG Roof Zero-Momentum Spin-Up	129
5.15.3	Four CMG Pyramid Zero-Momentum Spin-Up	130
5.16	Chapter Summary	130
	References	130
6	Momentum-Control System Array Architectures	133
6.1	The Nature of Momentum Devices	133
6.2	Momentum and Torque Capability of an Array of RWAs	134
6.3	Momentum and Torque Capability of an Array of CMGs	135
6.4	Double-Gimbal CMG Arrays	136
6.5	Single-Gimbal CMG Arrays	137
6.5.1	Scissored Pairs of CMGs	138
6.5.2	Collinear (Multiple-Type) Arrays	139
6.5.3	3/4 (3 of 4) Box Array	143
6.5.4	Pyramid Arrays	143
6.5.5	Dynamic Arrays	145
6.6	Blended Arrays and Other Designs	146
6.6.1	Double-Gimbal/Single-Gimbal Scissored Pairs	146
6.6.2	Langley “Six-Pac”	147
6.6.3	Single-Gimbal Six GAMS (Six-CMG Pyramid Array)	148
6.6.4	Scissored Pair with High-Torque Reaction Wheels	149
6.7	Variable-Speed CMG Arrays	149
6.8	Energy Storage	151
6.9	Optimization and Arbitrary Array Configurations	152
6.10	Chapter Summary	154
	References	154

7	Steering Algorithms	157
7.1	CMG Steering Algorithms	157
7.2	Origin of Pseudoinverse Methods	160
7.2.1	Blended Inverse	160
7.2.2	Moore–Penrose Inverse	160
7.3	Singularity-Escape Algorithms (Torque-Error Algorithms)	161
7.3.1	Singularity Robust Inverse	161
7.3.2	Singularity Direction Avoidance Pseudoinverse	162
7.3.3	Generalized Singularity Robust Inverse	163
7.4	Singularity Avoidance Algorithms	165
7.4.1	Generalized Inverse Steering Law	165
7.4.2	Local Gradient (LG) Methods	166
7.4.3	Constrained Gimbal Angle or Angular Momentum Methods	167
7.4.4	Limited Angular Momentum Methods	175
7.5	Singularity Avoidance and Escape Algorithms	177
7.5.1	Hybrid Steering Logic	177
7.5.2	Angular Momentum Artificial Potential Steering	178
7.5.3	Feedback Steering Law	179
7.5.4	Optimal CMG Attitude Control	180
7.6	Variable Speed Control Moment Gyroscopes	184
7.7	Chapter Summary	184
	References	184
8	Inner-Loop Control of Momentum Devices	187
8.1	Spin-Speed Control	187
8.1.1	CMG Spin-Speed Loops	187
8.1.2	RWA Spin Speed	188
8.2	Gimbal Rate Loops	189
8.2.1	Errors Mitigated by Gimbal Rate Loops	190
8.2.2	Impact on Vehicle Structure	190
8.2.3	Bandwidth Considerations	191
8.2.4	Friction and ACS Limit Cycling	192
8.3	Chapter Summary	192
9	Motors in Space	193
9.1	Motor Technology	193
9.2	Sizing a DC Motor	196
9.2.1	Sizing a Brushless DC Motor	197
9.2.2	Electrical	198
9.2.3	Numerical Example	199
9.3	Chapter Summary	200

10 Modeling Simulation and Test Beds	201
10.1 Math Modeling and Computer Simulation.....	201
10.1.1 First Principles	202
10.1.2 What Is the Question?	202
10.1.3 Modularity	204
10.1.4 Choices of States	204
10.1.5 Polarities	205
10.1.6 Body Models.....	206
10.1.7 Attachment Models.....	208
10.1.8 Integration.....	210
10.2 Hardware-in-the-Loop Test Beds	210
10.2.1 Precision Rotational Air-Bearing Systems	212
10.2.2 Anisoelasticity	214
10.2.3 Active Mass Balancing	214
10.2.4 Controlling the Mass-Balancing System	215
10.3 Chapter Summary	217
References.....	217
A Extended Equations of Motion for Spacecraft with CMGs	219
A.1 It Begins with A Particle	219
A.2 Components	220
A.3 Reference Frames for Spacecraft n-CMG System	221
A.4 Spacecraft n-CMG Array Kinematic and Kinetic Equations of Motion	221
A.4.1 Spacecraft Angular Momentum.....	222
A.4.2 CMG Gimbal Angular Momentum	224
A.4.3 CMG Rotor Angular Momentum	226
A.4.4 Spacecraft and Actuator Equations of Motion	228
A.5 Summary	232
B Stability Analysis of Momentum-Based Attitude Control Systems ..	233
B.1 Lyapunov Analysis	233
B.2 Rest-to-Rest Attitude Control	236
B.3 Attitude and Angular Velocity Tracking Control	239
B.4 Steering Algorithm Effects on Attitude Regulation and Tracking ..	240
B.5 Summary	242
Index	243

Author Biographies

Frederick A. Leve, Research Aerospace Engineer at the Air Force Research Laboratory, Space Vehicles Directorate, received his Ph.D. in Aerospace Engineering from the University of Florida in 2010. While at the University of Florida, he received the IAF Silver Hermann Oberth Medal and the AIAA Abe Zarem Award for Astronautics. Currently, he is the technical advisor to the Guidance, Navigation, and Controls Group and has published many papers in the area of attitude dynamics and control, specifically with respect to momentum control systems and also performs research in under-actuated control, fault tolerant control, control allocation, analytical mechanics, and system identification. Dr. Leve is a recipient of the 2014 AFRL Early Career Award.

Brian J. Hamilton, Engineering Fellow at Honeywell Aerospace, received a BSEE with Honors from the University of Illinois, 1976. Mr. Hamilton has nearly 40 years of experience at Honeywell (formerly, Sperry) and has participated in the development of CMG technology since its infancy. In recent years, his research focus has been on CMG array control and steering, and the general application of momentum systems to agile spacecraft attitude control. Other areas of specialty include nonlinear modeling, controls design, system optimization, and active magnetic suspension. Mr. Hamilton holds 12 patents.

Mason A. Peck, Associate Professor at Cornell University in Mechanical and Aerospace Engineering, received his Ph.D. in Aerospace Engineering from the University of California, Los Angeles, in 2001. He has worked as an aerospace engineer since 1994 and has been on the faculty at Cornell since 2004. From late 2011 through early 2014, he was NASA's Chief Technologist. In that role, he served as the agency's chief strategist for technology investment and prioritization and advocate for innovation in aeronautics and space technology. His research lab

focuses on fundamental research in space technology that can be advanced through flight experiments. Examples include Violet, a nanosatellite for demonstrating CMG steering laws, and KickSat, the world's first crowdfunded spacecraft. Dr. Peck holds 19 patents in the USA and the E.U. and has over 100 academic publications. He received the NASA Distinguished Public Service Medal in 2014.

Acronyms

CMG	Control moment gyroscope
DGCMG	Double-gimbal control moment gyroscope
IGA	Inner gimbal assembly
IV	Induced vibration
LOS	Line-of-sight
MBS	Mass balancing system
MCS	Momentum control system
rms	Root mean square
rpm	Revolutions per minute
RWA	Reaction wheel assembly
SGCMG	Single-gimbal control moment gyroscope
VSCMG	Variable-speed control moment gyroscope

Symbols

F_N	Inertial reference frame
F_{G_i}	i th CMG gimbal reference frame
F_{R_i}	i th CMG rotor reference frame
A	Arbitrary point in spacecraft reference frame
p_i	CMG nominal center of mass reference point at the intersection of the gimbal and rotor axes assumed fixed in the spacecraft body reference frame
C_B	Spacecraft body center of mass point
C_{G_i}	i th CMG gimbal center of mass point
C_{R_i}	i th CMG rotor center of mass point
ρ	Differential mass vector position from center of mass of a component
$\mathbf{r}_{B/A}$	Vector from point A to spacecraft body center of mass, C_B
$\mathbf{r}_{p_i/A}$	Vector from point A to point p_i
\mathbf{r}_{G_i/p_i}	Vector from point p_i to CMG gimbal center of mass point
\mathbf{r}_{R_i/p_i}	Vector from point p_i to CMG rotor center of mass point
$\hat{\mathbf{b}}_i$	Spacecraft body coordinate axis “ i ”
$\hat{\mathbf{s}}_i$	i th CMG spin coordinate axis
$\hat{\mathbf{o}}_i$	i th CMG output torque coordinate axis
$\hat{\mathbf{g}}_i$	i th CMG gimbal coordinate axis
m_B	Spacecraft bus mass
$m_{G,i}$	i th CMG gimbal mass
$m_{R,i}$	i th CMG rotor mass
m_{G,p_i}	i th CMG gimbal particle imbalance mass
m_{R,p_i}	i th CMG rotor particle imbalance mass
\mathbf{J}_s	Spacecraft rigid body inertia dyadic
\mathbf{J}_t	Rotor transverse inertia
\mathbf{J}	Spacecraft inertia dyadic for the spacecraft’s mass center, including the spacecraft as a rigid body and all momentum-control devices
\mathbf{J}_B^B	Inertia dyadic of spacecraft about its own center of mass
\mathbf{J}_A^B	Inertia dyadic of spacecraft about point A

$\mathbf{J}_{G_i}^{G_i}$	Inertia dyadic of i th CMG gimbal about its own center of mass
$\mathbf{J}_A^{G_i}$	Inertia dyadic of i th CMG gimbal about point A
$\mathbf{J}_{R_i}^{R_i}$	Inertia dyadic of i th CMG rotor about its own center of mass
$\mathbf{J}_A^{R_i}$	Inertia dyadic of i th CMG rotor inertia about point A
$J_{r,i}$	Scalar inertia component of i th CMG rotor about its spin axis
$J_{gr,i}$	Scalar inertia component of i th CMG gimbal-wheel assembly about its gimbal axis
$\mathbf{J}_{g,i}$	IGA inertia dyadic, i.e. everything that contributes to the IGA rigid-body inertia in all axes
$J_{g,\text{eff}}$	Effective scalar IGA inertia. This inertia includes everything rigid that the gimbal must accelerate along with the output-axis stiffness (K_{OA}) effect: $J_{g,\text{eff}} = J_g + \frac{h^2}{K_{\text{OA}}}$
$\mathbf{J}_{g,\text{eff}}$	Effective IGA inertia dyadic. This inertia includes everything that contributes to the IGA rigid-body inertia in all axes, along with the output-axis stiffness effect along the gimbal axis direction.
\mathbf{h}_A^B	Angular momentum of spacecraft bus about point A
\mathbf{h}_B^B	Angular momentum of spacecraft bus about its own center of mass
$\mathbf{h}_{p_i}^{G_i}$	Angular momentum of i th CMG gimbal about p_i
$\mathbf{h}_{G_i}^{G_i}$	Angular momentum of i th CMG gimbal about its own center of mass
$\mathbf{h}_{p_i}^{R_i}$	Angular momentum of i th CMG rotor about p_i
$\mathbf{h}_{R_i}^{R_i}$	Angular momentum of i th CMG rotor about its own center of mass
\mathbf{h}_r	Angular momentum vector of a single CMG rotor
\mathbf{h}	Angular momentum vector for a momentum system such that $\mathbf{h} = \sum_{i=1}^n \mathbf{h}_{r_i}$
h	Angular momentum body coordinate matrix representation for an array of CMG or RWA
h_s	Superspin
$\tau_{gf,i}$	Internal friction torque of i th CMG gimbal
$\tau_{rf,i}$	Internal friction torque of i th CMG rotor
$\tau_{r,i}$	i th scalar rotor torque for a single-gimbal CMG (for a perfectly aligned and rigid rotor)
$\tau_{g,i}$	i th scalar gimbal torque for a single-gimbal CMG (for a perfectly aligned and rigid IGA and gimbal)
τ_d	Scalar drag torque
τ_o	Vector output torque for a single-gimbal CMG (for a perfectly aligned and rigid IGA and gimbal). This torque acts on the spacecraft and is therefore is equal in magnitude but opposite in direction to the torque that acts on the CMG.
$\overset{\text{B}}{\omega}{}^{\text{B/N}}$	Angular acceleration vector of a spacecraft-fixed reference frame B relative to an inertial frame N. The overdot associated with a scalar derivative has been replaced with the letter B to indicate that the derivative has been taken relative to the B reference frame

$\omega^{\text{B/N}}$	Angular velocity vector of spacecraft body with respect to the inertial reference frame
$\omega^{\text{G}_i/\text{B}}$	Angular velocity vector of i th CMG gimbal with respect to the spacecraft body reference frame
$\omega^{\text{R}_i/\text{G}_i}$	Angular velocity vector of i th CMG rotor with respect to the i th CMG gimbal reference frame
ω	Scalar spacecraft angular rate or body coordinates matrix representation of spacecraft angular velocity (context sensitive)
\mathbf{v}_A	Translational inertial velocity of point A
$\Omega_{r,i}$	i th scalar CMG rotor rate
$\Omega_r, \dot{\Omega}_r$	Matrices of CMG rotor spin rates and accelerations
$\Delta, \dot{\Delta}, \ddot{\Delta}$	Matrices of CMG gimbal angles, rates, and accelerations
$\delta_i, \dot{\delta}_i, \ddot{\delta}_i$	i th CMG gimbal angle, rate, and acceleration
β	CMG array skew angle
γ	CMG array clocking angle
K_{OA}	Output axis stiffness
K_a	Performance ratio (maximum rate over maximum acceleration)
K_c	Performance ratio (maximum acceleration over maximum jerk)
K_T	Motor torque constant (torque per unit current)
K_{MD}	Motor K_M density (ft-lb/sqrt(W) per lb)
i	Index for a single CMG within a multiple-CMG array
n	Number of CMGs in a multiple-CMG array
m	Singularity measure
α	Singularity parameter and scalar angular acceleration (context sensitive)
j	Scalar angular jerk (context sensitive)
${}^{\text{B}}Q^{\text{A}}$	Direction-cosine matrix that relates the representation of a vector v in B coordinates (${}^{\text{B}}v$) to its representation in A coordinates (${}^{\text{A}}v$)

Chapter 1

Introduction

1.1 Spacecraft Design, Commercial Space, and Angular Momentum

The WorldView I Spacecraft shown in Fig. 1.1, successfully reached orbit on September 18, 2007.

Ball Aerospace, the prime contractor, and DigitalGlobe, the owner and operator of the satellite, celebrated this event as a technical success and commemorated the occasion with a press release that called it “a major contribution towards the advancement of the commercial remote-sensing industry by providing higher collection capabilities, more frequent revisit time, and greater imaging flexibility” (Ball Aerospace [1]). This satellite is one of several that now provides commercial earth imagery for customers that include Google Earth. It is an agile satellite, meaning that the satellite achieves comparatively high angular rates and accelerations. As a commercial agile spacecraft, it is the first of its kind.

A technology known as the control-moment gyroscope (CMG) makes Worldview uniquely agile. Until WorldView’s launch, the USA and Russian governments were the only owner/operators of spacecraft that use this technology. Examples include NASA’s Skylab, the Soviet/Russian space station MIR, and the International Space Station. These momentum-control devices enable spacecraft to absorb large external torque disturbances and to slew payloads quickly from one attitude to another. Power is a precious resource on even the largest spacecraft. So, the fact that CMGs apply these high torques with tens to hundreds of times greater power efficiency than other momentum actuators makes them an appealing choice in the design of contemporary earth-observation spacecraft.



Fig. 1.1 WorldView I satellite (Image Courtesy of DigitalGlobe Inc.)



Fig. 1.2 OrbView 4 Satellite (Image Courtesy of Orbital ATK)

Other commercial agile satellites, such as Orbview (see Fig. 1.2), DigitalGlobe's QuickBird (Fig. 1.3), Ikonos (Fig. 1.4), and GeoEye (Fig. 1.5), depend not on CMGs but high-torque reaction wheel assemblies (RWAs) as attitude-control actuators. By 2007, RWAs had been used for decades, in a variety of applications, despite that CMGs were known to offer orders-of-magnitude higher torque for the power. With the launch of WorldView I, momentum-control technologies that had been used



Fig. 1.3 QuickBird satellite (Image Courtesy of DigitalGlobe Inc.)



Fig. 1.4 Ikonos Spacecraft (Image Courtesy of GeoEye/DigitalGlobe)

only for government-sponsored spacecraft programs entered the commercial realm. Honeywell International provides the CMGs for the WorldView spacecraft. Ball was Honeywell's first commercial customer for its M95 CMGs, the smallest flight-qualified class of CMG available at that time.



Fig. 1.5 GeoEye Spacecraft (Image Courtesy of GeoEye/DigitalGlobe)

Now, nearly a decade later, CMG technologies are not only mainstream in commercial Earth observation, they are also appearing in new applications. CMGs have found their way into small spacecraft with scientific objectives, such as Cornell University's Violet nanosatellite shown in Fig. 1.6.

Violet is a 50 kg spacecraft with an ultraviolet spectrometer that is designed to make observations of the Earth's upper atmosphere to help astronomers calibrate observations of exoplanets. It has eight small CMGs, built by Goodrich Corporation. Honeybee Robotics has created golf-ball size CMGs suitable for 10–40 kg nanosatellites. The University of Florida built and launched similarly small CMGs (see Sect. 4.8). And Honeywell's miniature momentum control system (MMCS) provides a plug-and-play solution for 100–1000 kg spacecraft that require high-precision pointing performance (see Sect. 2.1.4).

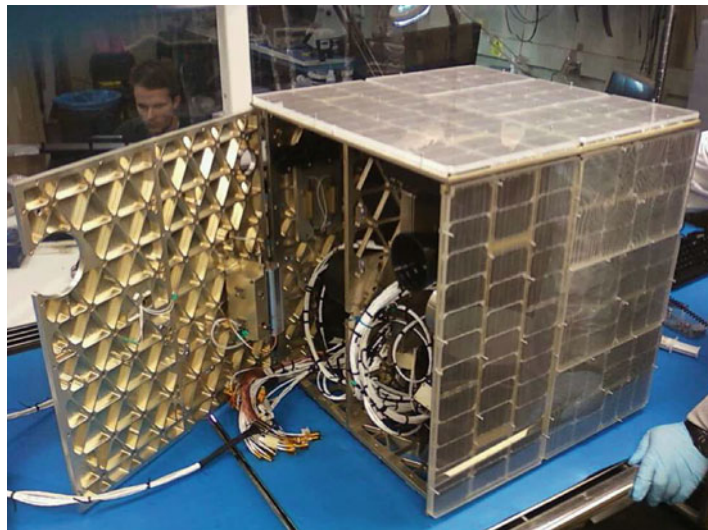


Fig. 1.6 Violet nanosatellite (Image Courtesy of Cornell University)

1.2 Momentum Control Devices and Attitude Control Systems

Spacecraft attitude control involves sensors and actuators, along with a feedback-control architecture that embraces the subtleties of spaceflight dynamics. Sensors such as star trackers and rate gyroscopes measure spacecraft motion, which onboard computers compare to desired kinematics. To correct this error, i.e., the difference between the measured and desired state, actuators such as momentum-control devices and thrusters apply torques to the spacecraft. The nature of these actuators—their torque and momentum capabilities, as well as their precision and speed of response—determines their usefulness for the range of missions that spacecraft are intended to achieve.

This book focuses on CMGs and RWAs, which are known as momentum-control devices. A spacecraft typically includes several such devices in an array. This array of actuators, along with electronics, high-level software, structural components, and possibly vibration isolators, comprises a momentum-control system (MCS). In turn, an MCS is part of the attitude-control system for a spacecraft. Figure 1.7 is a diagram that shows the relationships among these many nested elements.

Momentum devices produce torque by changing their stored angular momentum, realized in a spinning disc. Because momentum is a vector quantity, the product of angular velocity and inertia, there are two ways to effect this change. The simplest way is exploited in an RWA. The vector direction of the angular momentum of an RWA bolted to the spacecraft is constant-fixed in a spacecraft-fixed reference frame. The length or magnitude of the momentum vector changes as the wheel spins

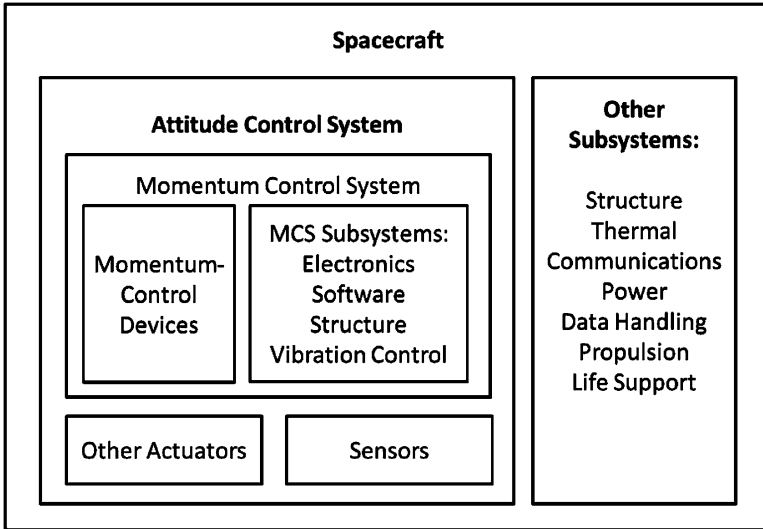


Fig. 1.7 Attitude-control centric view of spacecraft subsystems

faster or slower. In the case of a CMG, the wheel speed (and thus the magnitude of the momentum vector) is relatively constant, but a gimbal tilts the spinning rotor to change the direction of the momentum vector. The trades between these two technologies are many, and this book discusses them at some length. In each case, the device can store momentum up to a design maximum. That maximum value exists because a rotor of a given size is designed to spin at some maximum speed, typically determined by the tensile-strength limit of the rotor's material and its geometry. Going beyond that speed would incur excessive mechanical stress and fatigue, resulting in failure. Diagrams of a CMG and RWA are shown in Figs. 1.8 and 1.9.

The spinning rotors in an MCS serve two functions: momentum storage and torque application. From elementary physics, the MCS accumulates momentum as it imparts torque to the spacecraft (or reacts torque from the spacecraft, depending on one's perspective). This torque is internal, in the sense that the angular momentum of the overall spacecraft is a constant, regardless of what the MCS is doing. The MCS and the spacecraft body exchange angular momentum, but none is created. In this respect, an MCS is fundamentally different from a reaction-control system comprised of thrusters or jets. Momentum devices offer clear benefits in spacecraft design: years of operation without expending resources, the highest precision of any actuator, and freedom to place these actuators anywhere in the bus structure. But these benefits come with limitations. In a thruster-based system, the thrusters can apply torque in a given direction until the expendables have been exhausted, which may be hours to months. However, an MCS can apply torque in a single direction for only a limited time because the hardware can only accumulate a limited amount of

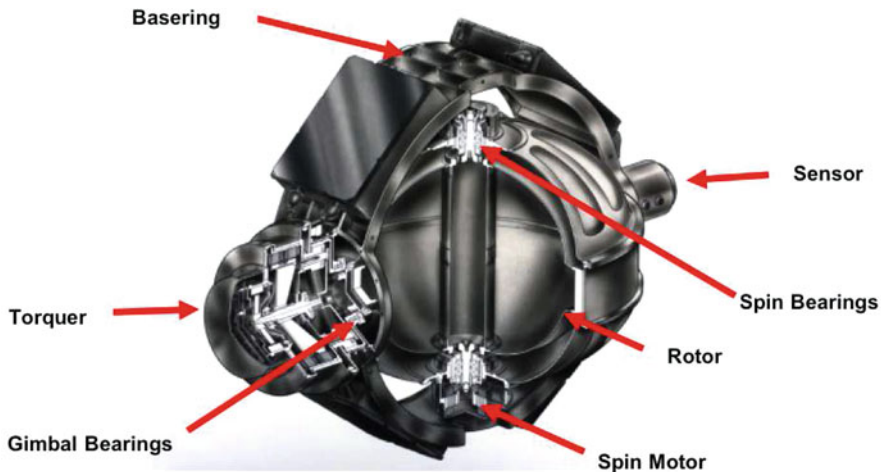


Fig. 1.8 Key components of a single-Gimbal CMG (Image Courtesy of Honeywell, Inc.)

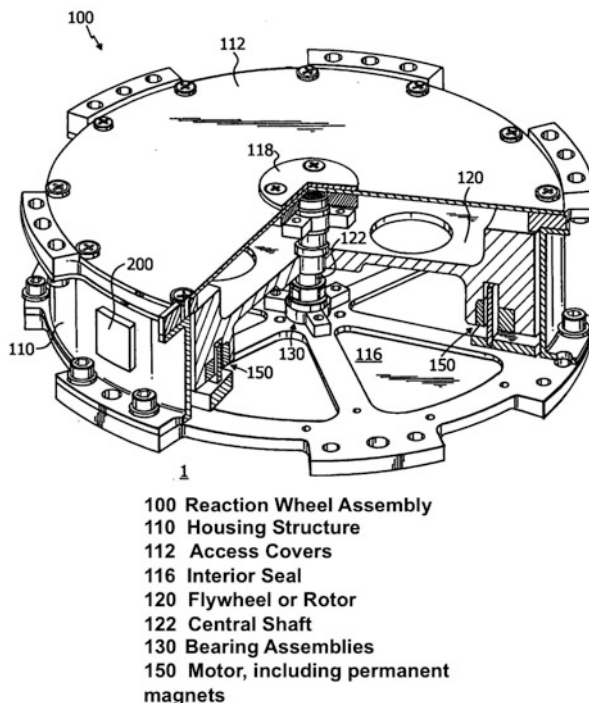


Fig. 1.9 Key components of a reaction wheel (Bialke [2])

momentum. Once the rotors have reached their maximum spin speeds or the gimbal angles have swung fully toward a given direction, the MCS cannot apply further torque to the spacecraft. Managing the momentum state of the MCS to prevent saturation or related singularities is a unique aspect of implementing momentum-control devices. Chapters 7 and 8 address this aspect in detail.

Propellant is a finite, expendable resource, while the electrical current required to change the momentum in a RWA or a CMG is typically renewable, through solar power. Therefore, thrusters are typically not used when internal torques would suffice. Another downside to thrusters is that they apply either coarse, impulsive torques or precise but long-duration ones. Chemical thrusters offer the former performance, and electric thrusters the latter. Attitude-control requirements often demand better pointing than chemical thrusters alone can provide, and they demand faster responses (higher bandwidth) than electric thrusters are capable of. Only an MCS is suited to this combination of precision and bandwidth. Table 1.1 summarizes these options.

An MCS also differs from a set of magnetic torque-coils that might be used in Earth orbit. Such devices impart a torque to the spacecraft without using expendable resources, torquing against the geomagnetic field, but the electromagnetic torque available cannot provide instantaneous three-axis attitude control because it can never lie along the geomagnetic field direction. The same is true of a gravity-gradient boom, which exploits the gradient of the Earth's gravity to cause a spacecraft to point toward nadir like a float on a fishing line. An MCS typically works alongside these external-torque actuators in order to provide a complete attitude-control solution: internal torques for high-agility and/or three-axis momentum storage, and occasional momentum unloading (or dumps) via thrusters or torque coils. This fundamental difference among attitude-control actuators drives spacecraft operations and has a direct impact on both the sizing of the MCS, and how it is used in practice. Chapter 3 addresses these issues in depth.

1.3 A Brief History of Spin

Momentum control has been a central element of successful space-systems architectures since the beginning of the space age. Some of the earliest spacecraft, such as Hughes' Syncom geostationary communications satellite, inherited a spin rate from the rockets that took them to orbit. However, earlier efforts along these lines had not been completely successful. The first successfully launched US spacecraft were the Explorer series, each of which famously, and unexpectedly, fell over into a so-called flat spin after it separated from the rocket spinning around its longitudinal, skinny axis. The skinny axis of a rigid body has the least moment of inertia. It turns out that spinning in this direction is a maximum-energy state, from which the spacecraft's dynamics can only degrade thanks to dissipative effects, such as structural damping and internal fluid motions. In the case of Explorer I and subsequent Explorer

Table 1.1 Comparison of attitude-control actuators

Actuators	Typical attitude-control applications	Agility ratio rate/acc (seconds) (smaller ratio is more agile)	Precision (deg)	ACS control bandwidth (Hz)	Torque/power (Nm/W)
Spin stabilization	Low-precision omnidirectional RF payloads and magnetospheric science	N/A	0.1–1 in 2 axes	N/A	N/A
Gravity-gradient boom	Coarse earth observation and technology demonstrations	N/A	5–20 in 2 axes	N/A	N/A
Magnetic torquers	Momentum dumps, nanosatellites in LEO, gravity-gradient augmentation	Low agility	1–10 in 2 axes	0.01–0.1	0.001–0.01
Momentum wheels	Astronomy, communications	N/A	0.001–1 in 3 axes	0.01–0.1	0.001–0.01
Reaction wheels	Astronomy, communications, earth observation	5–500	0.001–1 in 3 axes	0.01–1	0.001–0.1
Control-moment gyros	Earth imaging and radar, satellite servicing, asteroid grappling	0.5–5 (most agile)	0.001–1 in 3 axes, or better	0.1–1	1–10
Electric thrusters	GEO stationkeeping	Low agility	0.01–0.1 in 3 axes	0.001–0.01	0.0001–0.001
Chemical thrusters	Missile defense, interplanetary transfer, spin-speed adjustment and reorientation, momentum dumps	High agility	1–10 in 3 axes	0.1–1	Very high

spacecraft, long whip antennas extended from the body and dissipated this kinetic energy as they flexed, causing the spacecraft to fall over like an exhausted toy top after several hours in orbit.

In the early days of the Space Age, this skinny axis was known as the “roll” axis, using an aircraft convention that originated in nautical terminology. The coordinate axis often assigned to this axis was “Z,” and even today a typical large spacecraft associates its Z axis with the longitudinal, or skinny, axis of the rocket that takes it to orbit. Syncor and similar spacecraft learned from that mistake. They were built as squat cylinders, making the Z or roll axis the axis of maximum inertia, and therefore a minimum energy state. Syncor was therefore stable in Z spin, avoiding Explorer IV’s fate.

This so-called passive spin stabilization ensured some degree of passive attitude control for spacecraft in the early 1960s. Soon thereafter, RCA and Hughes began to exploit the dual-spin spacecraft principle: part of the spacecraft spins (known as the rotor), and part of it remains inertially fixed (known as the stator or platform). With the correct distribution of energy dissipation and mass between the rotor and the stator, the spinning portion ensures attitude stabilization of a conveniently launched, slender body that would otherwise be unstable. This innovation led to larger satellites, with more solar-panel area for more powerful payloads. The evolution of spinning spacecraft dynamics is shown in Fig. 1.10

The rotor of dual-spin spacecraft from the 1970s and 1980s soon gave way to momentum wheels. Those wheels serve precisely the same purpose as the rotor in a dual-spin spacecraft but, with higher speed and lower inertia, take up considerably less space and lead to higher-power, three-axis stabilized spacecraft buses. Some momentum wheels included a tip/tilt platform, such as on the Hughes/Boeing 601 class commercial satellites, allowing the fixed momentum to vary a little and control attitude with active feedback. The so-called momentum bias in these spacecraft ensured a stable attitude even in the presence of certain failures. The 1990s saw a general trend toward zero-momentum commercial satellites, including Lockheed Martin’s A2100, the Boeing 702 class spacecraft and others from Space Systems Loral, Ball Aerospace, and Orbital Sciences. These spacecraft use reaction wheels, with nominally zero momentum, for feedback control of attitude dynamics. Zero-momentum architectures are widely regarded as the most versatile, and lowest in power among the many ways in which angular momentum can be used in spaceflight, but with the risk that any failure that disables attitude control also leads to uncertain attitude motions.

While this trend from passive to active MCS control through RWAs continued in the commercial world, CMGs were prevalent among DoD spacecraft. Many journal publications from the late 1960s through the 1990s attest to innovations in CMG-based attitude control at Lockheed Martin, Boeing, and elsewhere. Throughout the decades, a key research question has remained: how does one distribute torque actuation among an array of CMGs, consisting of four or more, in order to avoid what are known as kinematic singularities among the actuators? It is known that no general-purpose solution allows unlimited freedom to traverse momentum space without torque limitation. Consequently, this problem has been solved for many

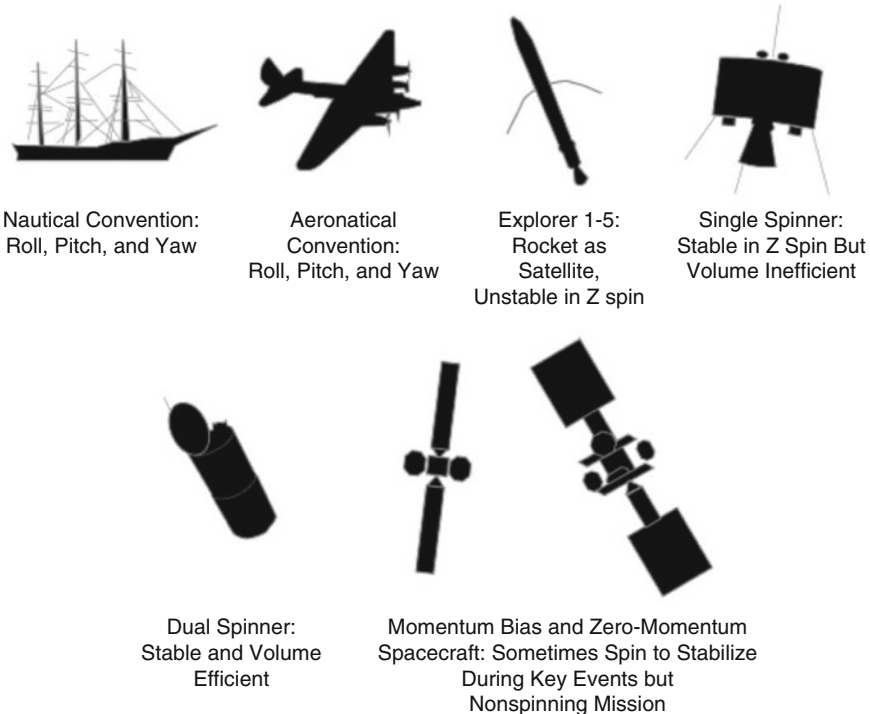


Fig. 1.10 Evolution of spinning spacecraft dynamics

special cases and in a broadly general, theoretical sense. However, a general-purpose, practicable solution that requires no future knowledge but that also exploits all possible momentum capability from a generic CMG array remains an important research objective.

1.4 The Proliferation of Momentum Control

From the 1960s through about 2000, large US prime contractors such as Lockheed Martin, Boeing, and Northrop Grumman, dominated the aerospace industry's use of CMGs in space. Now, US companies new to CMGs are pursuing satellite projects that take advantage of these capable actuators: as of this writing ATK (the former Swales in Beltsville, MD) and General Dynamics (the former Spectrum Astro in Gilbert, AZ), among others, have contemplated CMG enabled satellites.

RWAs have been used for space in the past for optical payloads that are sometimes known as reactionless coelostat telescopes (Loewenthal [3]). CMGs have more recently proven to provide lower-power reactionless robotic motions. A likely application of CMG robotics is in satellite servicing and asteroid manipulation

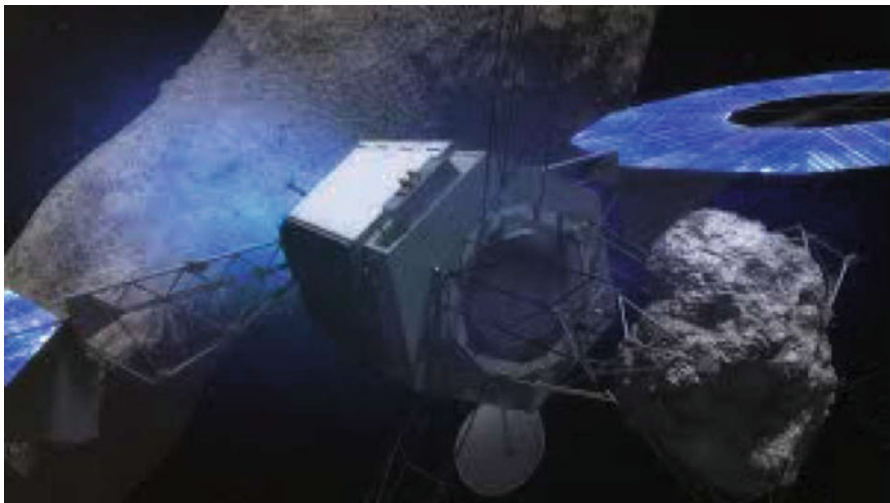


Fig. 1.11 NASA's asteroid redirect mission (ARM) (Image Courtesy of NASA)



Fig. 1.12 Vivisat's mission extension vehicle for satellite servicing (Image Courtesy of Vivisat)

because both applications benefit from a CMG's ability to absorb high external torques. A asteroid-mining or servicing spacecraft such as NASA's Asteroid Redirect Mission shown in Fig. 1.11 or Vivisat's Mission Extension Vehicle for Satellite Servicing shown in Fig. 1.12 would be able to keep its central body pointed without its central body experiencing torques from its robotic arms.

Government-funded human-space applications of CMGs are well established. They include not only Skylab, Mir, and ISS, but also the Astronaut Maneuvering Unit from the 1970s, which included six small CMGs. Someday we may see commercial human-space uses, such as hotels stabilized with CMGs.

And CMGs are moving beyond space applications. These devices turn out to be useful in ships at sea, including roll and pitch stabilization of small craft, as in the case of the SeaKeeper gyro. They are also being considered for automotive applications. Lit Motors, a San Francisco startup, intends to produce small two-wheel vehicles balanced by a feedback-control system centered on CMGs (see Chap. 2).

In the USA, commercial space is growing exponentially, with companies like SpaceX providing significantly lower cost access to space, Planet Labs launching dozens of CubeSats for global, persistent Earth imaging, and companies such as Deep Space Industries and Planetary Resources Inc. setting out to mine asteroids. An unintended consequence of the US International Traffic in Arms Regulations (ITAR) is that larger US companies have been forced to yield market share in some cutting-edge satellite technologies to overseas providers, although the USA is generally seen as leading the world in CMG technology. Long the province only of US companies, sophisticated momentum control is now being implemented throughout the world. For example, Surrey Satellite Technology Ltd. in the UK collaborated with Turkey to launch Bilsat, an early small-sat demonstrator of CMGs. EADS (in its earlier incarnation as Astrium) first built a CMG in the 1990s and continues to market it, and their subsidiary Thales/Alenia has been working on CMG-enabled spacecraft since the mid-2000s.

1.5 About This Book

This context motivates a thorough look at the technology of MCSs. The authors intend this book to serve as a technical resource for engineers, and that is why it covers a breadth of topics related to momentum control. It also provides depth in certain areas, such as the dynamics of momentum-control devices, requirements for MCSs, and a thorough treatment of CMG singularities that are entirely absent from the general texts available on spacecraft attitude dynamics, control, and astrodynamics. While of likely interest to that small, deeply idiosyncratic community of momentum-control experts, some of this unique material also ought to appeal to those with a more academic perspective. The aging of the USA aerospace engineering community means that new spacecraft engineers have fewer opportunities for mentorship and may have to take on more responsibility for challenging satellite design work than might have been expected a decade or two ago. Some of the material in this book represents sage advice collected from the experts, those who have been working in the field for many years. The technical content of this book begins in Chap. 2, with an overview of the applications of angular momentum: various spacecraft-mission architectures and operations

concepts, including agile Earth-observation, robotic servicing, human space, and some of the terrestrial applications. Chapter 3 develops requirements for spacecraft MCSSs. This discussion covers requirements flow-down from spacecraft-level issues such as day-in-the-life kinematics statistics, and other systems-engineering issues that ultimately trade risk in the context of size, weight, and power.

Chapter 4 begins a series of chapters on the core mathematics and physics of momentum devices. It offers a detailed analysis of the dynamics of spacecraft with RWAs and CMGs. Some attention is given to non-rigid effects, such as flexibility in rotors and gimbals, mass imbalances, friction, hysteresis, and materials issues. Chapter 5 offers a mathematical treatment of the singularities associated with CMG array architectures. Chapter 6 describes the many options for these architectures and offers recommendations for the most promising approaches for their use in spacecraft attitude control. Chapter 7 explains how to steer the CMGs around or within singularities for this wide variety of arrays. Appendices offer further detail on the extended equations of motion for unbalanced rotors and the impact of singularities on attitude controllability. These chapters bring together decades of academic literature and practical experience from around the world on these subtle matters. Because these chapters constitute the most mathematically demanding material in the book, it is no surprise that these topics are of current academic research interest.

Chapter 8 moves deeper within the momentum devices. It summarizes the inner-loop control of the rotors and gimbals, addressing issues such as sensors, control of the rotor spin rate and gimbal rate, and experimental parameter identification. Chapter 9 summarizes key concepts for motors in space. This section of the book wraps up with Chap. 10, which describes ways in which to represent the behavior of momentum devices in practical systems through computer modeling and test-bed validation.

The mathematical content here requires some background in vector mechanics and linear algebra. The notation the authors have adopted is explained and is meant to articulate the issues rigorously. It is consistent with many US journals and academic practice. We expect that most of the chapters will be accessible to a general audience with an engineering background.

References

1. Ball Aerospace, Ball aerospace-built worldview-1 satellite launched from vandenberg. Press Release (2007)
2. W. Bialke, Reconfigurable reaction wheel for spacecraft. US Patent 20,080,099,626 A1, 2006
3. S. Loewenthal, Reactionless, momentum compensated payload positioner. US Patent 5,751,078, 1998

Chapter 2

Applications

Virtually all spacecraft incorporate some form of momentum control. Even the simplest spin-stabilized spacecraft—nothing more than a rigid body stabilized by virtue of its own spin—might be considered to benefit from a form of momentum control. Dual-spin spacecraft incorporate a spinning “rotor” and a non-spinning “platform,” which achieves attitude stabilization through a similar but more versatile approach. Contemporary spacecraft use a wide range of momentum-control technologies—momentum wheels, reaction wheels, and several types of control-moment gyroscopes—with an ever-increasing number of applications. The applications discussed here focus on contemporary spacecraft, from small autonomous satellites to large human-space vehicles and earth-observation systems. However, the hardware and basic principles have found uses outside the field of aerospace engineering, largely in commercial applications. Examples include stabilization of trains, automobiles, and boats. As spinoffs from the high-tech, high-reliability world of aerospace make their way into other fields, one can expect to find reaction wheels and CMGs in even more surprising places.

2.1 Spacecraft Applications

2.1.1 *GEO Communications Spacecraft*

Perhaps the most commercially successful space application for momentum systems is the geosynchronous communications satellite. Arthur C. Clarke’s famous 1945 Wireless World article popularized the idea of a communications spacecraft that hovers above the Earth by orbiting at Earth’s spin rate. Thanks to that early start, GEO spacecraft were among the first to be profitable, beginning with spin-stabilized spacecraft in the early 1960s such as Hughes’ Syncom 2 (1963) and dual-spin satellites from RCA Astronautics and Hughes (among others). Momentum wheels

and reaction wheels became the preferred actuators for attitude stabilization of these ever larger spacecraft beginning in the 1980s, and that basic architecture has continued into the present.

The Hughes/Boeing 601 class spacecraft serve as an instructive example of a momentum-wheel architecture. The earliest examples include the Optus series of spacecraft (1987), but variants on this design continue to launch and operate successfully to this day. These spacecraft point an antenna farm—a payload comprised of many transponders and reflectors—toward the Earth. Pointing accuracy of a fraction of a degree is the goal for GEO spacecraft in general, and the 601 class is typical in this regard.

The solar array on the 601 spacecraft provides up to 4.8 kW of power. This level of power performance is unattainable from the smaller solar arrays of a cylindrical dual-spinner. Three-axis attitude control is required for these panels to point at the sun while the payload points at the Earth. Zammit [1] and Smay [2] offer considerable detail on this attitude-control architecture, which is summarized here. To achieve this performance, the spacecraft incorporates a momentum-wheel platform. This platform includes a momentum wheel and a tip/tilt table (or gimbals) capable of redirecting the wheel's angular momentum vector with small-angle motions. The wheel is aligned nominally with the spacecraft's pitch axis, which runs through the two solar wings and is directed along the Earth's north/south axis. This orientation keeps a momentum bias in a direction that passively stabilizes the spacecraft in an event of a failure of the attitude-control subsystem. The wheel is kept at a roughly constant speed (responding only to small errors in pitch angle). The jackscrews on the momentum-wheel platform (shown in Fig. 2.1) allow wheel to absorb disturbance torques in the roll and yaw directions.

The platform must precess this stored-momentum vector at one full rotation per orbit, since its direction is inertially constant while the spacecraft itself rotates around the Earth to keep its payload pointed at a fixed location on the surface.

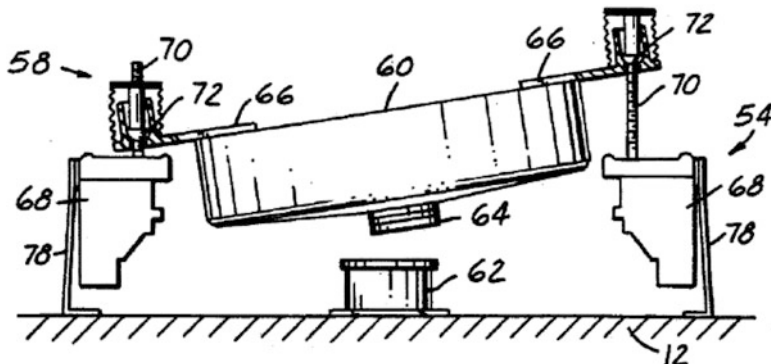


Fig. 2.1 Momentum-wheel platform (Yuan and Wittmann [3])



Fig. 2.2 Space Systems/Loral 1300 Series Satellite Bus providing hosted-payload capability for NASA’s laser communications relay demonstration (LCRD) (Image Courtesy of NASA)

The combined momentum bias and three-axis attitude control represent a successful superposition of 1970s-era passive stabilization with more modern three-axis control techniques.

Other GEO spacecraft are known as “zero-momentum” satellites because their reaction wheels do not store momentum that is intended for passive stabilization. For this reason, a momentum wheel and a reaction wheel are essentially the same hardware; they merely have different applications in the spacecraft attitude-control architecture. An example of a zero-momentum satellite is Boeing’s 702 class spacecraft, which was introduced in the late 1990s. Modern 702 spacecraft have solar arrays with wingspans larger than that of a Boeing 737 aircraft, and with power up to 18 kW (Stribling [4]). A similar spacecraft is shown in Fig. 2.2: the Space Systems/Loral 1300 series satellite bus, in this case configured for NASA’s laser communications relay demonstration. This larger size demands more headroom in the reaction-wheel array torque and momentum envelopes—i.e., the attitude-control subsystem cannot successfully react to the torque disturbances and store the resulting momentum with the very limited capability of momentum-wheel platforms. Instead, contemporary zero-momentum spacecraft use comparatively large reaction wheels, each offering up to 100 Nms of momentum and as much as 2 Nm of torque (Bialke and Stromswold [5]).

The zero-momentum approach also offers greater versatility in the operations concept, for example, in the case where a spacecraft is not in a perfectly equatorial orbit. Such a satellite might drift north/south during its lifetime to eliminate the cost

of propellant for north/south stationkeeping (Lim and Salvatore [6]). In doing so, the spacecraft also cannot simply align its pitch axis normal to the orbit plane at all times, as is the case for the 601. Instead, three-axis attitude control provides torque to follow a more subtle attitude trajectory through the reaction wheels and stores whatever momentum accumulates due to disturbance torques (from the environment, the payload, and other effects). The attitude-control subsystem dumps that momentum occasionally through reaction-control jet activity, whether chemical thrusters or electric thrusters.

Zero-momentum spacecraft use an array of reaction wheels, often four of them. These four wheels are oriented so that the failure of any single wheel results in an array whose wheel spin axes still robustly span three dimensions. There are many approaches to the design of these arrays, some of which are discussed in Chap. 6.

2.1.2 Agile Spacecraft Missions and ConOps

The concept of operations, or ConOps, for a spacecraft lays out the method by which operators use the spacecraft to achieve its mission. The ConOps of a commercial GEO spacecraft is comparatively straightforward, sometimes requiring only one operator to watch over several such satellites at a time. Others, such as spacecraft that perform Earth imaging in LEO, are more demanding. Their subtler ConOps involve frequent acquisition and loss of signal as the spacecraft flies in and out of view of ground stations. The momentum-control system is at the core of how these spacecraft function and how well they perform.

Earth imaging spacecraft such as Ball Aerospace's WorldView-3 use an array of several CMGs as a momentum system (Poli et al. [7]). These spacecraft typically operate in LEO, where they are as close as possible to the Earth's surface to optimize the size of objects on the ground that their optics can resolve. However, they are also high enough that the atmospheric drag can be overcome by an affordable amount of propellant, for a useful lifetime. This process of optimizing the design to trade off among altitude, payload performance, lifetime, and propellant is beyond the scope of this book, and it does not very directly involve the momentum system. The reason is that the specific altitude within typical LEO orbits only slightly influences the speed with which the spacecraft must reorient, or slew, to capture images.

The attitude-control subsystem has two key objectives: (1) perform large-angle, high-speed slews to direct the payload toward a point of interest on the ground and (2) maintain the attitude with sufficient accuracy and precision to allow that payload to capture imagery as it passes over the point of interest. Objective (1) demands high torque and momentum storage. Torque accelerates or decelerates the spacecraft, and momentum storage establishes the peak angular velocity that the spacecraft can reach. In addition, the rate at which this torque can change is important: it influences angular jerk, the derivative of acceleration, which turns out to drive the design of the gimbal of a CMG. The total duration of these slews depends on rate, acceleration, and jerk, as well as the flexible response of the spacecraft, fluid slosh, and other behaviors. However, it is the MCS capability that primarily determines the speed with which an Earth-imaging spacecraft can move from target to target.

This agility directly translates into profitability: the faster the slews, the more data can be collected, and the more product the spacecraft can deliver to its customers.

These two objectives work against each other, to a large extent. Fine precision, low-disturbance attitude control is hard enough. It demands very low gimbal rates to produce gentle torques that do not exceed jitter requirements. And yet this goal must be achieved with actuators that are also capable of imparting hundreds to thousands of Nm of torque. So, the dynamic range of the CMG gimbals, the dynamic and static balance of the rotors, and the structural stiffness of the MCS, are key parameters that flow down from the ConOps. Over the years, they have led to CMG technology that is necessarily both precise and powerful.

2.1.3 Space Stations

Despite that the vast majority of CMGs have been used in Earth-observation spacecraft, the most well-known applications for CMGs are in human space: Skylab, Mir, and the International Space Station.

The International Space Station (ISS) serves as an instructive example. Its MCS incorporates four double-gimbal CMGs in the Zarya module. The two gimbals per CMG enable the ISS's control system to redirect the momentum from each CMG toward any point on a sphere, with the result that the momentum envelope of the

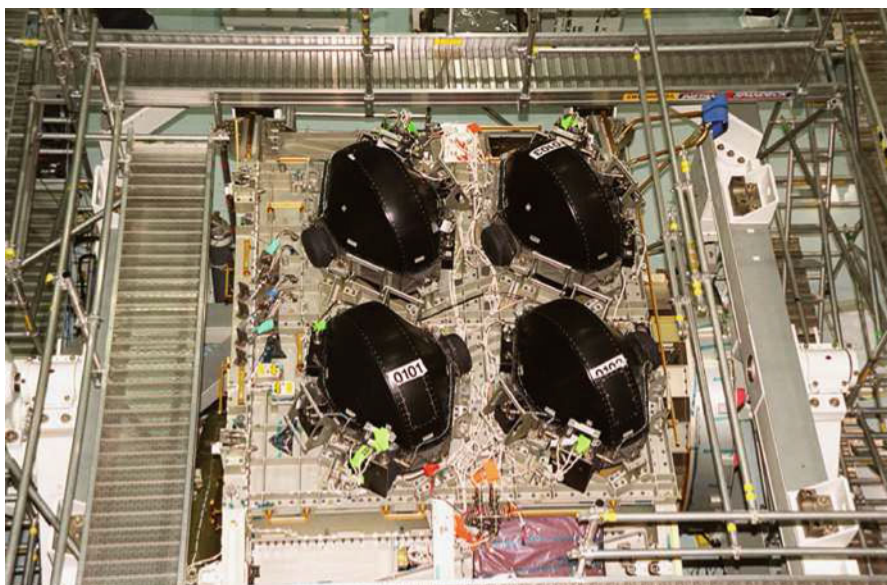


Fig. 2.3 The four ISS CMGs shown in 2000 at Kennedy Space Center's Space Station processing facility (Image Courtesy of NASA)

ISS's CMG array is a sphere four times the radius of any one of its four CMGs' angular momentum. Figure 2.3 shows this arrangement. The ConOps of the ISS includes a zero-propellant maneuver, in which the combination of gravity-gradient torque, atmospheric drag, and solar radiation pressure are largely balanced by the attitude of the body and the orientation of its vast solar array (Bedrossian et al. [8]).

Despite this innovative approach to minimizing momentum accumulation, the CMGs still need to absorb disturbances. They do so with extremely large rotors (4760 Nms) and powerful gimbal motors, producing 258 Nm output torque (L-3 [9]). The large momentum-storage capability is understandable: ISS is the largest spacecraft ever built, weighing over 400,000 kg, and one would expect large actuators for a large vehicle. But the gimbal-motor torque is disproportionately high compared to single-gimbal CMGs. It results from the double-gimbal configuration. The reason is that in such a CMG, the motion of one gimbal tilts the rotor's momentum and causes a gyroscopic torque that the second gimbal must react. In contrast, a single-gimbal CMG imparts this gyroscopic torque directly to the CMG's base ring, and from there into a stiff spacecraft bus structure, without the need for electrical power to constrain the motion. This significant savings in size, weight, and power motivate the nearly universal choice of single-gimbal CMGs in space applications.

Heritage is a powerful justification for any spacecraft design choice. ISS uses double-gimbal CMGs in part because Skylab did. In the 1960s, when Skylab was being designed, there had been only limited experience with CMGs, and no NASA project had ever used them. At that time, the problems with kinematic singularities associated in a single-gimbal CMG array were believed to be insurmountable—that one could not fly a spacecraft stably with such actuators. This belief persisted for long enough to determine Skylab's double-gimbal CMG architecture and establish the heritage for ISS. A straightforward sizing exercise suggests that an array of contemporary single-gimbal CMGs could also serve the needs of ISS and would benefit from the decades of technology development that have made CMGs a reliable solution for high-torque spacecraft.

The ISS CMGs are an outstanding engineering accomplishment. They are successfully controlling ISS and have been doing so for years. Nevertheless, they also experienced failures in the early 2000s related to electronics and to spin bearings. It is not surprising that as the first (and only) of their kind, these CMGs would represent some technical risk. The Skylab CMGs also experienced failures, the first occurring 12 days after launch: again, a bearing-related failure, which is the most common mechanical failure mode for a momentum actuator. This apparent trend—two space stations, two sets of CMG failures—should not be taken as evidence of CMG reliability in general. In fact, contrary to what these examples may suggest, no spacecraft has ever had its mission prematurely ended by a failure of a single-gimbal CMG.

2.1.4 Small Spacecraft

Small spacecraft *per se* do not represent an application area. However, they are often considered unique in that they hold significant promise for highly responsive design, build, and test. The DoD's operationally responsive space (ORS) office focuses on small spacecraft for this reason, among others (Foust [10]). One of its goals is to reduce the time to develop and launch a spacecraft by orders of magnitude: months or days instead of the current practice of over a decade.

Small scale also offers increased pointing agility, but not simply for geometric reasons. In fact, scaling every feature of a large, agile satellite's geometry down to a smallsat scale does not change its agility at all. The reason is that the spacecraft's rigid-body inertia drops with the fifth power of length (all things being equal), and so does the inertia in its momentum devices. So, the ratio of momentum to actuator inertia—roughly vehicle angular rate—is preserved for simple length scaling. The same is true for angular acceleration and jerk.

But there is an advantage. A smaller rotor can spin faster because the tensile stress in the rotor drops for smaller radii. Similarly, the structural natural frequencies of the momentum-device increase for smaller scale, all things being equal. Therefore, for a given rotor- and gimbal-speed control-loop bandwidth, the control/structure interaction is less. Alternatively, these control loops can be increased in bandwidth and remain lower than the structural frequencies. So, with higher rotor speeds and higher-bandwidth inner loops in the momentum devices, small spacecraft can achieve greater agility than their larger analogues. Momentum devices for such systems must be designed to accommodate the higher base-rate effects, as described in Chap. 3. They also may expend more electrical power to maintain rotor speed than a similar device with a lower-speed rotor.

Nevertheless, such designs are possible, as evidenced by the Violet spacecraft. This satellite is one of the entrants in the University Nanosatellite Program of the Air Force Research Lab. Violet is capable of at least 10 deg/s, 10 deg/s², and 50 deg/s³, thanks to its comparatively low inertia (about 2 kg·m² in any axis) and its Goodrich/Ithaco small CMGs. It may be capable of as high as 40 deg/s, 40 deg/s², and 60 deg/s³ (Gersh and Peck [11]). Figure 2.4 shows a drawing of the interior (left) and a photo of two of the CMGs in the partly integrated spacecraft (right).

By providing an in-orbit testbed for steering algorithms, the Violet project is designed to enable guest investigators to prove out next-generation CMG steering laws. In this respect, Violet's mission was designed to complement that of AFRL's advanced PnP technologies (APT) satellite, the spacecraft that had formerly been known as TACSAT-5 (Department of the Air Force [12]). Among other objectives, APT was meant as an experimental platform for Honeywell's plug-and-play momentum-control system, their Mini-MCS (MMCS). Violet's CMG experiments are distinct but complementary to those articulated in the 2009 TACSAT-5 Broad Agency Announcement.

- APT's objective in this area was to experimentally validate the MMCS, focusing on its suitability for plug-and-play integration in a responsive, agile spacecraft

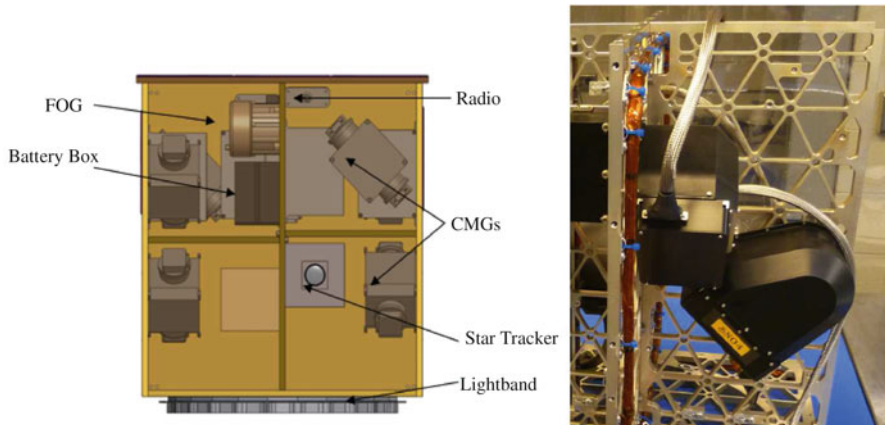


Fig. 2.4 Violet interior (*left*) and photo of two CMGs mounted on bus structural panels (*right*)

bus. In doing so it evaluated a specific CMG array architecture appropriate for responsive space. In contrast, Violet is designed to investigate the general problem of high-performance CMG steering, without explicit relevance to responsiveness.

- Violet’s experimental objectives include CMG array architectures of four, five, and six CMGs that are different from the APT array. The result is that the two spacecraft together represent a broad range of array architectures.
- APT’s CMGs and its bus were more than an order of magnitude larger than Violet’s. They occupy different operational spaces for tactical spacecraft. So, taken together, the two spacecrafts’ CMG experiments represent a broad assessment of CMG steering performance across a range of spacecraft scale.
- Violet is designed to experiment with very high agility (10–40 deg/s), while APT was meant to evaluate its CMG performance for a maximum base rate of 3 deg/s. These kinematics may be relevant for different missions, but the larger dynamic range of the two spacecraft taken together would have made the CMG experiments relevant for a wider range of applications than would either spacecraft on its own.
- APT’s MMCS was designed so that the CMGs are mechanically aligned relative to each other with high precision, and this alignment is unaffected by its soft isolation mount. In contrast, Violet’s CMGs are individually isolated and mounted. The two spacecraft will therefore be able to evaluate CMG steering in the presence of these two architectures to determine experimentally the relative benefits.

Despite APT's cancelation, the Honeywell MMCS remains a promising prospect for small-spacecraft applications because it fills a capability gap between the very small scale and the very large. This gap is indicated in Fig. 2.5. Figure 2.6 is a drawing of Honeywell's mini-MCS.

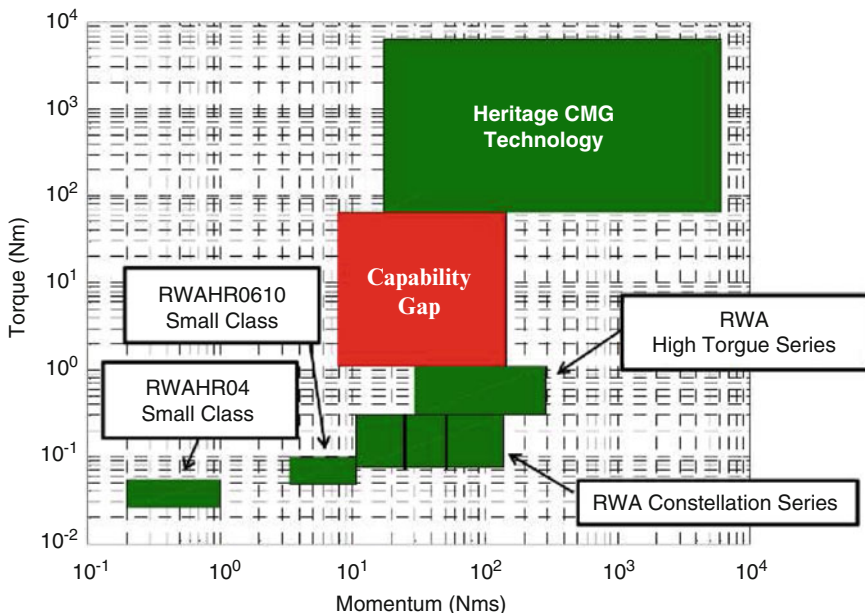
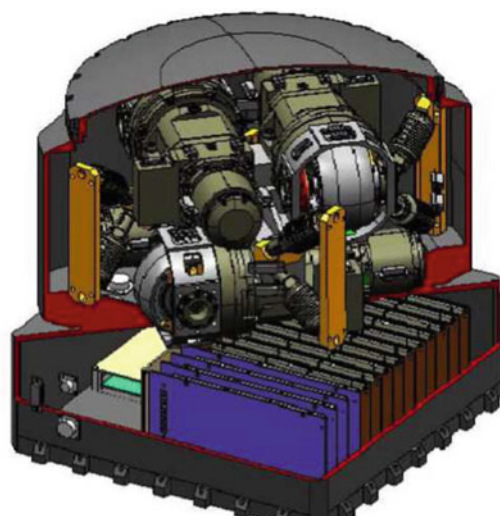


Fig. 2.5 Torque vs. momentum for some common CMGs and reaction wheels (McMickell et al. [13])

Fig. 2.6 Isometric cut-away view of miniature momentum-control system (McMickell et al. [13])



TacSat-2's mass properties and agility requirements sized the MMCS: 370 kg, with a maximum inertia of $190 \text{ kg}\cdot\text{m}^2$. A slew-rate requirement of 3.0 deg/s and angular acceleration of 1.5 deg/s^2 was meant to accommodate planned ORS missions (McMickell et al. [13]). The integrated momentum devices provide a ready solution for momentum control in a small spacecraft, filling that gap and enabling a small spacecraft to achieve the responsiveness that ORS seeks.

So-called momentum-control assemblies comprise a set of at least three devices (CMGs and/or RWAs). An MCS benefits from combining actuators, electronics, and software into an integrated package. In this package, the devices are pre-aligned and vibration-isolated, with integrated control and steering algorithms, health-monitoring, and fault tolerant software (Hamilton [14] and Hamilton and Underhill [15]). These combined attributes translate to a system that is lower mass, has better vibration rejection, and is better aligned and held to greater tolerances than separately integrated and controlled momentum devices.

Honeywell was at the forefront of developing MCS technology. With the advancements in hybrid bearings, ironless armature spin motors,, and modern singularity avoidance algorithms (see Chap. 7), Honeywell was able to dramatically reduce the mass, volume, and power draw of a momentum-control system while keeping performance constant and in many cases even increasing (Davis [16]).

Examples of two current MCS designs developed by Honeywell are the MCS8 (formally called MMCS) and MCS200. These systems consist of a four-roof CMG array with electronics. They are shown in Figs. 2.7 and 2.8 (McMickell et al. [13]).

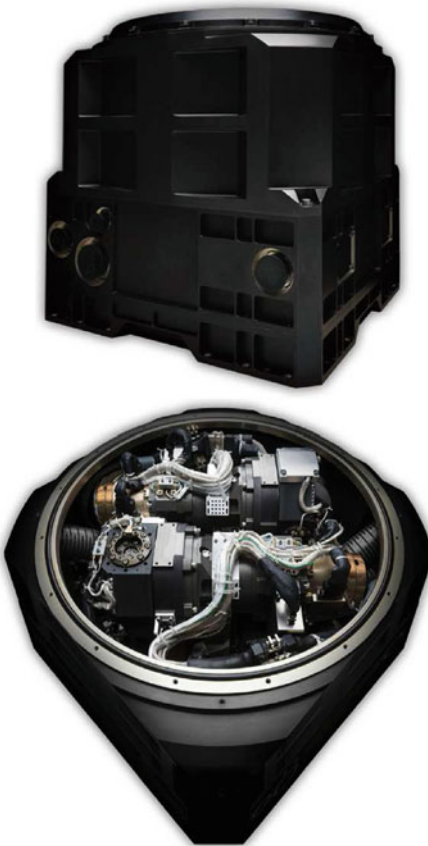
2.1.5 Satellite Servicing

Technologies for satellite servicing have seen accelerated growth in recent years. Thanks in part to Congressional support for this area within NASA's technology budget, the Satellite Servicing Capabilities Office at Goddard Spaceflight Center has demonstrated a number of successes in fluid transfer and mechanical grappling in orbit for spacecraft that include commercial satellites. This capability can extend the life of existing satellites and enable failed satellites to complete their missions. When satellite servicing becomes common, requirements on satellite reliability may be relaxed, making spacecraft more affordable.

The work has its origins in Shuttle-era repair missions beginning with Solar Max (1984). Several other commercial spacecraft retrievals and repairs followed, culminating in the series of Hubble Space Telescope repair missions in the 1990s. Currently at least two commercial companies are working in this area: ITT Exelis and ViviSat. The latter is a collaboration between ATK and Space Systems/Loral. Furthermore, DARPA has been sponsoring work on in-orbit assembly of spacecraft from components reclaimed from other spacecraft, known as the Phoenix Program.

When the servicing spacecraft makes contact with its client (or target) such as in Fig. 2.9, the angular momentum of the two becomes that of a single, joined, rigid body and manifests as angular velocity of that body. It is possible, in fact nearly

Fig. 2.7 MCS8 (Courtesy of Honeywell Defense and Space)



certain, that the mass center of the two spacecraft would be offset from the point of contact and from their relative velocity. Consequently, the angular momentum of the pair can be nonzero after contact, even if neither has angular momentum about their respective mass centers before contact.

Presumably only one spacecraft actively controls its attitude at the moment of contact. Its attitude control responds to this change in angular velocity by commanding the momentum system to apply torque. The suddenness of this change requires high torque and suggests that an array of single-gimbal CMGs may be the best choice for the momentum system of a satellite-servicing vehicle. To date, no such momentum system has been implemented. Perhaps as these capabilities evolve, in the form of a system like NASA's proposed RESTORE spacecraft, the need for CMGs in this application will become evident (Long et al. [17]).

Even more forward-looking concepts for on-orbit assembly at NASA have been considered, for example, the assembly of large space structures where the launch of the entire system is impossible. An example of such a mission is the assembly of large space structures from a multitude of heterogeneous, smaller satellites, as



Fig. 2.8 MCS200 (Courtesy of Honeywell Defense and Space)

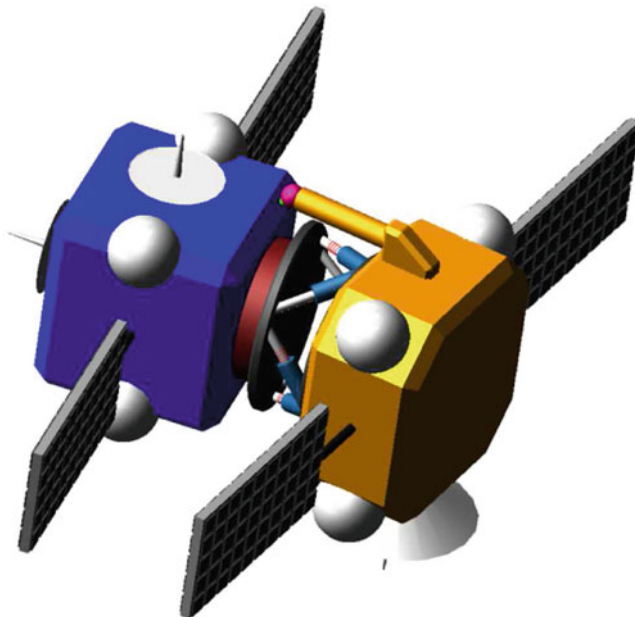


Fig. 2.9 Servicing satellite docking with tumbling defunct satellite

suggested in Fig. 2.10. Such missions require precise attitude control in addition to a high torque and angular momentum capacity, both possibly achieved through an array of CMGs.

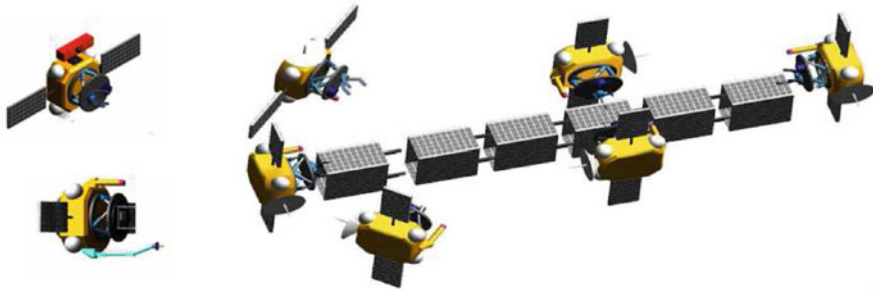


Fig. 2.10 On-orbit assembly through heterogeneous satellite platforms

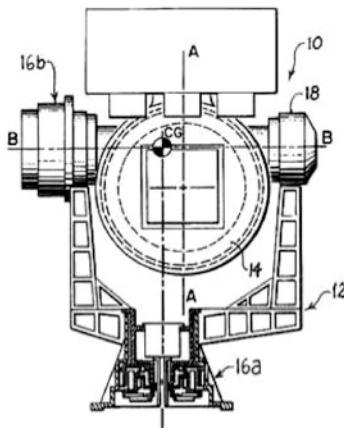
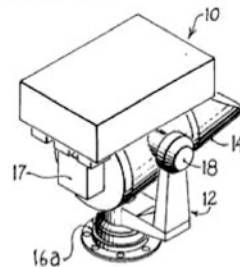
2.1.6 *Asteroid Grappling*

The problem of how to manipulate a resident space object is a common thread between satellite servicing and asteroid grappling. An important difference is that the mass properties and hard points for grappling are likely well known in the case of satellite servicing. However, an asteroid has poorly understood mass properties and may be nothing but a weakly bound collection of rubble. A satellite servicing mission may be able to feed-forward the contact disturbance. However, the unknown mass properties of the asteroid make this prospect less likely in asteroid rendezvous scenarios.

NASA's proposed Asteroid Redirect Mission is intended as a low-cost demonstration of critical technologies for Mars exploration, using existing hardware wherever possible. It also may open the door to asteroid mining and related applications of in-situ resource utilization (Strange et al. [18]). The uncertainties inherent in asteroid manipulation and the importance of mission assurance in the NASA context once again point to the need for a CMG-based attitude-control system for asteroid applications of the future.

2.1.7 *Space Robotics*

Robotics in space benefit from managing the angular momentum of a multibody system, such as a robotic arm, so that the spacecraft on which the arm is mounted feels minimal reaction. In the absence of a ground against which to react, such robotic systems pose a number of technical challenges. There are several ways to achieve reactionlessness, but a novel approach is to embed momentum devices within the multibody system, using those internal moments to steer the various links. An example is shown in Fig. 2.11.

FIG. 1**FIG. 2**

U.S. Patent

May 12, 1998
Sheet 1 of 5

5,751,078

Fig. 2.11 Reactionless Gimbal (Loewenthal [19])

This approach has been proposed for coelostat telescopes, which are optical systems that may include a “coudé” or bent path. These jointed telescopes benefit from reactionless motors, such as a reaction wheel whose momentum absorbs the motion of the telescope body. The result is a mechanically quieter system that reduces vibration of spacecraft components such as solar arrays, leading to lower optical jitter.

CMGs have also been proposed as a means to manage the momentum within a multibody system, such as a robotic arm with a camera mounted as its end-effector. A scissored pair of CMGs replaces a single reaction wheel in this concept, enabling far more agile motions for a given electrical power (Carpenter and Peck [20]). Figure 2.12 illustrates this concept. Figure 2.13 shows a prototype of a three-link system (Carpenter and Peck [20]).

2.2 Terrestrial Applications

Early technological innovation in momentum devices for space benefited from terrestrial advances in tribology and materials science. In fact, in the 1800s precursors of modern CMGs were used for nautical applications. The Sperry Gyroscope Company (founded in 1910) is the ancestor of today’s Honeywell Defense and Space Electronics Systems, where most contemporary CMGs are built. In recent years, space technology has begun to inform terrestrial applications in automotive and nautical domains, bringing momentum-control full circle.

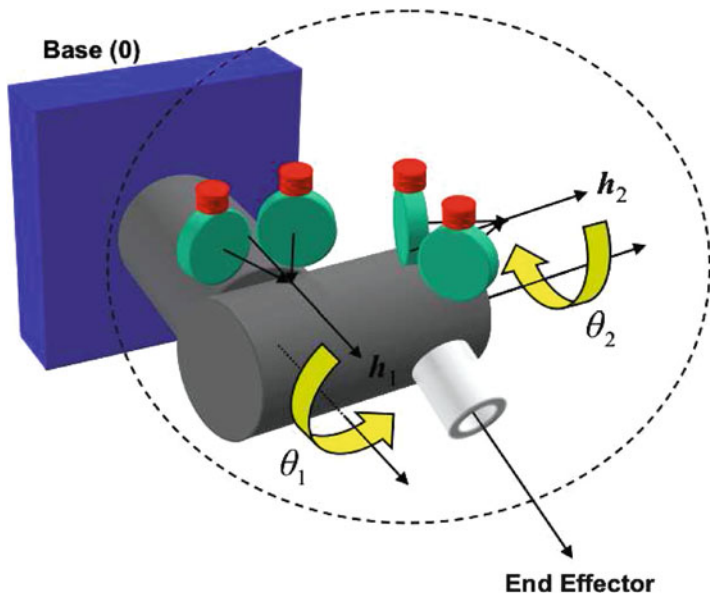
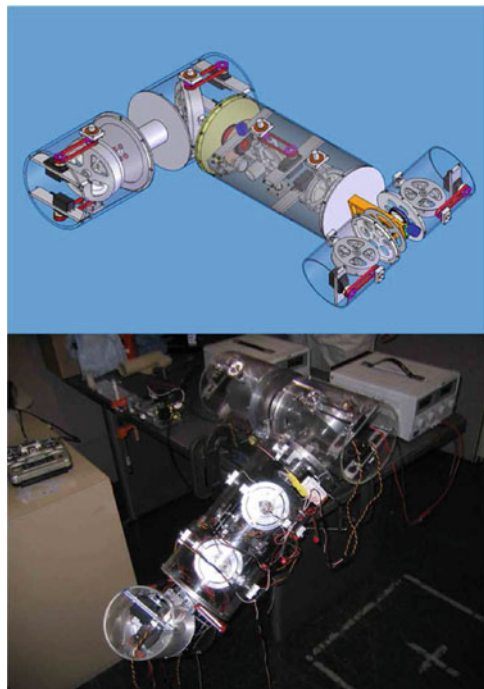


Fig. 2.12 Two-axis coelostat system with scissored-pair actuation

Fig. 2.13 CAD model of three-link robotic system with CMG scissored pairs (*top*) and prototype (*bottom*)



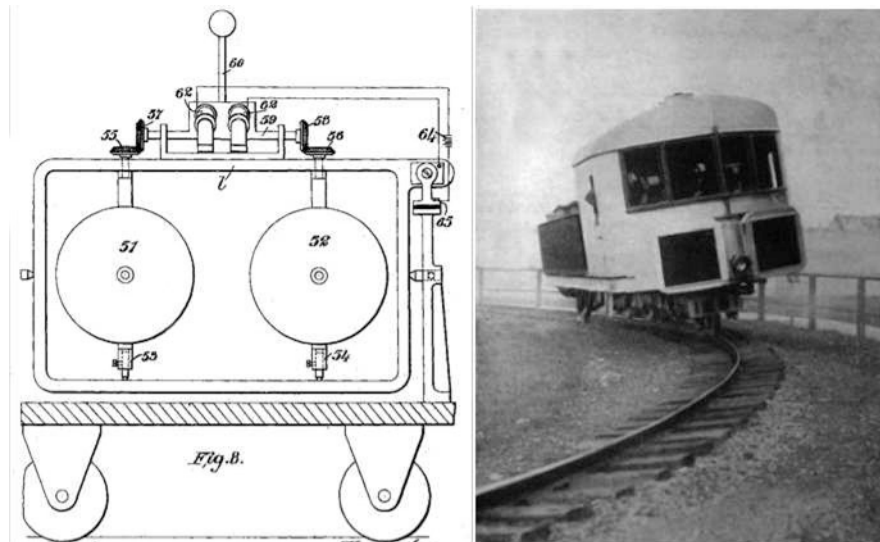


Fig. 2.14 Brennan's gyroscopic monorail. Patent (*left*), and prototype (*right*)

2.2.1 *Brennan's Monorail*

An early terrestrial application of CMGs is Louis Brennan's monorail concept (Brown [21]). Figure 2.14 shows two rotors, which resemble a scissored pair, capable of stabilizing a two-wheel cart. Gearing between the two rotors directs the gyroscopic torque along the rail direction, preventing the train from tipping over (Brennan [22]).

Brennan's monorail was featured at the Japan-British Exhibition at the White City, London, in 1910. The car carried 50 passengers on a circular track at up to 20 mph. Brennan built two such vehicles, but the concept ultimately failed to develop commercially.

2.2.2 *Wolseley's Two-Wheeled Wonder Car*

As far back as 1914, CMGs were used to stabilize two-wheeled vehicles. One such example was the Wolseley's Two-wheeled Wonder Car shown in Fig. 2.15 built in 1914. The stabilizing gyro concept for the car which consisted of 40-in. gyroscope spun at 3000 rpm, connected to weighted pendulums was finished in 1913 and the car was made public in 1914.



Fig. 2.15 Wolseley's two-wheeled wonder car

2.2.3 *Lit Motors*

Lit Motors' C-1 vehicle is a modern-day application of Brennan's principles in many respects. However, it contains a number of innovations in the feedback control of these momentum devices that would have been completely unknown 100 years ago. Its two-wheel automobile combines the speed and efficiency of a motorcycle with the accessibility of a sedan, thanks to roll stabilization provided by a scissored pair of single-gimbal CMGs. Figure 2.16 shows the C-1 in motion and its internal scissored pair.

2.2.4 *Nautical Roll and Pitch Stabilization*

The use of spinning rotors to stabilize roll (sometimes pitch) of a sea vessel goes back to the nineteenth century. These devices were passive, transmitting base rate to torque that was taken out through friction in the gimbal. In 1931 the luxury vessel Conte Di Savoia was fitted with three large gyros meant to provide a comfortable environment for its passengers. Figure 2.17 shows two of these devices.

Seakeeper Inc. currently produces a line of actively controlled CMGs for a range of seagoing vessels. They are designed to achieve 70–90 % roll reduction on boats up to 20 t, vessels 30–50'. It is a substantial advancement over its nineteenth and twentieth century predecessors, with digital feedback control of the gimbal and evacuated rotor housing. These CMGs are the largest in existence, far outperforming even the ISS CMGs in torque and momentum with up to 35,000 Nm of output torque and 78,000 Nms of angular momentum. Figure 2.18 shows five installed in a yacht.



Fig. 2.16 Lit motors C-1 vehicle (*top*) and internal scissored pair (*bottom*) (Image Courtesy of Lit Motors)

2.3 Chapter Summary

Spacecraft must manage their orientation to achieve their missions, whether through passive techniques such as spin stabilization or through active attitude control. Momentum actuators expend no propellant, and their operating lifetime often exceeds a decade. For these and many other reasons, momentum control is ubiquitous in space. It has been so since the dawn of the space age, and these principles continue to inform the design of contemporary spacecraft. An ever-increasing number of applications ensures the relevance of momentum-control principles and the value of investment in momentum-device technology development for decades to come. Some of these applications bring space technology down to earth. Examples include automotive systems like Lit Motor's C-1 and nautical applications that include roll and pitch stabilization with SeaKeeper Gyros. These examples demonstrate that the value of momentum-control technology development is not exclusive to systems for earth observation and human space. This technology can have a broad impact on robotics, transportation, and even human health in ways that the early pioneers of gyroscopic actuation likely would not have imagined.

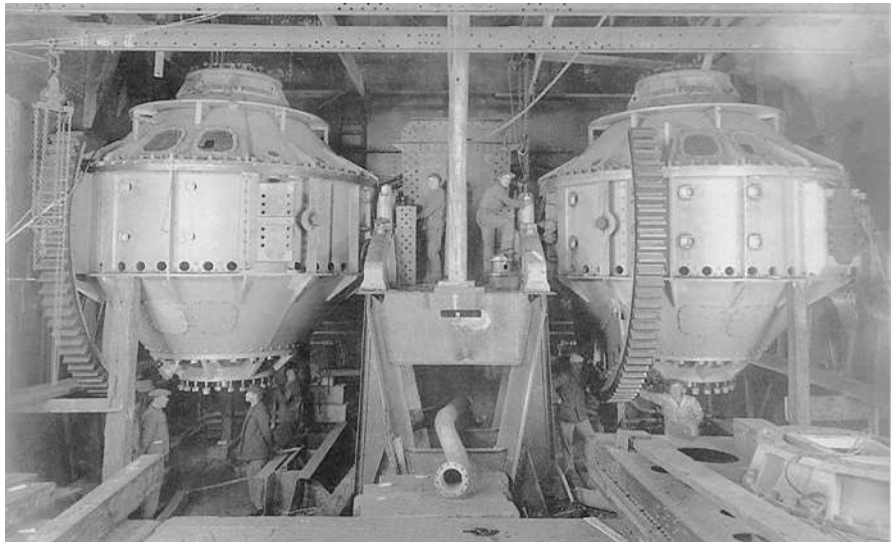


Fig. 2.17 Two of the Conte Di Savoia roll stabilizers



Fig. 2.18 Five Seakeeper gyros (Image Courtesy of Seakeeper, Inc.)

References

1. S. Zammit, Control and dynamics simulation facility at hughes space and communications, in *AIAA Modeling and Simulation Technologies Conference*, New Orleans, LA, 1997, pp. 10–01
2. J. Smay, Universal spacecraft attitude steering control system. US Patent 5,692,707, 1997
3. M. Yuan, A. Wittmann, Tilting momentum wheel for spacecraft. US Patent 5,112,012, 1992
4. R. Stribling, Hughes 702 concentrator solar array, in *Photovoltaic Specialists Conference, 2000. Conference Record of the 28th IEEE* (IEEE, 2000), pp. 25–29
5. B. Bialke, E. Stromswold, Reaction wheel actuator with two newton-meter torque capability for increased spacecraft agility, in *Proceedings of the 6th International ESA Conference on Guidance, Navigation and Control Systems*, 2006
6. W. Lim, J. Salvatore, Method and system for maintaining communication with inclined orbit geostationary satellites. US Patent App. 12/657,188, 2010
7. D. Poli, E. Angiuli, F. Remondino, Radiometric and geometric analysis of worldview-2 stereo scenes. *Int. Arch. Photogramm. Remote. Sens. Spat. Inf. Sci.* **38**(1), 1 (2010)
8. N. Bedrossian, S. Bhatt, M. Lammers, L. Nguyen, Y. Zhang, First ever flight demonstration of zero propellant manuevertm attitude control concept, in *Guidance, Navigation, and Control Conference*, vol. AIAA-2007-6734 (*Hilton Head, South Carolina*), 2007, pp. 1–12
9. L3 Space and Navigation, Double-gimbal cmg datasheet (2015), <http://www2.l-3com.com/spacnav/pdf/datasheets/>
10. J. Foust, Emerging opportunities for low-cost small satellites in civil and commercial space, in *24th AIAA USU Small Satellite Conference*, 2010
11. J. Gersh, M. Peck, Violet: a high-agility nanosatellite for demonstrating small control-moment gyroscope prototypes and steering laws, in *AIAA Guidance, Navigation and Control Conference*, 2009, pp. 10–13
12. Air Force Material Command, *Plug and Play (PnP) Spacecraft Technologies (TacSat-5)*, Broad Agency Announcement (BAA-RV-09-01), AFRL/RVKV-Kirtland AFB (2009)
13. M. McMickell, P. Davis, F. Leve, C. Schudrowitz, A momentum control system for agile responsive space satellites, in *8th Responsive Space Conference* (AIAA, 2010)
14. B. Hamilton, Turnkey cmg-based momentum control for agile spacecraft, in *AAS Advances in the Astronautical Sciences*, vol. 149, 2013
15. B. Hamilton, B. Underhill, Modern momentum systems for spacecraft attitude control. *Adv. Astronaut. Sci.* **125**, 57 (2006)
16. P. Davis, Momentum system concepts and trades for the new class of smaller lower cost satellites. *Adv. Astronaut. Sci.* **125**, 13 (2006)
17. M. Long, A. Richards, D. Hastings, On-orbit servicing: a new value proposition for satellite design and operation. *J. Spacecr. Rocket.* **44**(4), 964 (2007)
18. N. Strange, T. Landau, G. Lantoine, T. Lam, M. McGuire, M. Burke, L. Martini, J. Dankanich, Overview of mission design for nasa asteroid redirect robotic mission concept, in *33rd International Electric Propulsion Conference* (The George Washington University, Washington, DC, 2013)
19. S. Loewenthal, Reactionless, momentum compensated payload positioner. US Patent 5,751,078, 1998
20. M. Carpenter, M. Peck, Reducing base reactions with gyroscopic actuation of space-robotic systems. *IEEE Trans. Robot.* **25**(6), 1262 (2009)
21. D. Brown, Energetics of control moment gyroscopes in robotic joint actuation. Ph.D. Thesis, Cornell University, 2009
22. L. Brennan, Means for imparting stability to unstable bodies. US Patent 796,893, 1905

Chapter 3

Requirements Development for Momentum Control Systems

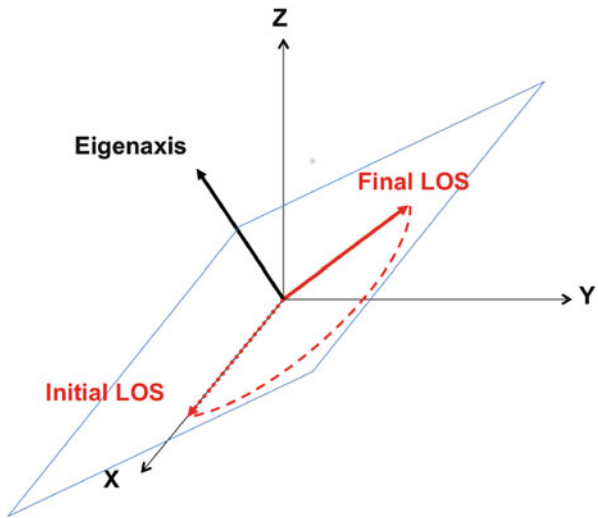
This chapter addresses the subject of how to flow spacecraft agility requirements down to an array of momentum devices and provides guidelines for choosing the appropriate technology. We shall see that the design trades in selecting and sizing momentum devices span orders of magnitude in performance, complexity, and cost. Therefore, to arrive at an efficient and cost-effective design, it is important not to over-specify the momentum-system requirements.

3.1 Quantifying Agility Requirements

We begin the process by quantifying an “agility” metric. A typical day in the life of a spacecraft attitude control system is generally allocated to two modes of operation. The first consists of tracking a target or commanded attitude profile. This mode drives requirements for stability and precision but generally does not influence the sizing of the momentum system because vehicle accelerations and rates are low in this mode. The second mode of operation, executing slew maneuvers between targets or attitudes, is where the need for agility resides. A more agile vehicle completes these maneuvers in a shorter period of time, and thus requires some combination of more vehicle rate and more vehicle acceleration. These kinematics drive the sizing of the momentum system.

Euler tells us that a rigid body can rotate about a single eigenaxis to slew from any attitude to any other, and thus for quantifying agility requirements, we shall employ eigenaxis slews (Fig. 3.1). The figure shows the line of sight (LOS) associated with the spacecraft’s payload as it slews from its initial orientation to its final orientation. This simplifies the problem to a single degree of freedom.

For a first cut at the requirements, we need to know only the angle of rotation about the eigenaxis and how long the spacecraft has to perform the maneuver. The requirements can be represented in a plane whose abscissa is time and ordinate

Fig. 3.1 Eigenaxis slew

is slew angle. For a typical day in the life, a spacecraft's slew maneuvers are represented by a collection of points in this plane. To size an MCS, we must compare these points to the capability of the MCS in that plane.

3.1.1 Slew Angle vs. Time

To analyze the problem, we must make some assumption regarding the nature of the slew maneuver profile. One example might be bang-bang acceleration. In this scenario, the vehicle accelerates as quickly as possible to some maximum velocity, then decelerates as quickly as possible at the end of the maneuver to return to the rest state. Clearly, this approach results in the fastest possible slew within the limits on the available acceleration and velocity.

There are reasons why we might choose to use a less aggressive slew profile. For example, an aggressive slew might “ring up” flexible modes in the spacecraft structure, lengthening settling time, and thereby compromising the benefit of the rapid slew. In these cases, it is common to remove various frequencies from the slew by pre-filtering the commanded motion or choosing a smooth angle-vs-time profile. An example of such a slew is the versine discussed in Chap. 4, a $1-\cos(t)$ function. A versine slew exhibits longer slew times given the same limits on acceleration (α) and velocity (ω) when compared to the bang-bang, but the frequency content may exclude the natural frequencies of the spacecraft structure. Another less aggressive approach is to limit vehicle jerk (j), the first derivative of acceleration. We shall see that in the case of CMGs, the hardware limits vehicle jerk because the rate of the CMG gimbal (and thus the vehicle acceleration) cannot be changed instantaneously. For these reasons, the analysis here focuses on a bang-bang jerk motion. This work

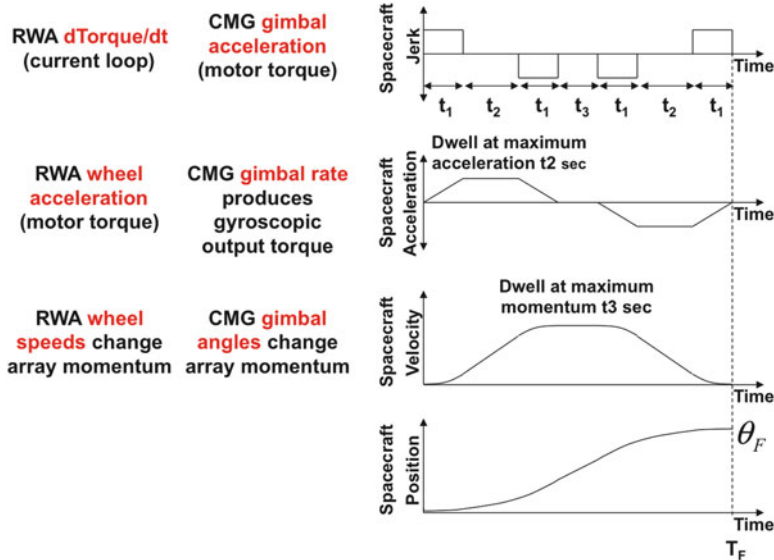


Fig. 3.2 The bang-bang jerk slew maneuver

can be modified to accommodate the chosen slew profile for a given mission, or appropriate margin can be added to these basic results.

The plots of Fig. 3.2 illustrate the bang-bang jerk slew profile, in which a finite spacecraft jerk is assumed. When this jerk is applied for t_1 seconds, the spacecraft reaches its maximum acceleration capability.

The spacecraft dwells at this peak acceleration if necessary for t_2 seconds, so that the velocity reaches the maximum available. The spacecraft then dwells at maximum velocity for t_3 seconds, if necessary, then begins a mirror-image deceleration. At the end of a slew T_F seconds in length, the spacecraft arrives at the displacement θ_F with zero velocity, acceleration, and jerk.

The text to the left of the plot identifies the physical behavior of the CMG or RWA that corresponds to jerk, acceleration, or velocity of the vehicle. For example, consider scalar angular acceleration, α which we know from one-dimensional Newtonian mechanics ($\tau = J\alpha$) results from torque τ . In the case of a reaction wheel, this torque comes from the spin motor (which causes wheel acceleration in the opposite direction). However, for a CMG, the output torque is gyroscopic, following the vector relationship $\tau = \omega^{G/B} \times \mathbf{h}_r$. The vector $\omega^{G/B}$ in this equation is gimbal angular rate, as discussed in Chap. 4. This shift by one time derivative from the CMG kinematics to the spacecraft kinematics is a characteristic of CMGs which must be understood in the sizing of the actuators. The maneuver plotted in Fig. 3.2 is characterized by the following relationships, given the fixed jerk, j :

$$\begin{aligned} T_F &= 4t_1 + 2t_2 + t_3 \\ \theta_F &= j(t_1)(t_1 + t_2)(2t_1 + t_2 + t_3) \end{aligned} \quad (3.1)$$

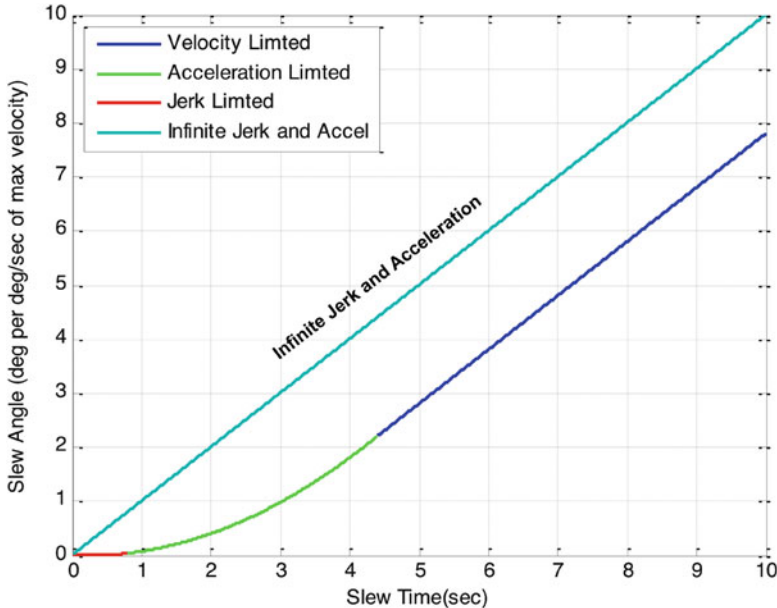


Fig. 3.3 Angle vs. time

A plot of total slew angle θ_F vs T_F consists of three distinct segments. A very short slew might consist only of four periods of jerk-limited motion, t_1 seconds each, with $t_2 = t_3 = 0$. In this case, t_1 is insufficient for the acceleration to reach its limit, and the equations reduce to

$$\begin{aligned} T_F &= 4t_1 \\ \theta_F &= j(t_1)(t_1)(2t_1) = j \frac{T_F^3}{32} \end{aligned} \quad (3.2)$$

Such a short slew is called “jerk-limited” because the limits on acceleration and velocity are not reached, and therefore only the jerk limit is relevant. Figure 3.3 plots θ_F vs T_F for a random choice of acceleration and jerk limits, and with the velocity limit normalized. The angle during the jerk-limited segment is cubic in T_F and is shown in red. For longer slews, t_1 reaches its maximum value (because the spacecraft reaches its acceleration limit), and t_2 begins to increase from 0. In this region, the slew is “acceleration limited” because the time is constrained only by the maximum acceleration; the maximum velocity is never reached. In this region, shown as green on the plot, the relationship is quadratic in T_F . Finally, for still longer slews, the spacecraft reaches maximum velocity and dwells there for t_3 seconds. For motion that falls within the “velocity-limited” segment (blue in the plot), larger displacement requires additional time, which increases linearly in inverse proportion to the velocity limit.

The unachievable, ideal case is indicated with the text “infinite jerk and acceleration.” The horizontal distance between the dark blue segment and this ideal line is the additional time required due to limitations on acceleration and jerk. In momentum-system design, there is often a trade to be made between torque and momentum, i.e., spacecraft acceleration and velocity. In view of the preceding discussion, that trade is influenced by time available for the slew. Very short slews may place more value on acceleration, and therefore actuator torque, while longer slews almost always benefit from higher vehicle velocity, and therefore momentum (Hamilton and Underhill [1] and Hamilton [2]).

3.1.2 Performance Ratios: Vehicle

We now introduce the concept of performance ratios as a convenient way to score the agility of a vehicle. Using these metrics allows us to discuss certain key time-based quantities independently of the actual angular deflection.

The previous section established that the time t_1 is bounded by the ratio of maximum acceleration to maximum jerk. Of similar importance is the ratio of maximum velocity to maximum acceleration. Both ratios have dimensions of time, which proves useful. With this in mind, we shall define two parameters, Kc and Ka :

$$Kc = \text{max acceleration} / \text{max jerk}$$

$$Ka = \text{max velocity} / \text{max acceleration}$$

Kc is the time required for the spacecraft to reach maximum acceleration given maximum jerk, and Ka is the time it takes to reach maximum velocity given maximum acceleration. By manipulating Eq. (3.1), we can identify the times at which the transitions between the segments occur as a function of the ratios, as shown in Fig. 3.4.

The jerk and acceleration limits are not shown in Fig. 3.3 but are now indicated in the lower left of Fig. 3.4 for the specific case of $Kc = 0.2$, $Ka = 2$. In the formulas, ω_{SC} is the maximum spacecraft rate. At this point in the requirements-analysis process, limits on velocity, acceleration, and jerk are not yet known. And yet, because we know the ratios among them, we can say exactly how much longer a large angle slew (blue) takes in practice compared to the ideal slew (cyan) that does not account for hardware limitations: $Ka + Kc$ or 2.2 s in this specific example. Furthermore, any slew lasting less than 4.4 s cannot reach the maximum design velocity and thus is acceleration limited. Similarly, any slew under 0.8 s is jerk-limited. Given information about how rapidly the spacecraft is required to complete its slews, we now have powerful insight into how to select quantities that directly drive the hardware design.

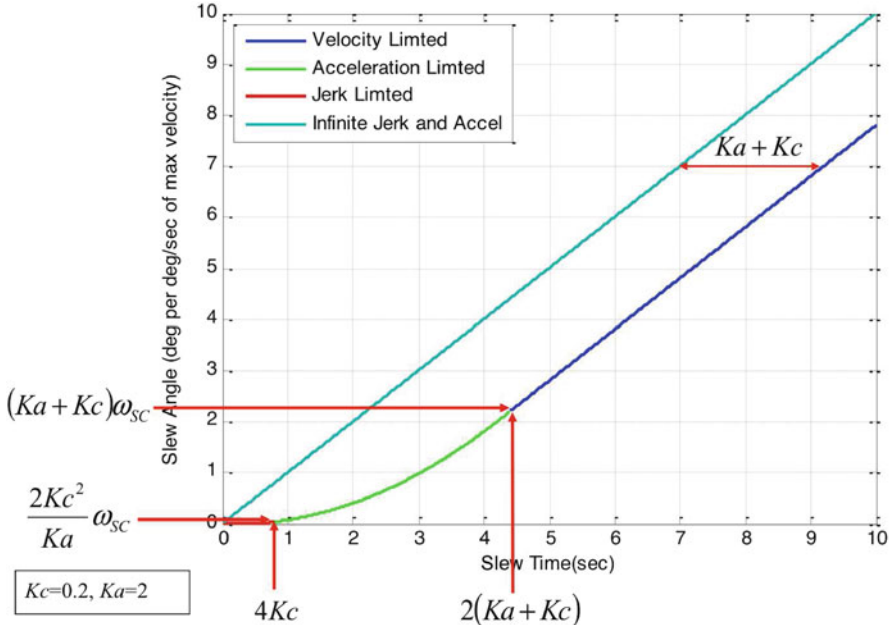


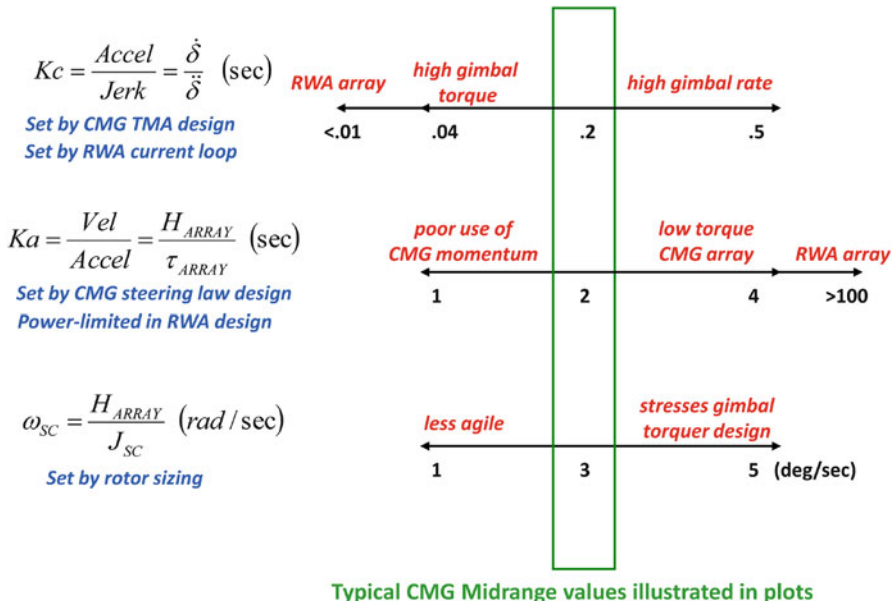
Fig. 3.4 Segment transition points

3.1.3 Performance Ratios: Momentum System

We now recall that for a vehicle slewing about a single axis, $H = J\omega$ and $\tau = J\alpha$, where in this context, J is the vehicle inertia about the eigenaxis. So if we define a quantity Ka to be the ratio of vehicle ω/α , then it is also the ratio H/τ . This ratio is important because momentum and torque are the key performance parameters of the array of momentum devices. Similarly, as in the annotations of Fig. 3.2, if Kc is the ratio of vehicle α/j , it is also the ratio of the CMG gimbal $\dot{\delta}/\ddot{\delta}$. With these general principles in mind, let us examine typical values of these ratios for realistic momentum devices, as illustrated in Fig. 3.5.

The ratio Kc represents the time the vehicle takes to reach maximum acceleration (torque). For an RWA, where achieving the necessary torque requires only applying current to the motor, this happens very quickly (Kc is very small). However, for a CMG, achieving the necessary vehicle torque requires accelerating the gimbal to its maximum rate. For typical CMGs, reaching this peak gimbal rate takes around 200 ms. This time is driven by the gimbal torque-motor design.

The ratio Ka represents the time the vehicle takes to reach maximum velocity (given maximum acceleration). For an RWA, where torque is limited by power considerations, this number is typically large (>100 s), i.e., an RWA can take



Typical CMG Midrange values illustrated in plots

Fig. 3.5 Typical performance ratios

minutes to accelerate to its maximum speed. However, a CMG can change its momentum direction over the angular range of interest in seconds. The low values of K_a possible using CMGs make agile vehicles practical.

Some caution must be exercised in choosing K_a and K_c to be very far from these typical values. We know that performance is driven by the sum of these two, and K_a is generally larger. One might therefore jump to the conclusion that reducing K_a as much as possible is the right choice, and this might be achieved by increasing gimbal rate (more torque). The fallacy here is made evident by recognizing that increasing gimbal rate also increases the value of K_c , thus diminishing the return. The H and τ available at the array level are also influenced by how the array is controlled (see Chap. 7), and this is another way to influence K_a .

3.1.4 Vehicle Velocity

The shape of the curve in Fig. 3.4 and the times associated with the different segments are completely determined by the ratios K_a and K_c . The final quantity referred to in Fig. 3.5 is the maximum vehicle velocity. This quantity scales the ordinate (slew angle) axis of Fig. 3.4, completing the picture. We now have a way to directly relate these three parameters to the slew angle vs. time requirements.

It is useful to note that these relationships hold for spacecraft of similar agility regardless of their size. Recalling that $H = J\omega$, the chosen vehicle velocity combined with the inertia of the vehicle directly influences the net momentum that the array of CMGs or RWAs must produce. This requirement in turn influences the size of the momentum devices, and thus the size, weight, and power of the momentum system.

3.1.5 Summary

This section established the general approach for translating vehicle agility into momentum-system requirements. Once we know the momentum and Ka required, we can begin the process of momentum device selection. Other factors will also enter into these trades, as explained below.

3.2 Momentum Device Technology

Momentum devices fall into two broad categories. First, the RWA, is a single degree-of-freedom device consisting of a rotor and a motor. In this device the rotor speed is manipulated, producing a momentum vector of varying length, whose direction is fixed in the body frame. The other category, the CMG, is any of various devices employing motorized gimbal mechanisms to redirect the rotor spin axis. In this device the rotor is typically spun at a constant speed, resulting in a momentum vector that has fixed length, but varying direction. Either type of device can be used to produce attitude control torques by exchanging momentum with the spacecraft. But we shall see that there are practical advantages to using certain device types for certain applications. This section discusses each of the devices. Subsequent sections examine each of the key trades and offer guidelines for selection.

3.2.1 Torque, Momentum, and De-mystifying Precession

Before we can discuss these devices, we must digress briefly to review some fundamental physics. Of interest is what happens to a body when it experiences a torque. Chapter 4 provides the foundational mechanics. This section seeks to complement those mathematics with physical insight.

We begin with a body at rest, for example, an RWA rotor with zero spin speed. Its angular momentum, \mathbf{h} , is zero. By definition torque is the rate of change of momentum in an inertial frame, $\boldsymbol{\tau} = \frac{d\mathbf{h}}{dt}$, and both are vector quantities. If we apply a constant torque in the y direction for time dt , as shown on the left side of Fig. 3.6, the resulting angular momentum is $d\mathbf{h}$ in the y direction. If we continue to apply the

torque for another dt seconds, and then another, the net angular momentum vector continues to grow in the y direction. Since the angular momentum of a body is related to its inertia and rate by $\mathbf{h} = \mathbf{J}\omega$, body rate increases by $d\omega$ for each dt time increment. This increase is an acceleration, α , following the familiar equation:

$$\tau = \frac{d\mathbf{h}}{dt} = \mathbf{J} \frac{d\omega}{dt} = \mathbf{J}\alpha \quad (3.3)$$

Now, what if the body is not initially at rest? We next consider the case in which the body is initially spinning about the x axis of Fig. 3.6, such as in the gimbal mount of a CMG. Its initial angular momentum, \mathbf{h}_r , is large (relative to the magnitude of $d\mathbf{h}$) in the x direction. If we apply a constant torque as before about the y axis for time dt , the resulting angular momentum is the vector sum of the initial \mathbf{h}_r and the $d\mathbf{h}$ in the y direction. If we continue to apply the torque for another increment dt , and then another, the net angular momentum vector continues to change and begin to arc over toward x , as illustrated in the right side of Fig. 3.6.

The figure shows how the net momentum vector varies for this case. As we can see, the net momentum started in the x direction and is rotating about an axis out of the plane of the page. With the passage of each dt , the net vector rotates through an additional angle $d\delta$ in accordance with $d\mathbf{h} = d\delta \times \mathbf{h}$. This result says that the torque results in a body rate (not an acceleration as before), and that rate is about an axis out of the plane of the page. Specifically,

$$\tau = \frac{d\mathbf{h}}{dt} = \frac{d\delta}{dt} \times \mathbf{h} = \omega \times \mathbf{h} \quad (3.4)$$

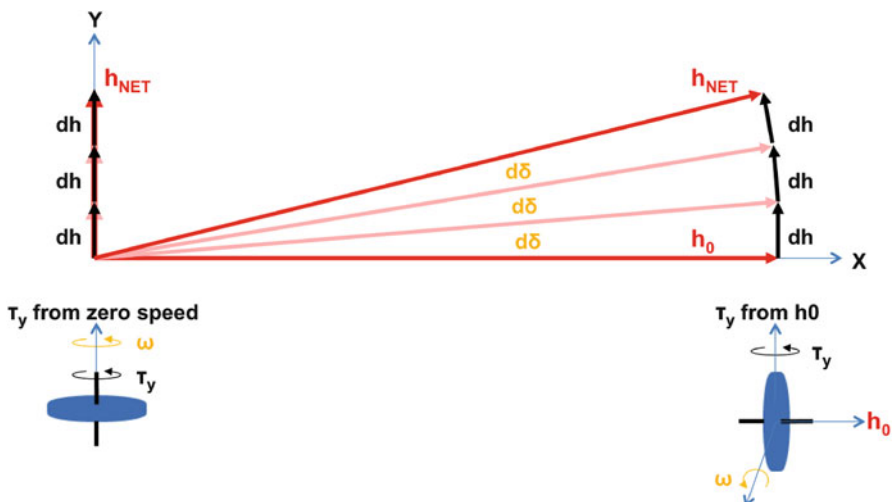


Fig. 3.6 Increments of momentum

Equation (3.8) is the classical precession result from undergraduate studies of gyroscopic dynamics. For many, the spatial (cross product) and temporal (one time derivative) differences between $\tau = \mathbf{J}\alpha$ and $\tau = \omega \times \mathbf{h}$ are inexplicable and simply taken on faith. But we can now see that both behaviors are the direct result of the same $\frac{d\mathbf{h}}{dt}$ when a torque is applied. This is a recurring theme: when studying momentum devices, it is much more instructive to visualize momentum vectors than torque.

3.2.2 The Reaction Wheel

This momentum device operates in a single degree of freedom, with the spin axis of the rotor fixed to the vehicle structure by spin bearings as illustrated in Fig. 3.7. The output torque is produced directly by the same motor that controls rotor speed. That is, the motor acts on the rotor, and reacts on the spacecraft—hence the name “reaction wheel.” The action on the rotor causes it to accelerate as $\tau = \mathbf{J}\alpha$, as discussed in the previous section.

In the production of torque, this machine uses mechanical shaft power equal to torque times the spin speed of the rotor: $P = \tau \cdot \omega$. As such, it uses the greatest energy possible in changing its angular momentum. Typical large RWAs have maximum rotor speeds in the range from 2000–6000 rpm, with small RWAs going even higher. At 2000 rpm, 1 Nm of torque (0.74 ft-lb) requires 209 W of power, without even considering the heat power dissipated in the motor, electronics and bearings. To reduce the power, one could modify the rotor design by reducing its speed and increasing its inertia (size, weight), but these trades have disadvantages of their own. Therefore reaction wheels capable of greater than 1 Nm of torque are rarely seen.

Fig. 3.7 Reaction wheel

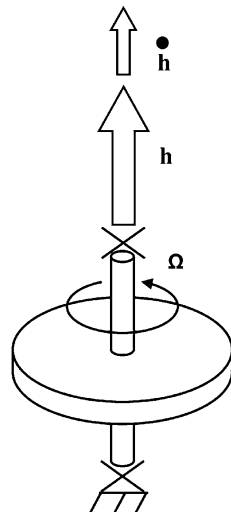
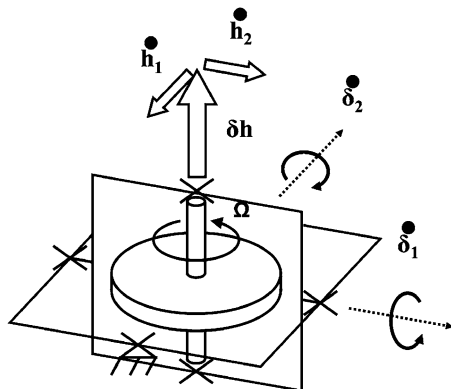


Fig. 3.8 Double-gimbal control moment gyroscope



3.2.3 The Double-Gimbal Control Moment Gyroscope (DGCMG)

Unlike the RWA, which fixes the spin axis to the vehicle using bearings, this device allows the rotor's spin axis to rotate in the spacecraft reference frame using a double-gimbal mount, as illustrated in Fig. 3.8. Also unlike the RWA, the rotor's spin speed is constant during normal operation.

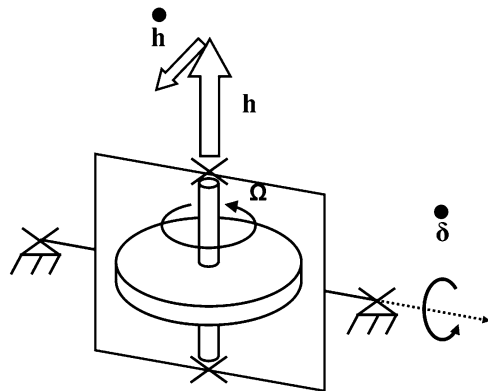
In this configuration, the rotor acts as a free gyroscope. It has an angular momentum vector \mathbf{h} , directed along its spin axis, with magnitude $J_r\Omega_r$. When torque acts on the rotor, it precesses in accordance with $\tau = \boldsymbol{\omega} \times \mathbf{h}$ as derived in Sect. 3.2.1.

As in the RWA, the output torque of this device (the torque applied to the spacecraft) is directly the result of motor reactions. The outer gimbal motor reacts directly, while the inner gimbal motor reacts through the outer gimbal bearings. As such, the motors that position these gimbals must be sized to produce the entire output torque for which the device is designed in addition to their own control torques.

However, unlike the RWA, the rotation speed of these motors is very low compared to the spin speed of the rotor. We recall that the RWA motor is severely limited in torque capability due to the mechanical power ($P = \tau \cdot \omega$). The CMG does not have this limitation, and can therefore produce greater output torques.

It can be shown (see Chap. 9) that, holding the power density and K_M density constant, both the power and weight of a typical motor increase as the $2/3$ power of torque. As the motor size increases, so do the gimbals and their associated structure. Introducing gearing can help. However, eventually it becomes a challenge to design a double-gimbal CMG with reasonable and prudent structural mode frequencies and we again reach a limitation on torque production. This limit generally falls in the rough vicinity of 50–100 Nm. Perhaps the largest DGCMGs ever built are those produced for the International Space Station, which are rated at 300 Nm.

Fig. 3.9 Single-gimbal control moment gyroscope



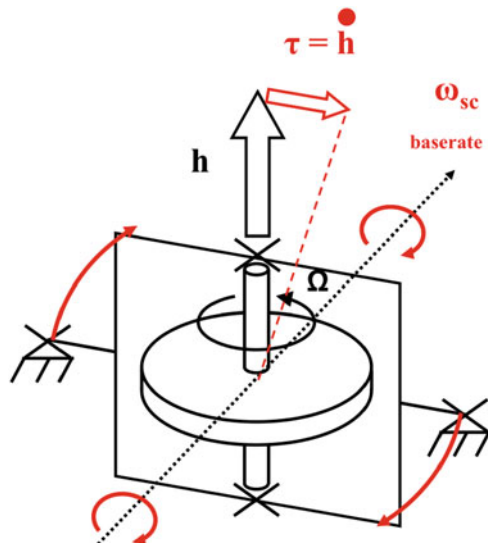
3.2.4 The Single-Gimbal Control Moment Gyroscope (SGCMG)

The single-gimbal CMG (SGCMG), as illustrated in Fig. 3.9, can be thought of as the DGCMG of Fig. 3.8 with the outer gimbal (about δ_2 , above) removed. As a result, the rotor spin axis is constrained to move in the plane normal to δ . If we torque on the rotor with this single inner gimbal, we would expect the rotor to precess about the axis of the outer gimbal (δ_2 in a DGCMG). Since that gimbal has been removed, a constraint torque arises that eliminates motion in that axis, acting on the spacecraft through the inner gimbal bearings. This torque performs no mechanical work but is sufficient to cause the rotor instead to precess about the gimbal axis at the gimbal rate.

This curious by-product of gyroscopic physics results in a machine that possesses significant “torque amplification.” This term describes a device with a relatively small gimbal motor that can produce very large output torques. Indeed, if such a device were attached to a fixed test frame and had very stiff gimbals (imposing the constraint), one could not even tell by examining the dynamics of the gimbal axis that the rotor was spinning. The motor torque required is simply that necessary to accelerate the gimbal inertia to produce the desired gimbal rate. The output torque felt by the spacecraft is then the constraint torque $\tau = -\dot{\delta} \times \mathbf{h}$, where $\dot{\delta}$ is the gimbal rate and \mathbf{h} is the rotor momentum vector.

This torque-amplification effect makes the single-gimbal CMG the clear power-efficient choice for the most agile vehicles, requiring the largest torque output. Large SGCMGs are in service in spacecraft applications with output torques well in excess of 1000 Nm. Very large CMGs for terrestrial applications exist with output torque in excess of 100,000 Nm that only require a few kW to operate.

Fig. 3.10 Response to vehicle base rate



3.2.5 Vehicle Rate and the SGCMG Gimbal Torquer

The preceding section stated that the dynamics of a SGCMG gimbal is independent of rotor momentum for the case of a very stiff gimbal fixed to a test frame. We now consider the implications of having the device mounted to a spacecraft, which can be in motion. We call this spacecraft motion the “base rate” of the CMG.

Specifically, we consider the case in which the vehicle is rotating with an inertial velocity ω_s about the output axis of the SGCMG (dashed black in Fig. 3.10). Those same gimbal bearings that provided the constraint in the earlier discussion must now force the rotor to rotate with velocity ω_s about the output axis along with the vehicle. This configuration is illustrated in Fig. 3.10.

Because this is a gyroscope, if the bearings were to torque the rotor about the (dashed) output axis, the rotor would precess about the gimbal axis. To prevent this gimbal rotation, enough gimbal axis torque must be applied to make the rotor instead precess (along with the vehicle) about the output axis, thus unloading the bearings. If the gimbal torque motor is not strong enough to apply this torque, control of the gimbal is lost.

Only a torque about the gimbal axis can cause the gyroscope to move with the vehicle, and this torque must come from the gimbal torque motor. For large, agile vehicles, the base rate effect can quickly become the dominant sizing driver, often requiring the torque motor to utilize a gearbox and/or draw a lot of power.

As we are assuming the worst case, where the vehicle base rate is purely about the CMG output axis, the gimbal must produce a torque of $\tau_g = \omega_s h$. Remembering that the momentum of the CMG is sized to produce a desired vehicle momentum $H = J_s \omega_s$, we conclude that the requirement for gimbal torque is

$$\tau_g \approx J_s \omega_s^2 \quad (3.5)$$

We use the \approx sign above to acknowledge that this equation does not distinguish between CMG momentum (h) and array momentum (H). However, regardless that the gimbal torque may be somewhat less, the recognition that it varies as the square of vehicle rate is the basis for the note about high vehicle rates in the lower-right of Fig. 3.5.

As a rule of thumb, gimbal torque less than 5–10 Nm can be produced by a direct-drive CMG, i.e., without gears. Above this level, the weight and power of the gimbal usually drives a geared design. Geared CMGs are common on large, agile spacecraft, but they are more complex and expensive to produce.

3.2.6 Torque-Amplification Revisited

Now that we have quantified the effect of base rate on the gimbal torque, we can quantify the torque amplification. Earlier, it was suggested that the gimbal motor need only be sized to accelerate the gimbal inertia, but we now understand that it must also be sized to oppose the precession from base rate. So

$$\tau_g = J_g \alpha_g + \omega_s h \quad (3.6)$$

The output torque from the CMG has already been shown to relate to the gimbal rate, ω_g , as $\tau_o = -\omega_g \times \mathbf{h}$. Since these axes are always orthogonal, we have the scalar magnitudes

$$\tau_o = \omega_g h \quad (3.7)$$

Combining these two equations, and assuming the gimbal acceleration torque is small compared to precession, we find that for any momentum:

$$\text{torque amplification} = \frac{\tau_o}{\tau_g} \approx \frac{\omega_g}{\omega_s} \quad (3.8)$$

This is a very powerful observation for spacecraft, whose maximum rate rarely exceeds a few degrees per second. Gimbal are easily designed with rates of 1 rad/s or more, therefore a SGCMG can achieve torque amplification easily over a factor of 10 on most spacecraft, and nearly 100 on some.

Alternatively, Eq. (3.8) also explains why CMGs are not often found in applications such as aircraft, which might be rolled at 30 deg/s or more. The potential for high base rate reduces the amplification, drives larger torque motors and negates the advantage of the technology.

3.3 Momentum Device Technology Tradeoffs

3.3.1 Momentum and Torque

All of the candidate devices can be designed to store similar amounts of momentum. The design needs only a rotor with a certain combination of inertia and maximum speed. Given the same momentum, all the devices can produce similar spacecraft velocity, and/or absorb similar amounts of stored momentum.

However, distinctions among the various technologies discussed in Sect. 3.2, make it clear that the range of torque available varies dramatically. The discussion of Sect. 3.1, in which Ka is defined as h/τ , provides the key insight. A reaction wheel, which can have the same momentum as other momentum devices but is severely torque-limited, exhibits the highest Ka . The DGCMG is in the middle, and the SGCMG has the lowest value.

Ka defines the time it takes to accelerate the vehicle to maximum rate and thus determines how much longer a real slew requires than the ideal slew (one not constrained by the device physics). The trade, therefore, comes down to agility. Figure 3.11 illustrates the tradespace for the various MCS technologies. The plot

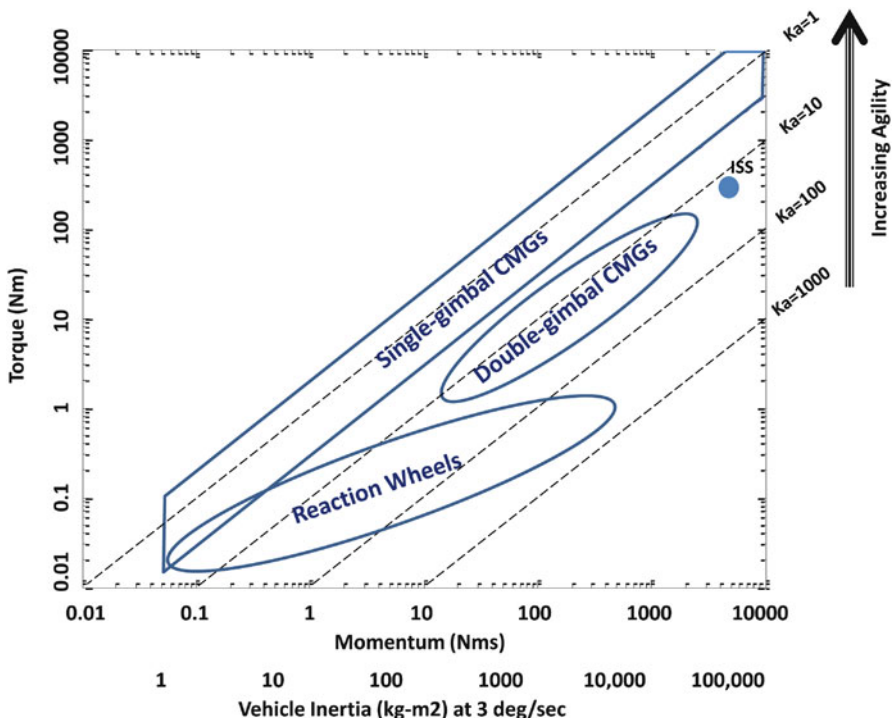


Fig. 3.11 Torque, momentum, and agility of MCS technologies

shows torque vs. momentum and includes dashed lines for various values of the agility metric, Ka . For convenience, the abscissa has a second scale showing the vehicle inertia that would require the indicated momentum for a slew rate of 3 deg/s. Reaction wheel designs fall in the region of torque less than 1 Nm, and the torque is even less for smaller devices with smaller motors. Because the torque does not drop linearly, lower Ka values are achievable using this technology on small spacecraft.

The design range for double-gimbal CMGs is generally less than 100 Nm, although the design mentioned earlier for the International Space Station is plotted with a single dot, illustrating how far out of family it falls. Because of the torque-amplification principle, devices with more momentum can produce larger torques using similar gimbal rates. This principle results in a linear slope.

Finally, the range suitable for single-gimbal CMGs provides the highest agility regardless of the size. Only SGCMGs can reach Ka values approaching 1, and they can do so over the entire tradespace. Recall that the CMG gimbal torque required is driven mostly by vehicle inertia and vehicle velocity squared, while a gimbal rate of 1 rad/s results in Ka near 1 for any size. This analysis neglects the effects of array steering on Ka , which are discussed in Chap. 7.

The lowest values on the plot presume that we are referring to traditional mechanical systems, fabricated with traditional techniques, and it is understood that by using MEMS technologies, even smaller devices are possible.

3.3.2 Power

As discussed previously, in producing torque the RWA uses mechanical power approximately equal to torque times spin speed. Typical large RWAs have maximum rotor speeds in the range 2000–6000 rpm, with small RWAs going even higher. At 2000 rpm, 1 Nm of torque requires 209 W of power, without even considering the heat power dissipated in the motor, electronics and bearings. However, when not producing torque and at low rotor speeds, RWA “bias” power can be very small.

CMGs, whose output torque is due to a mechanical constraint, require no transfer of energy to the rotor. This feature makes them much more efficient in torque production. One consideration, however, is that because they run continuously at high speed, they draw steady-state power to maintain that speed. This spin motor power (P_M) can be approximated as the product of spin-bearing drag torque (τ_d) and rotor speed, scaled up by a factor to account for heat dissipated in the motor windings:

$$P_M = s\tau_d\omega_r$$

The factor s varies nonlinearly as a function of motor design and operating point, but can be taken to be roughly 1.1. When P_M is combined with the bias power of the electronics, P_E , the sum is referred to as “quiescent” power, P_Q :

$$P_Q = P_M + P_E$$

The term “quiescent” implies this is power drawn even when the CMG is not being used to produce torque. Driven predominantly by τ_d , P_Q is larger when larger spin bearings are required, and at higher spin speeds. Increased quiescent power impacts not only the power that the spacecraft bus must supply to the CMG, but also increases the heat dissipated in the spin bearings. This dissipation in turn affects the thermal design. These impacts of quiescent power and heat in the cost of optimizing an MCS is why larger CMGs tend not be run at speeds in excess of 10,000 rpm. Smaller CMGs with smaller bearings are able to more readily take advantage of the benefits of high rotor speed in reducing CMG size. Recent work at Honeywell has shown that integrating vibration isolation technology within momentum systems can allow the use of smaller spin bearings by attenuating the launch loads that often drive their design.

3.3.3 *Vibration*

Like all rotating machines, momentum devices induce vibrations in the structure that supports them. These vibrations have a rich but well-understood spectral content. The spectrum is not broadband “white” or “colored” noise of the type that might be examined using power spectral density (PSD) plots. Instead, it consists of a comb of discrete frequencies at various multiples of the wheel speed. On a PSD plot, a tone at a discrete frequency would produce a peak that is infinitely narrow and infinitely tall. Therefore PSD plots are inappropriate to the study of these vibrations. Instead, we plot the root-mean-square (rms) sinusoidal amplitude of each component frequency, such as would be obtained from a Fourier analysis. We can calculate the total rms noise in a given band as the root-sum-square of the peaks in that band. Let us examine some of the sources of vibration in these devices.

One of the key contributors is rotor balance, both static and dynamic. Static balance measures how far the rotor center of mass is displaced from the spin axis. This displacement is responsible for a centripetal force $F = Mew^2$ transmitted to the spacecraft structure, where M is the rotor mass and e is the center-of-mass displacement. As such, the static balance is normally expressed in units of mass times displacement, for example, oz-in. Dynamic balance expresses how far the rotor’s principal axis of inertia is tilted from the spin axis and is generally measured in oz-in². The disturbance that arises is a torque vector, tracing out a cone around the spin axis. Static and dynamic balance effects are generally felt predominantly at the rotor spin frequency, with a small amount of harmonic content.

Another major contributor is bearing eccentricity. The bearings contribute a variety of frequencies because there are multiple rotation rates within them. The inner race of the bearing moves with the shaft at the rotor spin speed. The group of balls in their ball carrier rotates at a slower speed. Individual balls rotate at a higher speed. When we begin to track the frequency that results from dimensional tolerances or manufacturing flaws on various surfaces, we find these bearing frequencies, their harmonics, and beat (difference) frequencies between these tones.

At each frequency, the bearing pushes the shaft off the centerline in a circular motion. For certain frequencies, that circular motion can be “retrograde,” i.e., in the direction opposite the rotor spin.

There is generally a bearing at each end of a rotor shaft. Further complicating this spectrum is the fact that the tones from these two bearings are never identical. Consider the ball group frequency; it is determined by the diameters of the raceways and balls, all of which are subject to dimensional tolerance. As a result, while the tones on each end of the shaft are close, they are not exactly equal. The beat frequency between these nearly identical tones can have a period of many seconds or minutes. This beat accounts for the slow audible modulation in vibrations that we are accustomed to when listening to a rotating machine. It also makes routine measurements of the vibrations difficult to repeat unless very long time averages are taken and processed. Tones appear to come and go. The relative phase of the spinning vectors at each end of the shaft changes, resulting in excitation of different structural tones, etc.

Despite the stochastic nature of these vibrations, it is possible, with some care, to approximate their effect in computer modeling. When attempting to do so, the most important thing to recognize is that, unlike many disturbances, the “forcing function” arising from bearing rotation is neither a force nor a torque. The balls are much stiffer than anything else in a typical structure, and their geometric imperfections impose a displacement between the spinning shaft and the surrounding structure. In so doing, they are stiff enough to push everything else out of the way. They can bend shafts, housings, and support structure, etc., as necessary to achieve this end. As a result, the amount of vibration force applied by the bearing is determined by the structures to which it is attached. When modeling a bearing disturbance as an input to a finite-element model, we must represent the bearing by a very high-stiffness element (orders of magnitude higher than the rest of the structure), and then apply a force differentially across that stiffness of $F = kx$, where k is the element stiffness and x is the desired displacement. Typical bearing displacements vary from tenths to tens of microinches, with each tone having its own value. For a given bearing design, these values must be determined empirically, and their statistical nature across a production lot kept in mind.

All of the tones in the spectrum vary linearly with wheel speed, resulting in a comb of spectral content that shifts along the frequency axis with rotor speed. The CMG, whose speed is held constant, exhibits a stable and repeatable set of vibration frequencies. As such it is possible, within reason, to engineer these devices such that their disturbance frequencies do not coincide with the frequencies of certain key spacecraft structural modes. In fact, it is possible to “tune” the system on orbit to minimize such excitations by making small adjustments to the rotor speeds. By comparison, the RWA, whose rotor speed varies continually as momentum is exchanged, imparts vibration tones that sweep up and down the spectrum. In this case, it is not practical to avoid structure excitation by design.

3.3.4 Torque Accuracy

As the method of torque production for RWAs differs completely from that of CMGs, each must be discussed separately.

For a reaction wheel, the net output torque experienced by the spacecraft is equal to the motor torque less the friction torque of the spin bearings and any other source of drag. While the motor torque can be readily estimated from a measurement of the current, the effects of friction are difficult to predict and vary nonlinearly with speed, temperature, lubrication, etc. For a medium-sized RWA, it is not unusual for the friction torque to be 10 % of the full scale output torque of the device. Therefore, if the RWA were commanded to 5 % of full scale torque, the friction could be twice the control torque. This effect introduces significant error into the attitude control loop, often necessitating the use of a state-estimation strategy to determine the friction. Such strategies do not perform well when the rotor crosses zero speed (reverses direction). This is because friction and stiction variations are largest in this region, and speed measurements are generally poor near zero speed. Many spacecraft attempt to bias the RWAs in an array away from zero speed during normal operation. This can be achieved either by operating the spacecraft with a net momentum bias, or by including more than 3 RWAs and biasing them against each other, using the null space of the array as discussed in Chap. 6.

Like RWA bearings, the bearings of a CMG also exhibit friction. Because CMGs operate at a nearly constant spin speed, the spin-bearing friction is nearly constant. Spin-bearing friction is a consideration in system power but has little effect on performance. Because the CMG output torque is determined by gimbal rate, CMG gimbals usually employ inner loops controlling the gimbal rate. Therefore gimbal bearing friction effects are mitigated by closed loop control to a great extent. Typical gimbal rate-loop control bandwidths are on the order of 10–15 Hz. While the effects of friction on performance are far lower than for an RWA, they still appear as a slowly changing torque command passes through zero, i.e., when the gimbal rate changes direction. While the integral feedback in the rate loop “winds up” to offset the abrupt change in Coulomb friction, the gimbal momentarily stalls at zero rate. Geared CMGs exhibit this effect to a lesser degree than direct-drive ones.

Aside from friction effects, torque accuracy is generally the result of gain and offset errors. In the case of the RWA, the offset torque is low, but gain error can occur as a result of changes in motor K_t and the resistance of the current-sense resistor, both of which vary with temperature. The CMG performance, because of the closed rate loop, is driven by the performance of the tachometer that measures gimbal rate and the tachometer’s electronics. This is often an electromagnetic device such as a precision generator. Older CMGs with analog electronics did exhibit a rate-offset error due to electronics offset. Modern digital CMGs can mitigate this offset by monitoring changes in the gimbal position sensor in software and applying a slow correction. Gain error in an electromagnetic tachometer can still occur due to variations in K_t over temperature. Some modern CMGs employ digital encoder technology to measure gimbal angle and rate. Such devices have effectively zero error.

3.3.5 Array Control

In this section, we consider the ease with which a body torque in three dimensions can be produced by an array of momentum devices.

An array of n reaction wheels is by far the simplest to control. The change in net momentum (in 3 axes) that results from changes in individual rotor momentum (n rotors) is a $3 \times n$ Jacobian matrix A . Because the RWAs are mounted in fixed orientations on the vehicle, the coefficients of A are constant. The columns of A are the unit vectors in the direction of the RWA spin axes. By taking the inverse of A (for $n = 3$), or a pseudoinverse (for $n > 3$), we obtain a constant $n \times 3$ control matrix A^+ such that

$$\tau_{\text{RWA}} = A^+ \tau_{\text{cmd}} \quad (3.9)$$

This matrix allows the attitude control system or the momentum control system to calculate the torque to apply to each wheel to obtain the desired body torque.

For DGCMG, this mapping becomes more difficult. The output torques from this device are applied by the gimbals, and the rotor precesses in response. Each device has not only one gimbal fixed in the body frame, but also another whose torque axis varies with time. As a result, the Jacobian varies with gimbal angle, which can change quickly. Furthermore, a strategy to avoid gimbal-lock must be incorporated.

For SGCMG, array control is the most difficult. Again, the Jacobian varies with gimbal angle. In this case, the Jacobian relates changes in net momentum to changes in the CMG gimbal angles. Furthermore, arrays of SGCMGs exhibit a rich and complex set of internal singularities, which can make inverting the Jacobian impossible. Singularities and methods for steering arrays of SGCMGs around and through them are addressed at length in Chaps. 5 and 7.

3.4 Guidelines for Selecting Momentum Device Technology

Table 3.1 offers general guidelines summarizing the trades among various momentum-system technologies.

3.5 Chapter Summary

This chapter offers metrics for quantifying the agility of a spacecraft that apply directly to the selection and sizing of momentum devices. The most common momentum device technologies are described, along with various tradeoffs among them. Finally, general guidelines are presented for the selection of a momentum device for a specific application.

Table 3.1 Momentum device selection guidelines

	RWA	DGCMG	SGCMG
Agility (Fig. 3.11)	Best for station keeping, or slews that take minutes	Midrange	Most agile, slews completed in seconds
Power	Lower quiescent power	Higher quiescent power	
	Very inefficient in torque production	Midrange	Very efficient in torque production
Geartrain	N/A	Recommended for output torques in excess of 10 Nm	Recommended for gimbal torques in excess of 10 Nm [see Eq. (3.5)]
Vibration	Broad spectrum over operating speed range	Adjustable constant speed makes avoiding key modes possible	
Torque accuracy	Open loop torque errors due to friction	Errors mitigated by inner gimbal rate loop errors mitigated further by geartrain	
	Motor K_t , Rsense	Tach performance	
Control	Simplest, with constant control matrix	More complex, avoidance of gimbal lock	Most complex, internal singularity avoidance
Cost	\$	\$\$\$	\$\$

References

1. B. Hamilton, B. Underhill, Modern momentum systems for spacecraft attitude control. *Adv. Astronaut. Sci.* **125**, 57 (2006)
2. B. Hamilton, Turnkey cmg-based momentum control for agile spacecraft, in *AAS Advances in the Astronautical Sciences*, vol. 149, 2013

Chapter 4

Dynamics of Momentum-Control Systems

It is not enough to treat the momentum system as a black box, simply receiving power and control signals and imparting torque or momentum, as if it were any other element in a feedback-control block diagram. A momentum system offers unique opportunities to achieve robust and lightweight spacecraft designs, but taking advantage of these opportunities requires careful attention to rigid- and flexible-body dynamics. This chapter provides the foundational equations of motion for spacecraft with momentum-control devices and summarizes important flexible effects that drive the design of spacecraft that incorporate these actuators.

4.1 Notation

It may be that dynamics analysis is fundamentally unsuited to being expressed with the simple notation of other areas of physics; but for whatever reason, notation among dynamicists varies widely. There is so little universally accepted notation that we find it necessary to explain the approach taken here. The following approach is based on vector-dyadic (or tensor) notation, which recognizes the key distinction between vectors and matrices. A matrix is a collection of scalars—some say “measure numbers”—each of which represents the projection of a vector or a tensor onto a basis vector. For purposes of this discussion, the basis vectors are of unit length and always comprise a right-handed coordinate system as suggested in Fig. 4.1. In this figure, the three \mathbf{n}_i are basis vectors ordered so that $\mathbf{n}_1 \times \mathbf{n}_2 = \mathbf{n}_3$. All vectors we refer to are sometimes known as “free vectors.” They are mathematical objects with magnitude and direction but are not associated with a coordinate system and do not involve a coordinate-system origin of some kind. They are not rays emanating from a point. When referring to three numbers in a vertical stack, one often casually says “vector” when the more explicit term would be “column matrix.” Such matrices always presuppose a coordinate system. However, in this chapter we

Fig. 4.1 Right-handed coordinate system with three orthonormal basis vectors

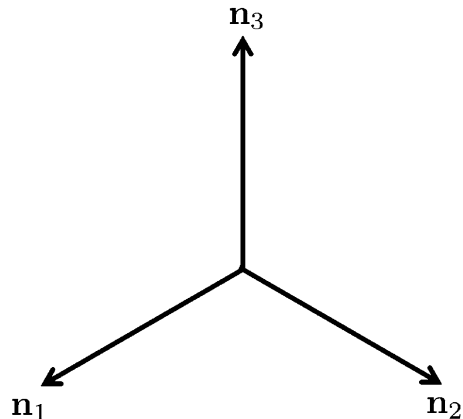


Table 4.1 Vector/dyadic notation

Scalar	<i>a</i>
Matrix	<i>v, D</i>
Vector	v
Dyadic	D

emphasize the coordinate-free world of vectors and tensors so that the derivations are unencumbered by a choice of coordinate system. Only when a coordinate system is helpful do we explicitly define one. A dyadic is a second-order tensor, which gives rise to a square matrix when it is projected onto the basis vectors of a coordinate system. The notation for a dyadic consists of juxtaposing pairs of vectors—simply writing one vector next to another. This placement does not imply multiplication, although the placement follows the order of operations for multiplication. For example, a dyadic **D** might be written in terms of two vectors \mathbf{c}_1 and \mathbf{c}_2 :

$$\mathbf{D} = \mathbf{c}_1 \mathbf{c}_2 \quad (4.1)$$

Algebraically manipulating dyadics uses familiar vector operations, such as cross product and dot products, on the individual vectors in the dyadics in a way that is analogous to the rules for matrix algebra, as in the examples provided in Table 4.1. We denote vectors and dyadics with boldface type. A scalar is denoted by an italic font. A matrix is written the same way except that it may include a left superscript indicating the coordinate system that led to the scalars in the matrix. This indication of a coordinate system is often missing when the choice is implicit or irrelevant. Note that a scalar is a special case of a matrix, one with dimension 1×1 , and the choice of coordinate system is therefore irrelevant. For clarity, often an upper-case letter is used to denote a matrix, while a lower-case letter denotes a scalar. Table 4.1 shows some examples. A matrix is a collection of scalars stacked in an $m \times n$ array. Examples include the column matrix, the row matrix, and the $m \times n$ matrix, examples of which are shown in Table 4.2. Here is an example of a vector. Call it **v**. Suppose

Table 4.2 Example matrix dimensions

Matrix type	Example
3×1 (Column) Matrix	$\begin{bmatrix} x_1 \\ x_2 \\ x_3 \end{bmatrix}$
1×4 (Row) Matrix	$\begin{bmatrix} x_1 & x_2 & x_3 & x_4 \end{bmatrix}$
2×3 Matrix	$\begin{bmatrix} x_{11} & x_{12} & x_{13} & x_{14} \\ x_{21} & x_{22} & x_{23} & x_{24} \end{bmatrix}$

there are three basis vectors fixed in the body of a spacecraft, \mathbf{b}_1 , \mathbf{b}_2 , and \mathbf{b}_3 . Then some scalars v_i can be defined such that

$$\mathbf{v} = v_1 \mathbf{b}_1 + v_2 \mathbf{b}_2 + v_3 \mathbf{b}_3 \quad (4.2)$$

Furthermore, one can extract the v_i simply by projecting \mathbf{v} onto each basis vector. For example,

$$\begin{aligned} v_1 &= \mathbf{b}_1 \cdot \mathbf{v} \\ &= \mathbf{b}_1 \cdot (v_1 \mathbf{b}_1) + \mathbf{b}_1 \cdot (v_2 \mathbf{b}_2) + \mathbf{b}_1 \cdot (v_3 \mathbf{b}_3) \\ &= \mathbf{b}_1 \cdot (v_1 \mathbf{b}_1) + 0 + 0 \\ &= v_1 \mathbf{b}_1 \cdot \mathbf{b}_1 + 0 + 0 \\ &= v_1 \end{aligned} \quad (4.3)$$

Consider another set of basis vectors, \mathbf{a}_1 , \mathbf{a}_2 , and \mathbf{a}_3 . If they differ from the \mathbf{b}_i , the scalars associated with the \mathbf{a}_i differ from the scalars associated with the \mathbf{b}_i . Since one cannot change a vector by choosing a different basis, then the scalars (which are basis dependent) cannot really be equivalent to the vector (the zero vector is a trivial exception). Hughes [1] introduced a convenient notation, the “vectrix.” A vectrix is simply a matrix of vectors. For example,

$$\mathbf{b} = [\mathbf{b}_1 \ \mathbf{b}_2 \ \mathbf{b}_3] \text{ or } \mathbf{a} = [\mathbf{a}_1 \ \mathbf{a}_2 \ \mathbf{a}_3] \quad (4.4)$$

This object has one row and three columns. It is not a shorthand for a 3×3 matrix of scalars. Vectrices are useful when dealing with vectors and bases. They lead to compact expressions such as

$$\mathbf{v} = [\mathbf{b}_1 \ \mathbf{b}_2 \ \mathbf{b}_3] \begin{bmatrix} v_1 \\ v_2 \\ v_3 \end{bmatrix} = [\mathbf{b}_1 \ \mathbf{b}_2 \ \mathbf{b}_3]^B \mathbf{v} \quad (4.5)$$

This matrix multiplication expresses the vector \mathbf{v} in terms of a vectrix of basis vectors and a column matrix of scalars. That column matrix is specific to the choice of basis. So, for clarity we indicate that choice with a left superscript on the column matrix ${}^B v$. Vectrices can also be used in vector expressions, such as the dot product and the cross product. The vector operation is performed for each element in the matrix that results from standard matrix algebra. For example,

$$\mathbf{c} = [\mathbf{a}_1 \mathbf{a}_2 \mathbf{a}_3] \cdot \begin{bmatrix} \mathbf{b}_1 \\ \mathbf{b}_2 \\ \mathbf{b}_3 \end{bmatrix} = \mathbf{a}_1 \cdot \mathbf{b}_1 + \mathbf{a}_2 \cdot \mathbf{b}_2 + \mathbf{a}_3 \cdot \mathbf{b}_3$$

$$\mathbf{C} = \begin{bmatrix} \mathbf{b}_1 \\ \mathbf{b}_2 \\ \mathbf{b}_3 \end{bmatrix} \cdot [\mathbf{a}_1 \mathbf{a}_2 \mathbf{a}_3] = \begin{bmatrix} \mathbf{b}_1 \cdot \mathbf{a}_1 & \mathbf{b}_1 \cdot \mathbf{a}_2 & \mathbf{b}_1 \cdot \mathbf{a}_3 \\ \mathbf{b}_2 \cdot \mathbf{a}_1 & \mathbf{b}_2 \cdot \mathbf{a}_2 & \mathbf{b}_2 \cdot \mathbf{a}_3 \\ \mathbf{b}_3 \cdot \mathbf{a}_1 & \mathbf{b}_3 \cdot \mathbf{a}_2 & \mathbf{b}_3 \cdot \mathbf{a}_3 \end{bmatrix} \quad (4.6)$$

Vector operations on a dyadic apply to either the first or the second vector, depending on whether the other vector in the operation is pre- or post-multiplied. Some common operations with the dyadic \mathbf{D} are shown in Table 4.3. A dyadic can be written in terms of vectrices and a matrix. For example, take the tedious-looking dyadic

$$\begin{aligned} \mathbf{J} = & J_{11}\mathbf{a}_1\mathbf{a}_1 + J_{12}\mathbf{a}_1\mathbf{a}_2 + J_{21}\mathbf{a}_2\mathbf{a}_1 + J_{13}\mathbf{a}_1\mathbf{a}_3 + J_{31}\mathbf{a}_3\mathbf{a}_1 \dots \\ & \dots J_{22}\mathbf{a}_2\mathbf{a}_2 + J_{23}\mathbf{a}_2\mathbf{a}_3 + J_{33}\mathbf{a}_3\mathbf{a}_3 \end{aligned} \quad (4.7)$$

It can be written

$$\mathbf{J} = [\mathbf{a}_1 \mathbf{a}_2 \mathbf{a}_3] \begin{bmatrix} J_{11} & J_{12} & J_{13} \\ J_{21} & J_{22} & J_{23} \\ J_{31} & J_{32} & J_{33} \end{bmatrix} \begin{bmatrix} \mathbf{a}_1 \\ \mathbf{a}_2 \\ \mathbf{a}_3 \end{bmatrix} \quad (4.8)$$

Table 4.3 Examples of dyadic operations. $\mathbf{D} = \mathbf{a}_1\mathbf{a}_2$; \mathbf{a}_1 and \mathbf{a}_2 are arbitrary vectors

Operation	Result	Description
$\mathbf{D} \cdot \mathbf{w}$	$= \mathbf{a}_1(\mathbf{a}_2 \cdot \mathbf{w})$	Vector: \mathbf{a}_1 multiplied by the scalar result of dotting \mathbf{w} onto \mathbf{a}_2
$\mathbf{v} \cdot \mathbf{D}$	$= (\mathbf{v} \cdot \mathbf{a}_1)\mathbf{a}_2$	Vector: \mathbf{a}_2 multiplied by the scalar result of dotting \mathbf{v} onto \mathbf{a}_1
$\mathbf{v} \cdot \mathbf{D} \cdot \mathbf{w}$	$= (\mathbf{v} \cdot \mathbf{a}_1)(\mathbf{a}_2 \cdot \mathbf{w})$	Scalar: scalar result of dotting \mathbf{v} onto \mathbf{a}_1 multiplied by the scalar result of dotting \mathbf{w} onto \mathbf{a}_2
$\mathbf{v} \times \mathbf{D}$	$= (\mathbf{v} \times \mathbf{a}_1)\mathbf{a}_2$	Dyadic: on the left, the cross product of \mathbf{v} and \mathbf{a}_1 ; on the right, \mathbf{a}_2
$\mathbf{v} \times \mathbf{D} \cdot \mathbf{w}$	$= (\mathbf{v} \times \mathbf{a}_1)(\mathbf{a}_2 \cdot \mathbf{w})$	Vector: the cross product of \mathbf{v} and \mathbf{a}_1 multiplied by the scalar result of dotting \mathbf{w} onto \mathbf{a}_2

Notice that there is no dot-product operation in Eq. (4.8). Carrying out what appears to be matrix multiplication merely places the vectors \mathbf{a}_i and \mathbf{a}_j next to one another in the appropriate combinations. The inertia dyadic takes the form of \mathbf{J} in Eq. (4.7), but with $J_{ij} = J_{ji}$; i.e., the inertia matrix is symmetric. We also distinguish between “coordinate system” and “frame of reference,” although, again, casual usage confuses the two. One sometimes says “frame” when “coordinate system” would be less confusing. A coordinate system consists of three orthonormal basis vectors ordered according to the right-hand rule. It is used to extract scalar and matrix values from vector-dyadic expressions and represent these expressions in terms of meaningful directions, such as compass points or the manufacturing coordinate system for a spacecraft. The choice of coordinate system has nothing at all to do with the underlying physics. It’s like tilting your head: the choice of coordinates does not affect what you’re looking at. In contrast, a frame of reference is a powerful physical concept that establishes the ground rules for how equations of motion are written. Such frames are also known as “observational frames of reference.” Ideas of space, time, and motion are central to this concept. Therefore, a frame is independent of arbitrarily chosen basis vectors and allows one to establish a common three-dimensional space for vectors and tensors considered in that frame. As one might expect, the attitude motions of spacecraft do not require that we distinguish among frames of reference with relative motion near the speed of light. If that were necessary, the story would be more complicated. Instead, in the cases considered here, a frame of reference may be fixed either in a body or in inertial space. An inertial frame is Newtonian, i.e., Newton’s laws can be stated in the familiar way in any such frame. Body-fixed frames are not necessarily Newtonian. One frame of reference may accelerate or rotate relative to another, and this relative motion can be described with kinematics. So, each rigid body considered here has a frame of reference associated with it, and rigid-body kinematics describes the relative motion among these frames. A table of symbols found at the beginning of the book defines key variables in these terms.

4.2 Spacecraft Attitude and Momentum-Device Kinematics

Attitude can be understood as the orientation of one set of basis vectors relative to another. Spacecraft attitude control seeks to drive this orientation toward some commanded value, for example, aligning the spacecraft’s nadir axis or a payload boresight with the vector from the spacecraft to a target on the ground or in space. In practice, spacecraft attitude is parameterized in a number of ways, the most common of which is the quaternion. It is favored because of its simplicity and compactness. However, direction-cosine matrices are sometimes used and, even more rarely, Euler angles. These and other attitude parameterizations are discussed thoroughly in (Staelnagel [2], Shuster [3], and Crassidis and Markley [4]). An attitude parameterization stores information about how two coordinate systems are related. For example, the direction-cosine matrix [derived in Eq. (4.6)] is an

attitude parameterization that allows one to transform the representation of any vector in one coordinate system to its representation in any other in a conveniently direct way:

$${}^B v = {}^B Q^{AA} v \quad (4.9)$$

This notation places the symbols for the “A” coordinate system—one for the direction-cosine matrix and one for the column matrix—next to one another. This placement helps ensure that coordinate systems are used consistently. Here

$${}^B Q^A = \begin{bmatrix} \mathbf{b}_1 \\ \mathbf{b}_2 \\ \mathbf{b}_3 \end{bmatrix} \cdot [\mathbf{a}_1 \mathbf{a}_2 \mathbf{a}_3] \quad (4.10)$$

This relationship arises because the vector is independent of coordinate system, and it can therefore be written in terms of either basis-vector set:

$$\mathbf{v} = [\mathbf{b}_1 \mathbf{b}_2 \mathbf{b}_3] \begin{bmatrix} {}^B v_1 \\ {}^B v_2 \\ {}^B v_3 \end{bmatrix} = [\mathbf{a}_1 \mathbf{a}_2 \mathbf{a}_3] \begin{bmatrix} {}^A v_1 \\ {}^A v_2 \\ {}^A v_3 \end{bmatrix} \quad (4.11)$$

Projecting onto the B basis vectors leads to

$$\begin{bmatrix} \mathbf{b}_1 \\ \mathbf{b}_2 \\ \mathbf{b}_3 \end{bmatrix} \cdot \mathbf{v} = \begin{bmatrix} \mathbf{b}_1 \\ \mathbf{b}_2 \\ \mathbf{b}_3 \end{bmatrix} \cdot [\mathbf{b}_1 \mathbf{b}_2 \mathbf{b}_3] \begin{bmatrix} {}^B v_1 \\ {}^B v_2 \\ {}^B v_3 \end{bmatrix} = \begin{bmatrix} \mathbf{b}_1 \\ \mathbf{b}_2 \\ \mathbf{b}_3 \end{bmatrix} \cdot [\mathbf{a}_1 \mathbf{a}_2 \mathbf{a}_3] \begin{bmatrix} {}^A v_1 \\ {}^A v_2 \\ {}^A v_3 \end{bmatrix} \quad (4.12)$$

After some simplification,

$${}^B v = I_{3 \times 3} \begin{bmatrix} {}^B v_1 \\ {}^B v_2 \\ {}^B v_3 \end{bmatrix} = {}^B Q^{AA} v \quad (4.13)$$

which is merely Eq. (4.6). While the fundamental physics is independent of coordinate system, certain traditional choices allow spacecraft engineers to communicate with momentum-device engineers about alignment of the hardware and important behaviors of the momentum system. For the spacecraft, canonical reference axes include roll, pitch, and yaw, which arose originally from nautical convention, then were applied to aircraft, and then to rockets. Roll, pitch, and yaw are often represented with \mathbf{x} , \mathbf{y} , and \mathbf{z} , respectively. Sometimes \mathbf{b}_1 , \mathbf{b}_2 , and \mathbf{b}_3 are used in place of \mathbf{x} , \mathbf{y} , and \mathbf{z} , and we adopt this more versatile convention. For many satellites, the pitch axis runs through the solar array (or solar wings), recalling that earlier aircraft use. Yaw is aligned with nadir or antinadir. The combination comprises a right-handed coordinate system, as shown in Fig. 4.2. The convention for specifying

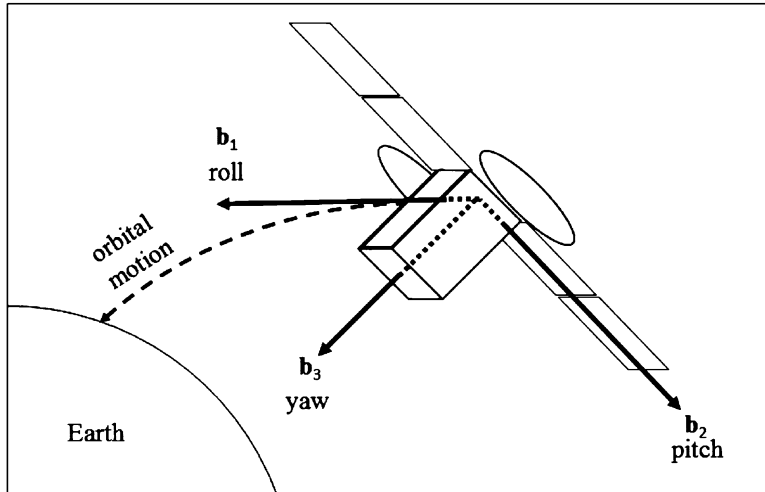


Fig. 4.2 Spacecraft reference coordinate system

the orientation of a momentum device focuses on its intended angular-momentum axis, i.e., the direction of the angular momentum for a perfectly built device. The actual angular momentum may vary because of dynamic imbalance, bearing runout, mechanical misalignment, and other terms; nevertheless, the coordinate system is based on the intended direction. For a RWA, that axis is a fixed parameter \hat{s}_i in the spacecraft body reference frame. The other axes are orthogonal to this one and merely specify how connectors and fasteners need to be accommodated in the design of the spacecraft bus structure to which the momentum device is mounted. So, an array of RWAs is traditionally specified in terms of the various wheels' \hat{s}_i directions. In contrast, a control-moment gyros (CMG)'s momentum axis is not fixed in the spacecraft structure. The gimbal motor causes it to precess. So, choosing coordinates is a little more subtle. For a CMG, it is the gimbal axis, \hat{g}_i , that is fixed in the spacecraft reference frame. The gyroscopic torque from the CMG, acting upon the spacecraft, lies along an output-torque axis \hat{o}_i , related to these other axes by

$$\hat{o}_i = \hat{s}_i \times \hat{g}_i \quad (4.14)$$

The \hat{s}_i vector changes direction with the gimbal angle δ . So, in the spacecraft coordinates B, its matrix representation ${}^B\hat{s}_i$ is

$$\begin{aligned} {}^B\hat{s}_i &= {}^B\hat{s}_i(0)\cos(\delta) + {}^B\hat{o}_i(0)\sin(\delta) \\ &= {}^B\hat{s}_i(0)\cos(\delta) + {}^B\hat{g}_i \times {}^B\hat{s}_i(0)\sin(\delta) \end{aligned} \quad (4.15)$$

where ${}^B\hat{s}_i(0)$ and ${}^B\hat{o}_i(0)$ indicate the direction of the rotor momentum and output-torque axes respectively, for $\delta = 0$ as shown in Fig. 4.3. The superscript “ \times ”

Fig. 4.3 CMG momentum in terms of reference axes for $\delta = 0$

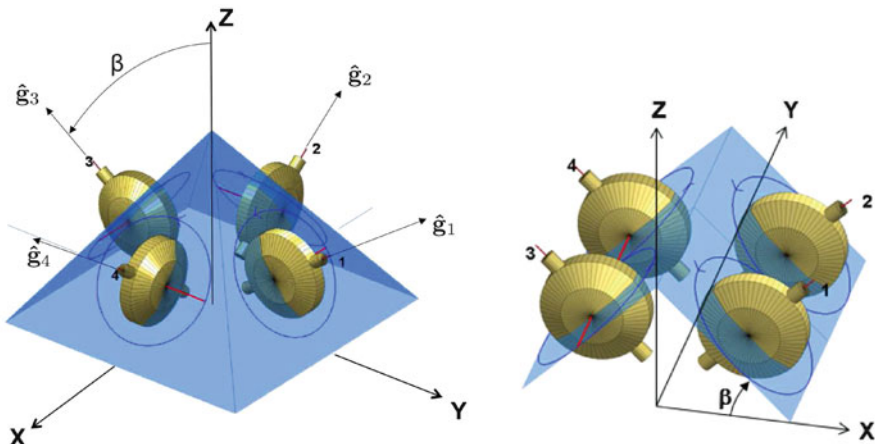
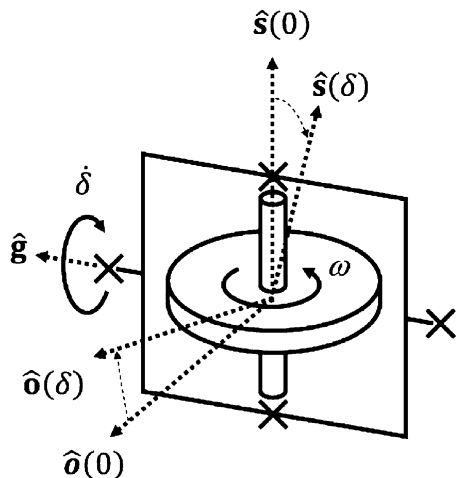


Fig. 4.4 β for a four-CMG pyramid and a roof array

indicates the matrix equivalent of the cross-product operation, as described in Eq. (4.32). This reference configuration is set by the CMG hardware and software. Figure 4.3 shows this relationship. An array of CMGs is traditionally described with one or two simple parameters, exploiting symmetry for a compact description. For a SGCMG array, the β angle specifies the plane within which each CMG's momentum can lie. A plane is fully described in terms of a normal vector. In the case of a SGCMG, that vector is clearly \hat{g}_i . So, β represents the tilt of \hat{g}_i away from a common reference, e.g., the vector that identifies the vertex of a pyramid or the centerline of a roof. Figure 4.4 shows β for a four-CMG pyramid and a roof array. The single parameter β is sufficient to specify the geometry of a roof array. A collection of scissored pairs does not even require β because their common output

axis can be specified in the same way as the torque axis for a RWA. However, for a pyramid, one can also specify an angle γ that describes the cant of each $\hat{\mathbf{g}}_i$ around the axis of symmetry. This cant or “clocking” angle is 90° for a regular four-CMG pyramid, 72° for a five-CMG pyramid, 60° for a six-CMG pyramid, and so on. However, only regular pyramids are of current interest. So, it is considered sufficient to specify β and the number of CMGs. Representing the alignment of the overall array in the spacecraft coordinates enables a Jacobian to be constructed. For example, in spacecraft coordinates, the gimbal axis of any of the four CMGs in the pyramid shown above is represented as follows:

$${}^B\hat{\mathbf{g}}_i = \begin{bmatrix} \sin(\beta)\cos(\gamma(i-1)) \\ \sin(\beta)\sin(\gamma(i-1)) \\ \cos(\beta) \end{bmatrix} \quad (4.16)$$

The momentum axis for an arbitrary gimbal angle is

$${}^B\hat{\mathbf{s}}_i(\delta_i) = \begin{bmatrix} -\cos(\delta_i)\sin(\gamma(i-1)) - \sin(\delta_i)\cos(\beta)\cos(\gamma(i-1)) \\ \cos(\delta_i)\cos(\gamma(i-1)) - \sin(\delta_i)\cos(\beta)\sin(\gamma(i-1)) \\ \sin(\delta_i)\sin(\beta) \end{bmatrix} \quad (4.17)$$

Therefore, the output axis is

$${}^B\hat{\mathbf{o}}_i(\delta_i) = \begin{bmatrix} \cos(\delta_i)\cos(\beta)\cos(\gamma(i-1)) - \sin(\delta_i)\sin(\gamma(i-1)) \\ \cos(\delta_i)\cos(\beta)\sin(\gamma(i-1)) + \sin(\delta_i)\cos(\gamma(i-1)) \\ -\cos(\delta_i)\sin(\beta) \end{bmatrix} \quad (4.18)$$

It may be of some historical interest that α , β , γ , δ , and ϵ were chosen to describe a general array of CMGs, whether comprised of SGCMGs or DGCMGs. The outer gimbal was specified with β , as is still the case for a SGCMG array. The inner gimbal lay in the same plane in the reference configuration, and its orientation was specified with α . γ specified the cant of this reference plane, and both δ and ϵ specified the respective gimbal rotations to orient $\hat{\mathbf{s}}_i$. This more general convention is no longer in use. Only the β and δ angles remain.

4.3 Equations of Motion for a Gyrostat with Balanced Rotors

A gyrostat is an assembly of interconnected rigid bodies whose relative motion does not alter the total inertia dyadic of the assembly. This definition describes many spacecraft of practical interest: rigid-body spinners, the simplest configuration, consisting of a single spinning rigid body; dual-spin satellites, which use a single axially symmetric rotor connected by a motor to a counterspun or non-spinning platform on which generally a payload is mounted; momentum-bias satellites, which

incorporate internal wheels to store angular momentum while the central body spins about a single axis or remains fixed in all three axes; zero-momentum satellites, which nominally have no angular momentum, except for what might be stored temporarily in preparation for momentum dumping, and which typically do not spin except to remain earth-pointed; and agile spacecraft, which undergo comparatively fast large-angle slews as they acquire and scan celestial or terrestrial targets with the help of CMGs. By this definition, the inertia dyadic \mathbf{J} of a gyrostat for its mass center is constant in body axes:

$$\mathbf{J} = [\mathbf{b}_1 \mathbf{b}_2 \mathbf{b}_3] \begin{bmatrix} J_{11} & J_{12} & J_{13} \\ J_{21} & J_{22} & J_{23} \\ J_{31} & J_{32} & J_{33} \end{bmatrix} \begin{bmatrix} \mathbf{b}_1 \\ \mathbf{b}_2 \\ \mathbf{b}_3 \end{bmatrix} = [\mathbf{b}_1 \mathbf{b}_2 \mathbf{b}_3]^B \mathbf{J} \begin{bmatrix} \mathbf{b}_1 \\ \mathbf{b}_2 \\ \mathbf{b}_3 \end{bmatrix} \quad (4.19)$$

where the \mathbf{b}_i are mutually orthogonal unit vectors constant in a body-fixed reference frame F_B . The 3×3 matrix in this expression is known as the inertia matrix for the body's mass center, which we denote as ${}^B\mathbf{J}$ to indicate that this body-fixed basis is used to express it. Wheels with perfect static and dynamic balance move in a way that does not change the wheel's contribution to the total inertia dyadic in a spacecraft-fixed reference frame. The same is true for CMGs if the combination of rotor motion and gimbal motion can be correctly described by the motion of a uniformly dense sphere whose mass center is fixed in the spacecraft. For these special (or approximate) cases, the inertia dyadic of the rigid body (\mathbf{J}_s) combines with that of its constant-inertia rotors

$$\mathbf{J}_r = \sum_{i=1}^n \mathbf{J}_{r,i} \quad (4.20)$$

to produce the sum

$$\mathbf{J} = \mathbf{J}_s + \mathbf{J}_r \quad (4.21)$$

The reason is straightforward and begins with a few definitions. The angular-velocity vector of a spacecraft body-fixed reference frame F_B relative to an inertial frame F_N is written $\boldsymbol{\omega}^{B/N}$. Similarly, F_{R_i} is a reference frame fixed in the i th rotor, and the angular velocity of F_{R_i} relative to F_B is $\boldsymbol{\omega}^{R_i/N}$. For n wheels of inertia $\mathbf{J}_{r,i}$, the momentum system's angular momentum is the sum

$$\mathbf{h}_r = \sum_{i=1}^n \mathbf{J}_{r,i} \cdot (\boldsymbol{\omega}^{B/N} + \boldsymbol{\omega}^{R_i/N}) \quad (4.22)$$

The total spacecraft angular momentum, \mathbf{H} can be written in terms of this wheel angular momentum \mathbf{h}_r :

$$\mathbf{H} = \mathbf{J}_s \cdot \boldsymbol{\omega}^{B/N} + \mathbf{h}_r \quad (4.23)$$

i.e.,

$$\mathbf{H} = \mathbf{J}_s \cdot \boldsymbol{\omega}^{B/N} + \sum_{i=1}^n \mathbf{J}_{r,i} \cdot (\boldsymbol{\omega}^{B/N} + \boldsymbol{\omega}^{R_i/B}) \quad (4.24)$$

Collecting on $\boldsymbol{\omega}^{B/N}$ results in

$$\mathbf{H} = \left(\mathbf{J}_s + \sum_{i=1}^n \mathbf{J}_{r,i} \right) \cdot \boldsymbol{\omega}^{B/N} + \sum_{i=1}^n \mathbf{J}_{r,i} \cdot \boldsymbol{\omega}^{R_i/B} \quad (4.25)$$

Defining

$$\mathbf{h} = \sum_{i=1}^n \mathbf{J}_{r,i} \cdot \boldsymbol{\omega}^{R_i/B} \quad (4.26)$$

and making a few substitutions results in a compact expression for the gyrostat's angular momentum:

$$\mathbf{H} = \mathbf{J} \cdot \boldsymbol{\omega}^{B/N} + \mathbf{h} \quad (4.27)$$

The equations of motion for the gyrostat can be derived simply from the derivative of this momentum in F_N and application of the Transport Theorem:

$$\frac{^N d\mathbf{H}}{dt} = \mathbf{J}_s \cdot \frac{^B d\boldsymbol{\omega}^{B/N}}{dt} + \frac{^B d\mathbf{h}}{dt} + \boldsymbol{\omega}^{B/N} \times (\mathbf{J} \cdot \boldsymbol{\omega}^{B/N} + \mathbf{h}) \quad (4.28)$$

The left superscript in this vector expression indicates the reference frame with respect to which a vector derivative is taken. It differs from the way in which we indicate the coordinate system used to represent a vector's components. It is unambiguous because this use is exclusive to vectors, while the coordinate-system notation is exclusive to matrices. The fact that a gyrostat's inertia dyadic is constant in a body-fixed frame motivates using the transport theorem to eliminate derivatives of the inertia dyadic that would appear if the derivative were taken with respect to F_N . The kinematics equations might be written in terms of a quaternion, direction-cosine matrices, and many other parameterizations of attitude [2, 3, 5].

4.4 Relative Equilibria and Stability of Gyrostats

The equations of motion are characterized by some simple equilibrium solutions. Of interest here are so-called relative equilibria, for which the derivatives in F_B are zero. Despite that wheel momentum and angular velocity are constant for a gyrostat in a relative equilibrium, the spacecraft may still spin. The motion is known as a

simple spin, a constant angular velocity along a body-fixed direction. In equilibrium (and with no applied moments), the equation of motion is

$$0 = \boldsymbol{\omega}^{B/N} \times (\mathbf{J} \cdot \boldsymbol{\omega}^{B/N} + \mathbf{h}) \quad (4.29)$$

The body-fixed torque due to wheel momentum, $\boldsymbol{\omega}^{B/N} \times \mathbf{h}$, balances the dynamic torque associated with the rigid body, $\boldsymbol{\omega}^{B/N} \times \mathbf{J} \cdot \boldsymbol{\omega}^{B/N}$. The net torque (the sum) is zero in equilibrium, a situation known as dynamic balance. If there were no wheels, the rigid-body torque in equilibrium would be zero on its own. The equation of motion would then represent spin about a principal axis of the rigid inertia matrix. For a given $\boldsymbol{\omega}^{B/N}$ this equilibrium condition determines the wheel momentum in the plane perpendicular to $\boldsymbol{\omega}^{B/N}$ in equilibrium. It does not constrain the wheel momentum parallel to $\boldsymbol{\omega}^{B/N}$, momentum which can be used to augment the dynamics in ways other than dynamic balance. Let us denote the projection of \mathbf{h} along $\boldsymbol{\omega}^{B/N}$ as the scalar h_s (spin-axis wheel momentum, also known as superspin). The selection of h_s for some spacecraft application is generally a design choice and is independent of dynamic balance. It is often used to augment the effective moment of inertia, stabilizing an otherwise unstable minor-axis spinner. In fact, dual-spin spacecraft, which are minor-axis rigid bodies due to geometry that allows them to fit well inside launch-vehicle fairings, owe their success to this passive approach to attitude stability. Such a design choice can be enforced through an additional equation

$$0 = \boldsymbol{\omega}^{B/N} \cdot \mathbf{h} = \Omega h_s \quad (4.30)$$

where $\Omega = \|\boldsymbol{\omega}^{B/N}\|$. The equilibrium system is described by four scalar equations that are linear in the three components of the 3×1 matrix

$$\mathbf{h} = \mathbf{h} \cdot \begin{bmatrix} \mathbf{b}_1 \\ \mathbf{b}_2 \\ \mathbf{b}_3 \end{bmatrix}$$

The four scalar equations are

$$A\mathbf{h} = \begin{bmatrix} \boldsymbol{\omega}^T \\ \boldsymbol{\omega}^\times \end{bmatrix} \mathbf{h} = \begin{bmatrix} \Omega h_s \\ \boldsymbol{\omega}^\times \mathbf{J} \boldsymbol{\omega} \end{bmatrix} \quad (4.31)$$

where $\boldsymbol{\omega}$ is the 3×1 matrix of components of $\boldsymbol{\omega}^{B/N}$ in the \mathbf{b} basis, and the superscript ‘ \times ’ indicates the matrix equivalent of the cross-product operation, i.e.,

$$\boldsymbol{\omega}^\times = \begin{bmatrix} 0 & -\boldsymbol{\omega}^{B/N} \cdot \mathbf{b}_3 & \boldsymbol{\omega}^{B/N} \cdot \mathbf{b}_2 \\ \boldsymbol{\omega}^{B/N} \cdot \mathbf{b}_3 & 0 & -\boldsymbol{\omega}^{B/N} \cdot \mathbf{b}_1 \\ -\boldsymbol{\omega}^{B/N} \cdot \mathbf{b}_2 & \boldsymbol{\omega}^{B/N} \cdot \mathbf{b}_1 & 0 \end{bmatrix} \quad (4.32)$$

A is a 4×3 matrix. $\text{Rank}(A) = 3$ if ω is nonzero. A simple proof of this statement is that ω^\times is rank 2, and ω^T cannot lie in its range space. Therefore, a matrix comprised of both ω^\times and ω^T must be rank 3. With this fact about $\text{rank}(A)$, h is found from a Moore–Penrose pseudoinverse:

$$h = (A^T A)^{-1} A^T \begin{bmatrix} \Omega h_s \\ \omega^\times J \omega \end{bmatrix} \quad (4.33)$$

The solution is

$$h = \frac{1}{\Omega^2} \begin{bmatrix} \Omega \omega & \omega^\times \omega^\times \end{bmatrix} \begin{bmatrix} h_s \\ J \omega \end{bmatrix} \quad (4.34)$$

or, in terms of the normalized matrix

$$\hat{\omega} = \frac{\omega}{\Omega} \quad (4.35)$$

the result is

$$h = \hat{\omega} h_s + \Omega \hat{\omega}^\times (\hat{\omega}^\times J \hat{\omega}) \quad (4.36)$$

This expression for h is a closed-form solution for the total, embedded angular momentum in a gyrostat for a given equilibrium angular velocity and desired superspin. It provides the foundation for passive stabilization of a rigid spacecraft spinning about any axis $\hat{\omega}$. It is well known that a spinning rigid body—a gyrostat with zero embedded momentum—has six relative equilibria for a given angular momentum, each corresponding to spin about one of the principal axes of the inertia matrix, either in the positive or negative sense. This result arises from the equilibrium condition for a rigid body,

$$0 = \boldsymbol{\omega}^{B/N} \times \mathbf{J} \cdot \boldsymbol{\omega}^{B/N} \quad (4.37)$$

which is simply Euler's equation with the angular-velocity derivative set to zero. This condition implies

$$\boldsymbol{\omega}^{B/N} \parallel (\mathbf{J} \cdot \boldsymbol{\omega}^{B/N}) \quad (4.38)$$

i.e.,

$$\lambda \boldsymbol{\omega}^{B/N} = \mathbf{J} \cdot \boldsymbol{\omega}^{B/N} \quad (4.39)$$

The three solutions for λ are the three eigenvalues of the inertia matrix ${}^B J$. The eigenvectors are the directions of the angular-velocity vector for each of these equilibria. Since an eigenvector and its negative are both solutions, there are six

such directions. The solution in which λ is the maximum principal moment of inertia represents a minimum-energy state for a given angular-momentum magnitude. Spin about this maximum axis is therefore stable when kinetic energy can dissipate, and this fact is used in many different spacecraft architectures to ensure mission success. Syncom 2, launched in 1963, was the first successful geosynchronous communications satellite. It is an example of a passively stable maximum-axis spinner. Spin about the minor axis is a maximum-energy state and is therefore unstable, diverging from the equilibrium over time, depending on the rate at which kinetic energy is lost. Each of the early Explorer series of spacecraft is an example of an unstable, minor-axis spinner. The intermediate axis is a saddle point that can be considered unstable, but in fact any perturbation away from this equilibrium represents large-angle motion about either the minimum or maximum-inertia axis. No spacecraft intended to be passively stable would be designed to spin about the intermediate-inertia axis. The situation is more subtle for a gyrostat with nonzero embedded momentum. Hughes [5] provides a detailed assessment of the equilibria for such spacecraft, using a polynomial whose roots can be used to find these equilibria. Here we offer a compact approach to finding these equilibria based on a generalized eigenvalue problem. For small $\|\mathbf{h}\|$ compared to $\|\mathbf{H}\|$, the gyrostat solution resembles that of a single rigid body, as one might expect. Larger values of embedded momentum can reduce the number of real equilibria to four or as few as two. For nonzero \mathbf{H} and $\boldsymbol{\omega}^{B/N}$, a gyrostat in equilibrium must exhibit

$$\boldsymbol{\omega}^{B/N} \parallel (\mathbf{J} \cdot \boldsymbol{\omega}^{B/N} + \mathbf{h}) \quad (4.40)$$

Equivalently,

$$\lambda \boldsymbol{\omega}^{B/N} = (\mathbf{J} \cdot \boldsymbol{\omega}^{B/N} + \mathbf{h}) \quad (4.41)$$

λ here plays a role very similar to how it appears in the case of a single rigid body. It is a scalar that is related to the magnitudes $H = \|\mathbf{H}\|$ and Ω by

$$\lambda = \frac{H}{\Omega} \quad (4.42)$$

Projecting \mathbf{J} onto the \mathbf{b}_i bases leads to the 3×3 inertia matrix ${}^B J$ (denoted simply by J here). In terms of these matrices,

$$\lambda \boldsymbol{\omega} = J \boldsymbol{\omega} + h \quad (4.43)$$

This statement is a matrix pencil: almost an eigenvalue problem in λ , but for the presence of h . An expression for six scalars that can be used to compute the corresponding directions of $\boldsymbol{\omega}$ for known H , J , and h is

$$\det \left(\Omega I - \begin{bmatrix} 2HJ^{-1} & J^{-2}(hh^T - H^2I) \\ I & 0 \end{bmatrix} \right) = 0 \quad (4.44)$$

where “det” indicates the determinant of a matrix, and I is the 3×3 identity matrix. Each eigenvalue Ω_k is a scalar angular-velocity magnitude for one of the equilibria. Only the real values correspond to physical solutions, and because the energy and momentum are real numbers, the non-physical solutions must be complex-conjugate pairs. Therefore, there may be two, four, or six real solutions. The direction of the k th angular-velocity vector is then given in terms of its \mathbf{b} components as

$$\omega_k = \left(\frac{H}{\Omega_k} I - J \right)^{-1} h \quad (4.45)$$

The stability of these equilibria can be assessed in a number of ways, as described in Hughes [5]. A fail-safe rule of thumb is that an equilibrium is stable if its value of λ is the largest of all six, again analogous to the single rigid-body case. This rule applies to any gyrostat and reduces to the maximum-axis rule for the case of a single rigid spinning body, for which there are two solutions (positive and negative spin). For a more general gyrostat, it is possible for the stability of positive and negative spin to differ. A spacecraft design that is informed by this principle benefits from a guarantee of passive stability as long as the momentum system can maintain constant momentum. Software failures related to the spacecraft attitude-control subsystem do not threaten stability as long as the operation of the momentum system is decoupled in these failure cases. Such a failure response is available in many contemporary RWAs, which are designed to hold the most recent speed command in the event of interrupted commands from the spacecraft databus.

4.4.1 RWA Spacecraft

Superspin is a technique that augments the open-loop dynamics to achieve passive stabilization. The term comes originally from dual-spin spacecraft, which typically separate from the launch-vehicle upper stage with a high spin rate (by today’s standards) of 30–60 rpm. After separation, a motor between the rotor and the platform causes one part to spin at a different rate from the other. The higher-speed portion is responsible for “super” spin. These two counter-rotating bodies exhibit gyrostat dynamics. Depending on the amount of energy dissipation in the bodies, the faster-spinning portion can stabilize the other, per the Iorillo stability criterion. Contemporary spacecraft can use superspin to stabilize a spacecraft that spins during some or all of its operations. Typically the flight software is responsible for establishing this embedded momentum by commanding the momentum system. By analogy to the maximum-axis principle, the simplest approach to superspin stabilization is to use the momentum system to make the effective inertia, λ , for that axis the largest among all six possible equilibria. In practice, λ is chosen to be at least 20 % greater when possible. For example, to stabilize a rigid body around one of its principal-inertia axes, the spacecraft design sets the effective inertia to be

$$\lambda \geq 1.2J_{mm} \quad (4.46)$$

where J_{mm} is the maximum principal moment of inertia of the rigid body. Superspin can be used to stabilize a spacecraft meant to spin around any axis, not exclusively one of these basis vectors. If wheel augmentation does not already provide sufficient effective inertia, the spin-axis momentum to achieve superspin would attempt to exceed that insufficient value λ_{\max} by 20 % through a new value:

$$\lambda \geq 0.2\lambda_{\max}\Omega \quad (4.47)$$

For the case of a rigid spinner, with λ equal to the rigid inertia for the desired spin axis,

$$h_s \geq (1.2J_{mm} - \lambda)\Omega \quad (4.48)$$

When the desired spin axis is not a passive equilibrium, it can be made so through dynamic balance. This technique consists of placing some of the momentum system's momentum vector perpendicular to the desired spin axis. In closed form, this dynamic-balance momentum is

$$h_d = \hat{\omega}^\times (\hat{\omega}^\times J\omega) \quad (4.49)$$

For example, a spacecraft intended to spin about its \mathbf{b}_3 axis $\hat{\omega} = [0 \ 0 \ 1]^T$ can use its momentum system to dynamically balance the J_{13} and J_{23} products of inertia with the following constant angular momentum:

$$h_d = \begin{bmatrix} -J_{13}\Omega \\ -J_{23}\Omega \\ 0 \end{bmatrix} \quad (4.50)$$

Both superspin and dynamic balance require less momentum to be effective when the spacecraft spin rate is low. In the limit, as the spacecraft approaches a non-spinning state, the only gyroscopic stiffness becomes that of the wheel. In that limit, the system is a momentum-bias spacecraft.

4.4.2 CMG Spacecraft

Spacecraft with CMGs exhibit the same equilibria as any other gyrostat when the gimbal angle of each CMG is held constant, whether by active torque from the gimbal motor or by mechanical resistance in the gimbal mechanism. In principle, such spacecraft can also use dynamic balance and superspin to augment the rigid-body dynamics to achieve a variety of architectural benefits. However, unlike a

spacecraft with RWAs, a CMG exhibits different behavior in the first few moments after attitude control no longer commands the momentum-control devices. This open-loop behavior depends on the friction and stiction in the CMG gimbals, which is not simple to predict. Nevertheless, the following general principles provide some insight. As in the reaction-wheel case, the equilibrium condition is

$$0 = \boldsymbol{\omega}^{B/N} \times (\mathbf{J} \cdot \boldsymbol{\omega}^{B/N} + \mathbf{h}) \quad (4.51)$$

but with the added constraint that the gimbal rate is also zero. Furthermore, in equilibrium, the spacecraft's motion does not accelerate any CMG's rotor about that CMG's gimbal axis. For the i th single-gimbal CMG and in the absence of resistance torques along the gimbal axis, that condition is

$$0 = (\boldsymbol{\omega}^{B/N} \times \mathbf{h}_{c,i}) \cdot \hat{\mathbf{g}}_i \quad (4.52)$$

where $\mathbf{h}_{c,i}$ is the i th CMG's angular momentum. The equilibrium solution therefore varies with the array geometry, and there is a larger family of solutions than in the case of the gyrostat with RWAs. A computer simulation would identify the stable configurations of CMG gimbal angles and rigid-body angular velocity that meets these constraints in the presence of stiction. Motor cogging, gear-tooth meshing, and bearing friction resist free rotation of the rotor about the gimbal axis. In the absence of attitude control, open-loop motion of the gimbals can quickly damp kinetic energy and place the spacecraft in an equilibrium spin. This damping effect resembles how mechanical gyroscopes have been used to resist and damp out rolling and pitching motion of ships at sea. In the space application, this effect can also be beneficial. It is a valuable way to ensure bounded dynamics, resulting in an equilibrium spin, during any one of several failures that leave the spacecraft without attitude control.

4.4.3 Large-Angle Slews

A conceptually simple way to describe a slew from one attitude to another is through Euler's Theorem for rigid-body motion. A consequence of that theorem is that one can always reorient a rigid body by rotating it about a single axis fixed both in the body and in an inertial reference frame. Let the attitude of the rigid body at the start time of the slew t_0 be described by a direction-cosine matrix ${}^NQ^{B(t_0)}$, and let its attitude at completion time t_f be described by ${}^NQ^{B(t_f)}$. The change in attitude, again parameterized as a direction-cosine matrix, is

$${}^{B(t_f)}Q^{B(t_0)} = ({}^NQ^{B(t_f)})^T {}^NQ^{B(t_0)} \quad (4.53)$$

The axis-angle representation of the attitude change is found from an eigenvalue decomposition of ${}^{B(t_f)}Q^{B(t_0)}$. It can also be found from the matrix logarithm of ${}^{B(t_f)}Q^{B(t_0)}$, and then the components of the rotation axis extracted from the resulting

3×3 skew-symmetric matrix. Specifically, the eigenvector ${}^B c$ of ${}^{B(t_f)} Q^{B(t_0)}$ that is associated with the eigenvalue 1 is the axis of rotation such that

$${}^{B(t_f)} Q^{B(t_0)} = \cos\phi I_{3 \times 3} + (1 - \cos\phi) {}^B c {}^B c^T - \sin\phi {}^B c^\times \quad (4.54)$$

The superscript B on ${}^B c$ does not specify time simply because the vector c is constant throughout the motion, per Euler's Theorem. The matrix ${}^B c$ therefore consists of the same three scalars regardless of the fact that the spacecraft's attitude is changing. In the case of an eigenaxis slew, the angle of rotation is $\phi(t)$. It starts at $\phi = 0$ and reaches a commanded (final) value $\phi = \phi_c$ has the following angular velocity:

$$\omega^{B/N} = \dot{\phi}(t)c \quad (4.55)$$

This behavior is also known in kinematics as a “simple spin” because the unit vector c does not change. For purposes of this discussion, the definition of “versine slew” is the following: an eigenaxis slew for which the angle follows a half-wave versine path in time until the end of the maneuver. “Versine” is the name for the following trigonometric function:

$$\text{versin}\theta = 2\sin^2\frac{\theta}{2} = 1 - \cos\theta \quad (4.56)$$

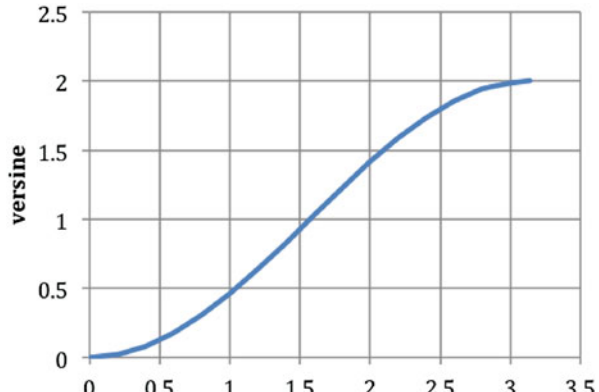
This function is illustrated in Fig. 4.5. For single-axis motion, let the initial angle for a versine slew be ϕ_1 and the total angle be $\Delta\phi$. Then the final angle is

$$\phi_2 = \phi_1 + \Delta\phi \quad (4.57)$$

Since the initial angle is arbitrary, let $\phi_1 \equiv 0$. Then

$$\phi_2 = \Delta\phi \quad (4.58)$$

Fig. 4.5 Versine



The kinematics of an angle-versine slew are

$$\begin{aligned}\phi(t) &= \frac{\phi_2}{2}(1 - \cos at) \\ \dot{\phi}(t) &= a\frac{\phi_2}{2}\sin at \\ \ddot{\phi}(t) &= a^2\frac{\phi_2}{2}\cos at \\ \dddot{\phi}(t) &= -a^3\frac{\phi_2}{2}\sin at\end{aligned}\tag{4.59}$$

where a is the timing parameter (not to be confused with the vector axis of rotation \mathbf{c} used earlier) and time t is such that

$$0 \leq t \leq \frac{\pi}{a}\tag{4.60}$$

This function is infinitely differentiable and therefore smooth from the perspective of actuation and numerical implementation. The maxima of these functions lead to expressions for the timing parameter a in terms of prescribed kinematic limits:

$$a_1 = \frac{\dot{\phi}_{\max}}{2|\phi_2|}, \quad a_2 = \left(\frac{\ddot{\phi}_{\max}}{2|\phi_2|} \right)^{1/2}, \quad \text{or} \quad a_3 = \left(\frac{\dddot{\phi}_{\max}}{2|\phi_2|} \right)^{1/3}\tag{4.61}$$

Here, the indices on a denote the degree of the derivative, not the initial or final point in the slew. The best choice of a is the maximum value (therefore the shortest slew time) for which the other two time histories are within their respective limits. That is,

$$\begin{aligned}\text{for } a_1 &= \frac{\dot{\phi}_{\max}}{2|\phi_2|}, \text{ require } \left| \frac{a_1^2 \phi_2}{2} \right| \leq \ddot{\phi}_{\max} \text{ and } \left| \frac{a_1^3 \phi_2}{2} \right| \leq \dddot{\phi}_{\max} \\ \text{for } a_2 &= \left(\frac{\ddot{\phi}_{\max}}{2|\phi_2|} \right)^{1/2}, \text{ require } \left| \frac{a_2 \phi_2}{2} \right| \leq \dot{\phi}_{\max} \text{ and } \left| \frac{a_2^3 \phi_2}{2} \right| \leq \ddot{\phi}_{\max} \\ \text{for } a_3 &= \left(\frac{\dddot{\phi}_{\max}}{2|\phi_2|} \right)^{1/3}, \text{ require } \left| \frac{a_3 \phi_2}{2} \right| \leq \dot{\phi}_{\max} \text{ and } \left| \frac{a_3^2 \phi_2}{2} \right| \leq \ddot{\phi}_{\max}\end{aligned}\tag{4.62}$$

A solution is always possible because each derivative increases monotonically with a . A rate versine is suitable for rate control, not necessarily for attitude control. The rate versine begins with an expression for $\dot{\phi}$ that is similar to the angle-versine expression for ϕ . The expression for angle is the integral, with the initial angle as the constant of integration (i.e., 0). The result is

$$\begin{aligned}
\phi(t) &= \frac{1}{2} \left[(\dot{\phi}_2 + \dot{\phi}_1) t - \frac{1}{a} (\dot{\phi}_2 - \dot{\phi}_1) \sin at \right] \\
\dot{\phi}(t) &= \frac{1}{2} (\dot{\phi}_2 - \dot{\phi}_1) (1 - \cos at) + \dot{\phi}_1 \\
\ddot{\phi}(t) &= \frac{1}{2} (\dot{\phi}_2 - \dot{\phi}_1) a \sin at \\
\ddot{\phi}(t) &= \frac{1}{2} (\dot{\phi}_2 - \dot{\phi}_1) a^2 \cos at
\end{aligned} \tag{4.63}$$

The maximum value of $\dot{\phi}$ occurs at the beginning or the end of the slew. Since these boundaries are given as conditions of the problem, the planning algorithm does not need to implement a means of observing the rate limits during the slew. Some means of rejecting infeasible commands in ground software, before such commands reach the spacecraft, would likely be implemented instead. The maximum acceleration and jerk provide conditions for the slew duration:

$$a_1 = \frac{2\dot{\phi}_{\max}}{|\dot{\phi}_2 - \dot{\phi}_1|}, \quad a_2 = \left(\frac{2\dot{\phi}_{\max}}{|\dot{\phi}_2 - \dot{\phi}_1|} \right)^{1/2} \tag{4.64}$$

As in the case of the angle-versine slew, the best choice is the maximum, subject to the requirement that the other derivative not exceed its kinematic limit:

$$\begin{aligned}
\text{for } a_1, \text{ require } \left| a_1 \frac{\dot{\phi}_2 - \dot{\phi}_1}{2} \right| &\leq \ddot{\phi}_{\max} \\
\text{for } a_2, \text{ require } \left| a_2^2 \frac{\dot{\phi}_2 - \dot{\phi}_1}{2} \right| &\leq \dddot{\phi}_{\max}
\end{aligned} \tag{4.65}$$

One may prefer to think of ϕ starting at some nonzero initial condition, ϕ_0 . For example, an attitude-control system might autonomously track this angle as a large error and continuously compute the eigenaxis parameters until the angle is small enough for the dynamics to be considered linear. In that case, ϕ_c in these expressions can be replaced with a delta angle, $\delta\phi = \phi_c - \phi_0$. Regardless of how the initial condition is specified, the results provide a smooth slew from the initial value to the final, commanded value regardless of the sign of these angles. These kinematics provide fundamental insight into the peak momentum, torque, and gimbal acceleration (in the case of CMGs) necessary to achieve a desired agility. Specifically, the axis of rotation determines the scalar inertia J_e that the momentum system must move:

$$J_e = \mathbf{c} \cdot \mathbf{J} \cdot \mathbf{c} \tag{4.66}$$

The actuator's peak performance derives from the slew kinematics according to

$$\begin{aligned} h_{\max} &= \dot{\phi}_{\max} J_e \\ \tau_{\max} &= \ddot{\phi}_{\max} J_e \end{aligned} \quad (4.67)$$

The gimbal's acceleration is driven by the jerk limit ($\ddot{\phi}$) and a variety of gimbal rate-loop requirements that were discussed in Chap. 3. These simple results do not take into account contingency, margin, and control-related phenomena such as overshoot, but it's a start. However, an eigenaxis slew is not necessarily the fastest route nor the most power-efficient. Fully optimizing for time and power would take into account the fact that the inertia varies across the range of possible paths. Slewing around an axis with lower inertia than that of the eigenaxis might speed up the maneuver. The momentum system torque and momentum envelope also comes into play: some corners of the array's performance envelope might be exploited for higher performance if an axis other than this geometrically shortest one is chosen. Finally, other spacecraft-specific constraints on orientation relative to the sun or the Earth, for thermal or communications reasons, might have to be accommodated, regardless of the purely dynamical benefits of a time-optimal slew. Eigenaxis slews provide useful insight, particularly at the early stages of spacecraft design, but a detailed design for an agile spacecraft's operations concept may ultimately demand different kinematics.

4.5 Control-Moment Gyroscopes

The dynamics of a CMG includes a wide variety of rigid-body, flexible, and nonlinear effects. This section derives the foundational equations for a CMG that is statically balanced—i.e., the mass centers of each component do not translate in a spacecraft-fixed reference frame during the motion of the CMG. In practice, this static imbalance and dynamic imbalance of the rotor induce vibration in the spacecraft structure, as do gear-tooth meshing and bearing-related disturbances. This induced vibration (IV) represents a high-frequency mechanical disturbance that can affect precision payloads. Imprecision in the gimbal motion because of motor cogging and the transmission of gimbal-motor torque through gears (among many effects) is responsible for so-called output-torque ripple (OTR), which is of lower frequency than IV. However, OTR can be of larger magnitude and influences the spacecraft pointing in ways that IV does not, such as excitation of low-frequency spacecraft flexible modes. These effects are taken up in Sect. 4.7. Although the multiple-gimbal case is the general one from a theoretical perspective, single-gimbal CMGs are preferred in practice because the torque produced by precessing the rotor is reacted by structural components rather than the motors on other gimbal axes, saving weight, and power. Acknowledging the widespread use of single-gimbal CMGs, this derivation assumes that \mathbf{h} comprises any number of internal

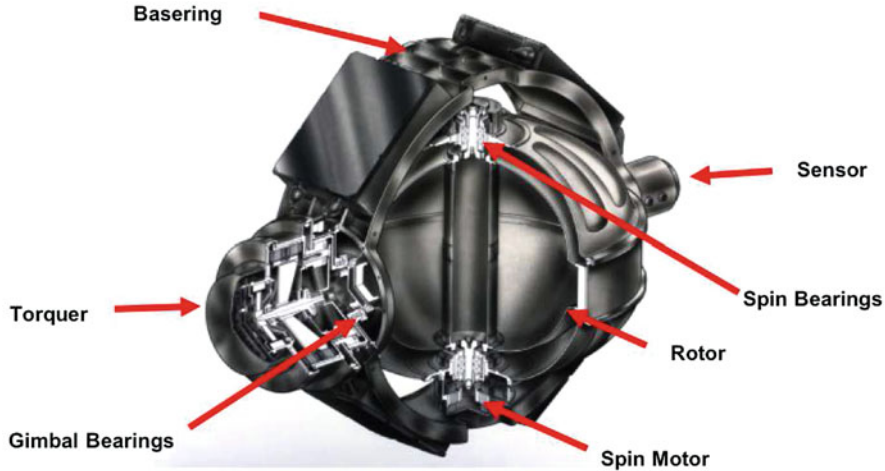


Fig. 4.6 Single-gimbal CMG (Image Courtesy of Honeywell, Inc.)

components with at most one gimbal axis each. Figure 4.6 shows the components of a single-gimbal CMG. Consider a spinning rigid spacecraft whose angular-momentum vector (\mathbf{H}) is given by

$$\mathbf{H} = \mathbf{J} \cdot \boldsymbol{\omega}^{\text{B/N}} + \mathbf{h} \quad (4.68)$$

as discussed above. The assumption that the internal components are statically balanced about their angular-velocity vectors means that the rigid body's mass center does not accelerate, that equations for the rotational dynamics alone completely describe the motion of the system. As in the case of the RWA spacecraft, we lump the momentum of the momentum devices due to the spacecraft's rotation in with that of the rigid body. That is, the term

$$\mathbf{J}_g \cdot \boldsymbol{\omega}^{\text{B/N}} + \mathbf{J}_r \cdot \boldsymbol{\omega}^{\text{B/N}} \quad (4.69)$$

does not appear here because it is accounted for in the spacecraft bus motion. Then, the remaining momentum of all n CMGs is

$$\mathbf{h} = \sum_{i=1}^n \mathbf{J}'_{g,i} \cdot \boldsymbol{\omega}^{G_i/B} + \mathbf{J}_{r,i} \cdot \boldsymbol{\omega}^{R_i/B} \quad (4.70)$$

in which another simplification is possible. Let the gimbal structure's inertia be $\mathbf{J}'_{g,i}$ defined so that an augmented inertia $\mathbf{J}_{g,i}$ can include the rotor's inertia:

$$\mathbf{J}_{g,i} = \mathbf{J}'_{g,i} + \mathbf{J}_{r,i} \quad (4.71)$$

Then

$$\mathbf{h} = \sum_{i=1}^n \mathbf{J}'_{g,i} \cdot \boldsymbol{\omega}^{G_i/B} + \mathbf{J}_{r,i} \cdot (\boldsymbol{\omega}^{G_i/B} + \boldsymbol{\omega}^{R_i/B}) \quad (4.72)$$

becomes

$$\mathbf{h} = \sum_{i=1}^n \mathbf{J}_{g,i} \boldsymbol{\omega}^{G_i/B} + \mathbf{J}_{r,i} \boldsymbol{\omega}^{R_i/G_i} \quad (4.73)$$

substituting the scalar gimbal speed $\dot{\delta}_i$, rotor speed $\Omega_{r,i}$, and the unit vectors along the gimbal and rotor-spin directions leads to

$$\mathbf{h} = \sum_{i=1}^n \mathbf{J}_{g,i} \cdot (\dot{\delta}_i \hat{\mathbf{g}}_i) + \mathbf{J}_{r,i} \cdot (\Omega_{r,i} \hat{\mathbf{s}}_i) \quad (4.74)$$

Because the gimbal and rotor are taken to be dynamically balanced, their respective inertia dyadics include no products of inertia. The inertia for the $\hat{\mathbf{g}}_i$ and $\hat{\mathbf{s}}_i$ directions are $\mathbf{J}_{g,i}$ and $\mathbf{J}_{r,i}$, respectively. So,

$$\mathbf{h} = \sum_{i=1}^n J_{g,i} \dot{\delta}_i \hat{\mathbf{g}}_i + J_{r,i} \Omega_{r,i} \hat{\mathbf{s}}_i \quad (4.75)$$

This spacecraft's dynamics resemble those of the RWA spacecraft. Both begin with the inertial derivative of the total angular momentum. However, for the CMG spacecraft, this derivative includes additional terms that result from the gimbals:

$$\begin{aligned} \frac{^N d \mathbf{H}}{d t} = & \mathbf{J} \cdot \frac{^B d \boldsymbol{\omega}^{B/N}}{d t} + \frac{^B d}{d t} \left(\sum_{i=1}^n J_{g,i} \dot{\delta}_i \hat{\mathbf{g}}_i + J_{r,i} \Omega_{r,i} \hat{\mathbf{s}}_i \right) \\ & + \boldsymbol{\omega}^{B/N} \times \left(\mathbf{J} \cdot \boldsymbol{\omega}^{B/N} + \sum_{i=1}^n J_{g,i} \dot{\delta}_i \hat{\mathbf{g}}_i + J_{r,i} \Omega_{r,i} \hat{\mathbf{s}}_i \right) \end{aligned} \quad (4.76)$$

The first term in parentheses can be made explicit:

$$\begin{aligned} \frac{^B d}{d t} \left(\sum_{i=1}^n J_{g,i} \dot{\delta}_i \hat{\mathbf{g}}_i + J_{r,i} \Omega_{r,i} \hat{\mathbf{s}}_i \right) = & \left(\sum_{i=1}^n J_{g,i} \ddot{\delta}_i \hat{\mathbf{g}}_i + J_{r,i} \dot{\Omega}_{r,i} \hat{\mathbf{s}}_i \right) \\ & + \left(\sum_{i=1}^n J_{g,i} \dot{\delta}_i \frac{^B d}{d t} \hat{\mathbf{g}}_i + J_{r,i} \Omega_{r,i} \frac{^B d}{d t} \hat{\mathbf{s}}_i \right) \end{aligned} \quad (4.77)$$

The body-frame derivatives of the gimbal axes and the rotor axes result from the kinematics of the CMG. The gimbal axis is fixed in F_B . So,

$$\frac{^B d}{dt} \hat{\mathbf{g}}_i = 0 \quad (4.78)$$

From the Transport Theorem and our definitions,

$$\frac{^B d}{dt} \hat{\mathbf{s}}_i = \frac{^{G_i} d}{dt} \hat{\mathbf{s}}_i + \boldsymbol{\omega}^{G_i/B} \times \hat{\mathbf{s}}_i = 0 + \dot{\delta} \hat{\mathbf{g}}_i \times \hat{\mathbf{s}}_i \quad (4.79)$$

This direction is that of the output torque ($\hat{\mathbf{o}}_i$). So,

$$\frac{^B d}{dt} \hat{\mathbf{s}}_i = \dot{\delta} \hat{\mathbf{o}}_i \quad (4.80)$$

Substituting this result into Eq. (4.77) leads to a complete expression for the time derivative of angular momentum for the CMG spacecraft with rotors that are not necessarily at constant speed:

$$\begin{aligned} \frac{^N d \mathbf{H}}{dt} = & \mathbf{J} \cdot \frac{^B d \boldsymbol{\omega}^{B/N}}{dt} + \left(\sum_{i=1}^n J_{g,i} \ddot{\delta}_i \hat{\mathbf{g}}_i + J_{r,i} (\dot{\Omega}_{r,i} \hat{\mathbf{s}}_i + \dot{\delta}_i \Omega_{r,i} \hat{\mathbf{o}}_i) \right) \\ & + \boldsymbol{\omega}^{B/N} \times \left(\mathbf{J} \cdot \boldsymbol{\omega}^{B/N} + \sum_{i=1}^n J_{g,i} \dot{\delta}_i \hat{\mathbf{g}}_i + J_{r,i} \Omega_{r,i} \hat{\mathbf{s}}_i \right) \end{aligned} \quad (4.81)$$

It is instructive to consider these terms individually:

- $\mathbf{J} \cdot \frac{^B d \boldsymbol{\omega}^{B/N}}{dt} + \boldsymbol{\omega}^{B/N} \times \mathbf{J} \cdot \boldsymbol{\omega}^{B/N}$ —This term represents the rigid-body motion due to spacecraft bus angular acceleration and angular velocity, as it would appear in Euler's Equation.
- $\boldsymbol{\omega}^{B/N} \times \left(\sum_{i=1}^n J_{g,i} \dot{\delta}_i \hat{\mathbf{g}}_i \right)$ —This term represents the gyroscopic effect on the spacecraft of the moving gimbal. While important in a high-fidelity simulation, the gimbal rate is much lower than that of the rotor and may be neglected for first-order torque- and momentum-sizing analyses. Neglecting it would be analogous to setting $J_{g,i} = 0$
- $\boldsymbol{\omega}^{B/N} \times \left(\sum_{i=1}^n J_{r,i} \Omega_{r,i} \hat{\mathbf{s}}_i \right)$ —This term represents the gyroscopic effect on the spacecraft of the spinning rotors at some instantaneous orientation. This term has a significant effect on the spacecraft dynamics. For each CMG, it is also a torque that the gimbal motor must react, i.e., the “base rate” effect. This effect is one of the design drivers for the gimbal motor.
- $\sum_{i=1}^n J_{g,i} \ddot{\delta}_i \hat{\mathbf{g}}_i$ —This term represents the torque on the spacecraft due to the gimbal's accelerating everything in the inner gimbal assembly, i.e., the rotor and the gimbal structure that supports it. This term is an important one in sizing the gimbal motor, but it may be neglected in simpler analyses that focus on momentum system torque and momentum capability.

- $\sum_{i=1}^n J_{r,i} \dot{\Omega}_{r,i} \hat{s}_i$ —This term represents the torque on the spacecraft due to spinning up or down the rotor. For typical single-gimbal CMGs, this event is rare, but it is an important effect for the case of variable-speed CMGs.
- $\sum_{i=1}^n J_{r,i} \dot{\delta}_i \Omega_{r,i} \hat{o}_i$ —This term represents the gyroscopic output torque on the spacecraft from gimbaling the rotor's angular momentum. This value dominates the output torque of a single-gimbal CMG.

A very simplistic model of a spacecraft with constant-speed rotors would include only the output-torque effect. In that case, the spacecraft's dynamics would be

$$\begin{aligned} \frac{^N d\mathbf{H}}{dt} = & \mathbf{J} \cdot \frac{^B d\boldsymbol{\omega}^{B/N}}{dt} + \sum_{i=1}^n J_{r,i} \dot{\delta}_i \Omega_{r,i} \hat{o}_i \\ & + \boldsymbol{\omega}^{B/N} \times \left(\mathbf{J} \cdot \boldsymbol{\omega}^{B/N} + \sum_{i=1}^n J_{r,i} \Omega_{r,i} \hat{s}_i \right) \end{aligned} \quad (4.82)$$

To construct a model suitable for attitude-control simulations, one can split this equation in such a way that the momentum system appears as a separate subsystem from the spacecraft body:

$$\begin{aligned} \frac{^N d\mathbf{H}}{dt} + \boldsymbol{\tau}_o = & \mathbf{J} \cdot \frac{^B d\boldsymbol{\omega}^{B/N}}{dt} + \boldsymbol{\omega}^{B/N} \times \left(\mathbf{J} \cdot \boldsymbol{\omega}^{B/N} + \sum_{i=1}^n J_{r,i} \Omega_{r,i} \hat{s}_i \right) \\ \boldsymbol{\tau}_o = & - \sum_{i=1}^n J_{r,i} \dot{\delta} \Omega_{r,i} \hat{o}_i \end{aligned} \quad (4.83)$$

The negative sign reflects the fact that the torque acting on the spacecraft is the opposite of what acts on the momentum system. These equations can be written in matrix form and solved for the angular acceleration. Here, the matrices have been constructed via the body-fixed basis vectors \mathbf{b}_i and are indicated as such with a left superscript B. In the absence of external torques,

$$\mathbf{B} \dot{\boldsymbol{\omega}} = \mathbf{B} J^{-1} \left[\mathbf{B} \boldsymbol{\tau}_o - \boldsymbol{\omega} \times \left(\mathbf{B} J \boldsymbol{\omega} + \sum_{i=1}^n J_{r,i} \Omega_{r,i} \mathbf{B} \hat{s}_i \right) \right] \quad (4.84)$$

$$\mathbf{B} \boldsymbol{\tau}_o = - \left(\sum_{i=1}^n J_{r,i} \dot{\delta}_i \Omega_{r,i} \mathbf{B} \hat{o}_i \right) \quad (4.85)$$

4.6 Actuator Jacobians

A Jacobian matrix A , or simply “Jacobian,” is an $n \times m$ matrix formed by taking the partial derivative of an $m \times 1$ real-valued function $F(x)$ with respect to an $n \times 1$ column matrix, x :

$$A = \frac{\partial F}{\partial x} = \begin{bmatrix} \frac{\partial F}{\partial x_1} & \cdots & \frac{\partial F}{\partial x_n} \end{bmatrix} = \begin{bmatrix} \frac{\partial F_1}{\partial x_1} & \cdots & \frac{\partial F_1}{\partial x_n} \\ \vdots & \ddots & \vdots \\ \frac{\partial F_n}{\partial x_1} & \cdots & \frac{\partial F_n}{\partial x_n} \end{bmatrix} \quad (4.86)$$

where F_i and x_i are the matrix components of the real-valued function and column matrix. A linear, scalar example offers some insight into the physical significance of a Jacobian. Consider a function for the output torque of a motor $\tau = Ki$, where τ is the output torque, K is the scalar gain known as a torque constant, and i is the input current to the motor. The partial derivative of the output torque $\tau(i)$ with respect to the output current i yields a scalar Jacobian in this case and, because K is a constant and not a function of i , it is the gain K . This gain amplifies the current, producing torque, for any value of i . The case for an array of RWAs is analogous. Where the gain K characterizes the amplification in the scalar example, the singular values of the Jacobian characterize it in the general case. A zero singular value is roughly analogous to zero gain, at least for some directions if not all. The angular momentum of the RWAs is the sum of all of the rotor speeds multiplied by their respective inertias. In the likely case where all RWAs have the same rotor inertia, the array angular momentum is

$$h = J_r \sum_{i=1}^n \Omega_{r,i} {}^B \hat{s}_i \quad (4.87)$$

The output torque is the time derivative of the RWAs’ array angular momentum. The chain rule yields

$$\frac{dh}{dt} = {}^B \tau_o = \frac{\partial h}{\partial \Omega_r} \dot{\Omega}_r = J_r [{}^B \hat{s}_1 \cdots {}^B \hat{s}_n] \begin{bmatrix} \dot{\Omega}_{r,1} \\ \vdots \\ \dot{\Omega}_{r,n} \end{bmatrix} \quad (4.88)$$

and therefore, the Jacobian for the RWA angular momentum with respect to the RWA rotor rates is

$$A = J_r [{}^B \hat{s}_1 \cdots {}^B \hat{s}_n] \quad (4.89)$$

Like the linear scalar example for the output torque of a motor, the Jacobian for an array of RWAs is constant. Therefore, if a momentum system includes three or more

RWAs with linearly independent spin-axes, its Jacobian cannot be singular. The case of a Jacobian for an array of CMGs is more complicated because the Jacobian is not constant. It is a function of the gimbal and rotor states. The Jacobian for an array of CMGs is

$$A = \frac{\partial h}{\partial \Delta} = \left[\frac{\partial h}{\partial \delta_1} \cdots \frac{\partial h}{\partial \delta_n} \right] \quad (4.90)$$

The rotor angular momentum is likely constant and uniform across all of the CMGs in an array. In that case, the Jacobian is a concatenation of all of the output-torque directions in the spacecraft body coordinates, multiplied by the CMG rotor angular momentum:

$$A = \frac{\partial h}{\partial \Delta} = h_r [{}^B \hat{o}_1 \cdots {}^B \hat{o}_n] \quad (4.91)$$

Therefore, singularities arise when the output-torque directions for the CMGs lie in a plane. Mathematically, this condition corresponds to a situation in which the matrix $[{}^B \hat{o}_1 \cdots {}^B \hat{o}_n]$ has rank less than 3. For an array of VSCMGs, the Jacobian for the array of CMGs and the array of RWAs are concatenated, but without the assumption that the rotor angular momenta are uniform (because VSCMG rotor rates vary). The VSCMG array Jacobian is therefore

$$A = \left[\begin{array}{cc} \frac{\partial h}{\partial \Delta} & \frac{\partial h}{\partial \Omega_r} \end{array} \right] \quad (4.92)$$

and the total output torque from the VSCMG array is

$${}^B \tau_o = A \begin{bmatrix} \dot{\Delta} \\ \dot{\Omega}_r \end{bmatrix} \quad (4.93)$$

This Jacobian is always full rank for nonzero rotor velocity if there are at least two VSCMGs in the array with linearly independent gimbal axes. However, rank alone is not the full story; there are deeper issues with VSCMG arrays, including loss of gyroscopic torque, that are discussed in later chapters. For an array of DGCMGs, the Jacobian is similar to that for an array of SGCMGs but contains an additional set of columns because of the additional gimbals. This Jacobian is

$$A = \left[\begin{array}{cc} \frac{\partial h}{\partial \Delta_1} & \frac{\partial h}{\partial \Delta_2} \end{array} \right] \quad (4.94)$$

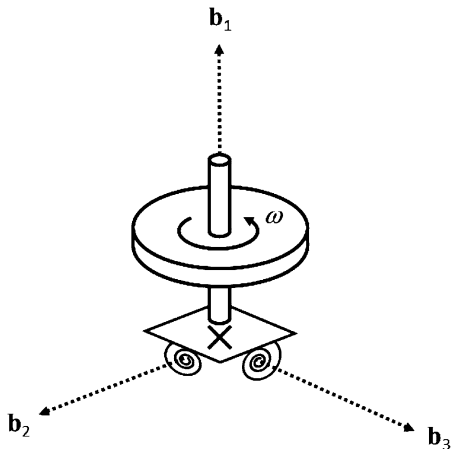
where Δ_1 and Δ_2 are the column matrices of gimbal angles for the inner and outer gimbals. Even with constant and uniform angular momentum among all the CMGs, the outer-gimbal Jacobian contribution is not a concatenation of unit vectors (Kurokawa [6]). It is often useful to measure the distance from singularity by the rank properties of the Jacobian for an array of momentum devices. In such a calculation, the Jacobian should be normalized (scaled by rotor momentum) before

it is used in a metric such as the manipulability, $m = \sqrt{\det(AA^T)}$ equal to the product of the singular values of the Jacobian (as discussed in Chap. 7). For example, with constant uniform angular momentum across all across all CMGs, the metric is $m = \sqrt{\det(\hat{A}\hat{A}^T)}$, where $A = h_r\hat{A}$. The normalization of the Jacobian provides not only a measure of singularity that is independent of CMG size, but it also serves as a numerically stable value in studies of singularity avoidance.

4.7 Rotor and Gimbal Structural Dynamics

The analysis of flexible dynamics on rotating bodies is a specialty discipline. The equations are difficult to formulate, and all but the most trivial cases must be solved numerically. This subtlety motivates some straightforward design principles: momentum devices are designed for high stiffness so that their flexible dynamics are decoupled from fundamental vibration modes of the spacecraft structure and from attitude-control loops. Separating these frequencies simplifies control design and improves the predictability of the spacecraft's flexible response in the context of launch-vehicle coupled loads analysis, among other advantages. This stiffness also is consistent with the need for flight hardware to survive high loads associated with launch-vehicle dynamics, including acoustic loads and rocket-engine vibrations. However, it is generally the stiffness, not material stress considerations, that drives the mechanical design of the actuators. RWAs and CMGs achieve stiffness in part by maximizing bearing span—that is, the distance between multiple bearings that support the rotor and (in the case of CMGs) the gimbal. The more widely separated the bearings, the larger the moment they can react, all things being equal. These devices also incorporate high-stiffness rotors, structural elements, and bracketry, while trying to minimize the mass of these elements. Details of the design are specific to the devices and the application are beyond the scope of this discussion. Nevertheless, two general behaviors are evident for a wide variety of actuators: (1) the vibration mode of the rotor, where gyroscopic effects couple rigid-body nutation to structural deflection of the rotor and (2) a CMG-specific effect in which the so-called output-axis stiffness increases the torque necessary from the gimbal motor in the form of an augmented inertia. The first effect is evident in a simple model of a spinning symmetric body on a two degree-of-freedom torsional spring. A body-fixed reference frame F_B is fixed to this rotor, and a coordinate system consisting of the \mathbf{b}_i basis vectors are also fixed in F_B . In this model, the body represents a rotor spinning at high speed about the axis \mathbf{b}_1 shown in Fig. 4.7. The compliant base permits the rotor to deflect about any axis in the \mathbf{b}_2 – \mathbf{b}_3 plane with uniform stiffness. This simplified representation includes an embedded angular-momentum vector, h_r about the \mathbf{b}_1 axis and assumes small-angle motion of the rotor in the transverse directions. For sufficiently small motion, the angular-velocity vector is the derivative of a three-parameter attitude representation consisting of a small rotation in each of three axes:

Fig. 4.7 Rotor on a compliant base



$${}^B \begin{bmatrix} \theta_1 \\ \theta_2 \\ \theta_3 \end{bmatrix} \approx {}^B \begin{bmatrix} \int \omega_1 dt \\ \int \omega_2 dt \\ \int \omega_3 dt \end{bmatrix} \quad (4.95)$$

the left superscript B indicates that the matrix of components is associated with the B coordinate system. However, the rotation in \mathbf{b}_1 is taken to be zero because the springs deflect only in the transverse direction. If the inertia dyadic for the rotor's mass center is $\mathbf{J}_r = J_r \mathbf{b}_1 \mathbf{b}_1 + J_t (\mathbf{b}_2 \mathbf{b}_2 + \mathbf{b}_3 \mathbf{b}_3)$, the equations of motion in matrix form are

$${}^B J_r {}^B \dot{\omega}^{B/N} + {}^B \omega^{B/N \times} ({}^B J_r {}^B \omega^{B/N} + {}^B h) = {}^B \tau_K \quad (4.96)$$

where again, the superscript \times indicates the matrix equivalent of the vector cross product, and τ_K is the torque that results from the transverse deflection of the rotor on its flexible base. Substituting $\dot{\theta}$ for ${}^B \omega^{B/N}$ leads to

$$\begin{aligned} & {}^B \begin{bmatrix} J_r & 0 & 0 \\ 0 & J_t & 0 \\ 0 & 0 & J_t \end{bmatrix} {}^B \begin{bmatrix} \ddot{\theta}_1 \\ \ddot{\theta}_2 \\ \ddot{\theta}_3 \end{bmatrix} + {}^B \begin{bmatrix} 0 & -\dot{\theta}_3 & \dot{\theta}_2 \\ \dot{\theta}_3 & 0 & -\dot{\theta}_1 \\ -\dot{\theta}_2 & \dot{\theta}_1 & 0 \end{bmatrix} \left({}^B \begin{bmatrix} J_r & 0 & 0 \\ 0 & J_t & 0 \\ 0 & 0 & J_t \end{bmatrix} {}^B \begin{bmatrix} \dot{\theta}_1 \\ \dot{\theta}_2 \\ \dot{\theta}_3 \end{bmatrix} + \begin{bmatrix} h_r \\ 0 \\ 0 \end{bmatrix} \right) \\ &= \begin{bmatrix} 0 \\ -k\theta_2 \\ -k\theta_3 \end{bmatrix} \end{aligned} \quad (4.97)$$

Again, the small-angle assumption eliminates coupling of this spring torque into the spin axis. The solution is

$$\begin{aligned}\ddot{\theta}_2 &= -\frac{1}{J_t}(h_r \dot{\theta}_3 + k \dot{\theta}_2) \\ \ddot{\theta}_3 &= -\frac{1}{J_t}(h_r \dot{\theta}_2 - k \dot{\theta}_3)\end{aligned}\quad (4.98)$$

Converting this second-order, coupled, ordinary differential equation into first-order form provides the state-space dynamics matrix

$$A = \begin{bmatrix} 0 & -\frac{h_r}{J_t} & -\frac{k}{J_t} & 0 \\ \frac{h_r}{J_t} & 0 & 0 & -\frac{k}{J_t} \\ 1 & 0 & 0 & 0 \\ 0 & 1 & 0 & 0 \end{bmatrix} \quad (4.99)$$

with eigenvalues (natural frequencies)

$$\lambda = \left(\left(\frac{h_r}{2J_t} \right)^2 + \frac{k}{J_t} \right)^{1/2} \pm \frac{h_r}{2J_t} \quad (4.100)$$

With no rotor momentum, these roots are simply the natural frequencies of an inertia on a torsional stiffness:

$$\lim_{h_r \rightarrow 0} \lambda = \pm \left(\frac{k}{J_t} \right)^{1/2} \quad (4.101)$$

One of these vibrational modes is rotational oscillation about one transverse axis, and the second is about the other transverse axis, as shown in Fig. 4.8. However for nonzero rotor momentum, these two modes couple and separate. In the limit of infinitely high rotor momentum (or zero stiffness), the eigenvalues approach:

$$\lim_{h_r \rightarrow \infty} \lambda = 0, \frac{h_r}{J_t} \quad (4.102)$$

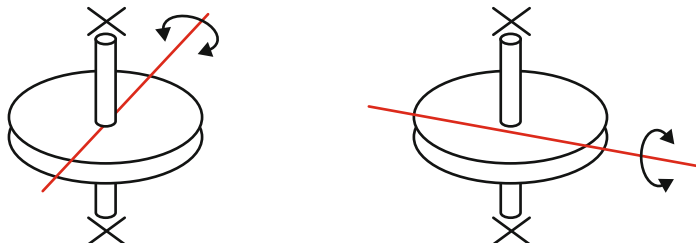


Fig. 4.8 Modes with no rotor speed

Fig. 4.9 Modes with rotor spinning

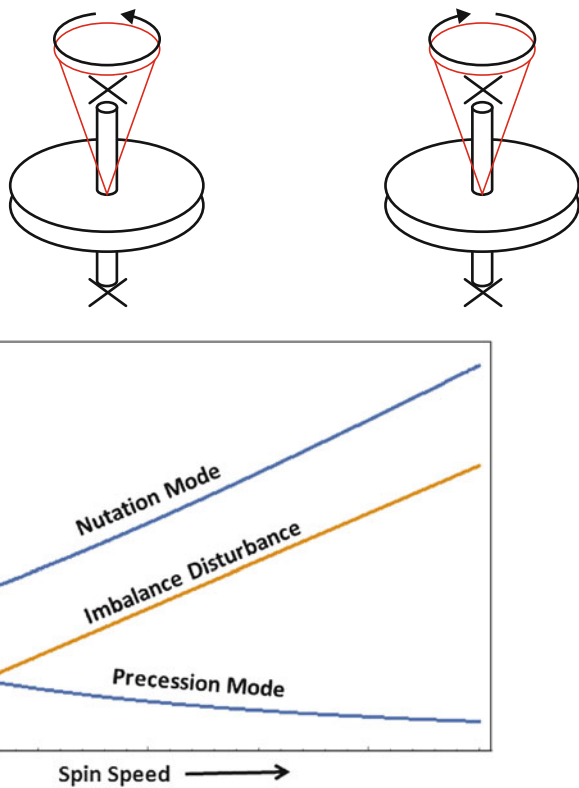


Fig. 4.10 Variations in natural frequency with spin speed

The “precession” frequency asymptotes to zero with increasing rotor momentum, and the “nutation” frequency asymptotes to the rigid-body nutation frequency. These gyroscopically coupled modes exhibit “coning” motion, with the nutation mode coning in the same direction as the rotor spin, and the precession mode in the opposite direction, i.e., retrograde, as shown in Fig. 4.9. If one of these mode frequencies coincides with the spin speed, excitation can result. Variations of natural frequency with speed can be seen in Fig. 4.10. The precession mode always intersects at the frequency $\sqrt{K/(J_r + J_t)}$. The nutation mode never crosses so long as $(J_r > J_t)$ i.e., the rotor is oblate (a disc), not prolate (a skinny cylinder). The precession mode, which can coincide with the spin frequency, cones in the retrograde direction. Retrograde modes exhibit an interesting phenomenon directly traceable to that of pole-zero cancellation. From a simple mathematical model, one might conclude that spin vibrations cannot excite retrograde modes because their eigenvectors are orthogonal. However, in a practical context these modes are excited through subtle effects that include imperfections, nonlinearities, and other unmodeled features. Rotor-spin vibrations can transmit energy through surrounding structure. The discussion above applies to RWAs. However, in a CMG, the stiffness

about X and Y axes is much different (one is the gimbal), resulting in completely different behavior. Clearly, the study of modal excitation on a spinning body is not trivial, even when the body is rigid.

The second flexible effect of general interest considered here is that of augmented inertia. This phenomenon arises because of compliance in all structural elements that are meant to constrain the CMG's momentum vector to move in a plane perpendicular to the gimbal axes. These elements include the rotor shell or web, the rotor shaft, rotor bearings, gimbal structure, gimbal bearings, and possibly elements of the gimbal drive train. The mechanical fixture between the spacecraft bus and the gimbal may also play a role. The combined stiffness of all of these elements, whether in series or in parallel, comprises the "output-axis stiffness." The phrase suggests that the stiffness is associated with the output axis of the CMG. Specifically, it is a stiffness that is responsible for constraining the output axis to remain perpendicular to the gimbal axis. One way to estimate the participation of these elements in the output-axis stiffness is to begin with an analytical model or a finite-element representation of this subsystem. Applying a couple M at the rotor rim in a direction parallel to the output axis deflects this model by an angle, ϕ , as shown in Fig. 4.11. The stiffness is the ratio of the couple to the angle. The more compliant this subsystem, the more that the rotor can tilt toward or away from the gimbal. As its momentum \mathbf{h} , projects along the gimbal axis $\hat{\mathbf{g}}$, the resulting change in momentum represents a torque that the gimbal must react. Here, the various parameters are shown as scalars because this analysis is much more simple than the general case that would be analyzed with a detailed model. For a given scalar gimbal rate δ and output-axis stiffness, K_{OA} , the output torque is approximately

$$\begin{aligned}\tau_o &= \dot{\delta} h_r \\ \tau_o &= -K_{OA}\phi\end{aligned}\quad (4.103)$$

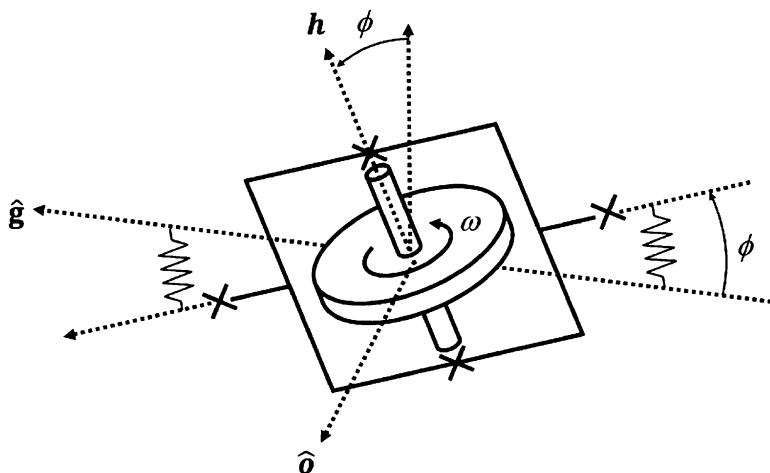


Fig. 4.11 Conceptual model of output-axis stiffness

or

$$\phi = -\frac{\dot{h}_r}{K_{OA}} \quad (4.104)$$

\mathbf{h}_r deflects by an angle ϕ in proportion to the CMG output torque τ_o causing angular momentum h_g to appear along the gimbal axis:

$$h_g = h_r \sin(-\phi) \quad (4.105)$$

For small angles,

$$h_g = -h_r \phi \quad (4.106)$$

Some substitutions lead to

$$h_g = \frac{\dot{\delta}h_r^2}{K_{OA}} \quad (4.107)$$

The time derivative of this momentum is the torque on the gimbal due to the output-axis stiffness effect:

$$\tau_{g,K} = \frac{\ddot{\delta}h_r^2}{K_{OA}} \quad (4.108)$$

The gimbal must accelerate an inertia $J_{g,\text{eff}}$ that combines the rigid inertia of the IGA and this output-axis stiffness effect:

$$\tau_g = \tau_{g,r} + \tau_{g,K} = J_{g,\text{eff}} \ddot{\delta} \quad (4.109)$$

Since the rigid IGA accelerates due to a torque

$$\tau_{g,r} = J_g \ddot{\delta} \quad (4.110)$$

the combined effect is the effective inertia

$$J_{g,\text{eff}} = J_g + \frac{h_r^2}{K_{OA}} \quad (4.111)$$

This simple expression conveniently represent the impact of compliant gimbal structure. Low stiffness costs power and ultimately increases the weight of the gear train and the gimbal. There is also a dynamic effect in addition to this quasistatic behavior: an initial rotation of the gimbal imparts an oscillatory disturbance that degrades spacecraft-pointing performance somewhat. These many impacts typically motivate a CMG design in which the output-axis stiffness is high enough that the

rigid inertia dominates the gimbal dynamics. Regardless of the stiffness of a specific design, this effective inertia must be accounted for in estimates of the gimbal torque required to achieve the attitude-control requirements at the spacecraft level.

4.8 Effects of Scaling CMG Actuators

With the rise of small satellites, or “smallsats,” for use in a wide variety of missions, the need for attitude actuators that meet volume, mass, and power requirements for precision pointing of these new spacecraft architectures has become immediate. Some miniature RWAs for slow-moving spacecraft have been available since the 1990s. Many contemporary smallsats, such as NASA’s Phonesat, simply incorporate brushless DC motors, using the motor’s own inertia as a rotor. Some small RWAs are packaged with attitude determination sensors as turnkey attitude-control subsystems—for example, Blue Canyon Technologies’ XACT unit. Even miniature CMGs have been developed to provide CubeSats with agile capabilities. The University of Florida’s IMPACT CMGs and Honeybee Robotics’ Microsat CMGs are examples. They are shown in Figs. 4.12 and 4.13, respectively. However, the performance of these momentum systems does not necessarily scale well. For small rotors, the overhead associated with motors, sensors, bearings, structure, slip rings, electronics, etc., can dominate the size and weight of the device. This overhead, in turn, makes the momentum devices a disproportionately larger fraction of the total spacecraft than is the case for large satellites. So, dynamics effects considered to be negligible for larger spacecraft must be reconsidered for these smaller ones. Some of the detrimental effects of small scale include:

- Lack of availability of small, high-performance components
- Lack of manufacturing procedures to meet alignment and other mechanical tolerances



Fig. 4.12 IMPACT single CMG (*left*) and IMPACT 4-CMG pyramid array (*right*) (Courtesy of Prof. Norman Fitz-Coy, University of Florida)



Fig. 4.13 Honeybee robotics Microsat CMGs (Image Courtesy of Honeybee Robotics)

- Less accurate position and rate sensors lead to less precise inner-loop control, necessitating more robust control architectures, unfamiliar operations concepts, or simply degraded performance
- Actuators may be on the same size scale as the spacecraft bus and therefore apply more disturbance (e.g., induced vibration and OTR) for smallsats
- Smallsats very rarely incorporate precise vibration isolation and have less mass with which to absorb vibration energy, leading to worse pointing performance
- Dynamics of the gimbal and other components that were once considered to be negligible are now more apparent. Without new, more detailed models and control approaches, they may lead to unexpected performance degradation

Miniature RWAs are by far the most common momentum-control actuators for smallsats. The primary drawback of RWAs, their low torque, becomes less important for small spacecraft. Companies such as Dynacon, Sinclair Interplanetary, Clyde Space, Maryland Aerospace Incorporated, and Blue Canyon Technologies in addition to some universities have built such actuators. The promise of higher agility through RWAs at the small scale is a benefit. Gimbal dynamics of small CMGs must be considered in modeling and control. Neglecting these dynamics produces inaccuracies when an inexact steering algorithm is used to find a solution to the gimbal rates to track a desired torque. Also, with the increase in gimbal inertia and the higher possible base rate of the smallsat using an array of oversized miniature CMGs, the CMG gimbal motors must offset the additional dynamics with high power draw. These effects lower accuracy and reduce torque amplification. For an in-depth derivation of the equations of motion for a spacecraft containing momentum systems with offset mass, as well as the effects of additional dynamics on the performance in terms of precision and torque amplification, see Appendix A.

4.8.1 Torque Amplification Degradation with Scaling

The performance of small CMGs for smallsat applications suffers from these scaling issues. This is due mostly to the lack of high-performance components at this scale in the industry base. Disproportionately higher bearing friction in the rotors and gimbals, lower torque-per-input-power motors, and higher base rates of the smallsats all threaten to limit the performance of smallsats in the near future. Consider the output torque of a SGCMG with constant rotor speed ($\dot{\Omega}_{r_i} = 0$):

$$\tau_{o,i} = J_{r,i}\hat{\mathbf{o}}_i\dot{\delta}_i\Omega_{r,i} + J_{g,i}\ddot{\delta}_i \quad (4.112)$$

where $J_{r,i}\hat{\mathbf{o}}_i\dot{\delta}_i\Omega_{r,i}$ is the gyroscopic output torque, and $J_{g,i}\ddot{\delta}_i$ the gimbal shaft torque. This simple model represents a case in which the gimbal axis is perfectly aligned and in which a negligible rotor torque maintains the rotor speed. Defining an input torque

$$\tau_i = \tau_{Gf_i} + J_{g,i}\ddot{\delta}_i + \mathbf{J}_{r_i} \cdot \boldsymbol{\omega}^{B/N} \cdot \hat{\mathbf{o}}_i\Omega_{r,i} \quad (4.113)$$

leads to an equation for the torque amplification of a smaller CMG:

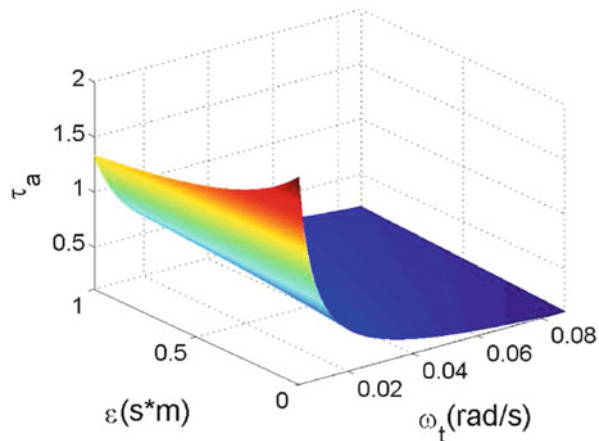
$$\tau_a = \frac{\tau_o}{\tau_i} \approx \frac{|J_{r,i}\hat{\mathbf{o}}_i\dot{\delta}_i\Omega_{r,i}| + |J_{g,i}\ddot{\delta}_i|}{|\tau_{Gf_i}| + |J_{g,i}\ddot{\delta}_i| + |J_{g,i}\ddot{\delta}_i + \mathbf{J}_{r_i} \cdot \boldsymbol{\omega}^{B/N} \cdot \hat{\mathbf{o}}_i\Omega_{r,i}|} \quad (4.114)$$

Equation (4.113) may be even further simplified if the gimbal friction, τ_{Gf_i} is negligible. With the previously stated assumptions

$$\tau_a = \frac{|h_{r_i}\dot{\delta}_i| + |J_{g,i}\ddot{\delta}_i|}{|J_{g,i}\ddot{\delta}_i| + \|h_{r_i}\boldsymbol{\omega}^{B/N}\|} = \frac{|\dot{\delta}_i| + |\frac{J_{g,i}}{h_{r_i}}\ddot{\delta}_i|}{\frac{J_{g,i}}{h_{r_i}}|\ddot{\delta}_i| + \|\boldsymbol{\omega}^{B/N}\|} = \frac{|\dot{\delta}_i| + \varepsilon|\ddot{\delta}_i|}{\varepsilon|\ddot{\delta}_i| + \|\boldsymbol{\omega}^{B/N}\|} \quad (4.115)$$

The value ε is a performance parameter that indicates how closely the CMG's gimbal torque resembles RWA torque (but about the gimbal axis): $\varepsilon \rightarrow 0$ if $h_{r_i} \rightarrow 0$ when the gimbal behaves as a RWA, and $\varepsilon \rightarrow \infty$ if the rotor angular-momentum approaches infinity or the gimbal inertia is negligible, approaching an ideal SGCMG, as is shown in Fig. 4.14 where the scalar $\omega_t = \boldsymbol{\omega}^{B/N} \cdot \hat{\mathbf{o}}_i$. As gimbal friction increases, torque amplification drops. Similarly, it is reduced when the magnitude of rotor angular momentum is small in comparison to the size of the gimbal inertia. These difficulties in fabricating small CMGs that meet the size, mass, and power requirements of smallsats make it likely that the torque amplification for such devices will be severely limited.

Fig. 4.14 Torque amplification versus spacecraft baserate and efficiency parameter



4.9 Chapter Summary

This chapter provides the physical basis for the motion of RWAs and CMGs in the context of spacecraft that use them for attitude control. It has been found that rigid-body dynamics successfully captures most of the behaviors of interest in these momentum devices. Accordingly, the chapter focuses on rigid-body models of them. It does so through a very general vector/dyadic representation of the physics. This coordinate-free approach offers compact and unambiguous derivations. Common coordinate systems are also presented. Some flexible effects are considered, specifically the mechanical compliance in the rotor and related structure, which produces coupled flexible/gyroscopic modes and can retard the gimbal acceleration in the form of an effective inertia. A momentum system offers unique opportunities to achieve robust and lightweight spacecraft designs, but taking advantage of these opportunities requires careful attention to rigid- and flexible-body dynamics.

References

1. P. Hughes, *Spacecraft attitude dynamics* (Courier Corporation, 2012)
2. J. Staelnagel, On the parametrization of the three-dimensional rotation group. *SIAM Rev.* **6**(4), 422 (1964)
3. M. Shuster, A survey of attitude representations. *Navigation* **8**(9), 439–517 (1993)
4. F. Markley, J. Crassidis, *Spacecraft Attitude Determination and Control* (Springer, Berlin, 2014)
5. P. Hughes, *Spacecraft Attitude Dynamics* (Wiley, New York, 1986)
6. H. Kurokawa, A geometric study of single gimbal control moment gyros (singularity problems and steering law). Technical Report 175, Agency of Industrial Technology and Science, Japan, 1998

Chapter 5

Singularities of Control Moment Gyroscopes

A book on spacecraft momentum control systems would not be complete without a discussion of geometric singularities inherent in CMGs. Therefore, this chapter starts with a discussion of common singularities associated with DGCMGs (e.g., gimbal lock) and then moves on to the more troublesome singularities associated SGCMGs. The mathematical structure of these singularities and how it relates to difficulties in avoiding them is also discussed in a way made more accessible to the reader not familiar with the subject matter. Also discussed is the location of singularities associated with an array of CMGs by way of a three-dimensional surface in the momentum space. This chapter concludes with some brief discussion on techniques to perform zero-momentum spin up of an array of CMGs in the presence of singularities at zero momentum.

5.1 Singular Values

Any matrix, whether square or nonsquare, can be decomposed using singular value decomposition as

$$A = U\Sigma V^T \quad (5.1)$$

where U and V are unitary matrices and

$$\Sigma = \begin{bmatrix} \sigma_1 & 0 & 0 \cdots 0 \\ 0 & \sigma_2 & 0 \cdots 0 \\ 0 & 0 & \sigma_3 \cdots 0 \end{bmatrix} \quad (5.2)$$

is a matrix of singular values, σ_i that may be arranged largest to smallest, i.e., $\sigma_1 \geq \sigma_2 \geq \sigma_3$ (Bernstein [1] and Meyer [2]). The rank of a matrix A is the number

of nonzero singular values present in the diagonal matrix, Σ . When a matrix has one or more zero singular values it is defined as being singular. If singular, it is not invertible. Nonsquare matrices by definition are not invertible and have at most a number of nonzero singular values equal to the smallest dimension of the matrix. Therefore, the maximum rank of a nonsquare matrix is the size of the smallest dimension of the matrix. For example the matrix

$$B = \begin{bmatrix} 1 & 0 & 0 \\ 0 & 2 & 0 \end{bmatrix}$$

has two nonzero singular values. Its rank is 2. The matrix

$$B = \begin{bmatrix} 1 & 0 & 0 \\ 0 & 0 & 0 \end{bmatrix}$$

has the same dimensions but is only of rank 1 because it has only one nonzero singular value, $\sigma_1 = 1$.

5.2 Coordinate Singularities Versus Geometric Singularities

There exist purely mathematical coordinate singularities, i.e., those associated with a possibly poor choice of parameterization. For example, a parameterization that involves tangent, secant, or cosecant functions of the gimbal angles becomes undefined at certain values of gimbal angle regardless of the physics. There are also geometric singularities that are fundamentally physical and must show up in any mathematical representation of the array's behavior. The differences between these two situations are discussed here.

5.2.1 Coordinate Singularities

Coordinates describe the state or configuration of a dynamical system. For example, angles and positions serve as coordinates that specify the configuration of many mechanical devices. Gimbal angles typically serve this purpose for an array of CMGs. The angular coordinate associated with rotation of the rotor is often ignored as a cyclic variable, a variable that constantly changes in a way that can be captured with a static parameter, such as scalar angular momentum h_r . Coordinate singularities can occur as the configuration changes and reaches a point where a mathematical function of the coordinates changes infinitely fast or is otherwise undefined. Such singularities arise because of the choice of coordinates. An analyst or a systems engineer makes this choice, for reasons related to convenience or legacy

definitions of the hardware. Therefore, the choice is arbitrary with regard to the physics of the problem and can be altered. Specifically, singular sets of parameters may be replaced with non-singular parameter sets that still describe the same system. Coordinate singularities can be found in the kinematic differential equations that propagate the system's evolution as a function of time or in expressions that relate these coordinates to others. Some specific examples follow.

Example 5.1. Consider the case of a three-coordinate attitude representation known as Euler angles that describes the attitude of one set of basis vectors relative to another. This attitude can be described by a sequence of three rotations through non-coincident axes. An example is the popular 3-2-1, i.e., yaw-pitch-roll rotation. The sequence begins with a rotation ψ about the Z (or 3) axis, followed by a rotation θ about y'' , and finally by a rotation ϕ about an axis x'' to convert from a coordinate basis consisting of the X , Y , Z axes to a coordinate basis in x' , y' , z' as shown in Fig. 5.1. The three direction-cosine matrices (DCMs) that make up the rotation sequence in Fig. 5.1 are

$$D_3(\psi) = \begin{bmatrix} c(\psi) & s(\psi) & 0 \\ -s(\psi) & c(\psi) & 0 \\ 0 & 0 & 1 \end{bmatrix}$$

$$D_2(\theta) = \begin{bmatrix} c(\theta) & 0 & -s(\theta) \\ 0 & 1 & 0 \\ s(\theta) & 0 & c(\theta) \end{bmatrix}$$

$$D_1(\phi) = \begin{bmatrix} 1 & c(\phi) & s(\psi) \\ 0 & c(\phi) & s(\psi) \\ 0 & -s(\phi) & c(\phi) \end{bmatrix}$$

where $c(\cdot) = \cos(\cdot)$ and $s(\cdot) = \sin(\cdot)$. The product of three DCMs is itself a DCM because of the algebraic properties of the group of rotation matrices:

$$D_{321} = D_1(\phi)D_2(\theta)D_3(\psi)$$

or expanded as

$$D_{321} = \begin{bmatrix} c(\theta)c(\psi) & c(\theta)s(\psi) & -s(\theta) \\ s(\phi)s(\theta)c(\psi) - c(\phi)s(\psi) & s(\phi)s(\theta)s(\psi) + c(\phi)c(\psi) & s(\phi)c(\theta) \\ c(\phi)s(\theta)c(\psi) + s(\phi)s(\psi) & c(\phi)s(\theta)s(\psi) - s(\phi)c(\psi) & c(\phi)c(\theta) \end{bmatrix}$$

(continued)

where this 3×3 matrix relates a matrix of the final ' axes to a matrix of the initial axes as follows:

$$[x' \ y' \ z'] = D_{321}[X \ Y \ Z]$$

Solving for the angles from this matrix is a step where the singularity can occur. The coordinate ψ is determined from the arctangent (inverse tangent) of the ratio $D_{321}(1, 2)/D_{321}(1, 1)$:

$$\psi = \tan^{-1} \left(\frac{D_{321}(1, 2)}{D_{321}(1, 1)} \right) \quad (5.3)$$

and

$$\phi = \tan^{-1} \left(\frac{D_{321}(2, 3)}{-D_{321}(3, 3)} \right) \quad (5.4)$$

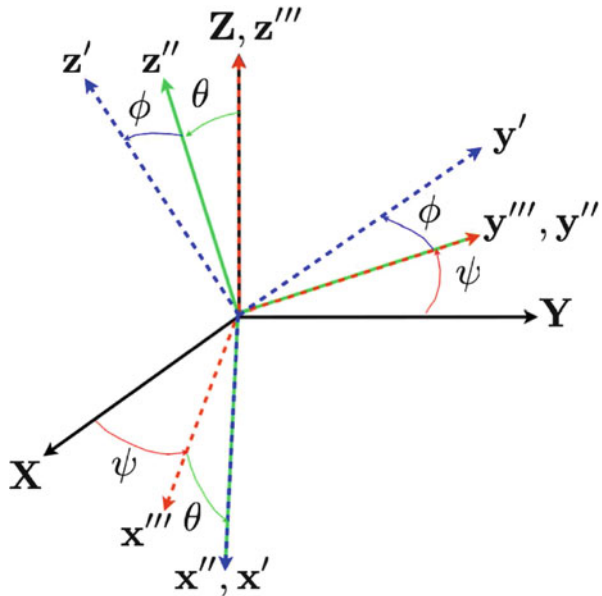
If either of the divisors in Eqs. (5.3) and (5.4) is zero, the value of ψ and/or ϕ is/are undefined. Therefore, singularities exist in the extraction of Euler angles from other parameter sets, in this case from DCMs. Stuelpnagel [3] explains that any three-parameter attitude representation must be singular, non-global, or ambiguous. Therefore, any use of a three-parameter attitude representation that is global and unambiguous risks introducing singularities. Consider the kinematic differential equations of the 3-2-1 Euler sequence

$$\begin{bmatrix} \dot{\phi} \\ \dot{\theta} \\ \dot{\psi} \end{bmatrix} = \frac{1}{c(\theta)} \begin{bmatrix} 0 & -s(\psi) & c(\phi) \\ 0 & c(\phi)c(\theta) & -s(\phi)c(\theta) \\ c(\theta) & s(\phi)s(\theta) & c(\phi)s(\theta) \end{bmatrix} \begin{bmatrix} \omega_1 \\ \omega_2 \\ \omega_3 \end{bmatrix} \quad (5.5)$$

where ω_i are the components of the angular velocity ω of one reference frame relative to another. Clearly, the kinematic differential equation in Eq. (5.5) is singular when $\theta = (2n + 1)\frac{\pi}{2}, n = 0, 1, \dots, N$. Therefore, coordinate singularities may be singular not only in their extraction from other coordinates but also in their kinematic differential equations used for propagating attitude.

Other examples of singular sets of attitude parameterizations are the Gibbs vector and Modified Rodrigues parameters. At least four coordinates are needed for an attitude description to be singularity free (Shuster [4]). This example illustrates that coordinate singularities can arise from how we chose to describe a system's kinematics. Furthermore, coordinate singularities can be avoided with a different choice of parameters. The next section shows that singularities directly associated with the system's physical behavior, not merely coordinate singularities, cannot be avoided with a change of parameters.

Fig. 5.1 Euler rotation sequence



5.2.2 Singularities Associated with Geometric Constraints

Singularities associated with geometric constraints (e.g., limited joint motion) are independent of the choice of coordinates. These singularities are fundamental products of the dynamical system's physics and cannot be avoided through mere mathematics. Caution should be exercised when dealing with systems that exhibit these singularities because coordinates that seem to describe a singularity-free system must be incorrect; the underlying physics of this system is lost in such an attempt, and any such description of its dynamics is incorrect. Some of the earliest literature on geometric singularities comes from that associated with robotic manipulators.

Example 5.2. A robotic manipulator system shown in Fig. 5.2 is represented as

$$\dot{x} = \frac{\partial x}{\partial q} \dot{q} = A(q) \dot{q}$$

where x is a column matrix of coordinates for the end-effector position and orientation relative to a fixed frame, \dot{x} is a column matrix of the rates (or coordinate derivatives), $A(q)$ is the Jacobian matrix as a function of the

(continued)

configuration space q consisting of joint angles, and \dot{q} is a column matrix of joint velocities. Typically, A is nonsquare and therefore noninvertible. The joint velocities \dot{q} corresponding to a desired \dot{x} are found through the Moore–Penrose pseudoinverse. In what follows, the rank of A is assumed to be the minimum of $\dim(x)$, $\dim(q)$. This inverse provides the minimum two-norm solution, i.e., the solution that lies entirely in the range space of A . This solution minimizes the joint rates, which is likely a preferred outcome for reasons of power and mechanical design. Motion in the null space of A does not influence \dot{x} ; therefore, null-space motion carries electromechanical cost with no performance benefits. A solution found via this pseudoinverse can also be interpreted as the minimum-error solution in the case of a least-squares estimate. The case of $\dim(x) < \dim(q)$ corresponds to an over-actuated robotic system. The Moore–Penrose inverse solution for this case is

$$\dot{q} = A^T(AA^T)^{-1}\dot{x}$$

Otherwise, if $\dim(x) > \dim(q)$, i.e., the system is underactuated,

$$\dot{q} = (A^TA)^{-1}A^T\dot{x}$$

For the special case where $\dim(x) = \dim(q)$, the familiar inverse of a square matrix provides the solution:

$$\dot{q} = A^{-1}\dot{x}$$

For this case, A is rank deficient when its rank is less than $\dim(x)$. Specifically, $\text{rank}(A) < 6$ for translation and rotation of a rigid end effector in a typical robotic arm. In that case, A is not invertible, and inverse that appears in the Moore–Penrose pseudoinverse is singular. In such cases, the robotic system contains kinematic singularities. An example of such a singularity is shown in Fig. 5.2 where the robot manipulator is maximally extended. Consider the three joint angles of the planar robotic manipulator Fig. 5.2, θ_1 , θ_2 , and θ_3 relative to the horizontal. Assume that its link lengths are equal to 1 and that only the position and velocity of the end effector are controlled. Then the position of the end effector is related to the joint angles by

$$r = \begin{bmatrix} \cos(\theta_1) + \cos(\theta_2) + \cos(\theta_3) \\ \sin(\theta_1) + \sin(\theta_2) + \sin(\theta_3) \end{bmatrix}$$

and the velocity of the end effector is

(continued)

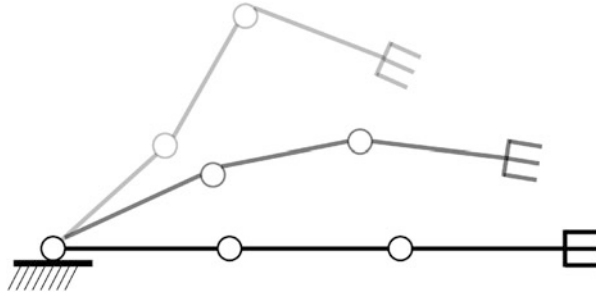


Fig. 5.2 Three-link robot manipulator at singular configuration of maximum extension

$$\dot{r} = \begin{bmatrix} -\sin(\theta_1) & -\sin(\theta_2) & -\sin(\theta_3) \\ \cos(\theta_1) & \cos(\theta_2) & \cos(\theta_3) \end{bmatrix} \begin{bmatrix} \dot{\theta}_1 \\ \dot{\theta}_2 \\ \dot{\theta}_3 \end{bmatrix} = A\dot{\Theta}$$

With the manipulator maximally extended, $\theta_1 = \theta_2 = \theta_3 = 0$, and

$$\dot{r} = \begin{bmatrix} 0 & 0 & 0 \\ 1 & 1 & 1 \end{bmatrix} \dot{\Theta}$$

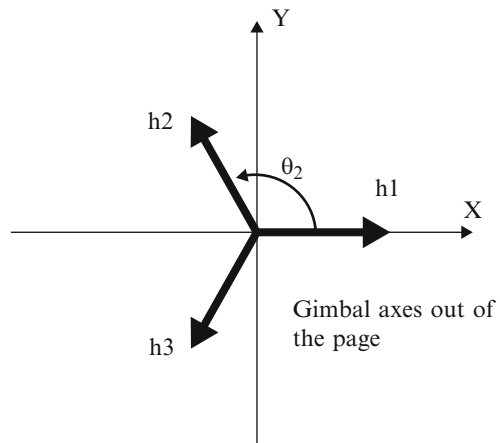
Clearly, this configuration is singular, i.e., where $\text{rank}(A) = 1$, of the robotic manipulator with singular direction, $u = \pm[1 \ 0]^T$. This singularity is analogous to the external or saturation singularities for CMGs discussed in subsequent sections.

A spacecraft with CMGs is a special case of a robotic system of this type, as observed by Bedrossian et al. [5], who relates the singularities associated with robotic manipulators to those associated with SGCMGs. Geometric singularities associated with CMGs are discussed below.

5.3 Control Moment Gyroscope Singularities

The Jacobian of an array of RWAs is constant in the spacecraft body. In fact its geometry is decided well before launch. The CMG Jacobian, in contrast, varies with the gimbal angles of the CMGs and therefore can become singular as the CMG gimbals rotate in flight (see Chap. 4). When the CMG Jacobian is singular, one or more directions exist where no torque is available at that instant. The singular direction consists of a single vector when the Jacobian is rank 2—a so-called rank-2

Fig. 5.3 Momentum vectors of three CMGs with parallel gimbal axes



singularity. It consists of a plane of singular directions when the Jacobian is of rank 1—a rank-1 singularity. However, redundant arrays of CMGs offer additional null solutions or null motion that may provide a means to skirt the singularity while maintaining the required angular momentum.

5.3.1 The Concept of CMG Singularity

As the Jacobian approaches a singularity, the gimbal rates necessary to produce a finite torque approach infinity. Near the singularity, the finite capability of the hardware makes the array incapable of producing torque in one or more directions. A loss of control of the vehicle would follow. So, not only is a CMG array singular when the Jacobian is rank deficient, the array is also effectively unusable for a finite region around these points. As an example, consider the momentum vectors of a planar array of three SGCMGs as shown in Fig. 5.3. All three gimbal axes are parallel and point out of the page. This array is not of practical interest on its own, but it helps illustrate the principle of interest here. The array is shown in a zero-momentum state. By rotating the three gimbals the spacecraft can redirect the net \mathbf{h} vector anywhere in this plane. Figure 5.4 shows how the gimbals can be rotated to produce maximum momentum in either the X or Y directions. The three CMGs combine to produce at most $3h$ momentum in the desired direction. When the array reaches this $3h$ state, it is impossible to increase the net $|\mathbf{h}|$ any further. This condition is known as a “saturation” singularity. Like any physically realizable mechanical system, the hardware comprising the array has limits, specifically a maximum gimbal rate. To avoid unexpected consequences of the reduction in torque authority (or analogously loss of feedback-control gain) that arises as the array approaches saturation, the attitude-control design must incorporate margin between the required momentum and the array’s limited capability. A more subtle situation

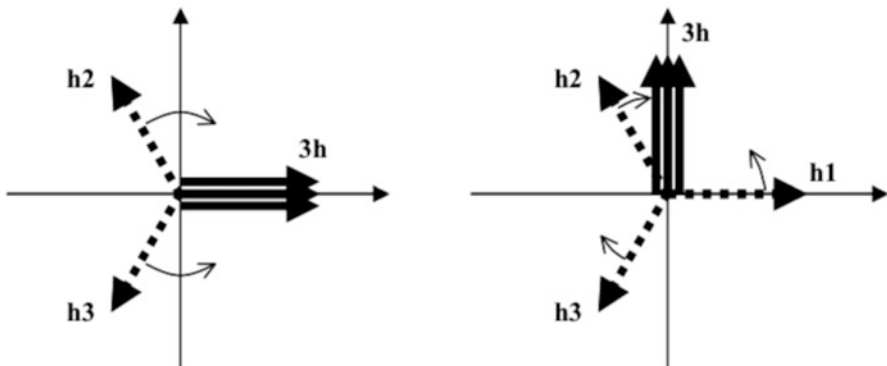
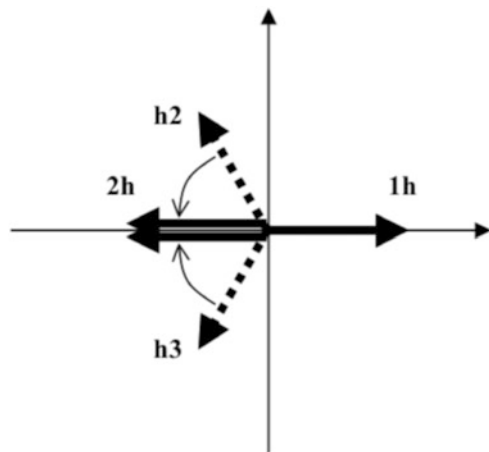


Fig. 5.4 Maximum momentum states of the array (saturation)

Fig. 5.5 A singular state of the array (internal)



occurs when the array is commanded to produce net momentum in the $-X$ direction (see Fig. 5.5). A simple steering algorithm would likely seek to change the gimbal angles δ_2 and δ_3 in the correct direction, but since

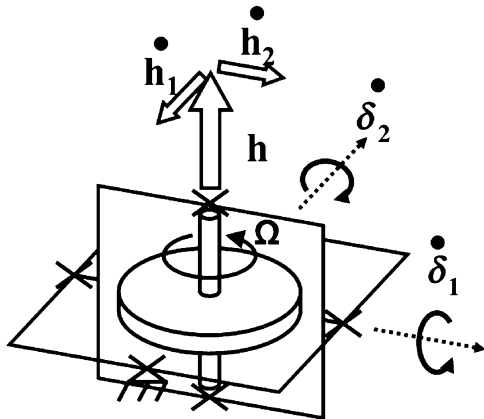
$$\frac{\partial h_X}{\partial \delta_1} = 0 \quad (5.6)$$

at this point, the algorithm would deduce that there is no value in changing δ_1 . The array momentum is now only $1h$ in magnitude, but there is no way to produce any more without producing error in the Y -axis. Specifically, no incremental change in gimbal angles increases h in the desired direction. This situation is called an “internal singularity” because it occurs within, not on, the saturation boundary of the available momentum volume. When one of the CMGs opposes the rest of the array in this fashion, the problematic CMG is known as a “hung gyro.” The avoidance of such singularities has been the subject of considerable research over the years. It has

Table 5.1 Singularity regions associated with the number of CMG in an array

CMG number in array	Singularity region
2	$0h, 2h$
3	$1h, 3h$
4	$0h, 2h, 4h$
5	$1h, 3h, 5h$
6	$0h, 2h, 4h, 6h$

Fig. 5.6 Double-gimbal control moment gyroscope

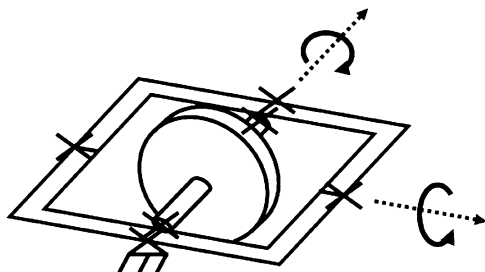


been shown that an array of three SGCMGs has singularities at $1h$ and $3h$, an array of four has singularities at $0h$, $2h$, and $4h$, an array of five at $1h$, $3h$, and $5h$, and so on. This is discussed further in Sect. 6.5.2, and Meffe and Stocking [6]. (Unlike this simple planar example, the so-called “ nh ” singular surface of most CMG arrays does not have magnitude nh). Table 5.1 lists the combinations of singular surface regions for the number of CMGs and their associated regions. Conventional wisdom has established a safe strategy: use a three-SGCMG array to avoid the singularity at $0h$ and size the momentum system such that attitude control never requires more than $1h$ from the array. In this way, the entire singularity problem is neatly sidestepped. However, this book argues against restricting the design to a $1h$ sphere of performance. Singularity-avoidance algorithms enable arrays of four or CMGs to achieve considerably larger momentum envelopes and/or reduce the size, weight, and power of the momentum system (see Chap. 7).

5.4 Double-Gimbal Control Moment Gyroscope Singularities

Double-gimbal control moment gyroscopes (DGCMGs), shown in Fig. 5.6, are among the most mechanically complex CMGs. This complexity is due to their multiple gimbals and the additional drive electronics, slip rings, and sensors needed for their use. Severe performance limitations or mass penalties arise from the physics of

Fig. 5.7 Gimbal lock in a DGCMG



these nested gimbals. There is also mathematical complexity with implications for flight-software development. The columns of the Jacobian for DGCMGs contain n vectors that are not in general unit-norm. In addition, parts of the Jacobian associated with the inner and outer gimbal are coupled functions of the inner and outer gimbal angles (see Chap. 4). Nevertheless, these mathematical complexities do not compromise the usability of such an array. The geometric singularities associated with an array of DGCMGs are much like those for a SGCMGs array with one exception—an array with three or more DGCMGs includes only passable internal singularities (Kurokawa [7]). Passable singularities are easily handled by one of various algorithms that provide null motion for singularity avoidance (see Chap. 7). Therefore, the full momentum volume is available in a singularity-free manner.

5.4.1 DGCMG Gimbal Lock

The most familiar of the singularities associated with DGCMGs is gimbal lock. Figure 5.7 shows this configuration. Gimbal lock for DGCMG occurs when the rotor spin axis aligns with the outer gimbal. With the gimbals in this configuration, the outer gimbal can no longer redirect the momentum vector. Mathematically, gimbal lock represents a loss of one control degree of freedom. In this configuration, the behavior of the DGCMG degrades to that of a SGCMG using the inner gimbal.

5.5 Single-Gimbal Control Moment Gyroscope Singularities

Typically four or more devices (RWAs or SGCMGs) are used for attitude control of a spacecraft. Such an array is known as “redundant.” In the case of RWAs, the redundancy is usually added for fault tolerance. The choice of a redundant SGCMG array offers an opportunity to avoid internal singularities, thereby increasing the momentum and torque capability of the array in a mass-efficient way. For all redundant arrays, the Jacobian A , is nonsquare and thus noninvertible. Unlike coordinate singularities, geometric singularities inherent in CMG arrays are not

only mathematical but also physical phenomena—there is physically no torque available in a singular direction or plane of singular directions. In addition, external singularities correspond to the maximum allowable angular momentum in any single direction. It is important to recognize that a CMG array’s singularities are physical because merely preventing a numerical divide-by-zero error is insufficient to address the problem. Instead, null motion is required. The effectiveness of avoiding internal singularities through null motion depends on the form of the singularity. This chapter classifies them as hyperbolic or elliptic. However, in the analysis of CMG singularities, the direction of the singularity is of the utmost importance: if the desired torque has components orthogonal to the singular direction, a proper steering algorithm could exploit this for singularity avoidance.

5.5.1 SGCMG Gimbal Lock

The case where all components of requested torque are along the singular direction is known as gimbal lock. It is impassable when a null-motion solution does not exist at the singularity. Unlike gimbal lock for a DGCMG, gimbal-lock for an array of SGCMGs occurs at any singularity for which

$$\dot{\Delta} = A^+ \dot{h} = A^T (A A^T)^{-1} \dot{h} = 0, \quad \dot{h} \neq 0$$

where Δ is a matrix of the gimbal rates $\dot{\delta}_i$. When gimbal lock occurs, the system is trapped in this singular configuration. Both hyperbolic and elliptic singularities can encounter gimbal lock depending on the commanded torque. However, unlike elliptic singularities, hyperbolic singularities offer the possibility of avoiding gimbal lock.

5.6 Classification of Singularities

Two distinct types of singularities exist, with different classes within them. As discussed previously, singularities for SGCMGs can be classified into the groups/subgroups shown in Fig. 5.8. As discussed above, saturation singularities at the limit of the array capability are common to any array. Such singularities, also known as *external* singularities, are accommodated in the sizing of the control system and are not germane to the discussion of singularity avoidance. Another class of singularities called *internal* singularities are of much greater importance. The array in Fig. 5.9 offers a practical example. For purposes of discussion, the “shared direction” for this roof array (as discussed earlier) is aligned with the Y axis of a reference coordinate system. Suppose that the gimbals in each plane were positioned so the momentum vectors (red) were opposite to one another, one pointing in the $+Y$ direction, the other in $-Y$, as shown. All the momentum

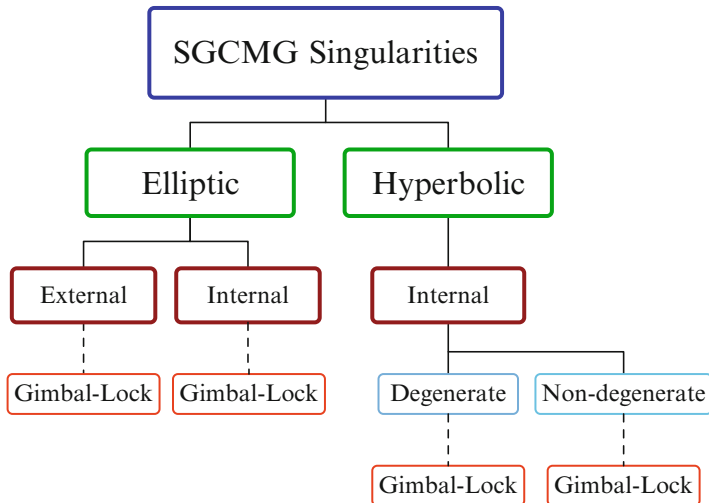
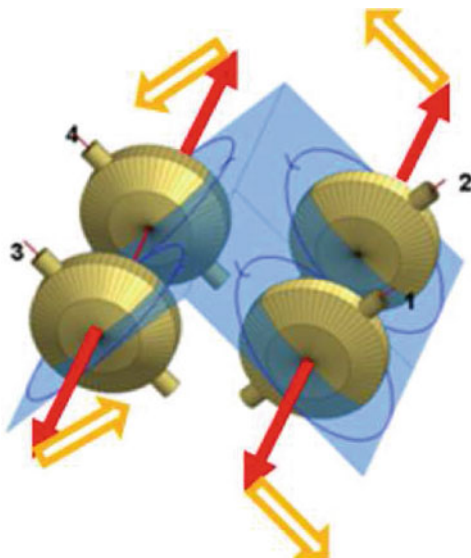


Fig. 5.8 Classification of SGCMG singularities

Fig. 5.9 Shared direction singularity configuration



vectors cancel. The array momentum is zero. No incremental motion of any of the four gimbals can change momentum along the Y axis. Therefore, no collection of gimbal rates can produce a Y torque from this configuration. This is an internal singularity—no torque available, and yet the momentum state is far from the limit of the array's capability. If only three CMGs are operating, there is a 1:1 map between gimbal angle sets and momentum states on \mathbb{R}^3 . Therefore, any internal singularity corresponds to a single momentum state, and the only way to avoid them

is not to go there. This absence of alternatives severely restricts how much of the momentum envelope can be used in practice. Thus a three-CMG array often uses its capability inefficiently. However, if four or more CMGs are operating, the same momentum state can be achieved through infinite combinations of gimbal angles, some of which may be non-singular. This opens the door to creativity in choosing how to steer the gimbals to avoid singularities.

5.7 Singularity Conditions Defined Mathematically

Typically, differential geometry is used to represent hyperbolic and elliptic internal singularities as surfaces or manifolds. Margulies and Aubrun [8] and Tokar and Platonov [9] were the first to use differential geometry for analysis of geometric singularities associated with SGCMGs. Margulies and Aubrun derived singularity type conditions from a differential-geometric singularity condition in the form of a quadratic product. Their results gave the names elliptic and hyperbolic to the geometric singularities associated with SGCMGs. Kurokawa [7] and Bedrossian et al. [10] compared the geometric singularities of SGCMGs to those of robotic manipulators, and set up the null-motion condition from Margulies [8] to consider the possibility of null motion at singularities. Bedrossian et al. derived a method of determining if a hyperbolic singularity is or isn't degenerate for a specific set of gimbal angles. Wie [11] extended the results of Margulies–Aubrun and Bedrossian et al. to show an example of a degenerate hyperbolic singularity contained at the zero-momentum state of a single scissored pair of SGCMGs. Kurokawa [7] investigated the singularities for two classes of arrays—those with parallel gimbal axes and those without. Through differential geometry and principles of curvature, he showed the properties of singularities for parallel and independent type arrays of up to six SGCMGs. The behavior of these internal singularities can also be explained through the use of linear algebra rather than use of differential-geometry. We use the methods presented in [10] to define singularity mathematically. It is customary to define an orthonormal basis $\{\hat{s}_i, \hat{o}_i, \hat{g}_i\}$ shown in Fig. 5.10, where \hat{s}_i is the spin axis of the flywheel, \hat{o}_i is the SGCMG torque direction, and \hat{g}_i is the gimbal axis direction of a SGCMG. A Taylor series expansion of the SGCMG angular momentum about a singular configuration, to second order, gives

$$h(\Delta) - h(\Delta^S) = \sum_{i=1}^n \frac{\partial h_i}{\partial \delta_i} \Big|_{\delta_i^S} \delta_i + \frac{1}{2} \frac{\partial^2 h_i}{\partial \delta_i^2} \Big|_{\delta_i^S} \delta_i^2 + \text{H.O.T.} \quad (5.7)$$

where $h(\Delta^S)$ is the angular momentum of a SGCMG array at a singular set of gimbal angles Δ^S , $\delta_i = \delta_i - \delta_i^S$, h_i is the angular momentum of the i th SGCMG, n is the number of SGCMGs in the system, and *H.O.T.* are the higher-order terms taken to be negligible because only admissible null solutions are considered. Therefore,

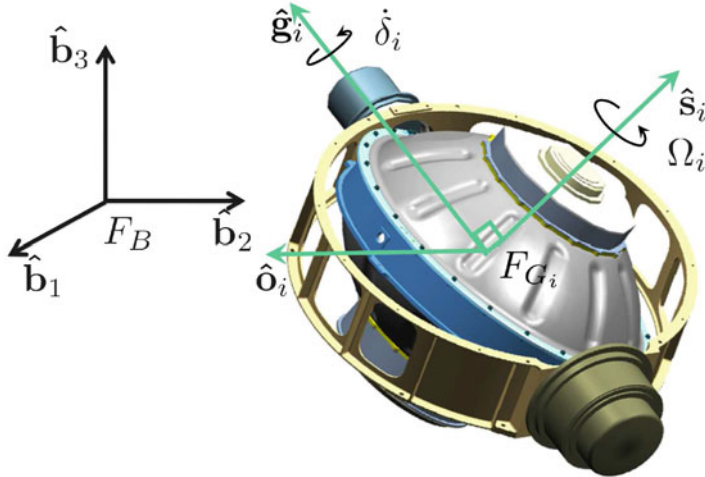


Fig. 5.10 CMG coordinate system fixed in the spacecraft body

the Taylor series expansion in Eq. (5.7) remains valid, i.e., convergent for the present case. The first term on the right-hand side (RHS) of Eq. (5.7) contains the i th column of the Jacobian:

$$\hat{o}_i = \frac{\partial h_i}{\partial \delta_i} \Big|_{\delta_i^S} \quad (5.8)$$

associated with the i th SGCMG's torque direction. The second term on the RHS of Eq. (5.7) is a Hessian and contains the partial derivative of the Jacobian's i th column with respect to the i th gimbal angle

$$\frac{\partial^2 h_i}{\partial \delta_i^2} = \frac{\partial \hat{o}_i}{\partial \delta_i} = -h_{r_i} \hat{s}_i = -h_i \quad (5.9)$$

Next, Eq. (5.9) is substituted into Eq. (5.7). The inner product of the result with the singular direction u , obtained from $\text{null}(A^T)$, yields

$$u^T [h(\Delta) - h(\Delta^S)] = \frac{1}{2} \sum_{i=1}^n u^T h_i \partial \delta_i^2 \quad (5.10)$$

The first term on the RHS of Eq. (5.7), $u^T \hat{o}_i$ has zero contribution because of the definition of the singular direction. Equation (5.10) can be written more compactly in matrix form as

$$u^T [h(\Delta) - h(\Delta^S)] = \frac{1}{2} \partial \Delta^T P \partial \Delta = 0 \quad (5.11)$$

where P is the singularity projection matrix defined as $P = \text{diag}(u^T h_i)$. By definition, null motion does not affect the total system angular momentum, which requires that $h(\Delta) = h(\Delta^S)$. Consequently, the left-hand side (LHS) of Eq. (5.11) is zero, i.e., $\partial\Delta^T P \partial\Delta = 0$. As in [10], null motion is expressed in terms of the basis $N = \text{null}(A)$, concatenated in matrix form as

$$\partial\Delta = \sum_{i=1}^n \lambda_i v_i = N\lambda \quad (5.12)$$

where λ is the column matrix of the scaling components of the null-space basis vectors v_i . In this concatenation step, the v_i are columns representing the null-space basis. So, $N \in \mathbb{R}^{n \times (n - \text{rank}(A))}$ is a $n \times (n - \text{rank}(A))$ real matrix for any system of SGCMGs. Substituting Eqs. (5.12) into (5.11) while observing the null-motion constraint, yields

$$\lambda^T S \lambda = 0 \quad (5.13)$$

As a result of this analysis, the singularity-definition matrix S is defined as

$$S = N^T P N \quad (5.14)$$

Therefore, it is always true that $S \in \mathbb{R}^{(n - \text{rank}(A)) \times (n - \text{rank}(A))}$. The eigenvalues of S determine whether a singularity is hyperbolic or elliptic. If S is definite, i.e., has all positive or negative eigenvalues, it contains only a trivial nullspace because only a $\lambda = 0$ satisfies Eq. (5.13). Therefore, situations where the S is definite constitute elliptic singularities. They are so named because of the ellipsoidal nature of the quadratic in Eq. (5.13). For example, it can be rewritten as the equation of an ellipse for a rank 2 singularity:

$$au_1^2 + bu_2^2 = r^2 \quad (5.15)$$

where u_1 and u_2 are components that are a function of the eigenvectors of S and null-space coefficients, λ , a , and b , are the eigenvalues of S or semimajor axes of the ellipse/ellipsoid/hyperellipsoid, and r^2 is the value of the result in Eq. (5.13) for arbitrary λ . When S is semi-definite, i.e., it has at least one $\lambda \neq 0$ at the point Δ^S , then the null space is non-trivial. That value of λ satisfies Eq. (5.13). Singularities that are semi-definite are known as hyperbolic in the literature even though they produce quadratic products that are paraboloids in Eq. (5.13) with one or more of the eigenvalues zero. If S is indefinite, the eigenvalues are positive, negative, and/or zero. In that case, Eq. (5.14) may equal zero even though S itself may not have a null space. For example, consider the case

$$S = N^T P N = [1 \ 1] \begin{bmatrix} -1 & 0 \\ 0 & 1 \end{bmatrix} \begin{bmatrix} 1 \\ 1 \end{bmatrix}$$

In this example the solution happens to equal zero, but that fact is unrelated to the rank of P . By analogy, non-trivial null motion or at least a null solution to the gimbal angles is possible near singularity and the possibility of singularity avoidance may hold for all S , semi-definite or indefinite. These singularities are named hyperbolic singularities due to the hyperboloid shape of the quadratic in Eq. (5.13). It should be noted that “possibility” is stressed because additional null solutions do not constitute a sufficient condition for the singularity to be passable, or avoidable through null motion. An example, which is discussed below, is the case of degenerate-hyperbolic singularities discussed in Bedrossian et al. [10].

5.7.1 Determination of Singularity Degeneracy

The authors in [10] were the first to include the null-space basis as part of determining whether a specific point of angular momentum offers null solutions, as shown in the preceding analysis. They also provided an analytic way to determine if all of such null solutions are singular, i.e., that the singularity is a degenerate hyperbolic singularity. When the Jacobian is rank 1, more terms are needed from the Taylor series expansion in Eq. (5.10) to determine if null solutions exist. Degenerate solutions of null motion in the vicinity of singularity lie on a local curve along which the Jacobian is less than full rank. Therefore, null motion at a degenerate hyperbolic singularity satisfies the null-motion condition in Eq. (5.13) and does not change the array angular momentum. Although the individual output-torque directions of the CMGs, (the columns of the Jacobian) may change, the Jacobian instantaneously remains less than full rank. To define a hyperbolic singularity as degenerate we first define the commonly used metric for the distance from singularity. This singularity metric is $m = \sqrt{\det(AA^T)}$ which is the product of the Jacobian singular values (Yoshikawa [12]). The objective is to find the hyperbolic-singularity null solutions for which $m(\Delta) > 0$, thereby showing that there may exist null motion that can move the system away from singularity. To accomplish this objective we first need to find the nonzero, i.e., non-trivial admissible null solutions λ that satisfy Eq. (5.13). Having found λ , we then determine if any of these null solutions meet the constraint $m(\Delta) > 0$. The analysis begins with a Taylor series expansion of m about a specific δ :

$$m(\Delta^S + \Delta) = m(\Delta^S) + \sum_{i=1}^n \frac{\partial m}{\partial \delta_i} \Bigg|_{\delta_i^S} \delta_i + \frac{1}{2} \sum_{j=1}^n \sum_{i=1}^n \frac{\partial^2 m}{\partial \delta_j \partial \delta_i} \Bigg|_{\delta_i^S} \delta_j \delta_i + \text{H.O.T.} \quad (5.16)$$

It is clear that $m(\Delta^S) = 0$ by the definition of singularity and

$$\frac{\partial m}{\partial \delta_i} \Bigg|_{\delta_i^S} = 0$$

because it is an unconstrained stationary point of m . Therefore, neglecting the H.O.T., Eq. (5.16) in matrix form is

$$m(\Delta^S + \Delta) = \frac{1}{2} \partial\Delta^T \frac{\partial^2 m}{\partial\Delta\partial\Delta^T} \partial\Delta \quad (5.17)$$

where the null solutions λ are incorporated as a linear combination of null-space basis vectors, and

$$W = N^T \frac{\partial^2 m}{\partial\Delta\partial\Delta^T} N = N^T M N \quad (5.18)$$

where M is the Hessian of m . The fact that near singularity $m > 0 \forall \delta$ implies that M and W are also positive definite. Therefore, a sufficient condition for null motion to permit the array to escape singularity, i.e., the hyperbolic singularity is not degenerate if $M > 0$. However, if W is singular and thus contains a null-space, solutions λ exist to keep the quadratic form in Eq. (5.17) zero. If these are the same solutions to the quadratic result in Eq. (5.13), the test for degeneracy is inconclusive. When this occurs, either no null solutions exist to move the system away from singularity or the H.O.T. in the quadratic forms in Eqs. (5.13) and (5.17) must be considered. Here, degeneracy of a hyperbolic singularity is found either through a local analysis and searching the entire set or through globally searching all of the null-space trajectories that produce the same angular momentum. Neither is a straightforward process. Some cases may arise, such as the four-CMG roof array, where null motion may be available at a singularity but where a connected set of null motions can reach a non-singular angular momentum in finite time.

5.8 Hyperbolic Singularities

The previous section defined singularities mathematically by the ability of null motion to pass through or avoid them. All such singularities lie inside the angular-momentum envelope shown in Fig. 5.19, and all points on the internal singular surface shown in Fig. 5.20 that correspond to a hyperbolic singularity have null solutions or null motion that has the possibility of being used for singularity avoidance. This section offers some examples of hyperbolic singularities.

5.8.1 Non-degenerate Hyperbolic Singularities

Non-degenerate hyperbolic singularities have a continuum of non-singular null solutions at singularity, where null motion is possible for singularity avoidance. The four CMG pyramid array has both hyperbolic and elliptic singularities (see

Chap. 6). The following example considers a four CMG pyramid array and uses the tools developed in the previous section to classify singular configurations for an array of CMGs. Consider the example for a four CMG pyramid array at a skew angle β taken from Bedrossian [13]. The “skew” angle is the angle of the plane of angular momentum of the rotor, spanned by rotating the gimbal, with respect to the horizontal axis of the SGCMG array. The skew angle is therefore the complement of the “inclination” angle (see Sect. 4.2).

Example 5.3. The angular momentum of this array is

$$h = h_r \begin{bmatrix} -c(\beta)s(\delta_1) \\ c(\delta_1) \\ s(\beta)s(\delta_1) \end{bmatrix} + h_r \begin{bmatrix} -c(\delta_2) \\ -c(\beta)s(\delta_2) \\ s(\beta)s(\delta_2) \end{bmatrix} + h_r \begin{bmatrix} c(\beta)s(\delta_3) \\ -c(\delta_3) \\ s(\beta)s(\delta_3) \end{bmatrix} + h_r \begin{bmatrix} c(\delta_4) \\ c(\beta)s(\delta_4) \\ s(\beta)s(\delta_4) \end{bmatrix}$$

$$A = h_r \begin{bmatrix} -c(\beta)c(\delta_1) & s(\delta_2) & c(\beta)c(\delta_3) & -s(\delta_4) \\ -s(\delta_1) & c(\beta)c(\delta_2) & s(\delta_3) & c(\beta)c(\delta_4) \\ s(\beta)c(\delta_1) & -s(\beta)c(\delta_2) & s(\beta)c(\delta_3) & s(\beta)c(\delta_4) \end{bmatrix}$$

For a four CMG pyramid array with zero angular momentum, a set of gimbal angles $\Delta = [90 \ 180 \ -90 \ 0]^T$ deg is a hyperbolic singularity that has the following Jacobian

$$A = h_r \begin{bmatrix} 0 & 0 & 0 & 0 \\ -1 & c(\beta) & -1 & c(\beta) \\ 0 & -s(\beta) & 0 & s(\beta) \end{bmatrix}$$

and singular direction

$$u = \begin{bmatrix} 1 \\ 0 \\ 0 \end{bmatrix}$$

The resultant projection matrix is

$$P = h_r \text{diag}(-c(\beta), 1, -c(\beta), 1)$$

and the null space of the Jacobian, concatenated in matrix form, is

$$N = \begin{bmatrix} -1 & 2c(\beta) \\ 0 & 1 \\ 1 & 0 \\ 0 & 1 \end{bmatrix}$$

(continued)

The resulting singularity-definition matrix is

$$S = 2h_r \begin{bmatrix} -c(\beta) & c(\beta)^2 \\ c(\beta)^2 & 1 - 2c(\beta)^3 \end{bmatrix}$$

The determinant of the singularity definitions matrix is $4h_r c(\beta)(c(\beta)^3 - 1)$. If $0 \leq \beta \leq \pi/2$, $c(\beta) > 0$, the term $4h_r c(\beta)$ can be neglected. Also, $c(\beta)^3 \leq 1$. So, S is either indefinite or semi-definite, and therefore this singularity is a hyperbolic singularity.

5.8.2 Degenerate Hyperbolic Singularities

Degenerate hyperbolic internal singularities occur when all of the null-space solutions for a particular point of angular momentum correspond to a singular Jacobian, leaving no room for instantaneous singularity avoidance. Hyperbolic singularities that are degenerate are also considered impassable and therefore may be handled in a manner similar to elliptic singularities. Consider the example of a degenerate hyperbolic singularity from Wie [11] for a pair of two SGCMG with parallel gimbal axes.

Example 5.4. The angular momentum and Jacobian for a set of two SGCMGs with parallel gimbal axes is

$$\begin{aligned} h &= h_r \begin{bmatrix} s(\delta_1) \\ c(\delta_1) \end{bmatrix} + h_r \begin{bmatrix} s(\delta_2) \\ c(\delta_2) \end{bmatrix} \\ A &= h_r \begin{bmatrix} c(\delta_1) & c(\delta_2) \\ -s(\delta_1) & -s(\delta_2) \end{bmatrix} \end{aligned}$$

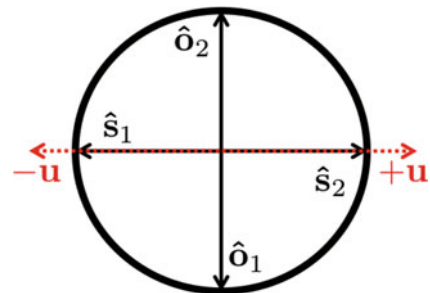
For this array, the singularity measure m is

$$m = s(\delta_1 - \delta_2)$$

Now, there are two singular configurations for this array: one in which $\delta_1 - \delta_2 = 0$, which is the saturation singularity at $2h$, and one that occurs internally at $h = 0$, when $\delta_1 - \delta_2 = \pi$. Because all hyperbolic singularities are internal, the latter case is of interest for degenerate hyperbolic singularities. By inspection, all $0h$ configurations must have $\delta_1 - \delta_2 = \pi$

(continued)

Fig. 5.11 Degenerate hyperbolic singularity



and thus are singular. This singular configuration is shown in Fig. 5.11. In addition, the singular condition continues to be in force when both gimbals are moving using null motion. Therefore, this point of angular momentum has only null-motion solutions that are always singular. Furthermore, any set of gimbal angles at this point of angular momentum is a degenerate hyperbolic singularity.

5.9 Elliptic Singularities

Elliptic singularities are those in which null motion does not exist for a specific value of array angular momentum. Since elliptic singularities do not permit null motion, the only way to escape singularity is for the array's angular momentum to be perturbed. This perturbation induces error in the spacecraft's motion relative to what the attitude-control subsystem attempts to achieve.

5.9.1 External Elliptic Singularities

Elliptic singularities comprise both external and internal singularities. As explained above, external singularities occur on the surface of the array angular-momentum envelope as shown in Fig. 5.20. Consider again the example of a four CMG pyramid array with skew angle β .

Example 5.5. For a four CMG pyramid array, the set of gimbal angles $\Delta^S = [90 \ 90 \ 90 \ 90]^T$ is an external elliptic singularity with angular momentum and Jacobian

$$A = h_r \begin{bmatrix} 0 & 1 & 0 & -1 \\ -1 & 0 & 1 & 0 \\ 0 & 0 & 0 & 0 \end{bmatrix}$$

and singular direction

$$u = \begin{bmatrix} 0 \\ 0 \\ 1 \end{bmatrix}$$

The resultant projection matrix is

$$P = h_r \text{diag}(s(\beta), s(\beta), s(\beta), s(\beta))$$

and the null space of the Jacobian concatenated in matrix form is

$$N = \begin{bmatrix} 0 & 1 \\ 1 & 0 \\ 0 & 1 \\ 1 & 0 \end{bmatrix}$$

The resulting singularity definition matrix is

$$S = 2h_r \begin{bmatrix} s(\beta) & 0 \\ 0 & s(\beta) \end{bmatrix}$$

The determinant of the singularity definitions matrix is $2h_r s(\beta)^2$ which is obviously positive meaning that S is definite and corresponds to an elliptic singularity. Therefore, no null motion can exist in the vicinity of Δ^S , and this singularity is elliptic and impassable. Also, note that a definite P proves the singularity to be an external singularity, i.e., maximum projection of angular momentum. S is always definite when P is definite, proving that external singularities are all elliptic.

5.9.2 Internal Elliptic singularities

Elliptic singularities that lie on the internal singular surfaces, such as those shown for the four CMG pyramid array in Fig. 5.20, are referred to as elliptic internal singularities. Unlike external singularities, these singularities are not a simple matter of sizing a CMG array; furthermore, since they occur instantaneously, they cannot be avoided by a naive algorithm on the fly. Consider the example for an internal singularity of a four CMG pyramid array.

Example 5.6. For a four CMG pyramid array, the set of gimbal angles $\Delta^S = [-90 \ 0 \ 90 \ 0]^T$ is an internal elliptic singularity with angular momentum and Jacobian

$$h = h_r \begin{bmatrix} c(\beta) \\ 0 \\ -s(\beta) \end{bmatrix} + h_r \begin{bmatrix} -1 \\ 0 \\ 0 \end{bmatrix} + h_r \begin{bmatrix} c(\beta) \\ 0 \\ s(\beta) \end{bmatrix} + h_r \begin{bmatrix} 1 \\ 0 \\ 0 \end{bmatrix}$$

$$A = h_r \begin{bmatrix} 0 & 0 & 0 & 0 \\ 1 & -c(\beta) & 1 & c(\beta) \\ 0 & s(\beta) & 0 & s(\beta) \end{bmatrix}$$

and singular direction

$$u = \begin{bmatrix} 1 \\ 0 \\ 0 \end{bmatrix}$$

The resultant projection matrix is

$$P = h_r \text{diag}(c(\beta), -1, c(\beta), 1)$$

and the null space of the Jacobian concatenated in matrix form is

$$N = \begin{bmatrix} -1 & 2c(\beta) \\ 0 & -1 \\ 1 & 0 \\ 0 & 1 \end{bmatrix}$$

The resulting singularity definition matrix is

$$S = 2h_r \begin{bmatrix} c(\beta) & c(\beta)^2 \\ c(\beta)^2 & 2c(\beta)^3 \end{bmatrix}$$

(continued)

The determinant of the singularity definitions matrix is $2h_r c(\beta)^4$ which is positive and therefore, the singularity is defined as elliptic. Therefore, no null motion can exist in the vicinity of Δ^S , and this singularity is elliptic and impassable. Also, P is indefinite and therefore, it is an internal singularity.

5.10 Passability and Impassability of Singular Points

Having defined and categorized the types of singularities encountered in CMG arrays, we can now discuss an important property of singular points which has direct practical applicability to the choice of array architectures and controls. The concept of passability for a singular point is neither consistent nor clearly explained in the literature. This probably has to do with the fact that there has been no set standard in defining passability in terms that are understood by more readers than the mathematically inclined. Therefore, here we will define in our own terms the passability of points of angular momentum and their corresponding singularities. Defining passability of points of angular momentum, provides a means for the user of a CMG-based spacecraft momentum control system to map out troublesome parts of the angular momentum workspace (see Sect. 5.11). In this discussion we must distinguish between a point in gimbal space (a specific set of n gimbal angles), and the corresponding point in momentum space (a vector in 3 axes). Any array of greater than three CMGs has many possible combinations of gimbal angles that map to the same point in momentum space. Some of these combinations of gimbal angles may be singular, others not. Passability is a characteristic of a point in momentum space, and it derives from an examination of the entire family of gimbal angle sets that map to that point. The concepts discussed in this section are not based on local analysis and therefore are different from those shown in [10, 14]. A point in momentum space is called passable if it is possible to change the point from singular to non-singular using only null rotations of the gimbals. Subcategories of impassable and passable singularities are shown in Fig. 5.12. Note that we cannot

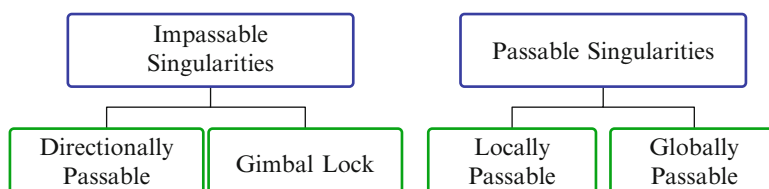
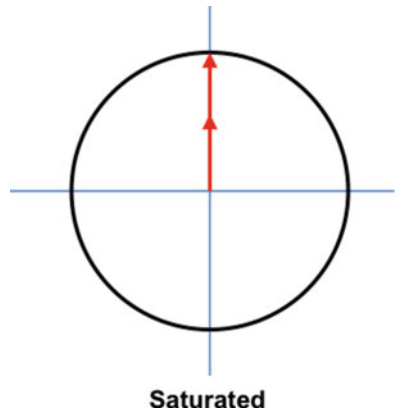


Fig. 5.12 Impassability and passability types

Fig. 5.13 Saturation singularity (elliptic)



simply extend the categories of singularities presented in Fig. 5.8. This is because passability is a property of the momentum point, and the singularities of Fig. 5.8 are properties of a specific gimbal angle set. In the rest of this section, we shall examine each of the different types described in Fig. 5.12. To illustrate, examples will be provided using simple planar arrays of CMGs with parallel gimbal axes. These arrays offer a convenient way to visualize the distinctions among the various categories of singularity.

5.10.1 Impassable Singular Points

First, consider a point in momentum space characterized as an elliptic singularity (see Sect. 5.9). As this point has no null motion, it must be impassable by definition. An example would be any point on the saturation boundary, such as shown in Fig. 5.13. There may be multiple gimbal angle solutions (e.g., mirror images) for this point of angular momentum, all corresponding to elliptic singularities, but they are not connected; and hence null motion does not exist between them. Next, we consider a point in momentum space characterized as a degenerate hyperbolic singularity (see Sect. 5.8.2). This point has possible null motion, but all possible gimbal angle sets are singular. Therefore this point must also be impassable by definition. An example is the origin of a two-disc, as shown in Fig. 5.14. The fact that these points are impassable does not imply that they are inescapable. However, traversing these points will, in general, result in torque error, i.e., the net momentum of the array must deviate from the intended momentum trajectory. Whether a torque error results depends upon the instantaneous direction of the commanded torque, and the singular direction of the gimbal set. Consider the following possibilities. *Torque command is in exactly the singular direction:* This case is referred to as “gimbal lock”. It is impossible to move in the intended direction. *Torque command has some components in the singular direction:* In this case, called “directional

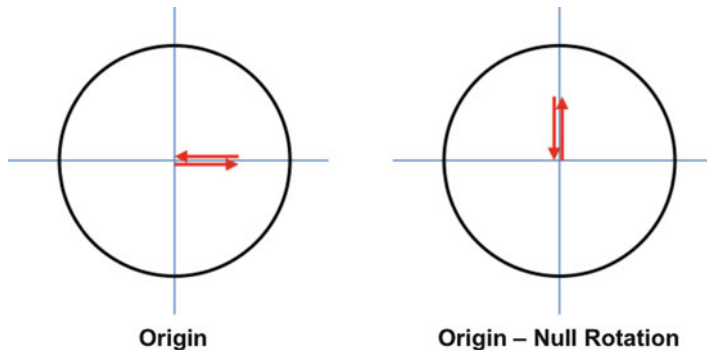


Fig. 5.14 Degenerate hyperbolic singularity

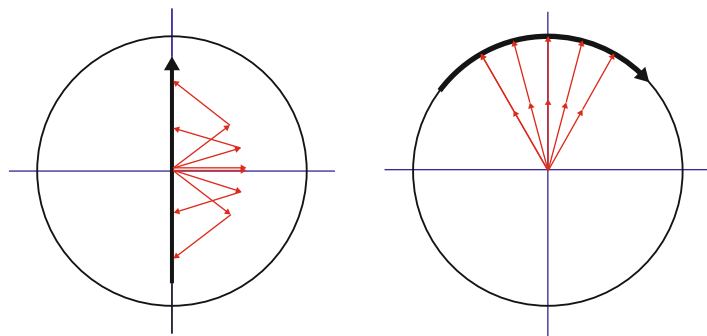


Fig. 5.15 ‘Directional’ passability

passability,” some of the desired torque can be provided, but there will be error. Nevertheless, the act of providing this torque moves us to a different momentum point, and may facilitate singularity escape. The practice of employing trajectories in the range space for singularity escape is discussed by Yamada and Jikuya [14]. *Torque command has no component in the singular direction:* In this case, despite the fact that the point is singular, we can traverse it with no torque error. This unusual case, illustrated in Fig. 5.15, is also referred to as “directional passability” and is possible for any singularity. Note how we can follow the indicated momentum trajectories exactly despite the singularities. The odds of the requested torque happening to fall precisely in the non-singular subspace of the Jacobian where no torque error is accumulated are vanishingly small. No practical system would be designed in the hope that this situation would occur; any torque required along the singular direction leads to attitude-control error. Therefore, a spacecraft would likely be designed to operate only in a situation with passable internal singularities.

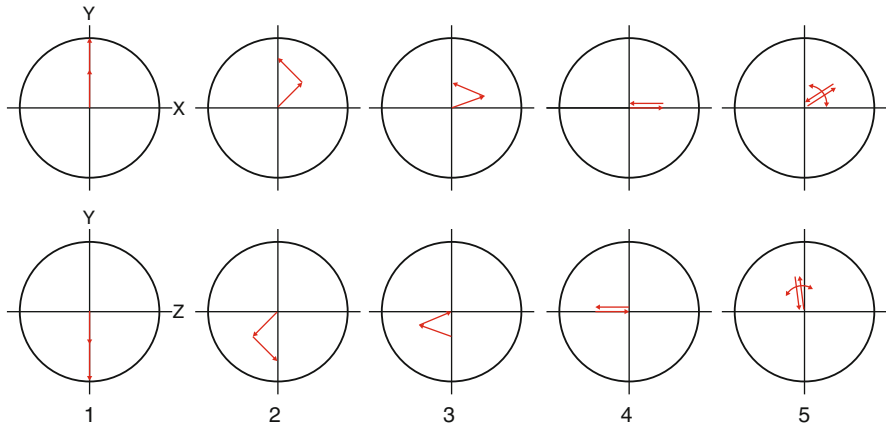


Fig. 5.16 Null space at the origin of the four-CMG roof array

5.10.2 Passable Singular Points

A point in momentum space may have gimbal angle sets characterized by non-degenerate hyperbolic singularity (Sect. 5.8.1). This point has a null space, and it is possible, using only null motion, to move from a singular to a non-singular set of gimbal angles. It is therefore passable by definition. Passable singular points fall into two subcategories, referred to as local or global. Unlike the subcategories of impassable points discussed previously, which depended upon the instantaneous torque command, local or global passability is a characteristic of the momentum point only. Categorizing the types of passability of “local” and “global” has some symmetry with the controls community’s viewpoint of locally and globally stable. *Local passability:* Consider the four-CMG roof array. This array consists of two of the two-CMG discs discussed earlier. The internal singular surfaces for the four-CMG roof array are shown in Fig. 6.8 as blue-green discs. These discs correspond to the origin of one pair of CMGs being swept by the $2h$ disc of the other pair. We can visualize the motion of the four CMGs in this array by drawing the two disks. In Fig. 5.16, the top row shows the disk in the XY plane, and the bottom shows the disk in the YZ plane. The shared axis of the array is “Y” in this example. Figure 5.16 illustrates the null space at the origin of the four-CMG roof array. Examination of snapshots 1–5 verifies that all of these gimbal angle sets map to the net momentum $[0 \ 0 \ 0]^T$, therefore motion between them occurs in null space. Snapshot 1 is singular, unable to produce torque in the Y direction. Snapshots 2 and 3 are non-singular. Snapshot 4 is singular again, and it is interesting to note that this is a “rank 1” singularity—the array can produce torque ONLY in the Y direction. Since four CMGs have rank 1, 3 degrees of freedom of null space are available. They could move to return to snapshot 3, or either of the disks could rotate in pairs to arrangements such as those shown in snapshot 5. Once the array has reached any of

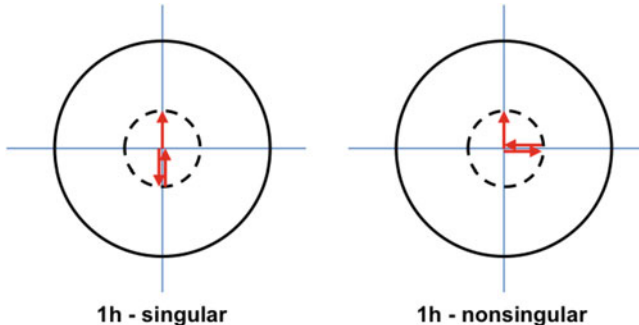


Fig. 5.17 Three parallel CMGs with globally passable singularities

the arrangements depicted by snapshot 5, it is again rank 2—each disc can produce torque in one direction. Thus it has two degrees of freedom of null space, and the CMGs in each disc can rotate in pairs, independently. However, note that there is no way (using only null-space motion) to get from one of these configurations back to the (non-singular) snapshot 3 without first passing through the arrangement of snapshot 4. Such difficulties earn this point in momentum space the characteristic of “local” passability. Specifically, while it is possible using only null space to return to a non-singular state (passable), it cannot be done instantaneously. It takes a finite amount of time to navigate the CMGs to arrangement 4, then 3. Of course, singularities such as those shown in snapshot 5 can be escaped instantaneously by using range space, but doing so results in torque error, as discussed earlier. This is why steering through the entire momentum envelope of a four-CMG roof array may require torque error at some points. The steering law design can influence where these errors occur, for example, moving them well away from the origin. *Global passability:* If all singular combinations of gimbal angles at a point in momentum space can instantaneously move in null space to a non-singular arrangement, the point is globally passable. An example of global passability is the $1h$ singular circle for three parallel CMGs, as illustrated in Fig. 5.17. From symmetry, we can see that any point on the $1h$ internal singular surface above is globally passable. It can then be shown that a six-CMG roof array, comprised of two sets of three parallel CMGs, has all of its internal points of angular momentum globally passable (see [7, 9]). Such an array can avoid all internal singularities with proper steering.

5.11 Singular Surfaces for SGCMG

It is beneficial to understand where in the angular momentum space singularities arise. The satellite attitude-control designer may wish to know all angular momenta that risk a singular Jacobian a-priori so that he or she may design an algorithm to escape or avoid such points. Typically, arrays of SGCMGs are redundant for the

purpose of dealing with singularities by use of null motion. This redundancy and the fact that the Jacobian elements are nonlinear functions of the SGCMG gimbal angles make it difficult to visualize a unique relationship between the solution of gimbal angles and the angular momentum. However, it is still possible to construct three-dimensional surfaces that represents the full extent of singular surfaces for the n -dimensional case. This is done by first constructing a basis for the singular directions $\mathbf{u} \in \mathbb{R}^3$ in terms of angular momentum. In terms of the orthonormal basis shown in Fig. 5.10, the singular direction is

$$\mathbf{u} \in \mathbb{R}^3 : \mathbf{u} \cdot \hat{\mathbf{o}}_i = 0, i = 1, 2, \dots, n \quad (5.19)$$

In this basis, all torque vectors lie in a plane, and \mathbf{u} is orthogonal to that plane. This constraint constitutes a maximum (or minimum) projection of $\hat{\mathbf{s}}_i$ onto \mathbf{u} . For simplicity, this development is restricted to the common case where the magnitude of angular momentum is the same for all SGCMGs in the array. For a given singular direction $\mathbf{u} \neq \hat{\mathbf{g}}_i$ where $\mathbf{u} = \hat{\mathbf{g}}_i$ occurs for DGCMGs and for roof arrays (see Chap. 6). The conditions for singularity are

$$\mathbf{u} \cdot \hat{\mathbf{s}}_i > 0 \text{ and } \mathbf{u} \cdot \hat{\mathbf{s}}_i < 0 \quad (5.20)$$

where the definition of the singular direction $\mathbf{u} \cdot \hat{\mathbf{o}}_i = 0$ must also hold, i.e., a singular direction must exist for singularity. From the orthonormal basis in Fig. 5.10,

$$\begin{aligned} \hat{\mathbf{s}}_i &= \hat{\mathbf{o}}_i \times \hat{\mathbf{g}}_i \\ \hat{\mathbf{o}}_i &= \hat{\mathbf{g}}_i \times \hat{\mathbf{s}}_i \\ \hat{\mathbf{g}}_i &= \hat{\mathbf{s}}_i \times \hat{\mathbf{o}}_i, i = 1, 2, \dots, n \end{aligned} \quad (5.21)$$

Define the projections $\varepsilon_i \triangleq \mathbf{u} \cdot \hat{\mathbf{s}}_i$ which are the projections of the P matrix in Eq. (5.11). Then the torque axis is

$$\hat{\mathbf{o}}_i = \varepsilon_i \frac{\hat{\mathbf{g}}_i \times \mathbf{u}}{\|\hat{\mathbf{g}}_i \times \mathbf{u}\|}, \mathbf{u} \neq \hat{\mathbf{g}}_i, i = 1, 2, \dots, n \quad (5.22)$$

which satisfies Eqs. (5.19) and (5.21), for all torque vectors. The resulting spin axis is

$$\hat{\mathbf{s}}_i = \varepsilon_i \frac{(\hat{\mathbf{g}}_i \times \mathbf{u}) \times \hat{\mathbf{g}}_i}{\|\hat{\mathbf{g}}_i \times \mathbf{u}\|}, \mathbf{u} \neq \hat{\mathbf{g}}_i, i = 1, 2, \dots, n \quad (5.23)$$

Because there are two singular directions—along the positive and negative directions, i.e., $\varepsilon_i \pm 1$ —at each point of singular momentum, there are 2^n singular configurations of gimbal angles of n SGCMGs, for any singular direction. Therefore, adding more SGCMGs does not necessarily provide better singularity avoidance. An example of a singular direction projected onto a CMG's axes is shown in

Fig. 5.18 Example of the singular direction in terms of CMG coordinate frame reconstructed from (Yoon and Tsiotras [15])

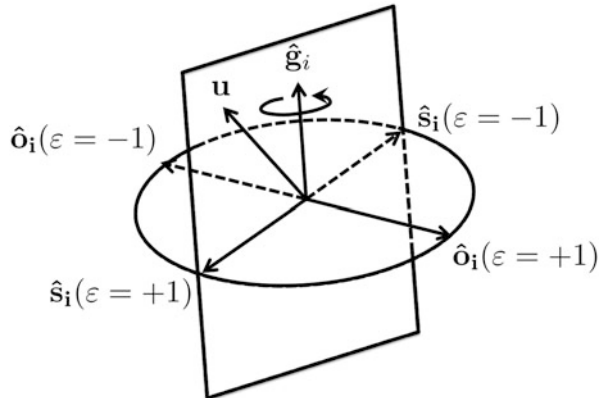


Fig. 5.19 External (saturation) and internal singular surfaces for four CMG pyramid array (external surface shown in red)

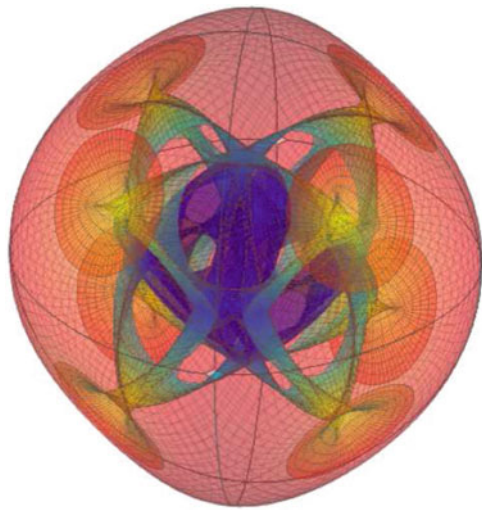
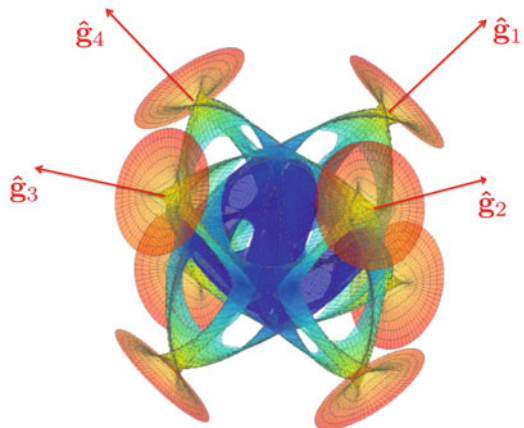


Fig. 5.18 in the coordinate system of a single SGCMG. In Fig. 5.18, the singular direction shares a plane with the i th gimbal axis, and the i th torque vector is always orthogonal to the i th spin axis. This geometry is consistent with the definitions in Eqs. (5.19) through (5.23). Summing Eq. (5.23) results in the total normalized angular momentum from the SGCMGs:

$$\bar{\mathbf{h}} = \sum_{i=1}^n \hat{\mathbf{s}}_i = \sum_{i=1}^n \varepsilon_i \frac{(\hat{\mathbf{g}}_i \times \mathbf{u}) \times \hat{\mathbf{g}}_i}{\|\hat{\mathbf{g}}_i \times \mathbf{u}\|}, \mathbf{u} \neq \hat{\mathbf{g}}_i, i = 1, 2, \dots, n \quad (5.24)$$

When $\mathbf{u} = \hat{\mathbf{g}}_i$ for any of the gimbal axes, Eqs. (5.22) through (5.24) corresponding to those gimbal axes are indeterminate. The locus of total normalized angular momentum $\bar{\mathbf{h}}$, from Eq. (5.24), for all $\mathbf{u} \in \mathbb{R}^3$ and all $\varepsilon_i \neq 0$, i.e., \mathbf{u} not collinear to $\hat{\mathbf{g}}_i$ produces the external singular surface known as the angular momentum envelope

Fig. 5.20 Internal singular surfaces for a four CMG pyramid array



and the internal singular surfaces. Typically, the sequence of signs of ε_i corresponds to the singularity region of the associated singular surface. For example, for a four CMG array with $\varepsilon = \{+, +, +, +\}$ or $\varepsilon = \{-, -, -, -\}$ corresponds to a $4h$ saturation-singularity region. $\varepsilon = \{+, +, +, -\}$, $\varepsilon = \{+, -, -, -\}$ or any other of the 16 combinations of ε with just one sign different, correspond to $2h$ singularity regions. The angular momentum envelope in Fig. 5.19 represents the case where the set of all $\varepsilon_i \neq 0$ of the array have equal sign. Similarly, each of the four internal singular surfaces shown in Fig. 5.20 for a four CMG pyramid array can be found by setting the sign of one of the ε_i to be different from the others. This process yields points inside the momentum envelope that may be singular. The subset of these points for which the rank of the Jacobian is less than 3 are the true singularities.

5.12 Characteristics of Singular Surfaces

The internal and external singular surfaces consist of the locus of points derived from all the singular angular-momentum points identified via Eq.(5.24). The external surface is the set of all singular momentum states corresponding to the maximum array angular momentum, i.e., $\varepsilon = \{+, +, +, +\}$ or $\varepsilon = \{-, -, -, -\}$. This limit makes sense physically: null motion cannot provide angular momentum beyond the array's capability. Within the saturation limit lie the internal singular surfaces. They are shown in Fig. 5.20 for the case of a four CMG pyramid. All points on this surface correspond to the possibility of internal elliptic or hyperbolic singularities. These surfaces are connected smoothly to the external singular surface in Fig. 5.19 by trumpet-like dimples. They are also sometimes referred to as "lily pads." These dimples are tangent to the plane orthogonal to a CMG's gimbal axis, along which none of that CMG's momentum can lie. There are four of these surfaces, each corresponding to one of the four CMGs in this array. Note that the

surface of the angular momentum envelope in Fig. 5.20, is almost a spheroid but for the dimples and the flat parts of the angular momentum envelope near them. A commonly cited choice of skew angle is $\beta = 54.74^\circ$ for this array because this angle produces the symmetry needed for the array to be as close to a spheroid as possible. However, only in the rare case where a spherical angular momentum envelope is of practical use would this angle be implemented: for example, an unlikely spacecraft with identical inertia and identical agility requirements in all axes. More commonly, the momentum envelope would be biased to maximize agility in the one or two directions where it has operational value (see Sect. 6.8). As more SGCMGs are added, the external singular surface becomes more spherical. However, adding more SGCMGs to most arrays does not eliminate the singularity problem. Actually, the number of singular combinations of gimbal angles for any singular direction goes up as 2^n . Therefore, it is incorrect to assume that more SGCMGs always offer more effective singularity avoidance. In addition, research has shown that it is beneficial to optimize the shape of the singular surface as well as to maximize the usable angular momentum. Such an approach can maximize the use of the angular momentum for attitude control instead of devoting gimbal activity to avoiding singularities (see Chaps. 6 and 7). Leve et al. [16] and Sands et al. [17] choose the orientation of SGCMG gimbal axes in the context of spacecraft inertia properties to maximize overall attitude-control performance. The singular surfaces discussed and those in general for SGCMGs are found by projecting the angular momentum from an n -dimensional set of gimbal angles to 3-D space. Therefore, the surfaces are usually subtle and hard to visualize. Techniques by Dominguez and Wie [18] and Meffe and Stocking [6] construct cross sections of the singular surfaces to show attachments of the internal to external singular surfaces as well as the singularity-free angular momentum.

5.13 Numerical Sensitivity in the Vicinity of a Singularity

According to Eq. (5.19), a SGCMG array singularity occurs when a singular direction \mathbf{u} exists that is orthogonal to all output-torque directions $\hat{\mathbf{o}}_i$. However, this result is theoretical and neglects hardware limitations and imprecision. In reality, rather than points of singularities, singularity regions exist where the array cannot produce the torque requested due to finite gimbal-rate limits. Accommodating these limits requires revisiting Eq. (5.19) with the following modification

$$\mathbf{u} \in \mathbb{R}^3 : |\mathbf{u} \cdot \hat{\mathbf{o}}_i| \leq \alpha(\dot{\delta}_{\max}), \quad i = 1, 2, \dots, n \quad (5.25)$$

where $\alpha(\dot{\delta}_{\max})$ is a parameter that limits the distance to singularity based on the maximum gimbal rates achievable. If the condition in Eq. (5.25) for all CMG torque vectors is less than $\alpha(\dot{\delta}_{\max})$, the Jacobian is close enough to singularity that at least one of the CMG cannot produce the gimbal rate needed to match the requested torque. The condition in Eq. (5.25) depends to some extent upon the steering

law. A simple planar case describes what is meant here by region of singularity. Consider the scissored pair of SGCMGs in Example 5.4. This pair of SGCMGs has singularities at $0h$ and $2h$, where the singularity at $0h$ is just a point. The Jacobian is

$$A = h_r \begin{bmatrix} c(\delta_1) & c(\delta_2) \\ -s(\delta_1) & -s(\delta_2) \end{bmatrix}$$

At the $0h$ singularity, the Jacobian and singular direction are

$$A = h_r \begin{bmatrix} 1 & -1 \\ 0 & 0 \end{bmatrix}$$

$$u = \begin{bmatrix} 1 \\ 0 \end{bmatrix}$$

For this system, let $h_r = 1$ and assume a 1° departure of the torque and angular momentum vectors from their original angle along the gimbal axis. The Jacobian for this case is

$$A = \begin{bmatrix} 0.9998 & -1 \\ -0.0175 & 0 \end{bmatrix}$$

Therefore, the requested torque is achieved by

$$\Delta = A^{-1}\dot{h} = \frac{1}{\det(A)} \text{adj}(A)\dot{h}$$

where $\text{adj}(A)$ is the adjoint of A or the cofactor transpose of the A matrix, and

$$\frac{1}{\det(A)} = -57.2987 \quad (5.26)$$

Equation (5.26) shows that a gain of approximately 57 to the gimbal rates needed to achieve the requested torque \dot{h} . It is clear that as the array approaches singularity, even without encountering it, $\det(A)$ becomes smaller. Therefore, the gain that multiplies the torque may lead to unachievable gimbal rates.

5.14 Variable-Speed Control Moment Gyroscope Singularities

A variable-speed control moment gyro (VSCMG) differs from a SGCMG in that it offers an extra control degree of freedom in the form of the rotor torque. This speed variation can be used for singularity avoidance, in principle. So, it is possible for

a set of two VSCMGs with linearly independent gimbal axes to provide full three-axis control to a spacecraft without a singular Jacobian (Yoon and Tsiotras [15]). However, the torque does not scale linearly to power. RWAs, like VSCMGs, also have variable-speed rotors that produce torque through rotor accelerations. They offer at best a 1:1 ratio of output to input torque. SGCMGs produce torque through a gyroscopic effect that amplifies the torque input to the gimbal axis to produce a much higher output torque. In practice, the VSCMG rotor torque is considerably lower than the CMG output torque—sometimes one or more orders of magnitude. Beyond about three orders of magnitude (as is the case in typical SGCMGs), this difference between rotor-torque capability and CMG output-torque capability makes any benefits of variable speed largely irrelevant. Enabling a large VSCMG to provide comparable torque through its rotor requires a comparatively heavy spin motor, introduces thermal challenges, stresses bearing design, and ultimately creates a less-than optimal system design. It may be that very small CubeSat CMGs (CSCMGs)—of a scale suitable for CubeSats—exhibit a more successful balance of rotor torque and gyroscopic output torque. To reduce the amount of RWA accelerations used for singularity avoidance, and therefore the input power used by VSCMGs, Schaub and Junkins [19] developed a mathematically elegant weighted Moore–Penrose pseudoinverse approach that used a local gradient to steer away from singularities and as well as tracking a desired rotor rate. Schaub’s and Junkins’ algorithm shows promise in converging to a set of desired rates or accelerations, thereby reducing the rotor accelerations needed for singularity avoidance. However, such approaches do not address the problem of the SGCMG Jacobian contribution that depends on the speed of the rotors. As the VSCMG rotor speed decreases, the contribution of the gyroscopic torque from the SGCMG is reduced linearly. Therefore, the fact that the rotor speed is often lower sacrifices output-torque capability. Even worse, if the CMGs’ rotor momenta vary too widely, voids can appear in the momentum envelope that resemble saturation singularities but within the interior. Such voids are not necessarily reflected in a singular Jacobian, but nevertheless these configurations are impassable by gimbal motions alone and represent angular-momentum values that cannot be achieved even for non-singular gimbal-angle configurations. These many issues explain why VSCMGs are not widely adopted in practice.

5.15 Zero-Momentum Spin Up

During launch, momentum devices are turned off. There are many reasons, including that the launch vehicle typically prohibits spacecraft actuators from operating until after separation. Also, many rotors are tied down to manage launch loads. Those tiedowns are released only after spacecraft separation. Thus, the momentum devices have zero gimbal and rotor speed, i.e., zero momentum at the beginning of mission operations. Specific procedures prevent the spacecraft from tumbling during on-orbit checkout and spin-up of the RWA or SGCMG. These procedures

spin up CMG rotors to maximum momentum capacity within power constraints while staying at zero momentum and keeping the array far from singularities. These requirements demand that zero-momentum spin up is performed in the null space of the momentum control system. There may be an infinite continuum of spin-up profiles that can be used to spin up the momentum control systems while keeping the array at zero momentum. Also, the generally low-torque rotor spin motors and power limitations within the momentum device mean that a spin-up maneuver in reality can take many hours. For example, the ISS CMGs spin up at approximately 17 rpm per minute, requiring about 6.5 h to reach their full speed of 6,600 rpm. In addition, uncertainties in actuator parameters such as alignments, gimbal and rotor inertias, and friction may impact spacecraft attitude during spinup. Kim et al. [20] addressed these parametric uncertainties and provided an asymptotic result to de-tumbling and zero-momentum spin up after launch tip-off of a four CMG pyramid array in their presence.

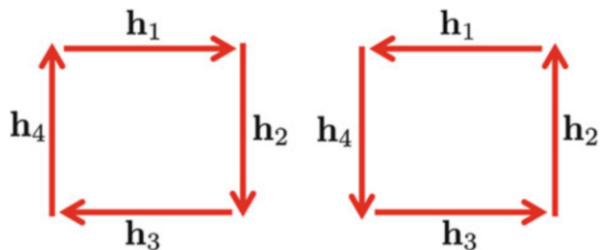
5.15.1 RWA Zero-Momentum Spin-Up

RWAs do not typically spin up to full speed during on-orbit checkout. Unlike SGCMGs, they have the ability to spin down to lower speeds, where viscous friction effects are less and therefore quiescent power is lower (see Chap. 3). Nevertheless, some RWAs may normally operate at a speed well away from zero in order to avoid imprecise torque that occurs at zero speed. For such RWAs, the initial spin-up maneuver is quite straightforward. They do not contain an extra degree of freedom in the gimbals, and RWA arrays involve no singular configurations as long as the array contains at least three independent RWA rotor axes. At least four RWAs are required if a RWA array is to be spun up in the null space to a set of speeds that minimizes zero crossings. Such a spin-up maneuver is typically quick: on the scale of minutes because the bias speeds of the rotors are usually a small fraction of full speed.

5.15.2 Four-CMG Roof Zero-Momentum Spin-Up

The strategy employed for spinning up the CMGs in a roof array involves biasing the momentum of one pane of the roof against the other along the axis they share. This allows both panes of the roof to be well separated from their $0h$ singularity at the origin. This singularity is discussed in Sect. 7.4.3.4, and illustrated in Fig. 7.8. If the four CMGs do not spin up with equal torque, whether due to spin motor tolerances or power-saving measures, the gimbal angles are adjusted as necessary to keep the net momentum from each pane of the roof equal in magnitude and opposite in direction.

Fig. 5.21 Non-singular zero-momentum configurations for a four CMG pyramid array



5.15.3 Four CMG Pyramid Zero-Momentum Spin-Up

There are two popular, mirror-image configurations for the four CMG pyramid that can be used for zero momentum and are far from singularity. These configurations place all of the angular momentum vectors in a plane (torque vectors not coplanar) as shown in Fig. 5.21. It is possible that the power needed to spin up all four CMGs simultaneously while maintaining zero momentum is infeasible. Therefore, the CMG rotors can spin up at least two at a time, with the anti-parallel spin axes, so as to minimize attitude perturbations and achieve the maneuver in a timely manner.

5.16 Chapter Summary

This chapter discusses one of the major issues inherent in control moment gyroscopes, known as singularities. What may appear as a purely mathematical phenomenon in the literature turns out to have important physical consequences for spacecraft design. Classifying singularities helps identify options for attitude-control architectures, such as the choice of arrays that lend themselves to singularity avoidance. The thorough understanding that these classifications make possible may help new momentum-control systems evolve more successfully into viable technology. This systems-engineering activity can benefit from creating visualizations of the singular surfaces in angular-momentum space. They help establish a common vocabulary for communicating the risks and opportunities that momentum systems offer. Balancing the optimistic enthusiasm of rigorously mathematical academic literature with the practical implications of dealing with singularities can provide insight that is sometimes lacking in new space-system concepts.

References

1. D. Bernstein, *Matrix Mathematics: Theory, Facts, and Formulas* (Princeton University Press, Princeton, 2009)
2. C. Meyer, *Matrix Analysis and Applied Linear Algebra* (SIAM, Philadelphia, 2000)

3. J. Stuepnagel, On the parametrization of the three-dimensional rotation group. *SIAM Rev.* **6**(4), 422 (1964)
4. M. Shuster, A survey of attitude representations. *Navigation* **8**(9), 439–517 (1993)
5. N. Bedrossian, Classification of singular configurations for redundant manipulators, in *1990 IEEE International Conference on Robotics and Automation, 1990. Proceedings.* (IEEE, 1990), pp. 818–823
6. M. Meffe, G. Stocking, Momentum envelope topology of single-gimbal cmg arrays for space vehicle control, in *Guidance and Control 1987*, vol. 1, 1987, pp. 19–32
7. H. Kurokawa, A geometric study of single gimbal control moment gyros (singularity problems and steering law). Technical Report 175, Agency of Industrial Technology and Science, Japan, 1998
8. G. Margulies, J. Aubrun, Geometric theory of single-gimbal control moment gyro systems. *AAS J. Astronaut. Sci.* **26**(2), 159 (1978)
9. E. Tokar, V. Platonov, Singular surfaces in unsupported gyrodyne systems. *Cosm. Res.* **16**, 547 (1979)
10. N.S. Bedrossian, J. Paradiso, E.V. Bergmann, D. Rowell, Redundant single gimbal control moment gyroscope singularity analysis. *AIAA J. Guid. Control. Dyn.* **13**(6), 1096 (1990)
11. B. Wie, Singularity analysis and visualization for single-gimbal control moment gyro systems. *AIAA J. Guid. Control. Dyn.* **27**(2), 271 (2004)
12. T. Yoshikawa, Dynamic manipulability of robot manipulators, in *1985 IEEE International Conference on Robotics and Automation. Proceedings.* , vol. 2 (IEEE, 1985), pp. 1033–1038
13. N. Bedrossian, Steering law design for redundant single gimbal control moment gyroscopes. Master's Thesis, MIT, 1987
14. K. Yamada, I. Jikuya, Directional passability and quadratic steering logic for pyramid-type single gimbal control moment gyros. Elsevier *Acta Astronaut.* **102**, 103 (2014)
15. H. Yoon, P. Tsiotras, Singularity analysis of variable-speed control moment gyros. *AIAA J. Guid. Control. Dyn.* **27**(3), 374 (2004)
16. G. Leve, F. Boyarko, N. Fitz-Coy, Optimization in choosing gimbal axis orientations of optimization in choosing gimbal axis orientations of a cmg attitude control system, in *AIAA Infotech@Aerospace Conference*, Seattle, WA, 6–10 April 2009
17. T. Sands, J. Kim, B. Agrawal, 2h singularity-free momentum generation with non-redundant single gimbaled control moment gyroscopes, in *45th IEEE Conference on Decision and Control*, 2006, pp. 1551–1556
18. J. Dominguez, B. Wie, Computation and visualization of control moment gyroscope singularities, in *AIAA Guidance, Navigation, and Control Conference and Exhibit*, 2002
19. H. Schaub, J. Junkins, Singularity avoidance using null motion and variable-speed control moment gyros. *J. Guid. Control. Dyn.* **23**(1), 11 (2000)
20. D. Kim, F. Leve, N. Fitz-Coy, W. Dixon, New startup method using internal momentum management of variable-speed control moment gyroscopes. *AIAA J. Guid. Control. Dyn.* **35**(5), 1472 (2012)

Chapter 6

Momentum-Control System Array Architectures

This chapter provides the analysis tools and fundamental theory for the design of an array architecture consisting of momentum devices. First, the properties of the actuator alignments and their effect on shaping the performance envelope of the momentum-control system are discussed. A survey of common array types for RWA, CMG, and mixed arrays follows. A discussion of performance metrics and methods used to optimize the array architecture concludes the chapter.

6.1 The Nature of Momentum Devices

Thrusters apply external forces to a spacecraft at a point where the thruster expels propellant. The combination of the thruster force vector and position relative to the center of mass results in an external torque on the spacecraft. Like thrusters, the performance envelope for an array of momentum devices depends explicitly on their alignment with respect to the spacecraft body. However, unlike thrusters, the location of momentum devices with respect to the spacecraft's center of mass is unrelated to its ability to influence the attitude. This is entirely due to rigid-body dynamics: all points on a rigid body experience the same angular velocity and angular acceleration. So, a torque applied to the rigid body accelerates all of its inertia in the same way, regardless of what mechanical means applies that torque. This must be the case—otherwise, the body would twist and warp in a non-rigid fashion. The fact that momentum devices apply torque, not force, to the spacecraft allows them to be placed anywhere on the body.

Momentum devices impart internal torque, which conserves angular momentum of the combined spacecraft and momentum-control system. The torque is transferred through the structure of the actuator to the spacecraft body. Along with mechanical design considerations (e.g., bearing and motor choices, rotor shapes and size), actuator alignment for an array of momentum devices is critical to system-level

performance. The following sections describe best practices in choosing alignments for momentum-control actuators in their array. Sources of these requirements are described in Chap. 3, and the dynamics of these actuators is discussed in Chap. 4.

6.2 Momentum and Torque Capability of an Array of RWAs

The momentum and torque capability of an array of RWAs depends on the actuators' alignment with respect to the spacecraft body as well as the rate and acceleration limits of the rotors. It is customary to assume that the RWAs in an array are identical; therefore, the rate and acceleration limits are uniform across all RWAs in the array. This assumption provides a straightforward means to visualize the performance capability of the array. Consider an array of three orthogonal RWAs. The momentum and torque envelopes for this array are box-shaped. For the momentum capacity, the sides of this box are of length $2h_{\max}$, which results from the positive and negative momentum limits for each of the three wheels. For torque, the sides are of length $2\tau_{\max}$. Therefore, the maximum angular momentum and torque for this array lies along the direction $h = \frac{\sqrt{3}}{3}[1 \ 1 \ 1]^T$, with a maximum momentum of $\sqrt{3}h_{\max}$ and torque of $\sqrt{3}\tau_{\max}$ along one of the vertices, as shown in Fig. 6.1. For a general array of three RWAs, not necessarily mutually orthogonal, the torque and momentum envelopes are parallelepipeds.

One of the two commonly implemented RWA arrays, an early favorite at NASA, is the three-orthogonal and one-skew (ortho-skew) RWA array shown in Fig. 6.2. In this array, the skew RWA can be used in one of two ways. First, it can act as a dormant spare which, because it has components in all three axes, can allow three-axis control to be retained in the event that any other single RWA fails. Second, it can be used to as part of a four RWA array. The simultaneous use of all four introduces a degree of freedom of null space, which allows operations such as avoiding zero wheel speeds (where friction can be troublesome), as discussed in Chap. 3.

Fig. 6.1 Angular momentum envelope for a three-ortho-skew RWA array

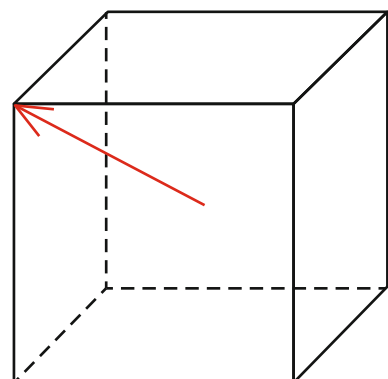


Fig. 6.2 Ortho-skew RWA array

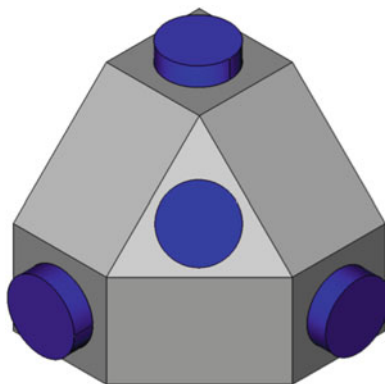
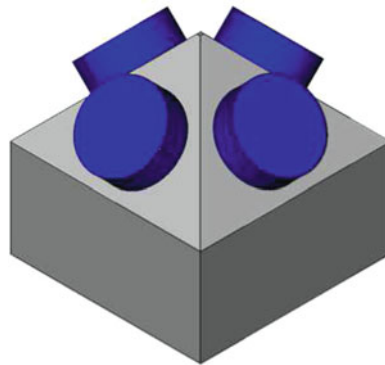


Fig. 6.3 Four-RWA pyramid array



This array of RWAs has one disadvantage. If any wheel other than the skew rotor fails, the resulting torque authority will be unequal among the three axes, with very little capability in the direction of the lost RWA.

The other common use of four RWAs is the four-pyramid array shown in Fig. 6.3. In this array, any single RWA failure leads to the same sort of angular momentum and torque envelope. This array still does not have equal control authority about every axis following a failure, but the capability is far better in any axis than the ortho-skew array, no matter which actuator fails. Markley et al. [1] offers more insight into optimizing momentum via the choice of an RWA array.

6.3 Momentum and Torque Capability of an Array of CMGs

Unlike an RWA, a CMG typically has constant-magnitude rotor angular momentum. The maximum angular momentum, or performance envelope, of CMG arrays consists of a surface where all points correspond to a singular Jacobian (see Chap. 5).

The envelope for an array of SGCMGs is determined by the alignment of all CMG gimbal axes. The locus of all possible angular momentum states of any single SGCMG is a circle (but not the points inside, i.e., not a disc) in the plane normal to its gimbal axis. The combination of these one-dimensional loci comprises the range of possible configurations. Therefore, a minimum of three SGCMGs is required for linear, three-axis attitude control.

The locus of angular momentum states of a single DGCMG is a sphere (but not the points inside, i.e., not a ball). Therefore, a minimum of two DGCMGs is required for full three-axis control, representing four independent degrees of freedom. The single redundant degree of freedom may be used for optimization or failure tolerance.

6.4 Double-Gimbal CMG Arrays

DGCMGs were used on the first US space station, known as Skylab.

Skylab was the first manned spacecraft to utilize large CMGs for momentum storage and attitude control, the first to utilize vehicle maneuvers for CMG momentum desaturation, the first to utilize a fully digital control system with in-orbit reprogramming capability and extensive automatic redundancy management, and the first to utilize an attitude reference system based on a four-parameter strapdown computation which allowed utilization of an all-attitude eigenaxis maneuvering scheme [2].

Skylab flew three orthogonal DGCMGs, shown in Fig. 6.4, with a momentum capability of approximately 3000 Nm-s (2200 ft-lb-s). Two modes of CMG control existed, two- and three-CMG control. After the initial sizing of the CMG momentum, the vehicle moments of inertia increased tenfold. Consequently, the two CMG control mode became hopelessly ineffectual, unable to handle the secular torques and maneuvers in addition to the cyclic torques. On the ninth day into the third manned mission, CMG no. 1 showed evidence of failure, and the mode was changed to two-CMG control. After the failure of CMG no. 1, CMG no. 2 began to show signs of distress as well, and the CMG control allocation and maneuver choice for Skylab was altered to prolong the life of CMG no. 2 until the end of the mission.

The International Space Station also uses DGCMGs. These CMGs were built by Bendix Corp, now part of L3 Space and Navigation. Each provides 4760 Nms of angular momentum with stainless-steel rotors that spin at 6600 rpm. The four-CMG array can store about 19,000 Nms in any direction. With two attitude-control degrees of freedom available each DGCMG, at least two CMGs are necessary to provide attitude control for the ISS. NASA's ISS program has six such CMGs: four on ISS and two spares. One of the spares replaced a CMG failed in June 2002. Another CMG was shut down because of high vibrations, suggesting bearing failure. So, currently three are operating on ISS.

While there are points in a DGCMG momentum envelope where higher gimbal rates are required for a certain torque to be achieved, a DGCMG array is not used for high torque. Its advantage over SGCMG arrays is its ability to distribute momentum

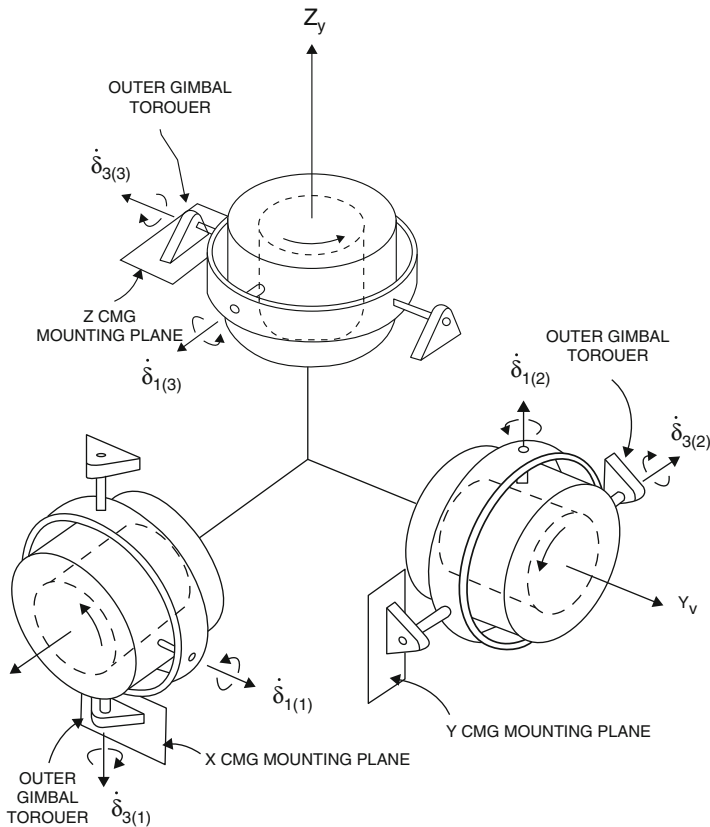


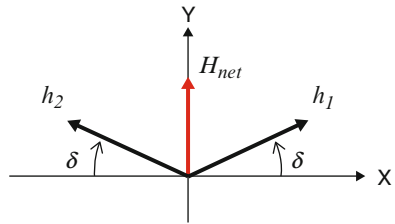
Fig. 6.4 Skylab's array of three orthogonal DGCMGs (Image Courtesy of NASA)

efficiently in any direction. This distribution is achieved at low gimbal rates, with attention paid to avoiding gimbal lock on any single CMG. This steering is a form of singularity-avoidance, but the challenges for DGCMGs in this regard are generally less demanding than in the case of SGCMGs.

6.5 Single-Gimbal CMG Arrays

This section discusses typical arrays of multiple CMGs and heterogeneous arrays of CMGs and RWAs.

Fig. 6.5 A scissored pair of CMGs



6.5.1 Scissored Pairs of CMGs

Perhaps the most intuitive array of CMGs for three-axis attitude control is an array of three orthogonal scissored pairs (Carpenter and Peck [3]). A scissored pair consists of two CMGs with parallel gimbal axes and a linear constraint that keeps the gimbal angles equal in magnitude. Without this constraint, these two CMGs could produce momentum anywhere within a disc of radius $2h$. However, for the scissored pair, the two gimbals are moved in such a way that the locus of net momentum forms a line. This configuration is illustrated in Fig. 6.5, in which the gimbal axes are out of the page. Since both CMGs sweep through the same angle, δ , at all times, the net momentum along the X -axis in the figure is always zero. The net momentum along Y is $2h_r \sin(\delta)$. The torque produced about the Y axis for a gimbal rate, $\dot{\delta}$, is $2\dot{h}_r \cos(\delta)$.

This constraint is, perhaps, the simplest form of steering law. It is so simple that it can be imposed by a gear train or mechanical linkage in place of algorithms involving feedback control. The 1970s era Astronaut Maneuvering Unit, which incorporated three scissored pairs, adopted this mechanical solution. Mathematically, the constraint requires gimbal rates of $\tau/(2h \cos(\delta))$ in opposite directions to produce output torque τ . A single scissored pair offers full access to every momentum state on the line and encounters no singularities (aside from, of course, saturation at $2h$). Without the constraint, a singularity exists at the origin of the disc, complicating the steering of even these two simple devices.

Using a mechanical linkage to impose the constraint is of particular value in the presence of base motion. For example, consider the case in which the array of Fig. 6.5 is nearly saturated (δ is near 90°), and the base to which the CMGs are mounted is instantaneously rotating about the X axis. Gyroscopic precession tries to rotate both gimbals in the same direction. If the gimbals are controlled separately, each gimbal motor would have to dissipate power to oppose this motion. However, if a mechanism forces the gimbals to rotate only in opposite directions, this mechanism maintains the constraint without mechanical work or power dissipation.

Because of their inherent simplicity, scissored pairs have been used in many applications such as robotic manipulators, astronaut maneuvering, and automobiles (Carpenter and Peck [3], Cunningham and Driskill [4], and Litmotors [5]). In one example, a scissored pair is aligned to produce roll torque to stabilize a ship at sea.

Because only one axis of torque is required, this application does not carry any penalty from the absence of transverse momentum that the constraint imposes.

This simplicity extends to the general case of three-axis attitude control. A set of three orthogonal scissored pairs of CMG has a maximum angular momentum envelope similar to that of the RWA array in Fig. 6.1 except that the sides of the cube-shaped envelope have length $4h$. However, the ease and simplicity of use of three orthogonal sets of scissor pairs comes with a cost: the spacecraft must operate six CMGs at all times for a $\pm 2h$ cube of angular momentum. A single failed CMG halves the capability in one axis and couples some transverse torques into the others, further reducing the capability in those directions. Therefore, if this array of CMGs is used, the satellite designer has chosen to trade complex steering algorithms for additional volume, mass, and power.

6.5.2 Collinear (Multiple-Type) Arrays

Scissored pairs are only one of a family of array types characterized by the use of two or more CMGs with common gimbal axes. The most popular of these so-called collinear arrays in the literature are the roof arrays. These arrays have two common gimbal-axis directions. The angular momentum and torque for CMGs with a common gimbal axis reside in a plane (“roof side”) shown as blue surfaces in Fig. 6.6 for the six-CMG and four-CMG roof arrays. Roof arrays are also known as “multiple-type” arrays in the literature (Kurokawa [6]). An older term for the two-triplet architecture shown in the figure is “single-gimbal double-trident,” which dates from 1980 or earlier (Rodden [7]).

Because roof arrays have only two planes of angular momentum and torque, they may experience rank-1 singularities. At a rank-1 singularity, torque is available in only a single direction. Nevertheless, roof arrays of four or more CMGs are

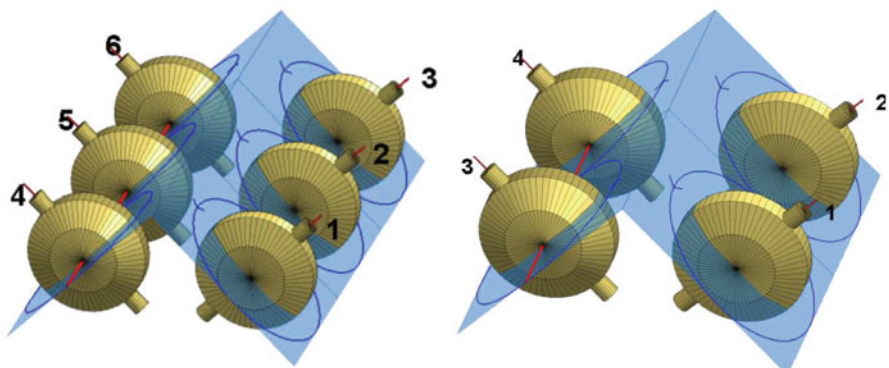


Fig. 6.6 Six-CMG roof array (*left*) and four-CMG roof array (*right*)

preferred over other CMG array architectures such as skew, pyramid, or symmetric type arrays because they have no elliptic internal singularities (see Chap. 5) and Tokar and Platonov [8]. Therefore, all roof arrays can provide a non-singular gimbal-angle solution at every point of angular momentum internal to the momentum envelope. This feature enables roof-array steering laws to achieve non-singular angular momentum close to the edges of the envelope. However, the fact that the internal singularities are hyperbolic does not guarantee that null motion is sufficient to pass a singularity for all combinations of gimbal angles. The null-space motion may have to be preplanned so that certain gimbal-angle combinations are avoided. For such cases, gradient methods are ineffective (Kurokawa [9]).

At this juncture, we digress briefly to introduce the subject of characterizing and plotting singular surfaces. Chapter 5 discussed singularities in detail and construction of singular surfaces, but here we introduce a common convention for describing the various singular structures and how to visualize them.

In general, arrays of CMGs are intended to provide momentum in a three-dimensional envelope. Because the direction of output torque from a SGCMG varies with gimbal angle, sets of gimbal angles may exist for which torque is not possible in all three axes. When this occurs, the array is said to be singular. Consider the four-CMG roof array of Fig. 6.6. With the gimbals positioned as shown, all spin axes, i.e., momentum vectors are parallel with the peak of the roof, which we call the shared axis. A small change to any gimbal angle in the array produces dH/dt in a direction orthogonal to the shared axis, and there is no small change of gimbal angles that can produce a dH/dt , i.e., a torque along the shared axis. Thus this set of gimbal angles is singular.

Once a set of gimbal angles like this is encountered, rotating any CMG gimbal angle 180° also results in a singular state. This gives rise to a convention for describing which of these singular states is present. In Fig. 6.7, if all four of the momentum vectors were not necessarily parallel, but pointing in the same direction, we would refer to this as a $4h$ singularity. For an n -CMG array, the nh singularities will always be on the saturation surface of the array. Next, if one of the CMGs was pointed oppositely from the other three, this would be referred to as a $2h$ singularity. The names derive from the “net” momentum in a simple configuration like this, but

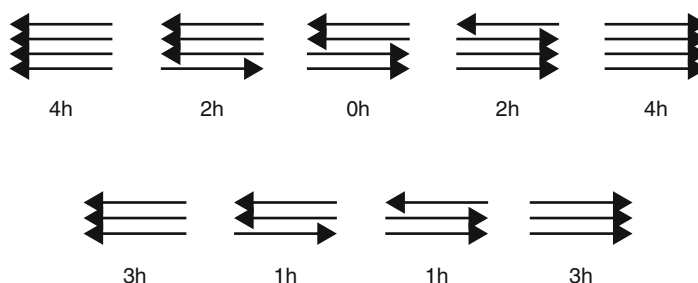


Fig. 6.7 Singularity designations

the reader is cautioned that the “ nh ” singular surfaces do not always have momentum magnitude of nh . Finally, if two CMGs point opposite the other two, the condition is known as a $0h$ singularity. These combinations are illustrated in Fig. 6.7. In general, we can determine this designation by projecting the momentum vectors onto the singular direction and examining their sign.

It follows from this definition that an array with an even number of CMGs can have $0h$, $2h$, ..., nh singularities, and an array with an odd number can have $1h$, $3h$, ..., nh singularities (see Table 5.1 for locations of singularities for arrays with typical numbers of CMGs). All the array momentum states corresponding to all of the singular gimbal sets are referred to as the singular surface or the set of singular surfaces. Examination of these surfaces can be useful in understanding the nature of singularities for a given array architecture.

The singular surfaces for the four-CMG and six-CMG roof arrays are shown in Figs. 6.8 and 6.9. Blue and cyan indicates internal singular surfaces, which for roof arrays of six or more CMGs are globally passable by null motion at all singularity points within the angular momentum envelope. Recall from Sect. 5.10, that passability is a local property; despite that null motion may be unable to escape a singularity associated with a specific set of gimbal angles instantaneously, such solutions may still be reached in finite time. In orange and red, the outer surfaces represent the external or saturation singular surfaces that are never passable through null motion, regardless of how much gimbal-angle motion occurs.

In general, these $0h$, $2h$, ..., nh surfaces, when plotted together, form a continuous connection between all possible singular momentum states. It is important to recognize, however, that points on the internal surfaces are shown in terms of three-dimensional angular momentum, not n -dimensional gimbal angles. So, such a

Fig. 6.8 Four-CMG roof-array singular surfaces

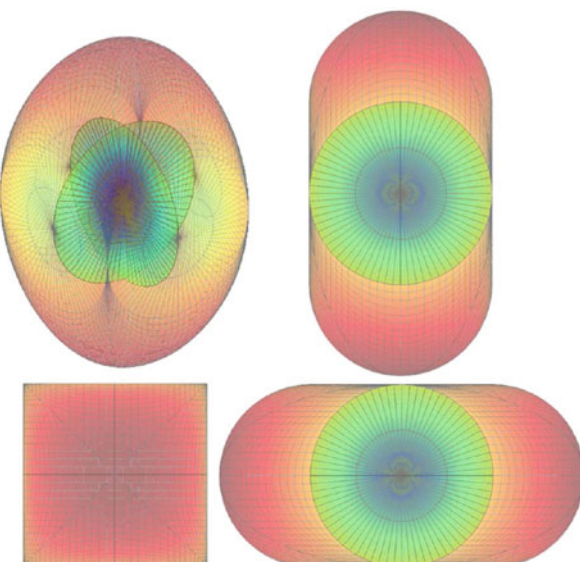


Fig. 6.9 Six-CMG roof-array singular surfaces

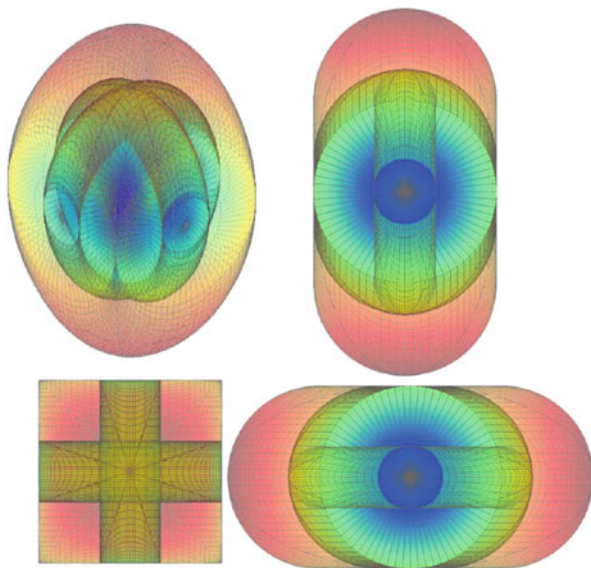
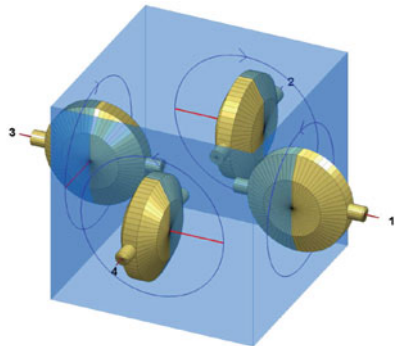


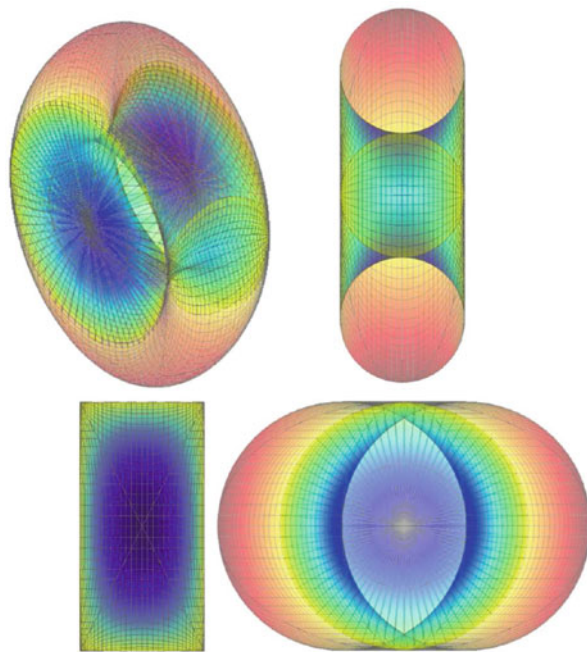
Fig. 6.10 Box-90 CMG array



point is not necessarily singular: it may be that some gimbal-angle sets are singular for that momentum, and some are not. Many of these points can be reached by combinations of gimbal angles that keep the array well conditioned. Choosing these combinations is the central challenge of steering algorithms that enable spacecraft to utilize an array effectively.

An example of the four-CMG roof array that has a 90° angle between the two sets of gimbal axes is also known as the box-90 array. The box-90 array is shown in Fig. 6.10.

Fig. 6.11 3/4-CMG box array singular surfaces



6.5.3 3/4 (3 of 4) Box Array

Whenever a single CMG fails in a box-90 array, the consequence is the 3/4 box array. Therefore, in the likely case that fault tolerance is required, the performance requirements must be met by a 3/4 box. Consequently, during typical operations, only three CMG out of four are active, with a dormant spare. The singular surfaces for the 3/4-CMG box array are shown in Fig. 6.11.

In Fig. 6.11, there are no singularities within a $1h$ sphere about zero angular momentum (Sands et al. [10]). The use of this $1h$ singularity-free sphere is one of the reasons this array is one of the first to have been used and has been the array of choice for many spacecraft. With three CMGs, there is no way of avoiding singularities through null motion because there is no null space (see Chap. 5). Therefore, any spacecraft-level performance requirements must be met within the singularity-free region of the momentum envelope.

6.5.4 Pyramid Arrays

Perhaps the most commonly discussed array architecture is the pyramid array. It frequently appears in the academic literature. It is also one of the most complex. The four-CMG pyramid array shown in Fig. 6.12 has independent gimbal axes, unlike

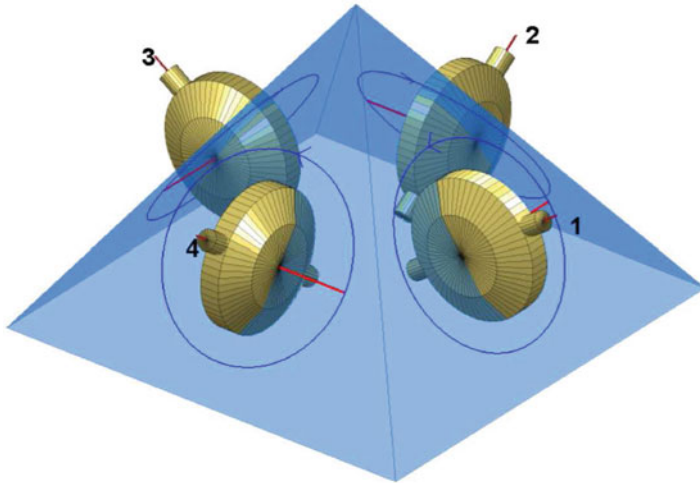


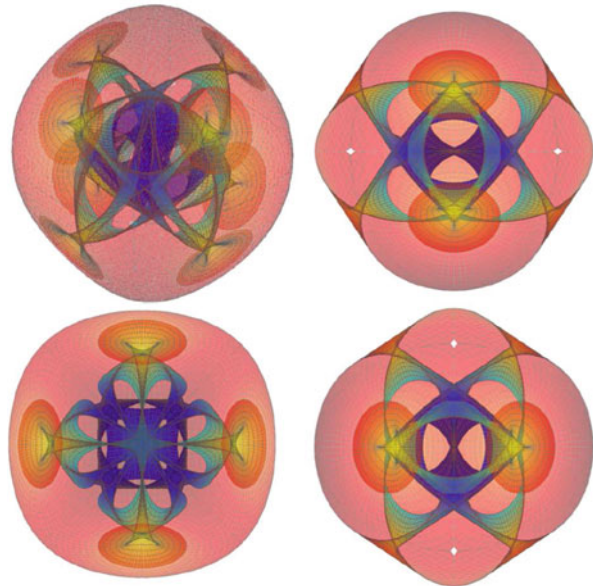
Fig. 6.12 Four-CMG pyramid array

collinear roof arrays. The figure shows that pyramid arrays of four or more CMGs never have a rank-1 singularity.

A four-CMG pyramid array at a skew angle, i.e., angle from horizontal to angular momentum plane of 54.74° produces a somewhat spherical three-axis symmetric angular momentum envelope. The envelope is indicated in orange and red, with internal singular surfaces in cyan and blue, in Fig. 6.13. The internal singular surfaces are smoothly connected to the angular momentum envelope. They contain trumpet-like funnels or tubes in which no angular momentum is available. These tube structures are smoothly connected to the angular momentum envelope through surfaces that resemble lily pads (orange). The circular outer edge of each lily pad is formed by sweeping the momentum vector of the CMG whose gimbal axis passes through it (Yoon and Tsiotras [11]). We recall that a SGCMG cannot access the points inside this circular locus.

This somewhat spherical momentum envelope provides roughly equal control authority in angular momentum and torque about any axis and provides a large volume of accessible momentum. Perhaps this uniformity in angular momentum and torque is the reason the four-CMG pyramid array initially became an object of academic study. The nature of academic publication encouraged many follow-on studies of this particular architecture. However, from a practical perspective, the angular jerk, acceleration, and velocity are of primary importance for many agile spacecraft, not this uniform distribution of momentum and torque. These agility metrics are calculated by inverting the spacecraft inertia onto the control authority (see Chap. 3). Therefore, equal momentum and torque about three axes does not correspond to equal agility about these axes. Moreover, many Earth-observing spacecraft, for example, those that perform push-broom imaging (sweeping the imager back and forth through small angles throughout the orbit). Such satellites

Fig. 6.13 Four-CMG pyramid array singular surfaces



require high torque and momentum about one or two axes, with less capability needed about the boresight axis of the imaging payload. An example of an application that takes advantage of agility in the third degree of freedom is described by Karpenko et al. [12] and Ross et al. [13]. They seek optimal slew trajectories that can exploit the reduced inertia axis to reduce overall slew time when compared with an eigenaxis slew.

The uniformity of the angular momentum envelope comes at a cost: the very complex internal singular surfaces shown in Fig. 6.13, which contain both passable non-degenerate hyperbolic singularities and impassable elliptic singularities. Recall from Chap. 5, in the case of impassable elliptic singularities, no null motion exists for singularity avoidance; therefore, passing through points of angular momentum near an elliptic singularity sacrifices accuracy in torque for attitude control. Also, unlike collinear arrays, the internal singular surfaces for a pyramid array are scattered throughout the angular momentum envelope. Therefore, the pyramid array has a smaller non-singular (or singular-but-passable) angular momentum envelope to offer the attitude control system.

6.5.5 Dynamic Arrays

Some have proposed making the gimbals of a CMG dynamic , in the sense that reorienting them can change the angular momentum envelope and corresponding singular surfaces during operations. Kojima [14] suggests frequent reconfiguration

as a singularity-avoidance approach. However, approaches that involve frequent reconfiguration during maneuvers ignore the influence of additional torque during reconfiguration. Essentially, such methods make the array of CMGs act as a semi-static DGCMG array and therefore come with a similar increase in volume, mass, power, and mechanical complexity as well as the loss in performance (see Chap. 3). This disadvantage can be overcome in the case where the CMG gimbals can be reconfigured with the CMG despun, and the new configuration locked into place with a mechanical constraint, as suggested by Bonn et al. [15], where it is a response to failures or infrequent changes in mission requirements.

6.6 Blended Arrays and Other Designs

The early days of CMG technology saw efforts to create heterogeneous arrays of momentum devices, or “blended arrays”. These arrays combine reaction wheels of various sizes, single- and double-gimbal CMGs, and some less-familiar devices. None have caught on, the most likely reason being that parts count, reliability, and related cost penalties motivate arrays of identical devices. Nevertheless, these early innovations deserve some recognition. And there still may come a day when one of them proves useful in a spacecraft architecture.

6.6.1 Double-Gimbal/Single-Gimbal Scissored Pairs

A pair of DGCMGs provides four independent control degrees of freedom, one for each gimbal axis. This number is sufficient for three-axis control of attitude, within the limits imposed by gimbal-lock singularities. In fact, it is more than enough (by one), but certain failures of one of the DGCMG’s components prevents the entire array from serving the needs of a three-axis attitude-control system. Adding a scissored pair as shown in Fig. 6.14 adds a degree of freedom—only one, because the gimbal-angle constraint subtracts one from what would otherwise be two independent SGCMGs. The result is an array that is single-fault tolerant, any single CMG failure leading to a momentum system capable of providing torque in three axes, again within the limits imposed by singularities. The steering law is straightforward, but this momentum system is considered to have high weight and volume for its performance (Rodden [7]). It is also suited primarily to a system with single-axis agility, since the scissored pair might apply torque along its axis that is hundreds of times as much as torque from one of the DGCMGs in the transverse axes.

Fig. 6.14 Two DGCMGs and one scissored pair of SGCMGs

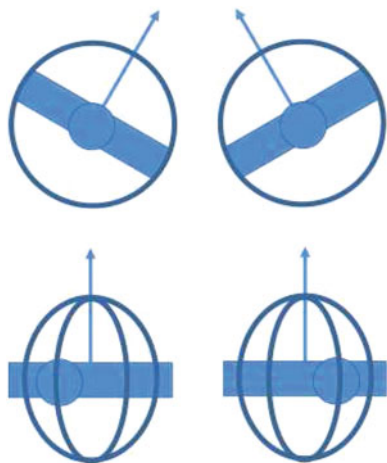
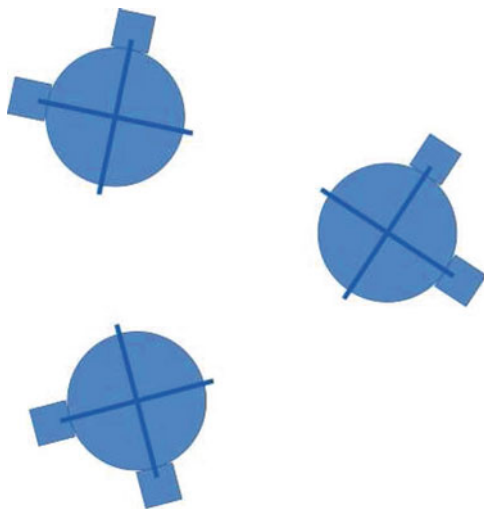


Fig. 6.15 Three DGCMGs uniformly distributed in a plane



6.6.2 Langley “Six-Pac”

A combination of three DGCMGs provides similar failure tolerance. This architecture has been referred to as the “Langley Six-Pac” see Rodden [7], in the specific case where the momentum vectors for zero gimbal angle lie in a plane and are separated by 120° , as shown in Fig. 6.15. A failure of any DGCMG results in an array with four remaining degrees of freedom, but the complex control law and high weight and volume has made it an unpopular choice.

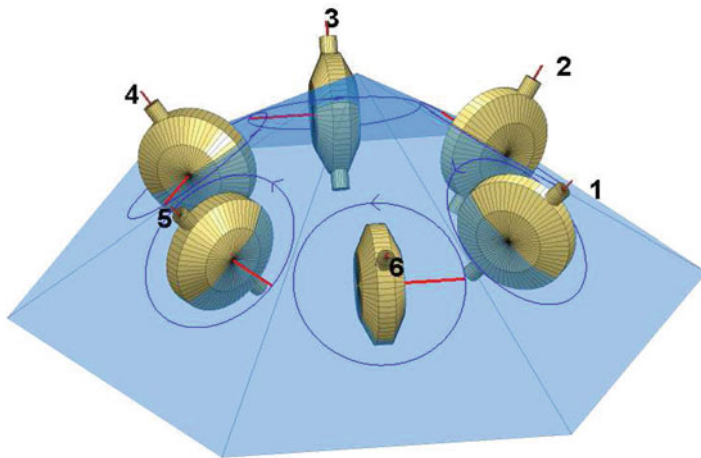
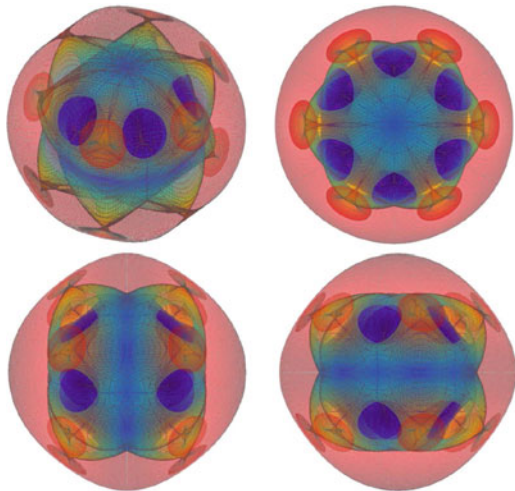


Fig. 6.16 Six GAMS pyramid array

Fig. 6.17 Six-CMG pyramid array singular surfaces



6.6.3 Single-Gimbal Six GAMS (Six-CMG Pyramid Array)

Six SGCMGs can be arranged so that each CMG momentum vector sweeps out a plane that forms one of the faces of a six-faceted pyramid. This so-called gimbaled-axis momentum system (GAMS) is known as the six-GAMS shown in Fig. 6.16, as described by Cornick [16] and Rodden [7]. Like any six-CMG array, this one offers active, multiple redundancy but represents lower weight and volume than DGCMG arrays for a given torque requirement.

The singular surfaces of the six-CMG pyramid array in Fig. 6.17 differ from the four-CMG pyramid array Fig. 6.13. The addition of two CMGs provides a

more nearly spherical momentum envelope, with a significantly larger momentum capacity at the expense of a more complex set of internal singular surfaces. These internal singular surfaces appear throughout the volume of the momentum envelope and also have more lily pads that connect internal structures to the edges of the envelope. Therefore, unlike the six-CMG roof array, the six-pyramid's increased momentum capacity and spherical symmetry alone does not eliminate geometric singularities. Nevertheless, Cornick describes this array as one in which an internal envelope can be exploited through an appropriate steering law.

6.6.4 Scissored Pair with High-Torque Reaction Wheels

A single scissored pair of variable-speed control-moment gyroscopes (VSCMGs) represents a three degree-of-freedom system with minimal hardware. Such an array may be suitable for applications in which single-axis agility is required, with limited control authority in the transverse directions. Such a design suggests severe volume constraints. In such circumstances, further simplifications may be motivated. For example, the gimbal angle might be limited to a finite range, eliminating the need for continuous rotation and thereby saving the mass and complexity of slip rings and related electronics.

Limiting the gimbal angle can be based on some straightforward sizing principles, as suggested in the following example. High-torque reaction wheels (such as Goodrich's TorqWheel) can provide about 2 Nm of torque about their spin axes. With 16.6 Nms of angular momentum and a 1 rad/s gimbal rate, this array can produce about 1/10 the torque in the transverse axes as it can along the spin axis, up to a gimbal angle of about 45°. The momentum and torque performance of this example are shown in the Fig. 6.18.

6.7 Variable-Speed CMG Arrays

The perennial search for new options for SGCMG singularity avoidance motivates the case of an array of VSCMGs. Basically, at the values of angular momentum where an array of SGCMGs would be singular, the VSCMG relies on rotor acceleration as a control DOF to provide the needed torque along the singular direction. As a consequence, an array of two or more VSCMGs with linearly independent

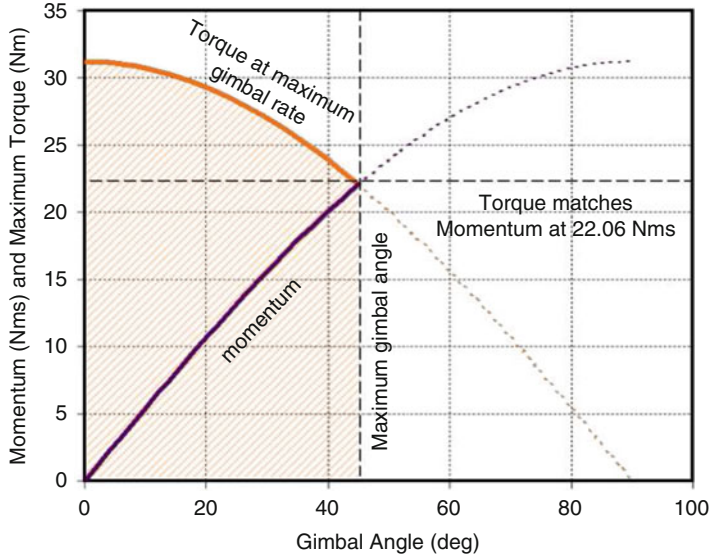


Fig. 6.18 Single-axis torque and momentum performance of a scissored pair with limited gimbal angles, for a factor of 10 greater momentum in one axis than in the axes transverse to it

gimbal axes sufficiently far from rotor-speed saturation is non-singular,¹ i.e., has the non-singular Jacobian shown in Eq. (6.1).

$$\dot{h} = [A(\Delta, \Omega) \ B(\Delta)] \begin{bmatrix} \dot{\Delta} \\ \dot{\Omega} \end{bmatrix} = D\dot{X} \quad (6.1)$$

As explained in Chap. 4, one of the major disadvantages of RWAs also impacts VSCMGs: their ratio of input power to torque is high. They require direct shaft power because their torque is proportional to the acceleration of the rotor. A few successful algorithms for minimizing rotor accelerations while avoiding CMG singularities can be found in Yoon [11] and Schaub [17]. Even neglecting the hardware and systems-engineering issues, the singularity-avoidance algorithms alone dramatically compromise the performance of a VSCMG array.

¹The avoidance of SGCMG singularities for an array of two or more VSCMGs with linearly independent gimbal axes assumes that the rotors do not reach their maximum speed or zero. With sufficiently many rotors at maximum speed, the array can no longer provide rotor accelerations to aid in SGCMG singularity avoidance. Similarly, when enough rotors have very little momentum, the gyroscopic torque vanishes, worsening the singularities.

The chief drawback of VSCMGs is that they sacrifice rotor speed to avoid singularities or for power management. Reducing rotor speed reduces torque amplification, and yet that amplification is the reason for using a CMG in the first place.

There are several other reasons why VSCMG arrays have not been used in attitude control on-board contemporary satellites. Some of these reasons arise from system-level concerns:

1. The spacecraft's jitter response varies with frequency. A constant rotor speed (as in a SGCMG) may permit the spacecraft to be designed to minimize structural amplification of the rotor-frequency disturbance. In contrast, variable rotor speeds make this approach infeasible.
2. Larger rotor motors are needed for rotor accelerations. This mass increases inner-gimbal inertia, thereby requiring a larger gimbal motor. The mass, volume, and power is therefore increased in such systems.
3. These systems demand more powerful motor electronics because the rotors require higher-bandwidth speed control than SGCMGs.
4. Singularity avoidance for arrays of SGCMGs is becoming well understood and proven on many systems, eliminating the motivation for more exotic solutions.
5. Higher bearing wear and shorter lifetime results from the heat introduced by higher rotor power.

These many reasons motivate contemporary spacecraft designs to maintain constant rotor speeds.

6.8 Energy Storage

An additional benefit of an array of VSCMGs is its ability to use the flywheels in RWA mode to provide not only CMG singularity avoidance, but also electrical power. Some of the earliest literature on using flywheels to store energy on spacecraft in the form of kinetic energy appeared as far back as the early '60s (Roes [18]). Batteries alone cannot generally provide large current to their connected loads; some form of capacitance usually complements batteries for this reason. Spacecraft that require very high, instantaneous power—perhaps satellites whose payloads involve directed energy—may realize mass savings by implementing flywheels whose kinetic energy can be converted to electrical energy (Babuska et al. [19]). Contemporary technology for flywheel energy storage is roughly competitive with satellite batteries, with power density around 100 W/kg. However, to achieve this energy storage and extraction efficiently, the flywheels typically require very high speeds, along with additional electrical circuitry for the conversion of kinetic energy into electrical energy. Magnetic bearings can reduce frictional losses and extend lifetime in the presence of these high speeds for such systems but also consume considerable power on their own in maintaining a stiff constraint. And they are unstable if power to the bearings is lost. Furthermore, high rotor speed comes with

Fig. 6.19 Honeywell
FACETS CMG



high mechanical stress in the flywheels. Therefore, an array of VSCMGs for energy storage and attitude control would have to trade the additional mass, electronics, and complexity for these modest power benefits. More traditional power subsystems are likely still the best choice.

NASA and the Air Force Research Laboratory (AFRL) have performed considerable research and development in the area of integrated power and attitude control (IPACS) (Notti et al. [20]). A popular program that looked at the use of flywheel energy storage and energy control is the Flywheel Attitude Control and Energy Transmission System (FACETS) formerly at AFRL in Kirtland AFB New Mexico (Fausz et al. [21]). In this program, three VSCMG were designed by Honeywell for AFRL (see Fig. 6.19) and were tested at AFRL on the ASTREX air-bearing satellite simulator by AFRL, Honeywell, and its contractors.

During this study, algorithms were developed to be validated on FACETS and published in the literature (Tsiotras et al. [22] and Yoon and Tsiotras [23]). NASA continued to study IPACS at their Glenn Research Center (McLallin et al. [24]). The programs were eventually cut, and there has been little applied research in this area since.

6.9 Optimization and Arbitrary Array Configurations

If the spacecraft's inertia and the statistics of its expected pointing time history are known a priori, then optimizing the CMG array geometry can take advantage of this knowledge. Such optimization seeks to increase the amount of non-singular angular momentum, the size or shape of the angular momentum, or some combination of the two. Examples of optimization for these mission-specific parameters may be found in Leve [25] and Sands [10].

A fairly intuitive example of a optimizing the shape of the angular momentum envelope is shown in Figs. 6.20 and 6.21. The objective of this optimization is to

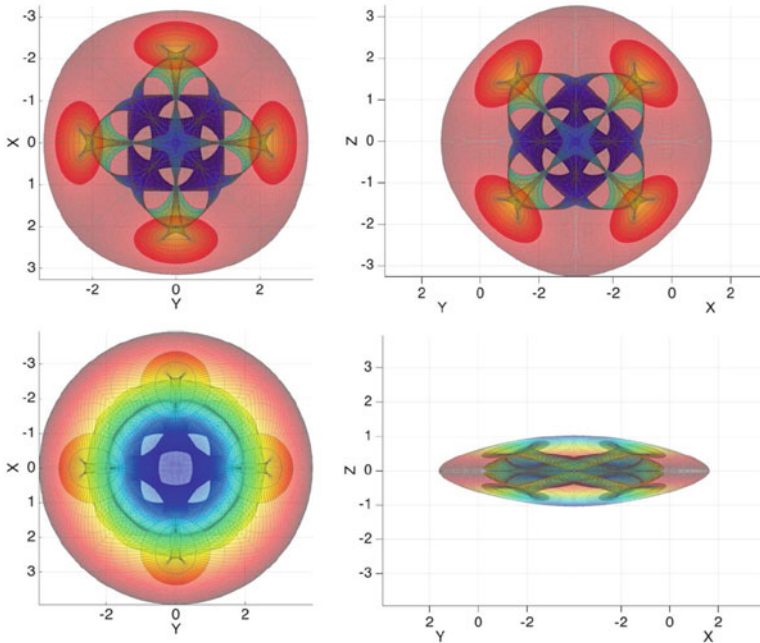


Fig. 6.20 Singular surfaces for a four-CMG pyramid array $\beta = 54.74^\circ$ (top) and $\beta = 30^\circ$ (bottom)

maximize the angular momentum about two of the three axes, i.e., to make the envelope more oblate. Reducing the CMG array skew angle β (See Chap. 4) has this effect, providing more angular momentum in the pitch/yaw plane. However, Fig. 6.20 shows that the internal singularities still appear throughout the angular momentum envelope and are both elliptic and hyperbolic for the four-CMG pyramid array. In contrast, the internal singularities for the six-CMG roof array in Fig. 6.21 are merely hyperbolic, offering the possibility of a non-singular solution for angular momentum value within the envelope.

As Figs. 6.20 and 6.21 show, the internal singular surfaces for both arrays differ, and those for the four-CMG pyramid array are spread throughout the entire momentum envelope including passable and impassable singularities. Therefore, even when the spacecraft inertia and its jerk, acceleration, and rate requirements are not considered in the optimization process, the location of internal singularities and their type is of higher importance than the volume of useable angular momentum. This example makes it clear that the shape and size of the angular momentum envelope is not the only driver of CMG array architecture. The architecture must also offer a workable singularity structure.

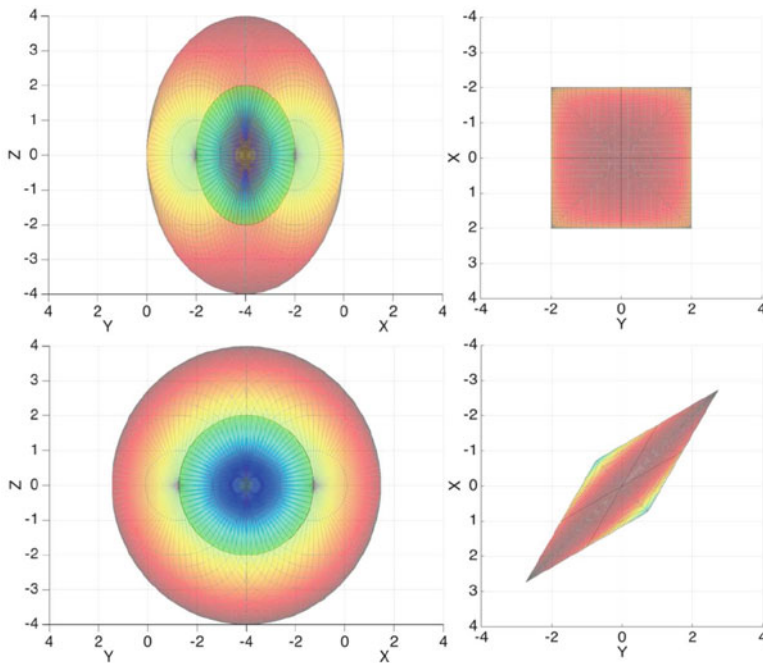


Fig. 6.21 Singular surfaces for a four-CMG roof array $\beta = 45^\circ$ (top) and $\beta = 15^\circ$ (bottom)

6.10 Chapter Summary

This chapter discussed how the performance of RWA and CMG arrays depend on the momentum devices' orientation within the spacecraft. Performance envelopes were generated for RWA and CMG arrays in terms of maximum angular momentum surfaces and, for the case of CMG arrays, internal singular surfaces. The geometry and the physical significance of these surfaces was discussed. Some common arrays used in practice were also introduced. It was shown that although it may seem beneficial to optimize an array of CMG for the shape of the angular momentum envelope, the more important requirements are vehicle rate and acceleration, which are driven by vehicle inertia. The types of internal singularities limit the array momentum that can be used to meet these agility requirements.

References

1. F. Markley, R. Reynolds, F. Liu, K. Lebsack, Maximum torque and momentum envelopes for reaction wheel arrays. *AIAA J. Guid. Control. Dyn.* **33**(5), 1606 (2010)
2. W. Chubb, H. Kennel, C. Rupp, S. Seltzer, Flight performance of skylab attitude and pointing control system. *AIAA J. Spacecr. Rocket.* **12**(4), 220 (1975)

3. M. Carpenter, M. Peck, Reducing base reactions with gyroscopic actuation of space-robotic systems. *IEEE Trans. Robot.* **25**(6), 1262 (2009)
4. D. Cunningham, G. Driskill, A torque balance control moment gyroscope assembly for astronaut maneuvering, in *NASA Ames Research Center 6th Aerospace Mechanics Symposium (SEE N72-26377 17-15)*, 1972, pp. 121–126
5. C-1 - Lit Motors, Lit Motors C1 (2013), <http://litmotors.com/c1/>. Accessed 13 Sept 2015
6. H. Kurokawa, A geometric study of single gimbal control moment gyros (singularity problems and steering law). Technical Report 175, Agency of Industrial Technology and Science, Japan, 1998
7. J. Rodden, Attitude control system lectures. Lecture Notes (1980)
8. E. Tokar, V. Platonov, Singular surfaces in unsupported gyrodyne systems. *Cosm. Res.* **16**, 547 (1979)
9. H. Kurokawa, Survey of theory and steering laws of single-gimbal control moment gyros. *AIAA J. Guid. Control. Dyn.* **30**(5), 1331 (2007)
10. T. Sands, J. Kim, B. Agrawal, 2h singularity-free momentum generation with non-redundant single gimballed control moment gyroscopes, in *45th IEEE Conference on Decision and Control*, 2006, pp. 1551–1556
11. H. Yoon, P. Tsotras, Singularity analysis of variable-speed control moment gyros. *AIAA J. Guid. Control. Dyn.* **27**(3), 374 (2004)
12. M. Karpenko, S. Bhatt, N. Bedrossian, I. Ross, Flight implementation of shortest-time maneuvers for imaging satellites. *AIAA J. Guid. Control. Dyn.* **37**(4), 1069 (2014)
13. I. Ross, M. Karpenko, A review of pseudospectral optimal control: from theory to flight. *Annu. Rev. Control.* **36**(2), 182 (2012)
14. H. Kojima, Singularity analysis and steering control laws for adaptive-skew pyramid-type control moment gyros. Elsevier *Acta Astronaut.* **85**, 120 (2013)
15. J.J. Bonn, M.A. Peck. Dynamic cmg array and method. US Patent 7,561,947, 2009
16. D. Cornick, Singularity avoidance control laws for single gimbal control moment gyros, in *AIAA Guidance, Navigation and Control Conference*, 1979
17. H. Schaub, J. Junkins, CMG singularity avoidance using VSCMG null motion (variable speed control moment gyroscope), in *AIAA/AAS Astrodynamics Specialist Conference and Exhibit*, Boston, MA, 1998, pp. 213–220
18. J. Roes, Electro-mechanical energy storage system for space application. *Prog. Astronaut. Aeronaut.* **3** (1961)
19. V. Babuska, S. Beatty, B. deBlonk, J. Fausz, A review of technology developments in flywheel attitude control and energy transmission systems, in *Proceedings of the IEEE Aerospace Conference*, vol. 4, 2004
20. J. Notti, A. Cormack, W. Klein, Integrated power/attitude control system (ipacs). *AIAA J. Spacecr. Rocket.* **12**(5), 485 (1975)
21. J. Fausz, D. Richie, Flywheel simultaneous attitude control and energy storage using a vscmg configuration, in *Proceedings of the 2000 IEEE International Conference on Control Applications*, 2000, pp. 991–995
22. P. Tsotras, H. Shen, C. Hall, Satellite attitude control and power tracking with energy/momentum wheels. *AIAA J. Guid. Control. Dyn.* **24**(1), 23 (2001)
23. H. Yoon, P. Tsotras, Singularity analysis and avoidance of variable-speed control moment gyros—part ii: power constraint case, in *AIAA Guidance, Navigation, and Control Conference*, Providence, RI, 2004
24. K.L. McLallin, R.H. Jansen, J. Fausz, R.D. Bauer, Aerospace flywheel technology development for ipacs applications. Technical Report TM-2001-211093, NASA, 2001
25. G. Leve, F. Boyarko, N. Fitz-Coy, Optimization in choosing gimbal axis orientations of optimization in choosing gimbal axis orientations of a cmg attitude control system, in *AIAA Infotech@Aerospace Conference*, Seattle, WA, 6–10 April 2009

Chapter 7

Steering Algorithms

This chapter discusses the methods of CMG torque allocation—techniques for finding CMG gimbal rates to provide a commanded torque. The literature often refers to these allocation techniques as steering algorithms or steering laws, of which pseudoinverse solutions are the most commonly discussed. The chapter surveys many of the classes of steering algorithms, starting with pseudoinverse methods, continuing with the more conservative methods based on limited gimbal angles and angular momentum, and ending with the less conventional and state-of-the-art optimal methods.

7.1 CMG Steering Algorithms

CMG steering algorithms allocate inputs to the actuators (gimbal speed and/or rotor acceleration) to provide a commanded torque on the spacecraft. Thruster allocation and magnetic torquer allocation are examples of similar problems on spacecraft, in which the actuators create an external torque on the spacecraft (force and torque in the case of thrusters). In contrast, steering algorithms for momentum devices work with limited angular momentum and abide by the constraint of conservation of angular momentum. RWA steering is rarely more sophisticated than a simple pseudoinverse of a constant matrix, the Jacobian discussed in Chap. 4. CMG steering is vastly more involved because the Jacobian changes in ways that depend on the past usage of the CMGs. It is one of the most challenging aspects of momentum systems and consequently the topic of primary interest in the literature.

A CMG steering algorithm serves as an interface between the attitude compensation and the individual actuators. The attitude-control system calculates a torque needed to accelerate the spacecraft toward a commanded attitude and angular velocity. The steering algorithm transforms this torque into individual CMG gimbal-rate commands. These commands are sent to the gimbals, which track the

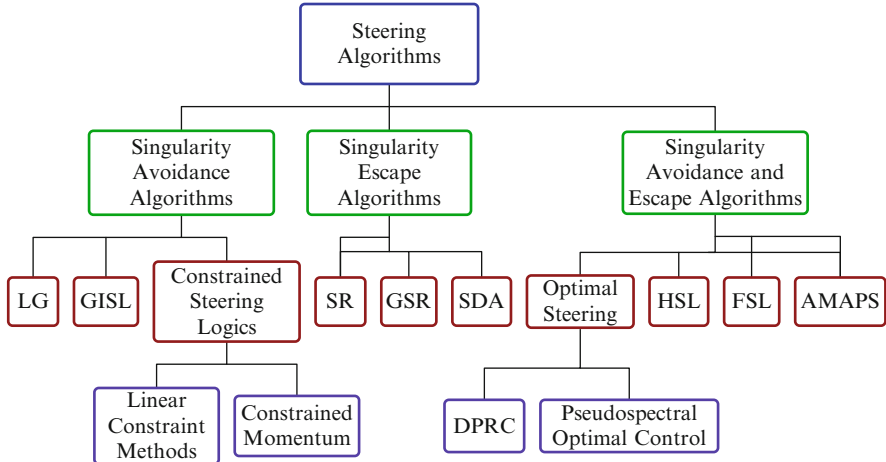


Fig. 7.1 Steering algorithms for SGCMGs

rate commands through closed-loop control as discussed in Chap. 8. However, it is very rarely the case that the command sent to the gimbals produces exactly the commanded gimbal rate or acceleration. Some reasons include uncertainty in gimbal-bearing friction and losses in the gear train, as well as the inherent limits of motors, which cannot respond with arbitrarily high or fast speed changes. Therefore, inner-loop control may be accompanied by feedforward: a known, time-dependent open-loop input. The gimbal's rate loop then rejects any remaining (unknown) disturbances. Such a control system can settle faster (be higher in bandwidth) without risking saturation due to overshoot. This architecture is common in CMG-driven spacecraft.

CMG steering algorithms may be considered successful when they accurately map spacecraft-level torque into actuator behaviors while avoiding singularities and thus high gimbal rates and accelerations. Successful algorithms comprise three categories, as shown in Fig. 7.1: singularity escape algorithms, singularity avoidance algorithms, and singularity avoidance and escape algorithms. Other approaches also appear in the literature, but this chapter is limited to these three types.

Singularity avoidance and inner-loop control are separate phenomena, but both impact feedback-control performance of a spacecraft with momentum control devices. For arrays of both RWAs and CMGs, saturation can occur on the array level as limits on array angular momentum (see Chap. 5) or at the actuator level as limits on the rotor and gimbal rates and accelerations. Chapter 8 discusses these issues in detail.

For the likely case in which rotor angular momentum is identical for all CMGs in an array, the location and form of singularities depends solely on the CMGs' alignments relative to one another. As discussed in Chap. 6, the behavior of momentum systems is independent of the devices' location within the spacecraft.

Steering laws enable the array to impart a commanded output torque, \dot{h} by “inversion” of the Jacobian A to compute $\dot{\Delta}$:

$$\dot{h} = A\dot{\Delta} \quad (7.1)$$

Decomposition of A into its range and null spaces is central to an understanding of steering algorithms. The gimbal-rate solutions can be decomposed as

$$\dot{\Delta} = \dot{\Delta}_f + \dot{\Delta}_n \quad (7.2)$$

where $\dot{\Delta}_f$ is a column of gimbal rates in the range space of A , so that $\dot{h} = A\dot{\Delta}_f$. With four or more CMGs, an array can exhibit the so-called null motions. This motion consists of non-zero gimbal-rate combinations that neither produce torque on the spacecraft nor (equivalently) change the array’s angular momentum. These combinations correspond to $\dot{\Delta} = \dot{\Delta}_n$. The quantity $\dot{\Delta}_n$ lies entirely in the nullspace of A , so that $A\dot{\Delta}_n = 0$.

With this nomenclature in place, we can state three objectives for the majority of steering algorithms in terms of forced and null motion: (1) impart a commanded torque, (2) escape singularity through the addition of torque error τ_e and/or avoid singularity through null motion $\dot{\Delta}_n$, and/or (3) follow a commanded gimbal-rate trajectory $\dot{\Delta}_d$ while simultaneously achieving (1) and/or (2). A cost function that is often used to assess a steering law’s success in meeting these objectives is

$$J = \frac{1}{2}\tau_e^T R \tau_e + \frac{1}{2}\dot{\Delta}_e^T Q \dot{\Delta}_e \quad (7.3)$$

where Q and R are positive definite, symmetric matrices,

$$\tau_e = \dot{h} - A\dot{\Delta} \quad (7.4)$$

and

$$\dot{\Delta}_e = \dot{\Delta}_d - \dot{\Delta} \quad (7.5)$$

Most published steering algorithms are known as pseudoinverse methods. They are found from taking the first variation of Eq. (7.3) and setting it equal to zero, at which point the solution for gimbal rates is a minimum-norm column matrix of values (i.e., when the matrices $R > 0_{3 \times 3}$ and $Q \geq 0_{n \times n}$). Most steering algorithms do not consider constraints on the gimbal rates and accelerations. These constraints are typically considered in the inner-loop controllers after the fact, where input power and accuracy may be sacrificed at the boundaries of the constraint, or they are accommodated in the trajectory-planning step, where the only permissible maneuvers are those that never cause the momentum devices to reach these limits.

7.2 Origin of Pseudoinverse Methods

Pseudoinverse methods are generally analytic solutions for a set of gimbal rates or accelerations that produce a commanded torque. They are all based on pseudoinverses of a nonsquare matrix, giving them their name.

7.2.1 Blended Inverse

Taking the first variation of Eq. (7.3) and setting it equal to zero leads to

$$\begin{aligned}\dot{\Delta} &= (Q + A^T R A)^{-1} (A^T R \dot{h} + Q \dot{\Delta}_d) \\ &= (Q + A^T R A)^{-1} A^T R \dot{h} + (Q + A^T R A)^{-1} Q \dot{\Delta}_d\end{aligned}\quad (7.6)$$

which has been given the name Blended Inverse (Tekinalp and Yavuzoglu [1]). Equation (7.6) is a steering law that achieves singularity escape through the addition of torque error, singularity avoidance through the addition of null motion, and tracking of commanded gimbal rates. While mathematically convenient, the torque error and indeterminacy near singularity may make such an approach unappealing in practice. However, typically A has at most full row rank. The most common case is $n \geq 3$ for CMGs to control three axes of torque, where the column size is n and the row size is 3. Only in the case of three CMGs could the resulting Jacobian (a 3×3 matrix) have both full row rank and full column rank. Therefore, from here on out, that where it is best suited, we will choose $Q \in \mathbb{R}^{3 \times 3}$ over $Q \in \mathbb{R}^{n \times n}$ and $R \in \mathbb{R}^{n \times n}$ over $R \in \mathbb{R}^{3 \times 3}$ separately for both parts of the RHS of Eq. (7.6). Therefore, in an effort to use the minimum-norm solution, i.e., use $A^T R^T (Q + A R^T A^T)^{-1} \dot{h}$ rather than $(Q + A^T R A)^{-1} A^T R \dot{h}$, the inverted quantities of the first term on the RHS of Eq. (7.6) will always be 3×3 .

7.2.2 Moore–Penrose Inverse

The simplest and possibly the most prevalent pseudoinverse in the literature is known as the Moore–Penrose inverse and it is found through the first variation of Eq. (7.6) with parameters ($Q = 0_{3 \times 3}$, $R = I_{n \times n}$, and $\dot{\Delta}_d = 0$):

$$\dot{\Delta} = A^T (A A^T)^{-1} \dot{h} \quad (7.7)$$

The Moore–Penrose pseudoinverse in Eq. (7.7) has but one objective, which is obvious from the choice of ($Q = 0_{3 \times 3}$, $R = I_{n \times n}$, and $\dot{\Delta}_d = 0$). This objective is to follow the torque command, sometimes known as perfect “torque tracking.” Another consequence of the Moore–Penrose solution is that the norm of $\dot{\Delta}$ is minimized

if a solution exists. But its simplicity also comes with limitations: the Moore-Penrose pseudoinverse is incapable of avoiding or escaping singularities and does not accommodate constraints on gimbal angles, rates, or accelerations.

7.3 Singularity-Escape Algorithms (Torque-Error Algorithms)

Singularity-escape algorithms have the goal of passing through singularities and recovering with minimal (but not necessarily zero) deviation from the commanded torque. The addition of a scalar or matrix whose only purpose is to maintain numerical conditioning of a matrix inverse gives these methods the name “dirty inverses;” they are inexact mappings from commanded torque to gimbal rates. This approach to numerical conditioning constitutes the “dirt” that can cause inaccuracy in the calculation near singularity.

7.3.1 Singularity Robust Inverse

One of the earliest singularity-escape methods is the singularity-Robust (SR) inverse (Bedrossian et al. [2]). This pseudoinverse is found through substitution of the parameters ($Q = \alpha I_{3 \times 3}$, $R = I_{n \times n}$, and $\dot{\Delta}_d = 0$) in Eq. (7.6) as

$$\dot{\Delta} = A^T (A A^T + \alpha I_{3 \times 3})^{-1} \dot{h} \quad (7.8)$$

with a possible choice of a singularity parameter

$$\alpha = \alpha_0 e^{-\mu m} \quad (7.9)$$

where α_0 and μ are positive constants. The term $m = \sqrt{\det(A A^T)}$ is known as the singularity measure or manipulability in the field of robotics (Yoshikawa [3]). The singularity measure is the product of the singular values of the Jacobian. Therefore, it provides a measure of the distance of the CMG array from singularity.

The SR-inverse is effective in escaping most singularities, and the escape time can be traded against the torque error through the choice of tuning parameters, α_0 and μ . Specifically, a system that can accept high torque error can escape the singularities quickly. Nevertheless, this escape time is not deterministic and must be bounded through Monte Carlo analysis. This non-determinism may be unacceptable for spacecraft architectures where delay in following a specified trajectory adversely impacts data collection.

The objective of the singularity parameter is to regularize the singular values of the matrix $A A^T$ at singularity so that the matrix to be inverted remains positive

definite, rather than losing rank. The solution, of course, is not exact when $\alpha \neq 0$. It therefore achieves a torque that deviates from the command when the array is nearly singular. In fact, the singularity parameter α adds torque error in all directions, which is clear from an SVD of Eq. (7.8):

$$\dot{\Delta} = A^T(AA^T + \alpha I_{3 \times 3})^{-1}\dot{h} = V \begin{bmatrix} \frac{\sigma_1}{\sigma_1^2 + \alpha} & 0 & 0 \\ 0 & \frac{\sigma_2}{\sigma_2^2 + \alpha} & 0 \\ 0 & 0 & \frac{\sigma_3}{\sigma_3^2 + \alpha} \\ 0 & 0 & 0 \end{bmatrix} U^T \dot{h} = A^{\text{SR}} \dot{h} \quad (7.10)$$

The torque error resulting from singularity escape for many pseudoinverse methods is $\tau_e = \dot{h} - A\dot{\Delta}$. For the SR-inverse this error is

$$\tau_e = \dot{h} - A\dot{\Delta} = \dot{h} - AA^T(AA^T + \alpha I_{3 \times 3})^{-1}\dot{h} = U \begin{bmatrix} \frac{\alpha}{\sigma_1^2 + \alpha} & 0 & 0 \\ 0 & \frac{\alpha}{\sigma_2^2 + \alpha} & 0 \\ 0 & 0 & \frac{\alpha}{\sigma_3^2 + \alpha} \\ 0 & 0 & 0 \end{bmatrix} U^T \dot{h} = \epsilon \dot{h} \quad (7.11)$$

where ϵ is a torque error amplification parameter that approaches zero as the singularity parameter α goes to zero.

Equation (7.11) clearly shows that the torque error is scaled not only by the size of the singularity parameter but also by the size of the torque command. Therefore, the attitude-control subsystem cannot assume a fixed amount of torque error at every singularity.

7.3.2 Singularity Direction Avoidance Pseudoinverse

To reduce the torque error introduced for singularity escape, the singularity direction avoidance (SDA) pseudoinverse localizes torque error to the singular direction only (Ford and Hall [21]). The SDA pseudoinverse does so by regularizing only the smallest singular value. The parameters defining SDA from Eq. (7.6) are ($Q = X$, $R = I_{n \times n}$, and $\dot{\Delta}_d = 0$), giving the expression

$$\dot{\Delta} = A^T(AA^T + X)^{-1}\dot{h} \quad (7.12)$$

where $X = U \text{diag}(0, 0, \alpha) U^T$ and α is the same singularity parameter from Eq. (7.9). Substitution of X into Eq. (7.12), taking the SVD, and sorting the singular values leads to

$$\dot{\Delta} = A^T(AA^T + X)^{-1}\dot{h} = V \begin{bmatrix} \frac{1}{\sigma_1} & 0 & 0 \\ 0 & \frac{1}{\sigma_2} & 0 \\ 0 & 0 & \frac{\sigma_3}{\sigma_3^2 + \alpha} \\ 0 & 0 & 0 \end{bmatrix} U^T \dot{h} = A^{\text{SDA}} \dot{h} \quad (7.13)$$

with torque error

$$\tau_e = U \begin{bmatrix} 0 & 0 & 0 \\ 0 & 0 & 0 \\ 0 & 0 & \frac{\alpha}{\sigma_3^2 + \alpha} \\ 0 & 0 & 0 \end{bmatrix} U^T \dot{h} = \epsilon \dot{h} \quad (7.14)$$

Compared to Eqs. (7.11), (7.14) clearly reduces torque error in an overall sense. Numerically stable and computationally efficient methods exist to compute the SVD. Therefore, real-time implementation of the SDA pseudoinverse in deterministic flight code is feasible. Also, a by-product of the SVD is that there is no need to invert AA^T : the inverse can be reconstructed from the product of the unitary matrices U and V and the singular values once the SVD has been performed as shown in Eq. (7.13).

Like the Moore–Penrose inverse and the SR inverse, the SDA pseudoinverse is susceptible to gimbal lock (see Chap. 5). This weakness becomes clear when one takes the SVD of MP, SR, and SDA pseudoinverses. At singularity, all of these pseudoinverse solutions for gimbal rates take the form

$$\dot{\Delta} = V \begin{bmatrix} \bullet & 0 & 0 \\ 0 & \bullet & 0 \\ 0 & 0 & 0 \\ 0 & 0 & 0 \end{bmatrix} U^T \dot{h} \quad (7.15)$$

where \bullet indicates a nonzero number. Now if the array is singular, $\dot{h} \parallel u = u_3$, the third column of the unitary matrix U for a rank 2 singularity. At singularity, Eq. (7.15) gives a zero result for the MP, SR, and SDA pseudoinverse methods, even when $\dot{h} \neq 0$ (see Chap. 5). As discussed in Chap. 6, for parallel-type (roof) arrangements, there is a possibility of a rank-1 singularity where there is a plane of singular directions and u is in that plane.

7.3.3 Generalized Singularity Robust Inverse

In an effort to mitigate the risk of gimbal lock in a pseudoinverse-based steering algorithm, the generalized singularity robust (GSR) inverse has been proposed (Wie et al. [4]). The parameters for Eq. (7.6) that define the GSR inverse are ($Q = E$, $R = I_{n \times n}$, and $\dot{\Delta}_d = 0$). They yield

$$\dot{\Delta} = A^T(AA^T + \alpha E)^{-1}\dot{h} = A^{\text{GSR}}\dot{h} \quad (7.16)$$

where α can be chosen as in Eq. (7.9), and

$$E = \begin{bmatrix} 1 & \epsilon_0 \sin(\omega_3 t + \phi_3) & \epsilon_0 \sin(\omega_2 t + \phi_2) \\ \epsilon_0 \sin(\omega_3 t + \phi_3) & 1 & \epsilon_0 \sin(\omega_1 t + \phi_1) \\ \epsilon_0 \sin(\omega_2 t + \phi_2) & \epsilon_0 \sin(\omega_1 t + \phi_1) & 1 \end{bmatrix} > 0 \quad (7.17)$$

where ϵ_0 is a positive amplitude, and ω_i and ϕ_i are the frequencies and phase shifts of the dither used to nudge or wiggle the array out of the local minimum of gimbal lock. Because this pseudoinverse is an explicit function of time, dithering may be successful in driving the array out of a singularity at gimbal lock. However, there is no guaranteed upper bound on the time required for escape. The time is impacted by uncertainty in the Jacobian due to unavoidable measurement noise, delay, and/or quantization in gimbal angles. Also, the effect of gimbal lock escape is embedded in the pseudoinverse non-linearly. Therefore, although this technique may be assessed with statistical modeling of slews and found to be successful in a large fraction of cases, using GSR or any torque error/singularity escape methods for CMG array steering is likely impractical when guaranteed accuracy in tracking a specific torque trajectory is of primary importance.

If some torque error is acceptable, a more deterministic way to escape gimbal lock is to perturb the commanded torque along directions orthogonal to the singular direction. Consider the commanded torque as a projection along the basis created by the unitary matrix U from the SVD of A as

$$\dot{h} = \beta_1 u_1 + \beta_2 u_2 + \beta_3 u_3 \quad (7.18)$$

where

$$\beta_i = \dot{h}^T u_i \quad (7.19)$$

In a gimbal-lock singularity, $\dot{h} = u_3$, and the majority of pseudoinverse solutions provide an improper result as shown in Eq. (7.15). Therefore such a method perturbs the commanded torque in Eq. (7.18) as

$$\dot{h} = \beta_1^* u_1 + \beta_2^* u_2 + \beta_3 u_3 \quad (7.20)$$

where the parameters β_1^* and β_2^* are nonzero away from singularities. The appropriate choice of these parameters ensures that gimbal-lock is impossible analytically, because at singularity, the commanded torque always has components orthogonal to the singular direction (Leve [5] and Leve et al. [6]). Away from singularity, the singularity parameters in Eq. (7.20) approach their true values β_1 and β_2 . However,

the method in Eq. (7.20) is still a torque-error method and does not track accurately the commanded torque trajectory near a singularity.

7.4 Singularity Avoidance Algorithms

Some singularities, i.e., non-degenerate hyperbolic singularities, offer the possibility of avoidance without the use of torque error (see Chap. 5). Such methods can be posed as pseudoinverse solutions with the addition of null motion used solely for singularity avoidance. These solutions are considered exact solutions and are precise, i.e., zero torque error except at saturation singularities. Developing this steering-law software goes hand-in-hand with defining the array architecture so that only hyperbolic singularities are encountered. Some of the most popular singularity-avoidance methods in literature are the local-gradient methods, as discussed in this section.

7.4.1 Generalized Inverse Steering Law

The generalized inverse steering law (GISL) is found through substitution in Eq. (7.6) of the parameters ($Q = B^T A$, $R = I_{3 \times 3}$, and $\dot{\Delta}_d = Q^{-1} B^T \dot{h}$) and made to be the minimum-norm solution as

$$\dot{\Delta} = [(A + B)^T A]^{-1} (A + B)^T \dot{h} \implies (A + B)^T [A(A + B)^T]^{-1} \dot{h} = A^{\text{GISL}} \dot{h} \quad (7.21)$$

where B is a $3 \times n$ matrix of torque directions (sine and cosine functions of gimbal angle), the i th column of which is orthogonal to the corresponding column of A , i.e., $B_i^T A_i = 0 \forall i = 1, \dots, n$ and not $B_i^T A_j = 0 j \neq i$ and $\forall i, j = 1, \dots, n$. Pre-multiplying both sides of Eq. (7.21) by A yields

$$A \dot{\Delta} = \dot{h} \quad (7.22)$$

Therefore, the GISL provides an exact solution for gimbal rates to deliver the commanded torque. The matrix B is responsible for this exactness because it adds null motion within the pseudoinverse. However, even for a GISL there is no possibility of escape from elliptic singularities because null motion does not exist for those cases. Therefore, GISL is classified as a singularity-avoidance algorithm as shown in Fig. 7.1.

7.4.2 Local Gradient (LG) Methods

Equation (7.6) provides the general form of pseudoinverse steering algorithms. Decomposing it with the Matrix Inversion Lemma (see [7]) separates range-space from null-space terms:

$$\dot{\Delta} = (Q + A^T R A)^{-1} A^T R \dot{h} + (Q + A^T R A)^{-1} Q \dot{\Delta}_d \quad (7.23)$$

Applying the Matrix Inversion Lemma yields

$$(Q + A^T R A)^{-1} = [Q^{-1} - Q^{-1} A^T (R^{-1} + A Q^{-1} A^T)^{-1} A Q^{-1}]$$

Now if the commanded gimbal rate, $\dot{\Delta}_d$ is within the null space, so as to provide singularity avoidance, the gimbal rates are $\dot{\Delta}_d = \beta [I_{n \times n} - A^+ A] d$, where β is a singularity parameter of the same form as Eq. (7.8), and $[I_{n \times n} - A^+ A]$ is a matrix that projects any vector d onto the null space of A . Substituting into Eq. (7.23) the quantity $\dot{\Delta}_d = \beta [I_{n \times n} - A^+ A] d$ and the second part of Eq. (7.23) provides

$$\dot{\Delta} = (Q + A^T R A)^{-1} A^T R \dot{h} + \beta [I_{n \times n} - A^+ A] d \quad (7.24)$$

Note that the second term on the RHS of Eq. (7.24) is invariant to choice of Q and R with the constraint that $\dot{\Delta}_d$ lies in the nullspace of A . The local gradient is derived from substituting the parameters ($Q = 0_{3 \times 3}$, $R = I_{n \times n}$, and $\dot{\Delta}_d = \beta [I_{n \times n} - A^+ A] d$) into Eq. (7.23):

$$\dot{\Delta} = A^T (A A^T)^{-1} \dot{h} + \beta [I_{n \times n} - A^+ A] d \quad (7.25)$$

The gradient-search direction d in Eq. (7.26) can be chosen to minimize a function that maximizes the array's distance from singularity. A convenient function to use in this optimization is $f = -m^2$, where

$$d = \frac{\partial f}{\partial \Delta} \quad (7.26)$$

The gradient-search direction in Eq. (7.25) has been shown to be effective in avoiding non-degenerate hyperbolic singularities for SGCMGs and singularities for DGCMGs in the literature (Kurokawa [8]). The LG method in Eq. (7.25) is an exact solution that can avoid non-degenerate hyperbolic singularities but is ineffective in avoiding elliptic singularities.

7.4.3 Constrained Gimbal Angle or Angular Momentum Methods

A particular class of single-gimbal CMG steering laws uses linear constraints (whether in hardware or software) to avoid singularities while instantaneously solving for gimbal rates without future knowledge and without intentionally inducing torque error. Several variations of this steering law exist in the literature (Kurokawa [8] and Havill and Ratcliff [9]). Here, we offer a generalized form of such a steering law that frees the algorithm development from specific array geometries (Jones et al. [10]). The following generalized mathematical description of steering laws with linear constraints uses two examples to explain the formulation: the familiar architecture of three scissored pairs and six CMGs arranged in two triplets.

The justification for this approach is articulated in Kurokawa's steering law survey [8]. He and others agree on the capabilities of an ideal steering law, which should be

1. Capable of handling singularities
2. Exact (error-free)
3. Instantaneous (requiring no future knowledge)
4. Technologically feasible in terms of computational power and hardware implementation
5. General with regard to maneuvers and CMG array

Null motion and constraint-based methods are the only categories that clearly meet the first three criteria. Equation (7.1) shows the general form of the equation for the torque in terms of an array of gimbal rates $\dot{\Delta}$ and a Jacobian A ,

CMG steering laws often solve Eq. (7.1) using a version of the Moore–Penrose pseudoinverse solution:

$$\dot{\Delta} = A^T(AA^T)^{-1}\dot{h} \quad (7.27)$$

Linearly constrained steering laws are no exception; however, in addition to describing the dynamics of the problem via the Jacobian, these steering laws also include linear constraint equations:

$$D = C\dot{\Delta} \quad (7.28)$$

Equation (7.27) can be augmented with Eq. (7.28) to include the constraints:

$$\begin{bmatrix} \dot{h} \\ D \end{bmatrix} = \begin{bmatrix} A \\ C \end{bmatrix} \dot{\Delta} = \bar{A} \dot{\Delta} \quad (7.29)$$

The matrix \bar{A} combines both of these partitions, with the pseudoinverse solution

$$\dot{\Delta} = (\bar{A}\bar{A}^T)^{-1}\bar{A}^T \begin{bmatrix} \dot{h} \\ 0 \end{bmatrix} \quad (7.30)$$

This description generalizes all variations of this class of steering laws where A is not necessarily square. However, if it is, the solution simplifies further and becomes

$$\dot{\Delta} = \bar{A}^{-1} \begin{bmatrix} \dot{h} \\ 0 \end{bmatrix} \quad (7.31)$$

In order for the \bar{A} matrix to be invertible, the constraint matrix C must contain rows that are linearly independent of the range space of A . When these constraints are guaranteed to maintain linear independence for the range of possible motions, the array becomes singularity-free. To achieve this goal, C must consist of constraint equations with some component orthogonal to the directions described by the rows of the Jacobian.

These additional equations provide a basis for the singularity-avoidance properties of the steering laws involved. Holonomic constraints specify the gimbal angles directly. They can be incorporated into this formulation by simply taking the derivative of the constraint involved and specifying a carefully chosen, non-singular initial gimbal-angle condition. The scissored-pair array constraint is an example and is summarized below. Non-holonomic constraints specify the path or some function of the gimbal rates without specifying angles *per se*. Further research may identify non-holonomic constraints of interest, but to date only holonomic constraints have been identified.

For simplicity, the examples here consider only exactly constrained systems, where the number of constraints m is equivalent to the number of CMGs beyond the minimum of three. Using exactly three CMGs leaves no null space for constraints to be added. For example, controlling a two-dimensional momentum space with three SGCMGs offers the opportunity for one constraint equation. Such a situation may be preferred: inverting the now square A matrix represents an opportunity for minimal computation, compared to the more computationally burdensome calculation of a numerically robust pseudoinverse.

An important practical consideration is that in order for a constraint-based steering law to operate properly, the constraint must be exactly enforced. The finite precision of typical software environments demand that some low-bandwidth feedback be used to avoid an accumulation of numerical error that would cause the CMGs to drift off the path consistent with the initial conditions and the constraint.

7.4.3.1 Linear-Constraint Methods

In a scissored-pair configuration, two SGCMGs are constrained such that their gimbal displacements are equal in magnitude but opposite in direction (Cunningham and Driskill [11]). The motion of the two momentum vectors resembles that of a pair

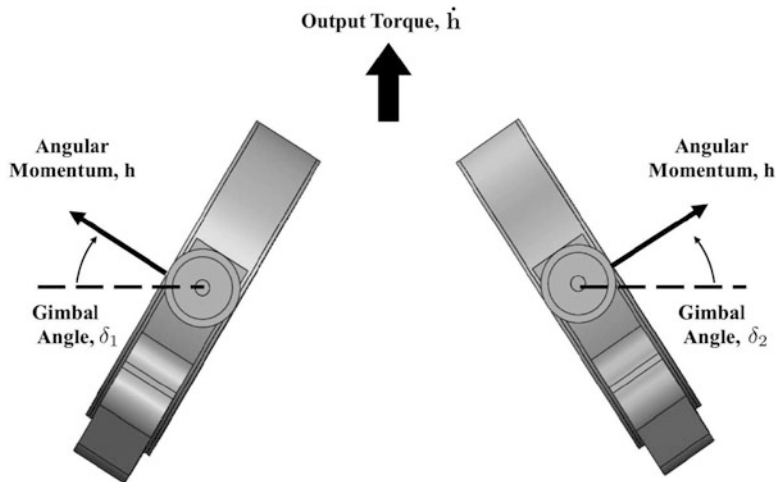
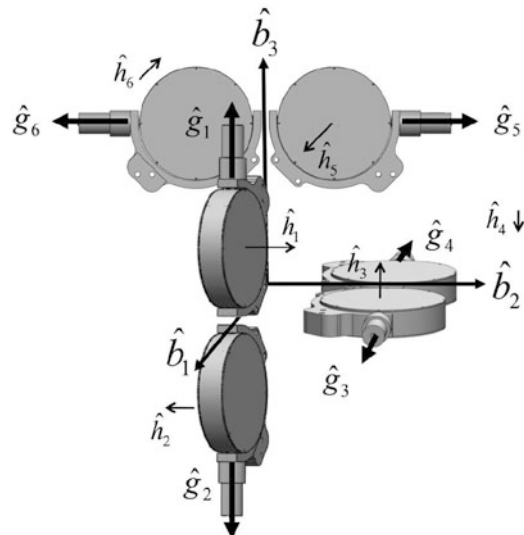


Fig. 7.2 Scissored pair constraint. The scissored pair of CMGs is constrained such that the gimbal angles are equal in magnitude and opposite in direction, which results in a net torque along a single axis

Fig. 7.3 Arrangement of three scissored pairs. This figure demonstrates one possible arrangement of the three scissored pairs of CMG that are required for six-DOF control of a spacecraft



of scissors—hence the name. The angles, as defined in Fig. 7.2, are constrained to be the same ($\delta_1 = \delta_2$). The scissoring motion caused by this constraint produces an output torque in a direction fixed along the reflection line between the two CMGs, as shown in Fig. 7.2. Thus, complete six degree-of-freedom control of a spacecraft requires three scissored pairs of SGCMGs. One potential arrangement is shown in Fig. 7.3.

Scissored-pair arrangements of SGCMGs are singularity-free except at the saturation singularities, where the pair is producing the maximum momentum of which it is capable in that direction. This configuration of CMGs is generally not considered mass efficient despite its singularity-avoidance properties and its relative simplicity because the angular momentum envelope is considerably smaller than other six-CMG arrays of similar mass. Nevertheless, the modularity of such a configuration and the prospect of commercially available, off-the-shelf scissored-pair units suggests that the configuration has some value at the system level.

The Jacobian for the array of three scissored pairs is

$$A = \begin{bmatrix} -c\delta_1 & -c\delta_2 & 0 & 0 & -s\delta_5 & s\delta_6 \\ -s\delta_1 & s\delta_2 & -c\delta_3 & -c\delta_4 & 0 & 0 \\ 0 & 0 & -s\delta_3 & s\delta_4 & -c\delta_5 & -c\delta_6 \end{bmatrix} \quad (7.32)$$

Each pair is constrained as follows: $\delta_1 - \delta_2 = 0$; $\delta_3 - \delta_4 = 0$; $\delta_5 - \delta_6 = 0$. Taking the derivative of these holonomic constraints produces a similar constraint on the gimbal rates:

$$\begin{bmatrix} 0 \\ 0 \\ 0 \end{bmatrix} = \begin{bmatrix} 1 & -1 & 0 & 0 & 0 & 0 \\ 0 & 0 & 1 & -1 & 0 & 0 \\ 0 & 0 & 0 & 0 & 1 & -1 \end{bmatrix} \dot{\Delta} \quad (7.33)$$

This constraint equation provides the C and D matrices. Augmenting the Jacobian with the constraint matrices provides \bar{A} :

$$\begin{bmatrix} \dot{h} \\ D \end{bmatrix} = \begin{bmatrix} \begin{bmatrix} -c\delta_1 & -c\delta_2 & 0 & 0 & -s\delta_5 & s\delta_6 \\ -s\delta_1 & s\delta_2 & -c\delta_3 & -c\delta_4 & 0 & 0 \\ 0 & 0 & -s\delta_3 & s\delta_4 & -c\delta_5 & -c\delta_6 \end{bmatrix} \\ \begin{bmatrix} 1 & -1 & 0 & 0 & 0 & 0 \\ 0 & 0 & 1 & -1 & 0 & 0 \\ 0 & 0 & 0 & 0 & 1 & -1 \end{bmatrix} \end{bmatrix} \dot{\Delta} \quad (7.34)$$

The well-known singularity avoidance properties of this constraint-based steering law can be demonstrated by showing that the rows of the constraint matrix in Eq. (7.33) are linearly independent of A . Using the fact that the column rank is equivalent to the row rank,

$$\begin{bmatrix} \dot{h} \\ D \end{bmatrix} = \begin{bmatrix} \lambda_1 \\ \lambda_2 \\ \lambda_3 \\ \lambda_4 \\ \lambda_5 \\ \lambda_5 \end{bmatrix} = 0_{6 \times 1} \quad (7.35)$$

$$\begin{aligned}
 -c\delta_1\lambda_1 - c\delta_2\lambda_2 - s\delta_5\lambda_5 + s\delta_6\lambda_6 &= 0 \\
 -s\delta_1\lambda_1 + s\delta_2\lambda_2 - c\delta_3\lambda_3 - c\delta_4\lambda_4 &= 0 \\
 -s\delta_3\lambda_3 + s\delta_4\lambda_4 - c\delta_5\lambda_5 - c\delta_6\lambda_6 &= 0 \\
 \lambda_1 = \lambda_2, \lambda_3 = \lambda_4, \lambda_5 = \lambda_6
 \end{aligned} \tag{7.36}$$

The solution is trivial ($0 = 0$) for angles below $\pi/2$, meaning that the system has full rank for gimbal angles below saturation, as seen in Eq. (7.37).

$$\begin{aligned}
 -c\delta_1\lambda_1 - c\delta_1\lambda_1 - s\delta_5\lambda_5 + s\delta_5\lambda_5 &= -2c\delta_1\lambda_1 = 0 \\
 -s\delta_1\lambda_1 + s\delta_1\lambda_1 - c\delta_3\lambda_3 - c\delta_2\lambda_3 &= -2c\delta_2\lambda_3 = 0 \\
 -s\delta_3\lambda_3 + s\delta_3\lambda_3 - c\delta_5\lambda_5 - c\delta_5\lambda_5 &= -2c\delta_5\lambda_5 = 0 \\
 \lambda_1 = \lambda_2, \lambda_3 = \lambda_4, \lambda_5 = \lambda_6
 \end{aligned} \tag{7.37}$$

7.4.3.2 Triplet Steering Law

If three CMGs are placed in a plane (a “triplet”), the additional CMG adds a degree of freedom, creating null space (so, for example, an infinite set of gimbal angles can correspond to the zero momentum state, as shown in Fig. 7.4).

For the case of three CMGs, one constraint equation is sufficient to fully constrain the system in a two-dimensional workspace. This constraint can be designed to successfully avoid the internal singularity while also providing the required torque by exploiting the null space of the Jacobian. Again, the constraint equation that fills this need must accomplish three objectives: (1) avoid singular configurations; (2) capture the maximum possible range of momentum values and (3) introduce no unwanted torque (Fig. 7.5).

The triplet configuration has a 2×3 Jacobian, as shown in Eq. (7.38), where A_1 and A_2 are the top and bottom rows of the planar Jacobian, respectively.

Fig. 7.4 Planar representation of CMG momentum. The angular momentum vectors of three planar CMGs span the two-dimensional momentum manifold in a non-deterministic way. This configuration shows one of the many zero-momentum configurations for the array

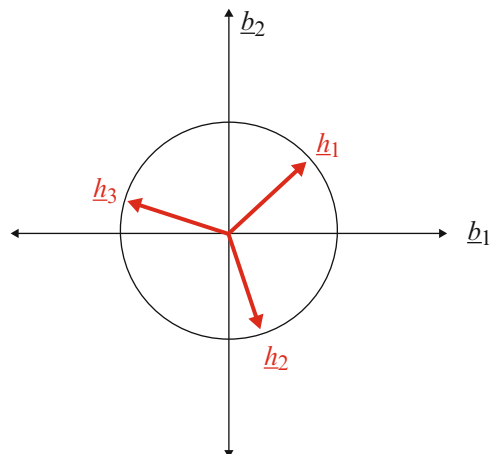
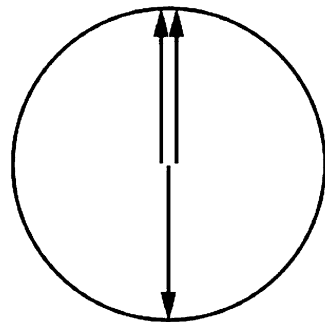


Fig. 7.5 Internal singularity for a triplet. The angular-momentum vector one of the CMGs cancels that of a second CMG. The third CMG's momentum is also parallel to one of those two, creating a situation where torque cannot be exerted in the direction parallel to the CMGs



$$A_{Planar} = \begin{bmatrix} -s\delta_1 & -s\delta_2 & -s\delta_3 \\ c\delta_1 & c\delta_2 & c\delta_3 \end{bmatrix} = \begin{bmatrix} A_1 \\ A_2 \end{bmatrix} \quad (7.38)$$

Singularities occur when the matrix being inverted in the Moore–Penrose pseudoinverse [Eq. (7.30)], in this case the augmented \bar{A} matrix is not full rank. In order to ensure that the constraint equation does not introduce more singularities, it is sufficient to write a constraint equation that is always linearly independent of the two existing rows of the Jacobian: for example, the cross-product of two linearly independent vectors. Thus, a singularity-free constraint equation must include a scaled component in the direction of the cross-product of the two rows of the Jacobian:

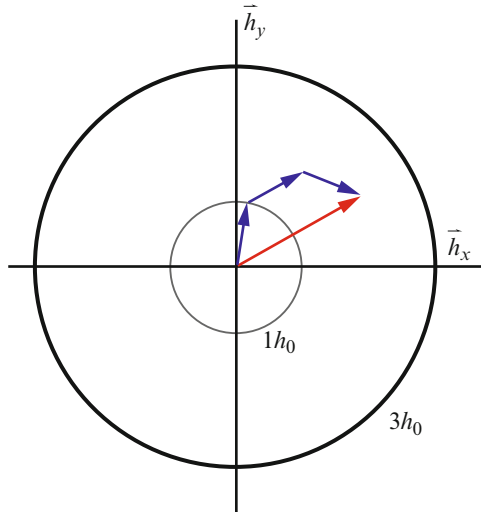
$$D = d = [\beta_1 A_1 + \beta_2 A_2 + \beta_c (A_1 \times A_2)] \dot{\Delta} = C \dot{\Delta} \quad (7.39)$$

where d is a scalar solution to the constraint equation, β_1 and β_2 are scaling values for the component of the vector in the direction of the Jacobian rows, and β_c is a non-zero scaling value for the constraint equation. This example uses a value of zero for β_1 and β_2 and a value of one for β_c , such that the constraint equation is as shown in Eq. (7.40).

$$D = [A_1 \times A_2] \dot{\Delta} = [s(\delta_3 - \delta_2) \ s(\delta_1 - \delta_3) \ s(\delta_2 - \delta_1)] \dot{\Delta} = C \dot{\Delta} \quad (7.40)$$

D determines the null motion needed to condition the array and steer it away from the internal singularity at $1h$. Because C is orthogonal to the two rows of A , the singularities of the augmented matrix \bar{A} [Eq. (7.29)] are simply the singularities of A . In this example, null-space commands keep the CMGs' momentum vectors in a trapezoid configuration. As shown in Fig. 7.6, with the momentum vectors head-to-tail, the trapezoid configuration is one in which one of the CMG momentum vectors is kept parallel to the total momentum vector (the vector sum of all three CMG vectors), while the other two momentum vectors form the sides of a trapezoid. All three vectors are parallel only at the edge of the momentum envelope. At the internal

Fig. 7.6 Triplet CMG momentum visualized as a trapezoid. A trapezoid configuration keeps the array non-singular by maintaining one of the three CMG momentum vectors parallel to the total momentum vector at all times. The three CMGs are shown in blue and the total momentum vector in red



singularity located at $1h$, the two vectors forming the sides are orthogonal to the vector parallel to the total momentum vector, an ideal configuration for traversing the singularity.

Given any total momentum vector within the array's envelope, there are six ways to arrange the CMGs such that they are in a trapezoidal configuration and their momentum vectors sum to the same total. The first step is to determine which of the six trapezoid configurations is closest to the current (non-trapezoidal) configuration. That is, determine which trapezoid configuration would require the least gimbal motion to reach from the current configuration. The next step is to obtain a value for D as shown in Eq. (7.41).

$$D = [A_1 \times A_2] \dot{\Delta} = [s(\delta_3 - \delta_2) \ s(\delta_1 - \delta_3) \ s(\delta_2 - \delta_1)] K \begin{bmatrix} \delta_{1t} - \delta_1 \\ \delta_{2t} - \delta_2 \\ \delta_{3t} - \delta_3 \end{bmatrix} \quad (7.41)$$

δ_{nt} is the gimbal angle the n th CMG would have if the array were in the trapezoid configuration closest to the current configuration, and K is a 3×3 diagonal matrix of gains. The values of the entries of K determine how much effort is used to drive the CMGs to their closest trapezoid configuration and are chosen such that as much null-space effort as possible is used to keep the array close to a trapezoid without exceeding CMG gimbal limits. The selection of entries in K can be done with a deterministic number of numerical iterations or by optimizing via a cost function. The values that produce the highest gimbal rates without exceeding the limits offer the fastest conditioning. They are then used to compute D as shown in Eq. (7.41). Once the D term is obtained, the gimbal rates can be found through a direct inversion of A as shown in Eq. (7.31).

When implemented, this steering law is not used close to the zero momentum state because the ambiguity of keeping a CMG momentum vector parallel to the zero

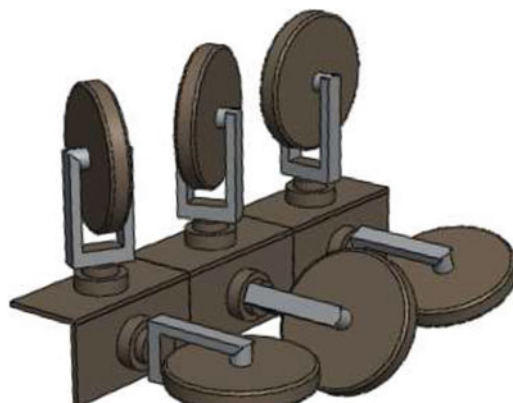
vector would cause large gimbal rates. The constraint is therefore modified such that within a small radius of the zero momentum state, a Moore–Penrose pseudoinverse rule is used instead. Since the radius in which the pseudoinverse rule is used is much smaller than $1h$, no problems with singularities are encountered by using the pseudoinverse, and the issue of very large gimbal rates near zero momentum is avoided. For example, the pseudoinverse rule may be used only within $0.1h$, which allows for enough null motion between $0.1h$ and $1h$ to properly condition the array. In the general case, the radius is chosen to be as small as possible but still large enough so that it is possible to traverse through the zero momentum state without gimbal rates exceeding the limit. The choice of this radius depends on the application-specific requirement on simultaneously available torque and momentum.

7.4.3.3 Expansion to a Six CMG Roof

This triplet analysis can be expanded to six SGCMGs by recognizing that two sets of triplets positioned such that the gimbal axes are offset relative to one another can be used together to exert torque in three directions. Such a configuration results in singularity-free control over two planes at an angle to one another, and thus spans \mathbb{R}^3 . In the example considered here, the gimbal axes are orthogonal to one another, as shown in Fig. 7.7. A six-CMG triplet steering law would require two constraint equations:

$$\begin{bmatrix} \dot{h}_x \\ \dot{h}_y \\ \dot{h}_z \\ D_1 \\ D_2 \end{bmatrix} = \begin{bmatrix} 1 & 0 & 0 & 1 & 0 & 0 \\ 0 & 1 & 0 & 0 & 0 & 0 \\ 0 & 0 & 0 & 0 & 1 & 0 \\ 0 & 0 & 1 & 0 & 0 & 0 \\ 0 & 0 & 0 & 0 & 1 & 0 \end{bmatrix} \begin{bmatrix} A_1 & 0 \\ C_1 & 0 \\ 0 & A_2 \\ 0 & C_2 \end{bmatrix} \begin{bmatrix} \dot{\delta}_1 \\ \dot{\delta}_2 \\ \dot{\delta}_3 \\ \dot{\delta}_4 \\ \dot{\delta}_5 \\ \dot{\delta}_6 \end{bmatrix} \quad (7.42)$$

Fig. 7.7 Two triplets of CMG at right angles



A_1 represents the Jacobian of the first CMG triplet and A_2 the Jacobian of the second triplet. C_1 and C_2 are the constraint equations, as described in Eq. (7.40), and D_1 and D_2 are solved for as described in Eq. (7.41). The transformation matrix in Eq. (7.37) is determined by the orientation of the two triplets. In this case, the gimbal axes are aligned with the y and z directions, such that the momentum envelope is greater in the x direction.

7.4.3.4 Gimbal-Angle Constraint Methods (Collinear Steering)

A CMG array is said to be “collinear” when its geometry includes sets of CMGs whose gimbal axes are parallel. The previous section used a collinear array as an example of linear constraints. This section discusses collinear arrays in general. The common case in which there are two such sets is referred to as a “roof” array (see Chap. 6). For example, consider a four-CMG roof array. Each “plane” of the roof contains two collinear CMGs whose gimbal axes are normal to the plane. Each CMG sweeps a circle of momentum in the plane. Adding the two circles associated with the two CMGs produces a momentum state anywhere within a disc of radius $2h$. To produce a net zero momentum, i.e., the “origin” of the disc, the CMGs must be directed oppositely. When the gimbals are in that orientation, both produce torque about the same axis. Therefore, that plane is singular. And, of course, if both discs are in this configuration, the array is singular.

The solution to this dilemma is to recognize that there are four CMGs in this array, and therefore the array has one degree of freedom of null space. As a result, an a number of different combinations of gimbal angles can produce the same net momentum vector. The steering law designer has the freedom to choose which set of gimbal angles to use, or put another way, to apply a gimbal-angle constraint. Imposing a constraint on the null space degree of freedom like this is referred to as “fixed map” steering. As a result of such a constraint, each momentum state maps to a unique set of gimbal angles.

In applying this approach to the four-CMG roof array, we refer to the axis where the two planes of the roof intersect as a “shared” axis. Both planes can produce momentum in this direction. Therefore one possible constraint is to “bias” the two discs against each other along the shared axis, as illustrated in Fig. 7.8. When the roof is producing zero net momentum, the discs have equal and opposite nonzero momentum along the shared axis; thus, both are well separated from the singularity at the disc origin, and the system is well conditioned.

7.4.4 Limited Angular Momentum Methods

In many cases, including the four-CMG roof array of the previous section, applying a gimbal-angle constraint does not eliminate the singularities; it merely changes the point in momentum space at which they are encountered. This constraint is

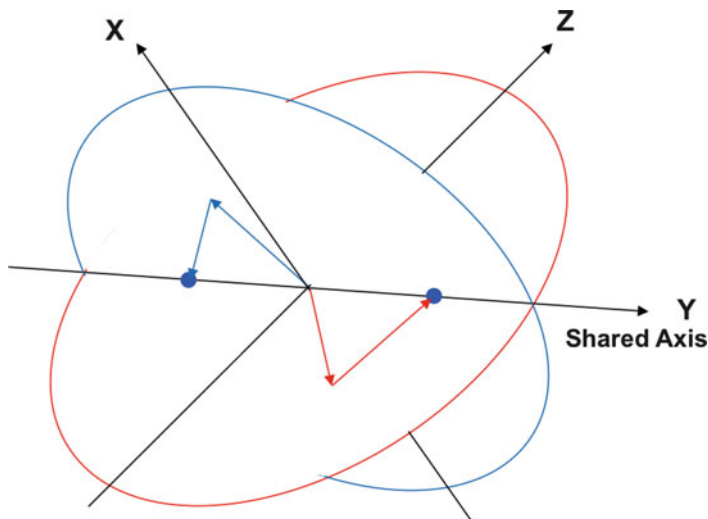


Fig. 7.8 Biasing along the shared axis

particularly useful for the four CMG roof array, since the singularity is at the origin. But if we start at our biased, net-zero momentum state (Fig. 7.8) and continue to apply torque about the shared axis, eventually one of the discs must encounter its origin singularity.

Strategies for managing this encounter are discussed elsewhere in this chapter. However, depending upon the requirements of the application, it may be acceptable simply to impose a limit on the net array momentum prior to reaching this point. This limit results in a simple and conservative control scheme with singularities avoided because they cannot be encountered. Some applications, such as missions that execute small slews in a short amount of time, do not have time for the gimbals to rotate very far during a slew. As such, they rarely access the extremes of the momentum envelope anyway and suffer little penalty from this practice.

Some care must be taken in how a momentum limit is implemented. Consider a large-angle eigenaxis slew, where the momentum limit is reached in the eigenaxis direction, resulting in maximum vehicle rate for the majority of the slew. One approach might be to arrest all gimbal motion until the commanded torque is in the direction that reduces momentum at the end of the maneuver. Doing so would not only impose the momentum limit but also would essentially stop all command response during the slew, leaving the ACS open. This open-loop behavior is a problem, as there is no cross-axis torque available to make small corrections and keep the slew trimmed about the correct axis.

7.5 Singularity Avoidance and Escape Algorithms

Some steering algorithms simultaneously avoid singularities through null motion or constraints and escape from singularities through torque error. Such algorithms benefit arrays of CMGs that contain both elliptic and hyperbolic internal singularities. Fully exploiting exact solutions at hyperbolic singularities consists of using of null motion when it is available and torque error only at elliptic singularities, i.e., singularity escape when no null motion is possible. Such steering laws can be implemented only when the form of the singularity (see Chap. 5) is known.

7.5.1 Hybrid Steering Logic

Parameters that identify the type of singularity must be incorporated in the steering algorithm. Chapter 5 explains that the parameters from the eigenvalues of the singularity definition matrix S and projection matrix P determine the form of a singularity: whether it is hyperbolic or elliptic. The steering algorithm must take this information into account for CMG arrays that contain internal elliptic singularities. The hybrid steering logic (HSL) does just that in the form of a pseudoinverse. The pseudoinverse expression for the HSL arises when the parameters ($Q = X = U\text{diag}(0, 0, \alpha)$, $R = I_{n \times n}$, and $\dot{\Delta}_d = \beta V\text{diag}(0, 0, 0, 1)V^T d$) are substituted into Eq. (7.6), taking into account the separation of the null- and forced-spaces in Eq. (7.24):

$$\dot{\Delta} = A^T(AA^T + X)^{-1}\dot{h} + \beta V\text{diag}(0, 0, 0, 1)V^T d \quad (7.43)$$

Equation (7.43) may appear to be simply a hybrid of the SDA algorithm in Eq. (7.12) and the LG method in Eq. (7.25), but there are some subtle differences. First, the null-space projection matrix $[I_{n \times n} - A^+ A]$ is singular when A is singular. For Eq. (7.25), the equivalent matrix $V\text{diag}(0, 0, 0, 1)V^T$ is now non-singular. Second, the singularity parameters— α for A^{SDA} and β for the LG—are different. They are defined by the form of singularity, i.e., hyperbolic or elliptic. For a four CMG pyramid array, the expressions α and β for this method are

$$\alpha = \alpha_0 e^{-a\bar{\alpha}} e^{\mu_1 m} \quad (7.44)$$

$$\beta = \beta_0 e^{-a\bar{\beta}} e^{\mu_2 m} \quad (7.45)$$

where α_0 , a , μ_1 , β_0 , b , and μ_2 are positive scalar constants and m is the singularity measure. Now, the form of singularity is found through the states $\bar{\alpha}$ and $\bar{\beta}$ which depend directly on the singularity definition matrix S as

$$\bar{\alpha} = |S_0 - \det(S)| \quad (7.46)$$

$$\bar{\beta} = \frac{1}{\alpha} \quad (7.47)$$

where S_0 is the maximum value that $\det(S)$ can achieve. S_0 is found heuristically or through optimization. The absolute value in Eq. (7.46) compensates for numerical error, producing a negative term. It should be clear from Eqs. (7.44) through (7.47) that at a hyperbolic singularity, $\det(S) \leq 0$. Therefore, Eq. (7.44) would reduce the effect of torque error in Eq. (7.43), thus reducing torque error and providing a more precise LG method. At an elliptic singularity, $\det(S) > 0$. Therefore, at an elliptic singularity, when null motion is ineffective, higher torque error is required to efficiently escape singularity.

The HSL is unique among pseudoinverse-based steering algorithms because it uses the information on the form of singularity to maximize steering precision and escape internal singularities, thus trading off the properties of LG and SDA depending on the type of singularity encounter. The singularity parameter metrics identified in Eqs. (7.44) and (7.45) must to be chosen with care to provide the desired performance (Leve and Fitz-Coy [12]).

7.5.2 *Angular Momentum Artificial Potential Steering*

Singularities can be thought of as obstacles to trajectories in momentum space. Such obstacles can be avoided through algorithms that utilize barrier functions known as repulsive artificial potential functions (APFs). An APF is a mathematical framework that represents vector-field sources and sinks as repulsive and attractive potentials. The gradient of the sum of these functions provides a trajectory that discourages the trajectory from approaching sources and encourages motion toward commanded trajectories in the form of sinks.

A set of APFs can be defined that combines objectives of an attractive potential for tracking a torque, angular momentum, or attitude and repulsive potentials for avoiding angular momentum saturation and singularities. Angular momentum artificial potential steering (AMAPS) is a method that uses such a framework for singularity avoidance. It trades torque error for singularity avoidance through soft constraints posed by APF (Munoz and Leve [13]).

The use of APF may introduce local minima where neither objective is satisfied (e.g., high torque error and/or close proximity to singularities), and yet the steering may converge here. Furthermore, repulsive APFs used to avoid singularities are inherently destabilizing because they introduce torque error to push the array configuration away from singularity. However, on a positive note, these functions are analytic, involve only minimal computation, and with the right tuning may provide useful local minima.

7.5.3 Feedback Steering Law

All steering algorithms presented up to this point require matrix inversions. Matrix inversions are expensive and require stable numerical algorithms regardless of singularities. Some steering algorithms avoid inverses altogether, taking an approach that differs from the pseudoinverse solutions. The possible benefit in computation comes at the expense of nonzero torque error.

An example of an inverse-free solution, different from that in [14], is known as the feedback steering law (FSL), in which the solution for gimbal rates needed to provide a commanded torque is found through construction of a linear system. This method is unique in that it does not correspond to a solution found from Eq. (7.6). Yet it is familiar, since it is based on linear-system analysis. Without going into detail, the linear system constructed for FSL has the dynamics

$$\dot{x} = A_K x + B_K u \quad (7.48)$$

$$\dot{\Delta} = C_K x \quad (7.49)$$

where the coefficient matrices in Eqs. (7.48) and (7.49) A_K , B_K , C_K are found by minimizing the cost function

$$J = \frac{1}{2} [\tau_e \dot{\Delta}]^T \begin{bmatrix} K_1 & 0 \\ 0 & K_2 \end{bmatrix} [\tau_e \dot{\Delta}] \quad (7.50)$$

$\dot{\Delta} \in \mathbb{R}^4$

which is exactly the SR inverse when $K_1 = 1$ and $K_2 = \lambda I$. However, for FSL, $K_1 = 1$ and the compensator $K_2 = K(s)$ and the coefficient matrices in Eqs. (7.48) and (7.49) are found through an H_∞ minimization of

$$\min_{K(s) \in \mathbb{R}^{3 \times 3}} \left\| \begin{bmatrix} w_1(s)[1 + AK(s)]^{-1} \\ w_2(s)K(s)[1 + AK(s)]^{-1} \end{bmatrix} \right\|_\infty \quad (7.51)$$

where the sensitivity weights

$$w_1(s) = \begin{bmatrix} A_K & B_K \\ C_K & 0 \end{bmatrix} \quad (7.52)$$

comprise a matrix function that bounds the bandwidth of the steering algorithm, and

$$w_2(s) = \frac{1}{\omega} I_{4 \times 4} \quad (7.53)$$

provides upper bounds on the gimbal rates. The final result is in the controller-observer form

$$\begin{aligned}\dot{h} &= A_K h + B_K \tau_e \\ \dot{\Delta} &= C_K h\end{aligned}\tag{7.54}$$

where $C_K = A^T b \omega \bar{P}$ (Pechev [15]). The constant b is the required bandwidth of the steering algorithm, and \bar{P} is the solution to the steady-state, i.e., infinite frequency Riccati Equation. The elegant steering algorithm in Eq. (7.54), unlike pseudoinverse solutions, is based entirely on linear systems theory and optimization and provides a way to limit the bandwidth and gimbal rate of the SGCMGs used for control while avoiding singularities. Also, it accomplishes these goals without matrix inversions.

However, this result derives from a steady-state Jacobian and therefore may not always produce an exact solution. Also, like the other methods based on the cost in Eq. (7.3), its solution involves mixed weighting of objectives and therefore may not produce an exact torque while attempting to limit gimbal rates.

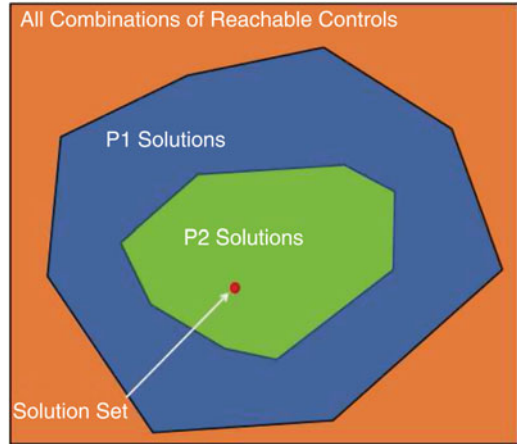
7.5.4 Optimal CMG Attitude Control

Allocation of torque among CMGs tends to optimize over some aspect of their control effect, such as the output-torque error from the CMG array, the magnitude of the gimbal rates resulting from their torque tracking, or some combination thereof, in terms of the objective function of Eq. (7.3).

However, most pseudoinverse methods that are derived from the cost function in Eq. (7.3) are locally optimal at best, and their performance is dominated by the choice of the weighting matrices R and Q (Leve [5]). One may want to optimize the CMG gimbal rates to minimize both the torque error and the electromechanical power, which is not exactly equivalent to the two-norm of the gimbal rates. At the same time, such a steering approach may have to obey constraints on the gimbal kinematics. Alternatively, optimal steering may simultaneously include attitude trajectory and CMG gimbal rates, obviating the need to minimize array-level torque. For such cases, the operations concept may call for solving the minimum-time attitude trajectory along with minimizing the gimbal-rate magnitudes. This section addresses optimal methods of control allocation that simultaneously optimize the attitude trajectory, error in attitude, rate, and torque, and electromechanical power/energy of the CMG, and/or some combination of these objectives.

Normally, the commanded torque is sent from the attitude control system and then mapped by a steering algorithm to the gimbal rates. From there, the inner-loop gimbal controller offsets friction while enforcing hard constraints for the maximum gimbal rate and acceleration. This methodology is neither optimal with respect to power and accuracy nor efficient for utilizing the entire performance envelope. With the exception of the FSL algorithm of Eq. (7.50), analytic solutions for steering algorithms are unable to handle such constraints. Constrained optimization techniques can permit a steering algorithm to be better than locally optimal, although not necessarily globally optimal.

Fig. 7.9 Searchable sets used for lexicographic optimization



7.5.4.1 Convex Optimization: Minimum Error-Dissipative Power Reduction Control

Steering a redundant array of RWAs and/or CMGs may prioritize accuracy in torque tracking more highly than other metrics such as the minimum input power to the actuators as secondary objectives. Such priority-based optimization processes are analogous to how we think as humans but are not how optimization techniques are typically structured. Consider, for example, a redundant RWA or CMG array control-allocation problem, in which there are infinitely many ways to impart a given torque, i.e., due to the null-space degree(s) of freedom in Eq. (7.2). These solutions constitute a searchable set, as shown in Fig. 7.9.

As an algorithm optimizes over torque-tracking accuracy, it reduces the set to only those solutions that have the optimal accuracy. Searching within this set can yield a subset of solutions that provide the minimal power for control allocation. The second priority may result in a multiple-solution set or a singleton. Now to provide a real-time, polynomial convergent solution of this priority-based optimization, the constraints and the cost may be structured as a convex function (not necessarily linear). This method of priority-based optimization is known as “Lexicographic Optimization” and relies on interior-point methods of convex optimization to find real-time, polynomial convergent solutions to the optimal control allocation of redundant arrays of RWA and CMG (Dueri et al. [16]). An example of the priority optimization for Minimum Error-Dissipative Power Reduction Control or ME-DPRC from Dueri et al. [16] for n RWA is

$$\begin{aligned} \min_{\Omega_{r,k+1}, \dot{\Omega}_{r,k}} J_1 &= \|\dot{h} - J_r A_s \dot{\Omega}_{r,k}\|_1 \\ \text{subject to } \Omega_{r,k+1} &= \Omega_{r,k} + \dot{\Omega}_{r,k} \Delta t, \\ -\Omega_{\max} &\leq \Omega_{k+1} \leq \Omega_{\max}, \quad -\dot{\Omega}_{\max} \leq \dot{\Omega}_{r,k} \leq \dot{\Omega}_{\max}, \end{aligned} \tag{7.55}$$

where Δt is the discretization time step, $\dot{\Omega}_{r,k}$ is the rotor accelerations at the k th timestep, Ω_{\max} is a vector of symmetric upper bounds on RWA flywheel rates, $\dot{\Omega}_{\max}$ is a column matrix of symmetric upper bounds on RWA flywheel accelerations, and \leq represents an element-wise inequality. Using the one-norm of the torque error makes the above problem an LP [17]. Let J_1^* be the minimum torque error. Then the second optimization (minimizing power) is posed as:

$$\begin{aligned} \min_{\Omega_{r,k+1}, \dot{\Omega}_{r,k}} J_2 &= \| (J_r \dot{\Omega}_{r,k} - \tau_{Wf,k}) \odot \Omega_{r,k} \|_1 \\ \text{subject to } \Omega_{r,k+1} &= \Omega_{r,k} + \dot{\Omega}_{r,k} \Delta t, \\ \| \dot{h} - J_r A_s \dot{\Omega}_{r,k} \|_1 &\leq J_1^*, \\ -\Omega_{\max} \leq \Omega_{r,k+1} &\leq \Omega_{\max}, \quad -\dot{\Omega}_{\max} \leq \dot{\Omega}_{r,k} \leq \dot{\Omega}_{\max}. \end{aligned} \tag{7.56}$$

where $\tau_{Wf,k}$ is the wheel friction torque at the k th time step from Appendix A, and the first inequality imposes minimum-torque error. Clearly, the first inequality constrains the second-priority optimization to search within the solutions left over from the first-priority optimization. That first inequality constraint is $\| \dot{h} - J_r A_s \dot{\Omega}_{r,k} \|_1 \leq J_1^*$. This method does exactly what is shown in Fig. 7.9. To keep the second cost convex, the shaft power is multiplied with current rotor rates. This assumption is reasonable for RWAs because rotor accelerations are typically not large enough that the rotor rates will be in a different regime at the next time step.

Unlike many methods of optimal control, lexicographic programming can be used as a real-time method of control allocation. However, it does rely on the ability to design a practical convex cost function and set of constraints. It also does not guarantee anything better than a locally optimal, i.e., a greedy-algorithm solution for the electromechanical power unless a receding-horizon approach is used such as model predictive control (Fisher et al. [18]).

7.5.4.2 Gauss Pseudo-Spectral Collocation Methods

Nonlinear optimization techniques may be appropriate when a spacecraft requires a global, or at least better-than-locally optimal, solution for attitude control, particularly when the optimization is inherently nonlinear and nonconvex. The most common of these techniques include direct and indirect methods. One approach is to solve an optimal control problem as a two-point boundary value problem, which is in turn numerically solved by shooting methods. Another is to construct a discrete nonlinear program to be solved as a set of algebraic equations at discrete points in place of differential equations.

Shooting methods have their problems: they require accurate initial guesses for convergence to the optimal solution; they may use integration methods that are not amenable to control and trajectories with discontinuities; and because they consider roughly the entire trajectory and control of the optimal solution, they are

not computationally efficient, in general. On the other hand, collocation methods discretize the controls and the trajectories at a set of points and use interpolation, typically by splines between the points, to provide a complete solution to the optimal-control problem. Such methods are more computationally efficient, while also able to handle discontinuities.

In simplest terms, collocation methods replace differential equations with algebraic equations solved at discrete nodes, called collocation points (Divya et al. [19] and Fahroo and Ross [20]). At the nodes, optimality is usually proved through costate mapping theorems. The proof shows that each discrete point where the optimal control solution is solved meets the optimality conditions.

For CMG attitude control, the most popular objective for optimization in the literature is minimum-time slewing. A frequently discussed collocation method for this objective comes from Gauss Pseudo-Spectral methods (Ross and Karpenko [22]). These methods use Gauss Quadrature to approximate the integrals and the derivatives of the differential equations at the nodes. These methods have been shown in simulation and test-bed hardware to provide gimbal rates and rotor accelerations of an array of CMGs and RWAs for minimum time maneuvers (Ross and Karpenko [22]). Also, such methods have been used in flight, specifically on the International Space Station, for optimal offloading of angular momentum while minimizing thruster use. These “zero-propellant maneuvers” have saved millions of dollars’ worth of propellant (Bedrossian et al. [23]).

A drawback to solving the entire nonlinear optimization problem in its original form is that the solution is rarely guaranteed to be globally optimal. It is also not clear how fast such an algorithm converges to the optimal solution. So, its real-time implementation must be evaluated on a case-by-case basis. Furthermore, the interpolation between the discrete points where the solution is solved may not in fact be optimal or even satisfy constraints. In addition, it is not practical to add additional points to the nonlinear program to avoid errors between points from interpolation because the number of discrete points in general exponentially increases the size of the problem and computational cost.

For these many reasons, such methods are typically most effective if used as an open-loop feedforward for a feedback controller to follow. When the parameters of the spacecraft—mass properties, sensor biases and scale factors, flexible dynamics, and actuator alignments and biases—are very well known, this approach can be effective. For precise attitude control, or attitude control for systems where knowledge of the full trajectory is not possible, the smallest amount of model uncertainty can cause unacceptable inaccuracies in spacecraft attitude tracking. In such a situation, care must be taken in choosing a nonlinear program approach such as Gauss Pseudo-spectral methods.

7.6 Variable Speed Control Moment Gyroscopes

VSCMGs and the steering algorithms that go along with them have been suggested as a solution to the singularity-avoidance problem. Some effective VSCMG steering algorithms have been developed by Shaub and Junkins [24] and Yoon and Tsiotras [25]. However, there are significant drawbacks from a hardware perspective, as discussed in Chaps. 4 and 5. These drawbacks explain why VSCMGs are not common in contemporary spacecraft.

7.7 Chapter Summary

The purpose, derivation, and differences in performance of steering algorithms for CMGs are the subject of this chapter. Singularities can be avoided/escaped through the choice of algorithm and/or through the choice of a CMG array architecture with non-degenerate hyperbolic singularities. In such arrays, null motion will always be effective in avoiding internal singularities. Singularities can also be avoided through constraining the gimbal angles or usable angular momentum, i.e., workspace for steering algorithm solutions. This limitation leads to a method that provides an exact solution within the constraints without addressing the singularities directly on-the-fly and provides some solutions that do not require a redundant set of CMGs.

References

1. O. Tekinalp, E. Yavuzoglu, A new steering law for redundant control moment gyroscope clusters. *Aerosp. Sci. Technol.* **9**(7), 626 (2005)
2. N. Bedrossian, J. Paradiso, E. Bergmann, D. Rowell, Steering law design for redundant single-gimbal control moment gyroscopes. *AIAA J. Guid. Control. Dyn.* **13**(6), 1083 (1990)
3. T. Yoshikawa, Dynamic manipulability of robot manipulators, in *1985 IEEE International Conference on Robotics and Automation. Proceedings*, vol. 2 (IEEE, 1985), pp. 1033–1038
4. B. Wie, D. Bailey, C. Heiberg, Singularity robust steering logic for redundant single-gimbal control moment gyros. *AIAA J. Guid. Control. Dyn.* **24**(5), 865 (2001)
5. F. Leve, Evaluation of steering algorithm optimality for single-gimbal control moment gyroscopes. *IEEE Trans. Control Syst. Technol.* **22**(3), 1130 (2014)
6. J. Leve, F. Munoz, N. Fitz-Coy, Gimbal-lock escape via orthogonal torque compensation, in *Proceedings of AIAA Guidance, Navigation, Control Conference*, 2011, pp. 1–10
7. A. Azzalini, *Matrix Inversion Lemma* (Wiley Online Library, 2006)
8. H. Kurokawa, Survey of theory and steering laws of single-gimbal control moment gyros. *AIAA J. Guid. Control. Dyn.* **30**(5), 1331 (2007)
9. J. Havill, J. Ratcliff, A twin-gyro attitude control system for space vehicles. Technical Report, NASA, 1964
10. L. Jones, R. Zeledon, M. Peck, Generalized framework for linearly constrained control moment gyro steering. *AIAA J. Guid. Control. Dyn.* **35**(4), 1094 (2012)

11. D. Cunningham, G. Driskill, A torque balance control moment gyroscope assembly for astronaut maneuvering, in *NASA Ames Research Center 6th Aerospace Mechanics Symposium (SEE N72-26377 17-15)*, 1972, pp. 121–126
12. F. Leve, N. Fitz-Coy, Hybrid steering logic for single-gimbal control moment gyroscopes. *AIAA J. Guid. Control. Dyn.* **33**(4), 1202 (2010)
13. J. Munoz, F. Leve, Artificial potential steering for angular momentum exchange devices, in *AAS/AIAA Spaceflight Mechanics Meeting*, 2012
14. S. Krishnan, S. Vadali, An inverse-free technique for attitude control of spacecraft using cmgs. *Elsevier Acta Astronaut.* **39**(6), 431 (1996)
15. A. Pechev, Feedback-based steering law for control moment gyros. *AIAA J. Guid. Control. Dyn.* **30**(3), 848 (2007)
16. F. Dueri, D. Leve, B. Acikmese, Minimum error dissipative power reduction control allocation via lexicographic convex optimization for momentum control systems. *IEEE Trans. Control Syst. Technol.* (2015 to appear)
17. S. Boyd, L. Vandenberghe, *Convex Optimization* (Cambridge University Press, Cambridge, 2004)
18. J. Fisher, R. Bhattacharya, S. Vadali, Spacecraft momentum management and attitude control using a receding horizon approach, in *Proceedings of AIAA Conference on Guidance, Navigation, and Control*, 2007
19. D. Garg, M. Patterson, W. Hager, A. Rao, D. Benson, G. Huntington, A unified framework for the numerical solution of optimal control problems using pseudospectral methods. *Elsevier Automatica* **46**(11), 1843 (2010)
20. F. Fahroo, I. Ross, Pseudospectral methods for infinite-horizon nonlinear optimal control problems. *AIAA J. Guid. Control. Dyn.* **31**(4), 927 (2008)
21. K. Ford, C. Hall, Singular direction avoidance steering for control-moment gyros. *AIAA J. Guid. Control Dyn.* **23**(4), 648–656 (2000)
22. I. Ross, M. Karpenko, A review of pseudospectral optimal control: from theory to flight. *Annu. Rev. Control.* **36**(2), 182 (2012)
23. N.S. Bedrossian, S. Bhatt, W. Kang, I.M. Ross, Zero-propellant maneuver guidance. *IEEE Control Syst.* **29**(5), 53 (2009)
24. H. Schaub, J. Junkins, Singularity avoidance using null motion and variable-speed control moment gyros. *J. Guid. Control. Dyn.* **23**(1), 11 (2000)
25. H. Yoon, P. Tsotras, Singularity analysis of variable-speed control moment gyros. *AIAA J. Guid. Control. Dyn.* **27**(3), 374 (2004)

Chapter 8

Inner-Loop Control of Momentum Devices

Implicit in a discussion of how to command the devices in momentum control system is the assumption that the devices faithfully track those commands. And yet, momentum devices exhibit several significant nonlinearities and can experience significant disturbances and errors. For this reason, momentum devices almost always include “inner loops” applying feedback control to the quantities of interest to ensure that those commands are tracked.

This chapter examines some of the key considerations in the inner loops of momentum devices. The goal is not to teach the art of inner-loop design but rather to explore the ways in which the inner loops can impact the spacecraft designer. Because these devices contain active feedback systems, they may interact with the spacecraft structure or controls. These interactions are usually of great interest in spacecraft design.

8.1 Spin-Speed Control

8.1.1 CMG Spin-Speed Loops

Both RWAs and CMGs provide means for adjusting the spin speed of the rotor. In the case of the CMG, the goal is generally to hold the spin-speed constant, at a speed that is traditionally about 6000 rpm. Some smaller devices and next-generation CMGs may feature even faster spin speeds, perhaps tens of thousands of rpm. In most cases, CMGs include an integral feedback loop to perform this function. So, the user need only command the desired spin speed. Spin loops’ compensation usually includes a free integrator, allowing them to offset the effects of spin bearing drag, both Coulomb and viscous.

During normal operation of a CMG, various influences cause the measured spin speed to vary. For example, the spin bearings exhibit an increase in drag torque when exposed to radial loads, such as the forces that result when the CMG is producing output torque. This additional drag reduces the rotor speed. Another more subtle example results because the rotor spin speed is measured not relative to an inertial reference, but rather with respect to the gimbal housing, which moves with the spacecraft. Imagine rotating the gimbal 180°, thus imparting momentum to the spacecraft in the direction opposing spin. The rotor speed is now measured relative to a body moving in the opposite direction, and thus speed appears to increase.

While these changes in speed are small, and in some cases, cyclic, the spin-speed control loop responds to them nevertheless. It is therefore advisable for the spin loop to be very low in bandwidth, for example, 0.1 Hz or less. A high-bandwidth spin loop would expend considerable power attempting to follow a specific speed precisely, when this is not really necessary.

CMG users often impose a tight specification on how well the spin loop should hold speed, and this is often because they have assumed in their steering-law design that the rotor speeds are constant. The user of a CMG array should recognize that the spin system draws additional power to hold speed during periods when the array is maneuvering the vehicle. If power is a concern, the user should relax the spin-speed control specification, permitting variation in spin speed at these times. By allowing the rotor's speed to vary by even a few percent, the spin system power can be limited to a specified value, with the result that the CMGs recover more slowly after a period of active maneuvering. A good steering-law design accommodates such variations in speed by taking into account the instantaneous rotor speed in computing CMG commands, resulting in no appreciable degradation in performance. It's clearly an advantageous trade: lower power for a little more algebra.

8.1.2 RWA Spin Speed

Most reaction wheels accept a torque command, which is mapped by the motor K_T to a spin-motor current command. The RWA electronics produce this current using a high-bandwidth current loop, on the order of kHz. The current loop uses integral control to overcome significant motor back-emf and variations in resistance with temperature, leaving only variations in the motor K_T as the primary error in motor torque. The rotor speed changes as a result of the accumulation of momentum while these torques are applied, but most RWA applications treat momentum as a by-product, where the primary action of the device is to produce torque.

The biggest drawback in operating an RWA in this manner is the error introduced by bearing friction. Friction torques act on the rotor and react on the spacecraft in exactly the same way as motor torques. Therefore, any friction torque represents an error between the commanded motor torque and the actual torque delivered to the

spacecraft. The Coulomb drag of the bearings can be estimated by the flight software and added to the command, but near zero speed the friction changes rapidly and is difficult to compensate. This difficulty motivates spacecraft RWA-array steering-law architectures that keep the speeds away from zero as much as possible.

Some RWAs include an integral speed-control loop. This is a useful way to mitigate the effects of friction. Thanks to conservation of angular momentum, the change in rotor momentum is equal in magnitude but opposite in direction to the change in momentum imparted to the vehicle. Since torque $\tau = dH/dt$ and the rotor inertia is well known, it follows that the change in rotor speed provides a precise measurement of the integrated torque applied to the spacecraft, regardless of whether it arose from the motor or friction torque.

Therefore, regardless of whether feedback control is integral to the RWA hardware or realized on the spacecraft side, the preferred approach is to integrate the desired torque, scale (by inertia) to the expected rotor speed, and close a speed loop to produce this calculated speed. A torque feedforward can also be employed to improve performance. Recognizing that the speed command to this loop is often characterized by ramping up and down at the maximum torque, the loop compensation should be chosen such that minimal error results from a ramp command.

We recognize that an RWA speed loop is a hierarchical “inner loop” in the forward path of the ACS. As such, the bandwidth of the speed loop can impose a limit on the available ACS bandwidth. However, in general, this is not an issue with typical ACS bandwidths at tenths of a Hz, and speed loops at a few Hz. These bandwidths are far enough apart that the control loops are uncoupled.

More sophisticated methods of RWA control and friction mitigation exist. In general, the performance of these control approaches is limited by the quality of rotor-motion feedback available. These limitations must be taken into consideration in specifying an RWA if loops are to be closed around it via spacecraft bus electronics.

8.2 Gimbal Rate Loops

In the case of CMGs, the motion of the gimbal(s) is also regulated with feedback control. As the output torque of the CMG is gyroscopic ($\boldsymbol{\omega} \times \mathbf{h}_r$), the precision with which the scalar gimbal rate, $\dot{\delta}$, is controlled directly impacts torque performance. This impact on precision motivates virtually all CMGs to feature integral gimbal rate loops and to respond to gimbal-rate commands. The design of these loops can influence the design and performance of the ACS, and of the spacecraft itself.

8.2.1 Errors Mitigated by Gimbal Rate Loops

One of the key motivations for closing gimbal rate loops is the need to manage gyroscopic precession-induced motor torques. When the vehicle is in motion, the gimbal motor must apply sufficient torque to prevent the gimbal from precessing, and this torque can be large (see Sect. 3.2.5). Indeed, for direct-drive CMGs (no gears between the motor and the gimbal axis), it is common for the precession due to vehicle rate to drive the design of the gimbal motor, requiring many times the torque needed for gimbal acceleration alone. This large “disturbance” must be attenuated by an assertive loop, usually including a free integrator to increase gain at low frequencies and minimize rate error. Gimbal rate loops usually have bandwidth in excess of 10 Hz. In contrast, ACS loops for spacecraft with such CMGs are unlikely to include feedback control with a bandwidth above a few Hz.

In addition to rejecting the precession disturbance, gimbal rate loops also mitigate forward-path errors such as motor ripple, cogging, and accuracy. The rate performance of the CMG thus approaches the performance of the gimbal rate sensor. Historically, gimbal rate has been measured by a precisely wound tachometer. This electromagnetic device is essentially a motor/generator that produces a back-emf in response to rotor rate. The device must be commutated, and traditionally the low voltage back-emf must be amplified with high-quality circuitry to avoid apparent rate offset due to offsets in the amplifier. With the advent of digital electronics, some CMGs have employed digital encoder technology to measure both gimbal angle and rate with high precision.

8.2.2 Impact on Vehicle Structure

In the design of positioning servos in general, a common mistake is to assume that the positioner itself is rigidly fixed and that only the body being positioned is moving. We understand that when the torque motor acts on the gimbal, it also reacts into the structure that attaches the motor stator to “ground.” In our case, “ground” is the interface that mounts the momentum device to the spacecraft bus structure.

Of concern is the case illustrated in Fig. 8.1, where the spacecraft interface appears as “local” structure, connected through compliance to the rest of the vehicle. An example of such a condition might be a CMG mounted to a flat plate, or deck,

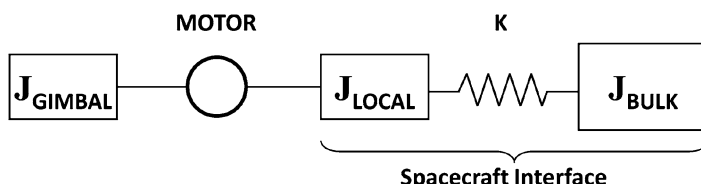


Fig. 8.1 A compliant spacecraft interface

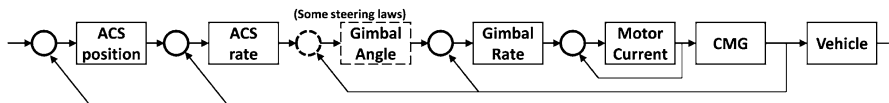


Fig. 8.2 Hierarchy of control

with local compliance. When the CMG is mounted to such a plate, its inertia lowers the frequency of bending modes in which this plate participates.

When the motor acts/reacts into the gimbal/local inertia, both bodies move. As a result, any structural resonance appears in the open-loop response of the gimbal rate loop. If the structural frequency is near the rate-loop crossover, the closed-loop system may be unstable. Spacecraft designers should recognize the importance of ensuring that CMG mounting interfaces are stiff and well coupled to the bulk of the spacecraft. This is particularly important when the CMGs are direct-drive, where the effect is more pronounced than in the case of a geared transmission.

8.2.3 Bandwidth Considerations

The CMG gimbal rate loop typically lies within a hierarchy of nested loops, as illustrated in Fig. 8.2.

As in all such hierarchical systems, loop stability demands frequency separation (a factor of 3 or 4 is typical) between the bandwidths at each level. This separation is necessary because the closed-loop phase rolloff of each level is evident in the open-loop response of the next outer loop, compromising its phase margin.

For example, to support an ACS with a position bandwidth of a few tenths of a Hz, the ACS rate bandwidth might be around 1 Hz. If the steering technology in use closes any loops (for example, on gimbal angle or momentum state), it would require a bandwidth of a few Hz, and the gimbal rate loop would therefore need bandwidth in the vicinity of 10–15 Hz. This bandwidth is typical for many CMGs. There is little margin in this strategy, and thus it is important for the ACS designer to be aware of the bandwidth of the CMG hardware, as well as any closed-loop dynamics in the steering technology chosen. These matters can directly influence the ACS design, or, alternatively, the ACS design might drive CMG performance requirements.

These design interdependencies might lead one to expect that the CMG rate-loop bandwidth would simply be over-specified, to reduce risk. The problem here, of course, is the one discussed earlier. If the CMG bandwidth is increased, its stability is threatened by higher-frequency structural modes. Stabilizing it would flow to a need for stiffer and therefore heavier spacecraft structure.

8.2.4 Friction and ACS Limit Cycling

The ball bearings used to support the CMG gimbal exhibit friction characteristics that are generally categorized based on their physical mechanism. Viscous friction opposes gimbal rate, and the torque increases nearly linearly with rate. Coulomb friction is “running drag,” which has a fairly constant torque over a wide range of gimbal rates, but always opposes the gimbal rotation. It therefore reverses polarity abruptly as gimbal rate passes through zero. Static friction, or “stiction,” causes a torque greater than the running drag to be required to get the gimbal moving again once it has stopped during a zero-rate crossover. Finally, when the gimbal is “stuck” at zero rate, a “pre-breakaway stiffness” is observed. So, the axis is never completely “stuck.”

All of this nonlinear behavior is generally negligible when the CMGs are used for agile slews requiring large torque. The large gimbal-rate commands quickly overcome the behavior near zero rate, and the viscous term is very small for the low rates typically associated with gimbals.

Of greater concern is the behavior when the vehicle is under precise control at a constant rate. When spacecraft accelerations are low, the CMG gimbal rates are near zero, and friction nonlinearities become apparent. When a rate reversal is required, the free integrator in the gimbal rate-loop compensation must have time to “wind up” enough torque to overcome static and Coulomb friction before the gimbal can rotate. And since the rate command is very small, the rate error is small, and the integrator ramps slowly. In a worst-case scenario, this apparent deadband behavior can result in a limit cycle in the ACS at a low frequency and amplitude.

In general, high-precision, preloaded ball bearings do not exhibit excessive static friction, but the reversal of the Coulomb friction is always present. The CMG manufacturer should be able to provide information on this behavior or include it in a dynamic model of their rate loop (for example, as a Dahl friction model). Armed with this information, the ACS designer should check for nonlinear limit cycles early in the design process. A describing-function analysis of the system is the best tool for determining both margin from limit cycle and strategies for modifying the design if necessary. Time-domain computer modeling can be used to validate the results of the analysis.

8.3 Chapter Summary

The inner loops of momentum devices can influence the spacecraft design. Each of the spin and gimbal loops commonly found is discussed. Choices surrounding this discussion can influence system power, performance and stability. Early decisions ranging from how the momentum devices are specified to the design of the spacecraft structure near the momentum devices are advised.

Chapter 9

Motors in Space

All momentum devices require a spin motor of some type to actuate the rotor spin axis. CMGs also require a motor on the gimbal axis. The torque and speed requirements for the gimbal motor design are typically much different from those for the rotor. These issues, among others, motivate the following discussion of motors commonly employed in spaceborne momentum devices. The objective of this chapter is to familiarize the reader with some of the key considerations with the goal of informing the analysis, implementation, and operation of momentum-control systems and the spacecraft that use them. Motor design is a broad specialty field that demands much more depth than offered here.

9.1 Motor Technology

Several types of motors find application in space products. AC induction motors can provide a simple solution for constant-speed applications where AC power is available, for example mechanical rate-sensing gyroscopes found in many aircraft. They find no application in momentum systems, however. Even for CMGs, in which the spin speed is held constant, that constant speed needs to be adjustable on orbit to provide the option of mitigating excitation of structure vibrations.

DC motors, both brushed and brushless, are found in space applications. However, the brushed motor, while simpler, is far less preferable for long-life applications. Brushes are a source of debris, EMI-producing arcing, and other problems. The brushless DC motor has a permanent-magnet rotor and two- or three-phase coils on the stator, as illustrated in Fig. 9.1.

When the coils are energized in sequence, a rotating field is produced that interacts with the field of the rotor to produce torque. Commutating the stator windings requires a position measurement and more complex drive electronics

Fig. 9.1 Two-pole, two-phase brushless DC motor

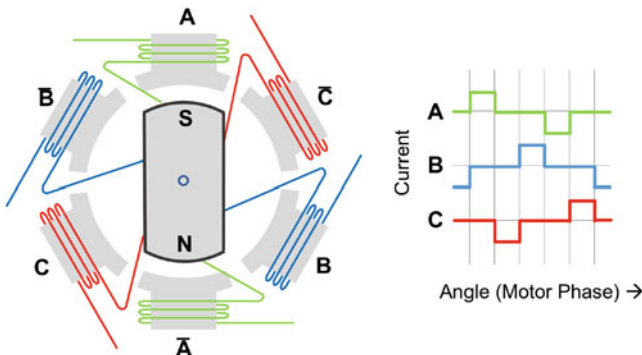
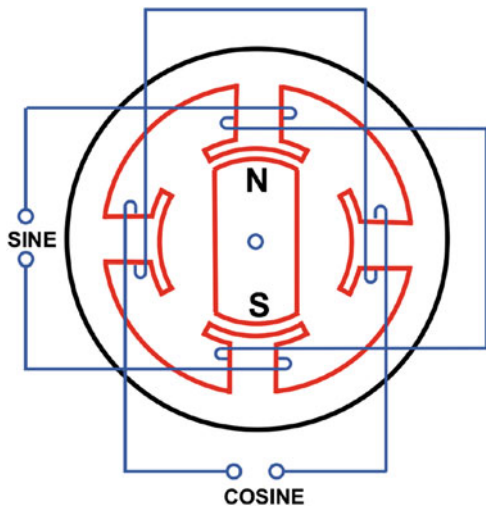


Fig. 9.2 Two-pole, three-phase brushless DC motor showing commutation

than do brushed motors. High-speed motors are often commutated discretely using Hall-effect devices to switch the appropriate coils on or off at the appropriate times, as shown in Fig. 9.2.

Commutation methods like this are most common for spin motors. Lower-speed, higher-precision applications use an actual rotor-angle measurement, such as from a resolver or encoder, and the coil currents are commutated sinusoidally to produce a nearly constant torque. Most CMG gimbal motors use this technology. Brushless DC motors tend to yield the most efficient and lightest design for typical space applications. A design based on brush motors would be suitable only for low-cost, short-duration technology-demonstration missions and even then would likely not be fully traceable to an operational space system.

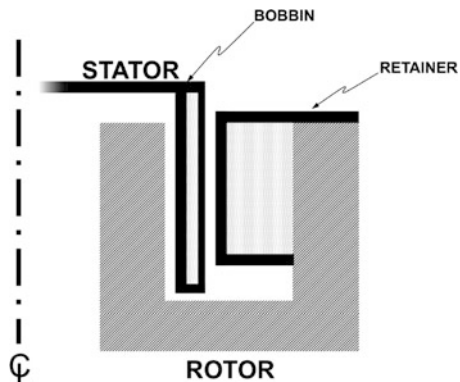
Stepper motors are a special case of the brushless DC motor. In this case, rather than commute the stator field to continually “lead” the rotor field, a stator coil is

energized, and the rotor is allowed to pull (opposite magnetic poles) into alignment, come to equilibrium, and stop. This action constitutes a “step.” Then the next coil in sequence is activated, resulting in another step. Designed to allow this to happen quickly, a stepper motor can then be operated without commutation as such; no position measurement is required. The distance travelled can be precisely controlled by counting the number of “steps,” and the motor is designed with a large number of magnetic poles for precise positioning. This simple scheme has found application in many space devices, including some CMG gimbal drives. However, this type of operation produces a broad vibration spectrum and is fairly power inefficient. The disturbance from such a spectrum is problematic because it is not readily attenuated with simple vibration-isolation techniques such as passive spring/damper devices.

One additional technology that is found in these devices is the “voice coil,” or “ironless armature” motor. A voice coil derives its name from its similarity to an amplified, electromagnetic audio speaker. This type of motor is used for high-speed applications, in which the separate windings must be commutated very quickly. As the time-varying stator magnetic fields of a conventional motor increase in frequency, problems arise with eddy currents that cannot be addressed using conventional laminations. Rather than exploiting the interaction of two magnetic fields, a voice-coil design directly uses the Lorentz force between a field and a current. As shown in Fig. 9.3, windings on an insulated bobbin are placed into the permanent magnet field of the rotor and commutated to obtain the necessary torque. The rotor design produces a uniform radial magnetic field, and coil current flows vertically through the field. The result is force directed out of the page and thus constitutes torque about the centerline of the motor.

The rotor field is constant in the rotor frame of reference; however, it is still rotating rapidly with respect to the stator. Care must therefore be taken to minimize leakage of the rotor field, and any material that can conduct eddy currents must be moved well away from the rotor field. For very high-speed motors, the care with which eddy-current losses are managed by design is critical to minimizing motor drag, which can easily result in excessive heat generation and power expenditure. Another key consideration in this type of motor is the thermal design. Unlike

Fig. 9.3 Ironless armature spin motor



other motors, the heat dissipated in the motor coils is being conducted through a bobbin made of a non-conductive material. In general, materials that do not conduct electrical current also do not conduct heat well. Thus this design must take particular care to provide adequate heat-conduction capability.

Regardless of the technology chosen, motors for space must be designed with the same concerns as any device for space. These concerns include avoiding materials that outgas in a vacuum, emphasizing conduction in thermal management, and robustness in the presence of launch vibration, particularly where small-gauge wiring is implemented. For these reasons, choosing an “off-the-shelf” motor is ill advised. Motors for space must be specified for the uniquely demanding space environment.

9.2 Sizing a DC Motor

This section offers general insights into the nature of motor sizing. This information is useful in understanding the general trends and design dependencies, and rapidly obtaining a rough idea of motor sizing for use in CMG design trades. For specific space-systems design, the best source of assistance is likely vendor data sheets and application engineers.

Motor sizing consists of two largely separable parts. One part is the mechanical design of the motor, i.e. the diameters and axial lengths of the rotor and stator, as shown in Fig. 9.4. These parameters size the permanent magnets, the amount of iron, and a weight allocation for copper based on the envelope available. Instead of

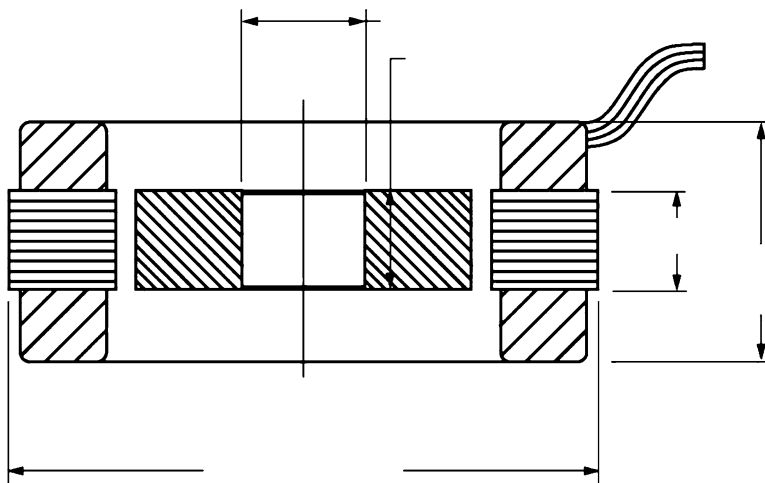


Fig. 9.4 Brushless DC motor mechanical design

going into detail on the trades available between length and diameter, this discussion simply assumes a typical ratio. The sizing of the motor determines the amount of torque it can produce.

Second, the copper allocation is detailed into a coil design by the choice of the wire gauge and number of turns. The motor torque constant K_T (ft-lb per amp) is affected by this choice.

There are, perhaps, as many ways to design a motor as there are designers. Each vendor has its own unique approach to the details. However, the laws of physics allow us to get the big picture without going into much detail. For example, we can estimate the power dissipation and weight of a motor knowing only the required torque. This is because the torque required directly influences the magnetic circuit design. Motors are often scored by their “motor constant,” known as K_M , which is expressed in ft-lb/ \sqrt{W} . This constant expresses the amount of torque the motor can produce for a given amount of power dissipated as heat. K_M depends upon the magnetic flux density, pole cross-sections, etc. It can be increased (thus dissipating less power) by increasing the weight of the motor (bigger magnets, larger poles), and, in general, this increase in K_M scales nearly linearly with weight. Therefore, we can expect that the “ K_M density,” K_{MD} , in ft-lb/ \sqrt{W} per lb would be a constant, over at least a fairly wide range of designs. For the class of motors typically found in momentum devices, a rule of thumb would be $K_{MD} = 0.07 \text{ ft-lb}/\sqrt{\text{W}}$ per lb. This rule assumes high quality magnets and optimized, unpackaged designs.

Another consideration in space motor sizing is the ability to conduct dissipated heat out of the device. Conventional wisdom has it that a certain number of Watts can be effectively transferred out of a motor (without excessive temperature rise) per pound of motor. In a small motor, less heat dissipation can be managed than a larger motor. This “power density,” K_{PD} , is expressed in Watts per pound. For the class of motors typically found in momentum devices, a rule of thumb would be $K_{PD} = 8 \text{ W/lb}$.

9.2.1 Sizing a Brushless DC Motor

Given these two constants K_{MD} and K_{PD} as guidelines, we can approximate the weight and power of a motor necessary to apply a particular torque. Using nothing more than dimensional analysis, we find that the weight of the motor must be:

$$W = \left(\frac{\tau}{K_{MD}\sqrt{K_{PD}}} \right)^{2/3} = \left(\frac{\text{ft-lb}}{\frac{\text{ft-lb}}{\sqrt{W} \text{ lb}} \sqrt{\frac{W}{\text{lb}}}} \right)^{2/3} = (\text{lb}^{3/2})^{2/3} = \text{lb} \quad (9.1)$$

and the power must be:

$$P_{\text{heat}} = \left(\frac{\tau K_{\text{PD}}}{K_{\text{MD}}} \right)^{2/3} = \left(\frac{\text{ft-lb} \frac{\text{W}}{\text{lb}}}{\frac{\text{ft-lb}}{\sqrt{\text{W lb}}}} \right)^{2/3} = (\text{W}^{3/2})^{2/3} = \text{W} \quad (9.2)$$

In the above, the power being calculated is the i^2R power dissipated in the motor coils as heat. The total electrical power drawn at the terminals includes mechanical power delivered to the load.

Equations (9.1) and (9.2) show that both weight and power increase as the 2/3 power of the required torque. Furthermore, neither of these quantities varies with how the coil is wound. These principles allow us to quickly approximate the cost of producing torque. If this cost is unacceptable, in some cases gearing can be employed to reduce the torque required.

9.2.2 Electrical

In the mechanical design equations above, an allocation is included in the weight for the copper wire. Next, we must take this copper and partition it into wire size and number of turns. This allocation dictates the resistance of the coil and the torque constant K_T (ft-lb/A). The fact that the same motor can be wound with different coils is evident in motor catalogs, where each motor size is available with different “dash numbers,” characterized by different K_T values.

If expressed in metric units of Nm/A, K_T has the same numerical value as the back-emf constant K_B , in Volts per rad/s. The reason for this identity derives from fundamental motor physics and is beyond the scope of this discussion. But as a result, increasing K_T has two direct effects. An increase means that it takes less current to produce a given torque, but it takes more voltage to overcome back-emf at a given speed. Generally, a given application has limited bus voltage. Therefore, the limit drives the decision. Starting from the spacecraft power bus, we must subtract the voltage drops related to power conditioning, drive transistors, wiring harness, etc. to arrive at the terminal voltage seen by the motor. In order to apply rated torque at rated speed, this available voltage must comply with

$$V > K_B\omega + iR = K_B\omega + \frac{\tau}{K_T}R = K_B\omega + \frac{\tau K_T}{K_M^2} \quad (9.3)$$

The previous equation uses the relationship below, which can be verified by dimensional analysis.

$$R = \left(\frac{K_T}{K_M} \right)^2 \quad (9.4)$$

In Eqs. (9.3) and (9.4), K_M is the motor constant itself, not the K_M density K_{MD} discussed earlier. This can be evaluated after the mechanical design phase because the weight is known.

Using Eq. (9.3) above, we choose a K_T that allows operation with the given bus voltage. This is the step where the required motor speed comes into play, as the back-emf is usually the dominant driver in required voltage. As a larger K_T implies less current to get the same torque, we might think increasing it would reduce power; but this is not the case. The resistance also changes, such that the power dissipated in the motor remains constant at the value derived in the previous section. Nevertheless, there are distinct advantages to a motor design with less current. Lower current simplifies the drive electronics, reduces power dissipation throughout the electronics and harnessing, reduces the weight of cabling, reduces EMI, etc. Therefore, the largest possible K_T should be chosen. If the motor requires high torque and high speed, the current increases, which drives the electronics design, and a point is eventually reached where the motor-design engineer must push back and require a higher system bus voltage. Machines with high torque and speed, i.e., mechanical power, cannot be expected to work efficiently, if at all, at low voltage.

Once K_T has been chosen, it is a simple matter to evaluate the coil resistance [from Eq. (9.4)], the current (from the definition of K_T), and any remaining parameters of interest. From this simple approach, we know enough about the motor to allocate a preliminary weight budget and flow requirements to the electronics design. We can even estimate the motor volume by assuming a reasonable ratio of iron and copper, the dominant weight drivers. To proceed beyond this point, it is advisable to work with a motor vendor applications engineer.

9.2.3 Numerical Example

Example 9.1. Suppose we are given the following requirements: design a motor that must produce 0.75 ft-lb at 30 rad/s. Assume that 20 V is available at the terminals of the motor. Assume $K_{MD} = 0.07 \text{ ft-lb}/\sqrt{\text{W}}/\text{lb}$, and $K_{PD} = 8 \text{ W/lb}$.

$$W = \left(\frac{\tau}{K_{MD}\sqrt{K_{PD}}} \right)^{2/3} = \left(\frac{0.75}{0.07\sqrt{8}} \right)^{2/3} = 2.4 \text{ lb} \quad (9.5)$$

$$P_{\text{heat}} = \left(\frac{\tau K_{PD}}{K_{MD}} \right)^{2/3} = \left(\frac{0.75(8)}{0.07} \right)^{2/3} = 19.4 \text{ W} \quad (9.6)$$

$$K_M = K_{MD}W = 0.07(2.4) = 0.17 \frac{\text{ft-lb}}{\sqrt{\text{W}}} \quad (9.7)$$

(continued)

Example 9.1 (continued)

Next, we solve Eq. (9.3) for K_T , getting

$$K_T = \frac{V}{\frac{4.448(12)}{39.37}\omega + \frac{\tau}{K_M^2}} = 0.3 \frac{\text{ft-lb}}{\text{A}} \quad (9.8)$$

$$i = \frac{\tau}{K_T} = \frac{0.75}{3} = 2.5 \text{ A} \quad (9.9)$$

$$R = \left(\frac{K_T}{K_M} \right)^2 = \left(\frac{0.3}{0.17} \right)^2 = 3.1 \Omega \quad (9.10)$$

Note that the heat power is $i^2 R = 2.52^2 \times 3.1 = 19.4 \text{ W}$, as expected. The total power drawn by the motor when delivering the spec torque at the spec speed includes both the power dissipated as heat, and the mechanical power delivered to the load (torque times speed, in appropriate units). So,

$$P_{\text{Total}} = 19.4 + 0.75 \left(\frac{4.448(12)}{39.37} \right) 30 = 50 \text{ W} \quad (9.11)$$

If we consider this result from the motor terminal perspective, the total power should be voltage times current = $20 \times 2.5 = 50 \text{ W}$.

If we now consult some vendor data sheets for high quality brushless DC motors, we should be able to find designs that are similar to this. Bear in mind that this approach provides only a rough approximation. In the final design, one must include margins for manufacturing tolerances, variations with temperature and life, etc.

9.3 Chapter Summary

This chapter discussed the various motor technologies found in spaceborne momentum systems. Simple equations were developed for rough sizing studies and rules of thumb for key constants were provided along with a numerical example. Detailed motor design should always be done in consultation with a motor vendor.

Chapter 10

Modeling Simulation and Test Beds

Ground-based validation of spaceborne momentum control systems and the attitude control systems that depend upon them offers a unique set of challenges. Computer simulations must include a variety of nonlinear phenomena found in momentum devices, which fundamentally limits the way these simulations can be architected. And because momentum systems rely on the conservation of angular momentum for proper operation, hardware-in-the-loop test facilities must reproduce the dynamics of a free body with great precision.

10.1 Math Modeling and Computer Simulation

Chapter 4 and Appendix A discuss the equations of motion for a spacecraft with an onboard momentum system. These equations can be of great value in understanding the physics of the problem, evaluating candidate control strategies, and other steps in the spacecraft-design process. As always in the development of such equations, various simplifications keep the scope of the development tractable. These simplifications include, for example, that all bodies are rigid, that all constraints are infinitely stiff, and that all rigid-body degrees of freedom are free and frictionless. When we reach the point in a development project where a time-domain computer simulation is justified, we must go beyond such simplifications. The intent of the effort is generally to create a tool that can evaluate the performance and/or stability of an intended design in the presence of real-world imperfections not included in these simple equations of motion. There are many aspects of momentum systems that directly impact overall vehicle performance that a simulation should address, for example:

- Friction, gear backlash, driver saturation, and other nonlinear effects
- Compliance in bearings and other joints between bodies
- Flexibility of the elements of the MCS, and the spacecraft itself

- Ripple and cogging effects in motors and other electromagnetics
- Induced vibrations from rotor balance and bearing eccentricities
- Gyroscopic coupling between flexible modes that can change both their frequency and mode shape

The following sections offer a proven approach to the architecture of such a nonlinear simulation. The examples shown depict MATLAB/Simulink models. However, the basic principles are suitable for any general-purpose computer-modeling environment. These Simulink diagrams closely resemble general feedback-control block diagrams; so, a reader familiar with feedback controls ought to be able to interpret them regardless of experience with MATLAB.

10.1.1 First Principles

When introduced into the model, many of the effects discussed above appear at the interfaces between rigid bodies and violate some of the simplifying assumptions of Chap. 4. As a result, those equations of motion cannot be used as the cornerstone of a precise time-domain model. Fortunately, it is not necessary to go back and attempt to include these effects in the derivation. Today's computers are fast enough to solve all of the complex interactions between bodies "on the fly," if we simply organize the model to allow it. Taking advantage of this capability requires a paradigm shift in which we abandon the instinct to perform complex multibody derivations and code the results. Instead, we should model each body separately, in a way that presumes nothing about what it will be connected to. Then we model the connections among the bodies, presuming no knowledge about what they are connecting. This is the method of "first principles" modeling. In fact, assembling such a model is generally easier and faster because it tends to be modular. And because each of the building blocks is a fairly simple model, the incidence of human error is reduced, along with debug time (or the risk of incorrect results). The method of first principles can be employed for models of any fidelity. For example, a component can be modeled as a rigid body with one degree of freedom, or three, or six, depending on the rigid-body constraints known to be present. Or it could be modeled as a flexible body with arbitrarily many degrees of freedom. With some care in bookkeeping, models with differing fidelity can be simply dropped into a simulation depending upon the needs of the analysis.

10.1.2 What Is the Question?

One of the most common mistakes in creating a computer model of a system is doing so without a clear understanding of its purpose. A model is created to answer certain questions, and these questions must be allowed to dictate the scope and fidelity of

the model. Today's computers are fast, but there are still practical limits. Here are some examples of how the question drives the model:

- A momentum system model is to be created as part of a spacecraft model to study slew times through day-in-the-life representations of targeting scenarios. This model needs to run hours of simulation time. So, in the case of current desktop computers, it is not practical for the integration step time to be a microsecond, or for bodies to have thousands of degrees of freedom. The runs would simply take too long. Phenomena producing poles or action at frequencies well beyond the bandwidth of the ACS under study should be neglected (e.g., above 20 Hz). Things that might have a direct effect on slew times like limits on rate, acceleration, jerk, actuator current, etc., should be included. Things that bear more on inner-loop stability and fine performance can be neglected.
- A momentum system model is to be assembled to verify the stability of the gimbal rate loop design in a CMG system. In this case, a run of only a few seconds is more than enough, but higher frequencies are involved. If, for example, a discrete-time loop is closed in a gate array, the sample time of the loop might be 10 kHz and has to be modeled. In general, subtleties like motor current loops and commutation can be neglected. Interactions with flexible modes of the surrounding structure are possible, and therefore body flexibility should be included. Effects of nonlinearities like friction and backlash can impact stability. Certain saturation limits might be important, but many can be neglected since stability analyses are usually performed in the domain of "small signals." Sources of vibration are forcing functions but do not directly affect loop stability. Therefore, they can be neglected.
- A model is to be assembled to verify that a high-speed three-phase wye spin-motor drive system will function properly at the rated speed. In this case, the model must incorporate the motor-coil inductance, pulse-width modulator, commutation, and current loop. We are studying sub-microsecond phenomena, but simulating only a handful of commutation cycles is enough to determine if the driver is working. At these frequencies the loops closed around the motor, and even the body flexible modes are so slow as to be negligible. So, we can focus only on the motor.

These examples illustrate that two key aspects of a simulation should be determined by the question being asked. First, the fidelity of the model: what degrees of freedom and phenomena must be included? The second aspect is the integration time of the model: what frequencies are important? A day may come when computers are so fast we can just model everything. But for now, we must use engineering judgment to consider these questions carefully.

10.1.3 Modularity

From the discussion in the previous section, one might be quick to conclude that the wide range of possible questions will result in the creation of many different models. Indeed, this is often the case. However, in today's reality of limited resources, it behooves us to be efficient and try to minimize such replication. One of the most compelling reasons for doing so is configuration control. At the same time these simulations are being assembled and used, the hardware design itself is often maturing. When changes happen, it becomes a logistical nightmare to maintain a large number of separate models in lockstep. But the penalty for not doing so is different teams on a spacecraft program all analyzing different versions of the design, likely leading to errors and delaying the completion of the work. The solution to this dilemma is to construct modular building blocks with varying levels of fidelity, so that all of the different models on a program can be assembled from the same blocks. When a change comes, the affected blocks can be updated in a common library and will flow to the various analyses as they are performed. Modeling by first principles facilitates modularity because each "block" is modeled without knowledge of the rest of the model. All that is necessary is some initial agreement on interfaces and architecture.

10.1.4 Choices of States

Consider a simple example of two single-degree-of-freedom masses connected by parallel spring and damper elements. Intuitively, we understand that this system has four states: the rate and position of each body. The block diagram of Fig. 10.1 illustrates how such a model might be connected. This topology can be substantially simplified if, as is often the case, we do not really need to know the positions of some bodies. Consider the example of Fig. 10.2. In this case, the topology of

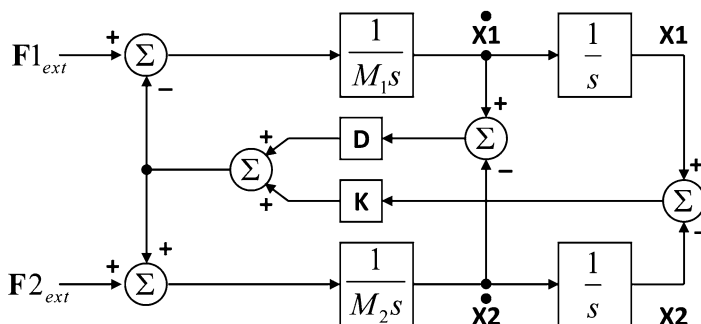


Fig. 10.1 Two-mass system

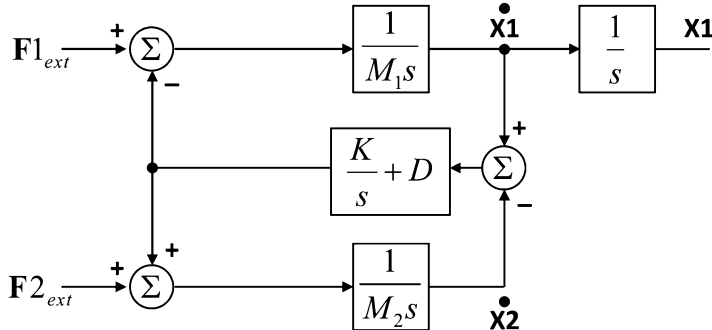


Fig. 10.2 Two-mass system feeding back rates only

the interconnecting bodies is much cleaner. The state in the spring model “ K/s ” integrates the displacement between two bodies, rather than the position of the second body. In all other respects, the models are identical. In multibody models that involve transformations among various coordinate systems, calculations of moment arms from points of force application, etc., the need to perform all of these calculations on both positions and rates as in Fig. 10.1 becomes a burden on computational resources. We therefore find the approach of Fig. 10.2 to be a useful means of constructing multibody models. Bodies take as inputs forces and/or torques, and they output rates. Connections, such as springs and dampers, take rates as inputs and output the resulting forces and/or torques that the connections will apply between the two bodies. Interconnecting these building blocks becomes trivial. Body positions are integrated only when required as outputs.

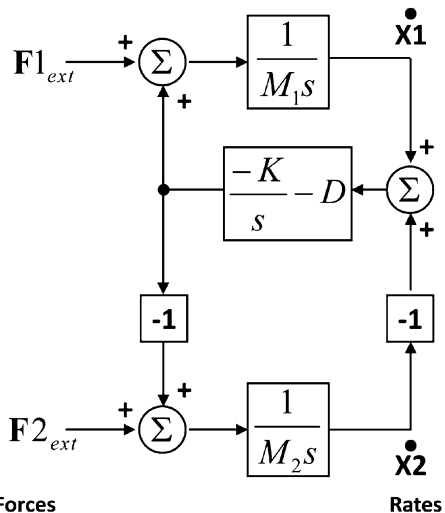
10.1.5 Polarities

One of the most common errors in modeling is incorrect signs on summations. By adhering to a simple set of rules, these errors can be all but eliminated.

- Positive forces or torques cause positive rate on a body.
- Positive differential rate into a passive attachment causes negative forces/torques, such as in Hooke’s Law, $F = -KX$.
- All forces/torques and rates add positively.
- Minus signs are placed between an attachment model and one of the two bodies, suggesting action/reaction. The choice is arbitrary in the sense that either can represent physically correct behavior. The choice merely defines whether positive displacement of the attachment is extension or compression.

An example of this approach is shown in Fig. 10.3. By definition, all feedback loops closed in such an architecture have either one or three minus signs, indicating that they are stable.

Fig. 10.3 Managing polarities



10.1.6 Body Models

As above, the model of a single body takes as inputs forces and/or torques, and it outputs rates. The rigid body can be modeled with anywhere from one to six degrees of freedom, depending upon the needs of the model. Furthermore, the rotational degrees of freedom can be constrained to small angles, or allowed to rotate freely. The small-angle approximation allows independent state integrations on each degree of freedom according to $\tau = J\alpha$. Without this approximation, the model must utilize the complete equations that capture the rotating-frame effects, i.e., Euler's Equation and the Transport Theorem, for all six degrees of freedom. Furthermore, if position information is required, it must be done using quaternion integration or some other non-singular attitude representation. While it is customary to model the body as located at its center of mass, in its own body-fixed coordinate system, it is convenient to express the inputs (F, τ) and outputs (rates) of the body model in the coordinate system of the attachments to other bodies or forces, at the points where they attach. This is illustrated in Fig. 10.4.

Transformations that include both the change in coordinates and the moment arm from CG to attachment point can be expressed as a 6×6 matrix, as shown in Eq. (10.1).

$$\begin{bmatrix} F \\ \tau \end{bmatrix}_{CG} = M \begin{bmatrix} F \\ \tau \end{bmatrix}_P \quad (10.1)$$

where:

$$M = \begin{bmatrix} I_{3 \times 3} & 0_{3 \times 3} \\ R^T & I_{3 \times 3} \end{bmatrix} \begin{bmatrix} A_P^{CG} & 0_{3 \times 3} \\ 0_{3 \times 3} & A_P^{CG} \end{bmatrix}$$

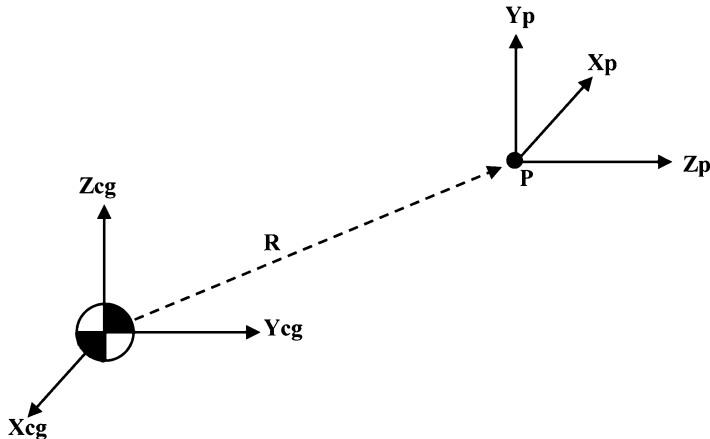


Fig. 10.4 Reconciling forces and torques applied at an attachment point “P”

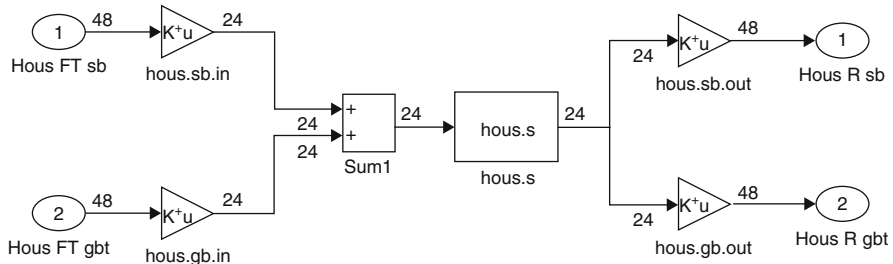


Fig. 10.5 Example modular body model

where: A_P^{CG} is the 3×3 transformation from the P frame to CG frame, and R^\times is the 3×3 skew symmetric “tilde” matrix for the column vector R . Figure 10.5 shows an example that illustrates the suggested approach to a modular body model. The block at the center of the model represents the vacuum housing of the four conventional CMGs in an array. The representation is a state-space linear system stored in the variable “hous.s.” Each housing is modeled at its center of mass as a small-angle rigid body with six degrees of freedom. Therefore, the state-space system has 24 inputs, outputs, and states. This state-space model is simply the concatenation of many $1/M_s$ and $1/J_s$ integrations. This body attaches to the rest of the model at four points: two spin bearings and two gimbal bearings. Each attachment is modeled with six degrees of freedom, thus a total of 96 inputs. The 24×48 input transformation matrices are assembled by block concatenation of the M matrices from Eq. (10.1) for the spin bearing and gimbal bearing attachment points, respectively. They transform the forces and torques applied at each attachment point to the body frame at the body CG, where all such inputs are summed. Each of the 48×24 output matrices is the

transpose of the analogous input matrix, and they transform the body *CG* rates to the rates at each attachment point, in the attachment coordinate system. This simple, modular construction is easy to assemble with minimal errors.

If the body is to be modeled as flexible, the recommended approach is to split the body into rigid states and flexible states using modal superposition. The rigid states can be modeled using either small- or large-angle attitude representations. The flexible model is obtained by a Craig–Bampton [1] extraction from a NASTRAN model or other flexible representation, using the boundary nodes required for the inputs and outputs. For the flexible model, the transformations are buried in the NASTRAN model. The inputs are not summed but applied directly at the individual model nodes. The outputs of the flexible model should be at the same points, in the same coordinate system as the rigid model, allowing the modal displacement rates to be added to the outputs of the rigid model.

10.1.7 Attachment Models

The model of a single attachment should take as inputs the rates of the bodies being attached, and it should output forces and/or torques. The inputs and outputs should already be in the chosen coordinates of the attachment model after conversion by the body models, allowing quantities to be directly combined without further coordinate transformation. The attachment can be modeled with anywhere from one to six degrees of freedom, depending upon the needs of the model. For example, a simple hexapod isolator model might use only a single degree of freedom for each isolator: force and displacement along the isolator axis. The key elements of this module are the representations of $K/s + D$, and the differential rates using balanced negations (reaction) as discussed earlier in Sects. 10.1.4 and 10.1.5. To that basic model, we then add any relevant nonlinear elements and other complications. Figure 10.6 models the eight spin bearings (two each) in the four CMGs of an array. They are modeled in six degrees of freedom, producing the 48 signals shown. Note that the output forces and torques from the state-space representation of $K/s + D$ (sb.s) act on the rotor and react on the vacuum housing. In the state-space model sb.s, the values for K and D are zero for the bearing spin axes. Instead, the four spin torques are calculated at the bottom of the model and added through the “*toRz*” matrix. The spin axis torques include the spin motor itself, models of Coulomb and viscous drag, and a model of how the drag varies when the bearings are subjected to load (such as during CMG torquing). For the spin bearings of a CMG, the Coulomb drag is essentially a constant. However for RWA spin bearings (or CMG gimbal bearings) a better model is required. The Dahl friction model is recommended in these cases (Dahl [2]). Finally, we see a model of spin-bearing disturbances due to bearing eccentricities. This model takes spin speed as input and produces a comb of sinusoids at various frequencies representing the bearing tones. Note that bearing eccentricities are properly modeled as forced displacements across the interface because the bearings are so much stiffer than the surrounding structure that they

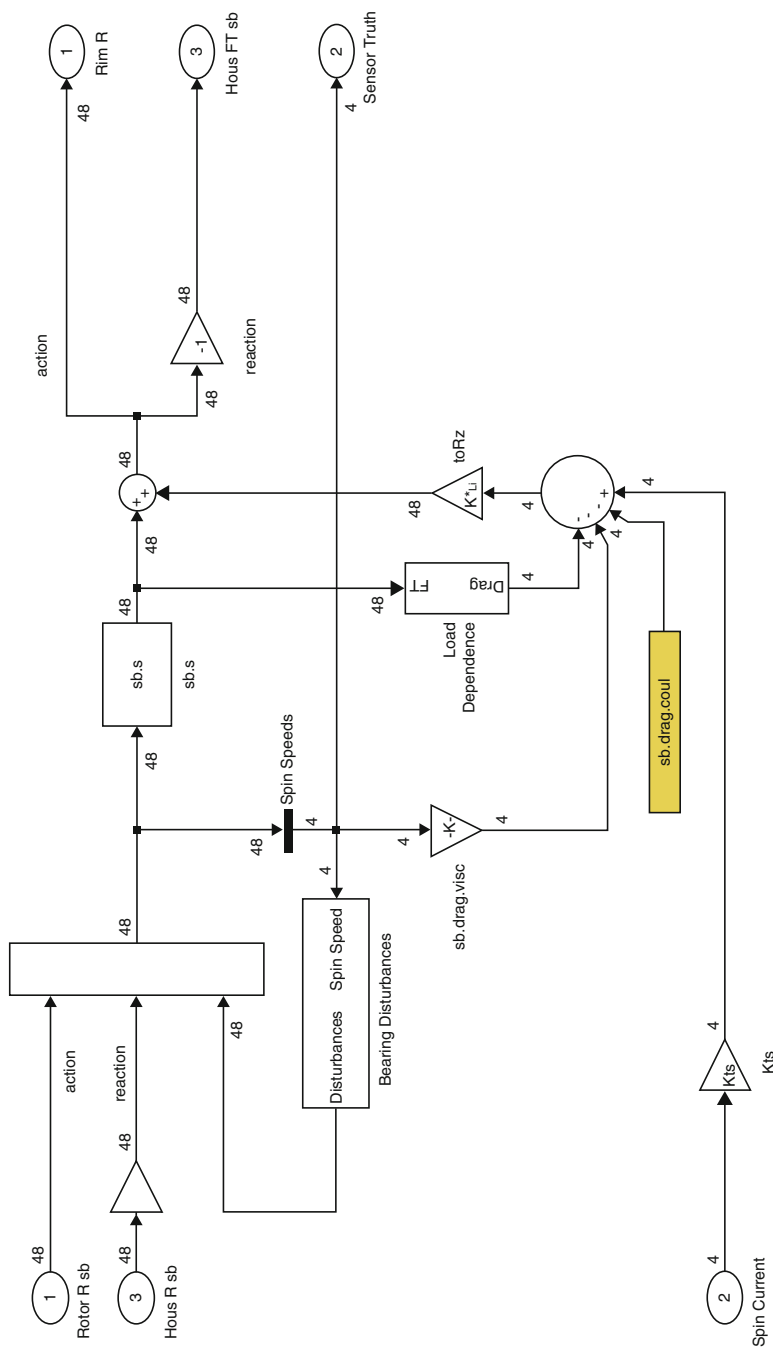


Fig. 10.6 Example modular attachment model

might as well be rigid constraints. Modeled in this way, the actual forces and torques that arise from the eccentricity depend on the surrounding stiffness, rather than just the bearings themselves.

10.1.8 Integration

Using building blocks such as those illustrated above, very high-fidelity representations of MCS-based attitude control systems can be produced using the architecture described herein. Such a model can be easily reduced or enhanced when necessary by changing the fidelity of the blocks. In keeping with the modular philosophy, the only place where any gyroscopic terms are found is in the model of the rotor body. All resulting gyroscopic effects, such as CMG output torque amplification, gimbal back torque due to precession when the vehicle is in motion, augmented gimbal inertia, and coupling of flex modes simply arise as the simulation solves the interactions among the modular bodies. The rotor can be modeled simply as a full, large-angle body that spins, but integrating the resulting motion would use substantial computer resources without a meaningful increase in fidelity. In general, it is advisable to use the simplifying assumption that the rotor spin speed is much greater than the angular velocity in other axes, allowing a simple gyroscopic coupling matrix to be derived and combined with a simpler body model. In this matrix, the rotor's angular momentum is taken to be the spin axis inertia times the rotor's spin speed. Numerical integration of the rotor's spin axis angular state need not be performed.

10.2 Hardware-in-the-Loop Test Beds

While modern computer simulations offer more risk reduction than ever before, there is no substitute for working with hardware. However, performing ground testing of MCS-based attitude control systems is particularly challenging. Momentum systems rely on the conservation of angular momentum within a closed system to exchange momentum with the spacecraft and affect control torques. As a result, hardware-in-the-loop test facilities must provide a surrogate spacecraft that approaches a truly closed system, i.e., no external torques. The quality with which this objective is achieved is the single overriding characteristic that defines the success of a test facility. Various technologies exist to simulate zero gravity, including such options as buoyant support or complex offloading mechanisms. But the most popular is the air bearing. This technology, familiar to anyone who has played air hockey, is simple, inexpensive, and can provide a nearly perfect zero-friction suspension. Sputnik launched in 1957. Explorer-1 launched in 1958.

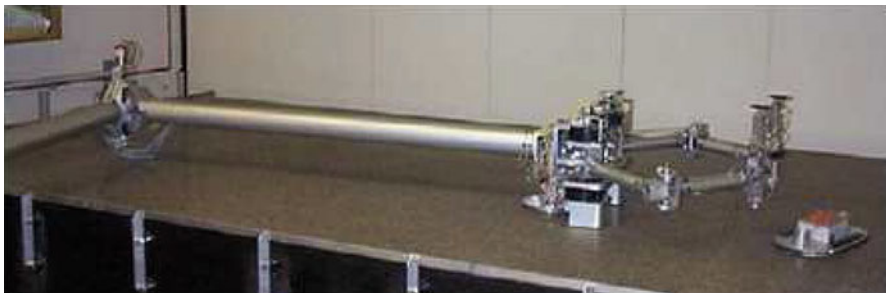
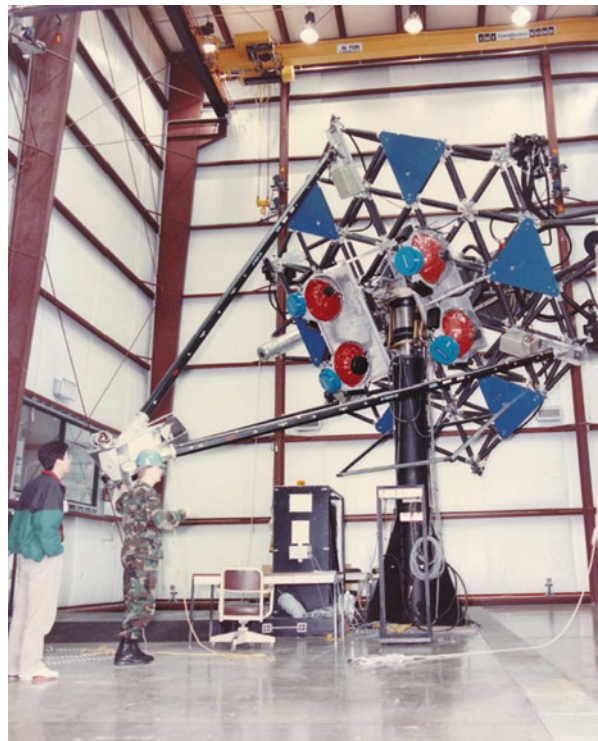


Fig. 10.7 Stanford's two-link manipulator arm (Image Courtesy of NASA)

The earliest air-bearing spacecraft simulator is documented in 1960. Truly these systems have played an integral role in verifying space technology since the beginnings of space exploration (Schwartz et al. [3]). Planar air bearings provide an ideal test bed for simulating two-vehicle dynamics, with two translational degrees of freedom and one rotational. Control techniques for relative orbital maneuvers and formation flying, rendezvous and docking can be fully developed and tested prior to launch. An example of a planar test bed is the Two-Link Manipulator Arm in Stanford University's Aerospace Robotics Laboratory, shown in Fig. 10.7. The Air Force Research Laboratory (AFRL) has been using large spherical air-bearing spacecraft simulators since the late 1980s. One of the first of these simulators was known as Advanced Structural Technology Research Experiment (ASTREX). ASTREX, shown in Fig. 10.8, housed four large Honeywell CMGs and had a spherical air bearing capable of supporting approximately 15,000 lbs. The AFRL used it for studies in structural control and damping for spacecraft beam-director pointing. Since its use on ASTREX, this air bearing has been used on multiple project platforms such as the Flywheel Attitude Control and Energy Transmission System (FACETS) and the mini-Agile Multi-Purpose Satellite Simulator (mini-AMPSS) (see Chap. 6). The air bearing is currently being used to test state-of-the-art spacecraft fault detection and isolation algorithms as well as fault-tolerant control techniques at the AFRL Space Vehicles Directorate at Kirtland AFB in New Mexico. Some test beds use rotational air bearings atop a planar carrier to achieve six degrees of freedom. An example of such a facility is Marshall Space Flight Center's "Flight Robotics Laboratory," shown in Fig. 10.9. The lab has a 44×86 ft precision flat floor. The Air Bearing Spacecraft Simulator used on the planar floor provides a 400 lb payload six degree-of-freedom motion via a floating spherical air bearing coupled with a cylindrical lift. While such a sophisticated facility can enable certain specific experiments, six degrees of freedom are not necessary for complete studies of an MCS-based attitude control system.

Fig. 10.8 AFRL ASTREX spacecraft simulator



10.2.1 Precision Rotational Air-Bearing Systems

Rigid-body studies of MCS-based attitude control systems require only the three rotational degrees of freedom. Flexible behaviors can be incorporated in such test beds if the moving components conform to the rules of gyrostats discussed in Chap. 4. In any case, external torques must be limited to the greatest extent possible. The scope of this problem is well understood. An important paper on the subject was delivered by G. Allen Smith at the Role of Simulation in Space Technology conference held at Virginia Tech in 1964. Smith presented a description of several systems, along with an overview of the torques which act on the rotor of an air bearing. Smith defined four classes of disturbance torques and listed particular sources for each group, as follows:

I. Torques Arising from Platform

- Static Unbalance
- Dynamic Unbalance
- Anisoelasticity
- Material Instability (stress, temperature, humidity, evaporation)

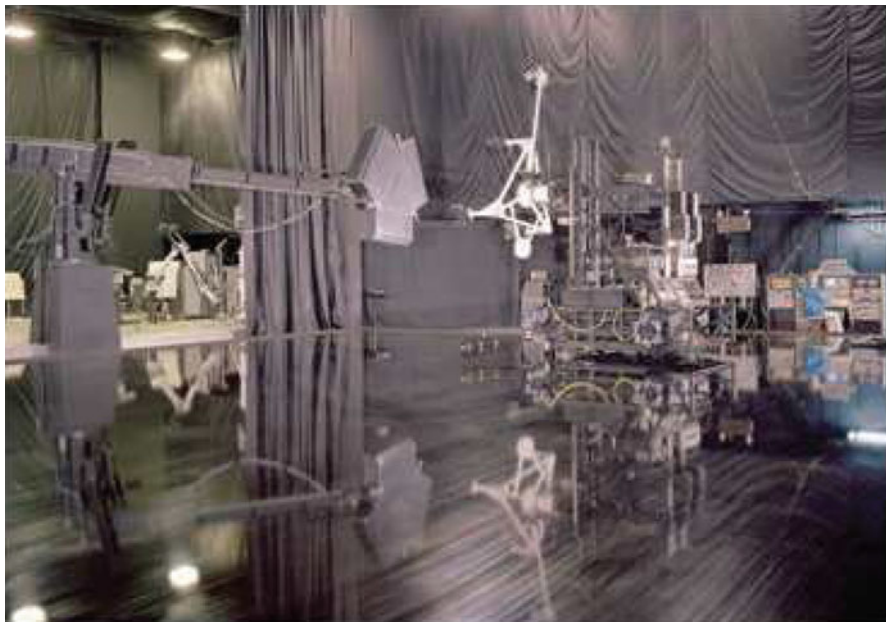


Fig. 10.9 MSFC's flight robotics laboratory (Image Courtesy of NASA)

- Gravity Gradient
- Equipment Motion (solenoids, relays)

II. Torques from Bearing

- Aerodynamic Turbine Effect
- Exhaust Air Impingement

III. Torques from Environment

- Air Damping
- Air Currents
- Magnetic Fields
- Vibration
- Radiation Pressure

IV. Torques from Test System

- Electrical Wire to Base
- Mass Shift in Bearings and Loose Fits
- Battery Discharge
- Reaction Jet Supply Discharge
- Replacement of Components

Most torques from groups I and IV can be mitigated through test bed design: well-designed structures outfitted with well-chosen components. Group II effects received more attention in the early development of air-bearing systems than they do now; although internal bearing effects may be important in the design and operation of industrial gas bearings, they impart a negligible effect upon most systems we are considering. Several facilities have developed large-scale means to mitigate environmental torques (group III). Thermal and air currents often cause the grossest effect and are simplest to eliminate: several NASA facilities are installed within vacuum chambers. The facility designed for the Boeing Company's Lunar Orbiter Attitude Control Simulator could not make use of this solution, as it was piloted. Instead, the room design included full air circulation and thermal control. Further, the system was mounted on a 90,000 lb concrete slab supported by seven air springs; thus the system was effectively isolated from seismic effects. Marshall Space Flight Center installed one of their systems within a set of Helmholtz coils in order to cancel the effect of the terrestrial magnetic field on the payload.

10.2.2 Anisoelasticity

Perhaps the most difficult of the sources listed above is anisoelasticity. This effect, while relatively unknown, directly influences balance stability as the test article rotates. To understand it, one needs only recognize that the test article cannot be infinitely stiff. As a result, there is some sag between the support point and the test article's extremities due to gravity. How much sag exists depends on the distribution of mass and stiffness in the direction of the gravity load. If the stiffness of the structure varies with the direction of loading, as most do, it is said to be "anisoelastic." The center of mass of such structures varies with attitude, and the changing mass center introduces a secular pendulum-like disturbance torque. Consider the simple structure of Fig. 10.10. At left, the large dumbbell is sagging. So, an additional mass is added above the pivot (red) to raise the CG and balance the system. At right, after rotating clockwise 90°, the large dumbbell, which is much stiffer in this direction, is no longer bending. The balance mass that compensated for the sag in the initial orientation now makes the system asymmetric (and sags itself), resulting in both horizontal and vertical CG shifts.

10.2.3 Active Mass Balancing

The effects of anisoelasticity prevent a physically realizable structure in gravity from remaining passively, perfectly balanced at all attitudes. The solution is an active system that can move mass to make CG adjustments under computer control. One facility which makes use of this technique is Honeywell's Momentum Control System test bed, shown in Fig. 10.11 (Hamilton [4]). This facility features three

servo-driven ballscrew linear stage that move small blocks of aluminum along rails. This arrangement allows the test bed's mass center to be adjusted in three degrees of freedom. The paths of motion of the masses are directed at the center of rotation of the spherical air bearing so that the acceleration of the masses represents virtually no torque. These masses eliminate torque due to mass-center offset. They actively place the mass center of this 1400 kg test bed to within a few microns of the air-bearing's center of rotation.

10.2.4 Controlling the Mass-Balancing System

When contemplating the design of a control system using these actuators, the first and foremost requirement must be to prevent the mass-balancing system (MBS) from interacting with the ACS under test. The actions of the MBS must be transparent so as not to interfere with or corrupt the experiment being performed on the test bed. One key step towards this goal is the choice of feedback for the controls. We recall that a key goal of the test bed is to behave as a closed system for the conservation of angular momentum. This is necessary for proper operation and testing of MCS-based systems. It follows, therefore, that the purpose of the MBS is to make the net angular momentum of the test bed system remain constant in the inertial frame (implying a lack of external torque). The net angular momentum of the test bed vehicle consists of the sum of the momentum vectors of the vehicle itself, and all of the CMGs mounted thereon. We can calculate this vector from the following information, all of which is readily available:

- Vehicle rate (from the rate gyros onboard)
- Vehicle inertia
- CMG wheel speeds (from the CMG tachometer telemetry)
- CMG wheel inertias
- CMG gimbal angles (from the CMG resolver telemetry)

It is important to note the significance of this principle. It means we can develop a quantity to be used as feedback for the MBS system that is entirely based on the

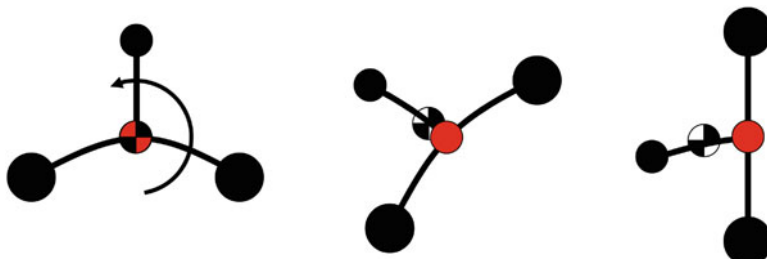


Fig. 10.10 Simple anisoelastic structure



Fig. 10.11 Honeywell's momentum control system test bed

state of the hardware. No information from the ACS is required. The ACS need not even be closed and operating. The feedback quantity is always valid, whether the system is quiescent or in the middle of a slew. Under ideal conditions, actions of the ACS do not change the quantity, because the change of the CMG array momentum will be equal and opposite the change of the vehicle momentum. This again underscores the independence of the MBS and ACS controls. Figure 10.12 illustrates the architecture of the MBS controls. It shows the development of the rate of change of net vehicle momentum $\dot{\mathbf{H}}$, which the central path tries to drive to zero. Having calculated a desired rate of change for the external torque, the algorithm uses a cross-product with the gravity vector to determine the desired rate of change

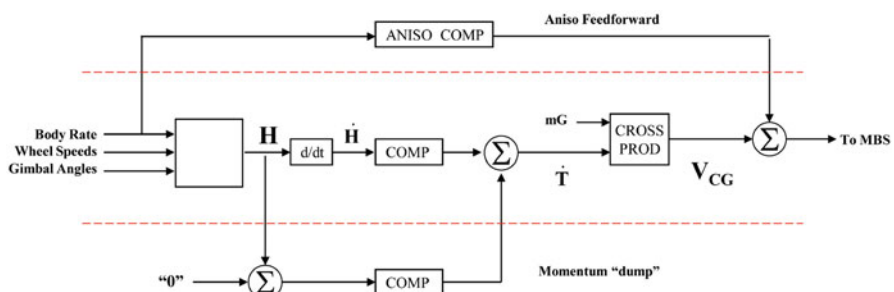


Fig. 10.12 Control of a mass-balance system

of the body CG. This command then goes to the MBS actuators. We wish to keep the bandwidth of this loop closure low (tenths of Hz). As such, it does a fairly poor job at rejecting rapidly changing external torques, such as may arise during an agile slew. Turning to a common controls solution, we have added a “feedforward” path at the top of Fig. 10.12. This path anticipates the needed correction as soon as the body begins to move and can apply the correction with the bandwidth of the MBS actuators. Finally, an additional feature is evident at the bottom of Fig. 10.12. When working with momentum systems in the lab, just as in space, it is useful to have a way to “dump” any momentum accumulated over time. The MBS controls described thus far have only the objective of preventing the net momentum from changing. This additional loop closure acts to drive the net momentum to zero, thus providing the dumping function. This functionality should be provided at a bandwidth much lower than that of the main balance loop for stability, and it can easily be removed by opening the loop. For clarity and simplicity in this description, only the fundamental philosophy of an MBS control system has been provided. Someone working in the field will note, for example, that we make no distinction between the moving body frame (on which the MBS rides) and the lab frame (where the vector mg is constant). Furthermore, effects due to the rotation of the Earth are neglected here, an omission that is justified because of the significant difference in frequency content involved. As such, we take momentum to be conserved in the lab frame.

10.3 Chapter Summary

This chapter has discussed methods used in testing and validation of MCS-based attitude control systems, both in computer simulations and hardware-in-the-loop tests. A proven architecture for computer modeling of these nonlinear devices has been offered. The architecture employs first-principles methods, and a disciplined approach to the choice of states, placement of negation, and organization of the model. The approach lends itself to the inclusion of nonlinear elements where necessary throughout the model, and avoids the violation of any assumptions that might have been made had pre-computed multibody equations of motion been used. The preferred method for hardware-in-the-loop testing of MCS-based systems was shown to be the three degree-of-freedom air-bearing suspension. The most difficult challenge in creating such a test facility is the effect of structural anisoelasticity on mass balance in gravity. A method for overcoming this problem using an active system was described.

References

1. M. Bampton, R. Craig Jr., Coupling of substructures for dynamic analyses. *AIAA J.* **6**(7), 1313 (1968)
2. P. Dahl, A solid friction model. Technical Report, Aerospace Corporation Report TOR-158(3107-18), 1968

3. J. Schwartz, M. Peck, C. Hall, Historical review of air-bearing spacecraft simulators. *AIAA J. Guid. Control. Dyn.* **26**(4), 513 (2003)
4. B. Hamilton, Honeywell's momentum control system testbed, in *AAS Advances in the Astronautical Sciences*, vol. 151, 2014

Appendix A

Extended Equations of Motion for Spacecraft with CMGs

It is typically assumed when the subject of dynamics is taught that the origin of a system's mass properties, and angular and linear momenta are understood. However, without understanding of the true origin of these characteristics of a system, knowing when terms from the derivation of the equations of motion can be neglected becomes unclear.

The purpose of this chapter is to treat dynamics of a spacecraft with an array of CMGs all the way from the particle, to component, to system angular momenta and from here, rigorously find the generic vector equations of motion. The equations of motion will be derived, making note of steps left out in most of the literature. This appendix is not meant to stray away from or repeat material in the Dynamics chapter, but to provide the analytics behind the whole process of deriving the equations of motion of the discussed multi-body system and its corresponding angular momenta and inertias. Also, from this appendix, the reader should be able to follow the steps needed to derive more complex multi-body system equations of motion. Except for some needed additional notation, the notation will be the same notation adopted from Chap. 4.

We would like to acknowledge Prof Norman Fitz-Coy at the University of Florida from whose notes, much of the mass integral equations of motion in this appendix are directly derived and expanded upon.

A.1 It Begins with A Particle

Imagine that all matter is made up of particles of a zero volume and inertia that contain mass. A set of these particles (at least 2) creates a system. With a system, there is a center of mass and even an effective inertia. Imagine a barbell with a massless bar shown in Fig. A.1.

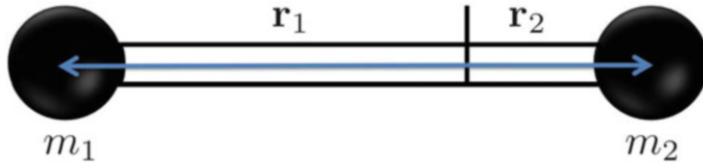


Fig. A.1 Two-particle mass Barbell

The center of mass position is equal to the ratio of the masses of the particles multiplied by the vector distance of the bar from a datum position (invariant to where that datum is chosen), over all masses.

$$R_C = \frac{\sum_{i=1}^n m_i \mathbf{r}_i}{\sum_{i=1}^n m_i} \quad (\text{A.1})$$

where m_i are the masses of the n particles at position vectors, \mathbf{r}_i from the datum position and the products $m_i r_i$ are known as the first mass moments. Now if the number of particles $n \rightarrow \infty$, and a constraint exists so the distances between all of these particles are fixed, a rigid body is formed.

A.2 Components

A system may contain many components, and some that may or may not be a rigid body (e.g., nonempty propellant tank is not a rigid body), contains a continuum of particles attached together that are bound together by internal forces. If we take an integral with respect to the differential mass over a continuum of the body, we get its mass

$$m_B = \int_B dm \quad (\text{A.2})$$

Now the equation for the center of mass position of a body is analogous to what was shown in Eq. (A.1), except for a continuum of particles,

$$R_C = \frac{\int_B \rho dm}{\int_B dm} \quad (\text{A.3})$$

The term $\int_B \rho dm$ is known as the first mass moment of a body B and it is equal to zero whenever the datum chosen for measurement of the particles' locations is the center of mass. In general, spacecraft are separated into separate subsystems, and these subsystems are made up of separate components. For example, a typical spacecraft will have the following subsystems or main elements:

- Communications and Ground Station Network
- Command and Data Handling
- Electrical Power System
- Propulsion
- Structures, Thermal, and Health Monitoring
- Payload
- Orbit control and trajectory generation
- Attitude Determination and Control

Within the attitude determination and control system (ADCS), there are sensors such as gyros, accelerometers, RWA and CMG rotor and gimbal encoders and hall sensors, star trackers, horizon sensors, magnetometers, etc. As for actuators, the ADCS may contain magnet coils/torquers, RWAs, CMGs, and/or thrusters.

For a spacecraft hosting an array of CMGs, you can think of three distinct components that make up the system. First you have the spacecraft bus that consists of the spacecraft and its subsystems excluding the CMGs. The CMGs themselves have two separate components or bodies, rotors and gimbals that hold the rotors. Therefore, we will derive the generic mass integral equations of motion considering the three distinct components of this system, spacecraft, gimbals, and rotors, respectively.

A.3 Reference Frames for Spacecraft n -CMG System

Consider the generic geometric diagram of a spacecraft consisting of a single CMG in Fig. A.2. The system is made up of three distinct components, a spacecraft bus consisting of all components that are not the CMGs (e.g., solar panel, propellant tank, payload, sensors, structure, and electronics) and the CMGs' rotor and gimbals.

The list of symbols at the beginning of the book lists the reference frames, masses, points, position and velocity vectors, masses, and inertias associated with Fig. A.2.

A.4 Spacecraft n -CMG Array Kinematic and Kinetic Equations of Motion

The kinematic equations of motion are those equations which show the relationship of the motion between all components of the systems with respect to the inertial frame without the presence of forces or torques. Therefore, these equations depend solely on the geometry (i.e., angles and positions) of all components in the system relative to each other and to the inertial frame. For rigid bodies, these equations are typically written in terms of quaternions, direction cosine matrices, or some other attitude representation and the corresponding angular velocity.

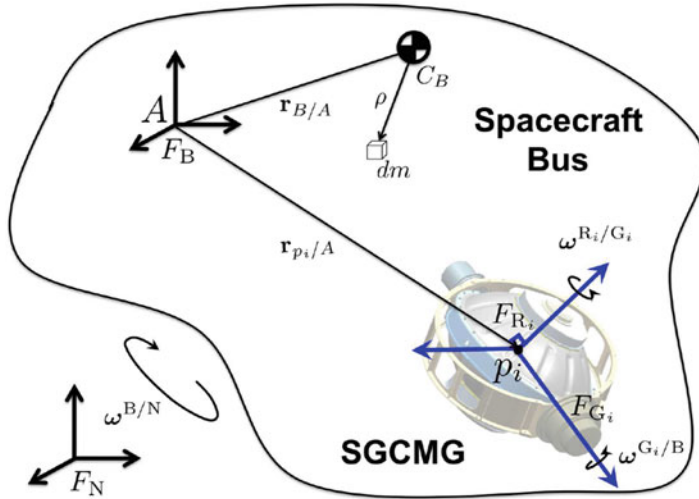


Fig. A.2 Spacecraft-CMG system geometric diagram

The kinetics equations, or the equations relating the spacecraft's rotational motion with respect to an internal or external torque are found by first deriving all components of angular momentum in the system.

A.4.1 *Spacecraft Angular Momentum*

The first and largest component of our system is the spacecraft bus. The angular momentum for a body X is of the form $\mathbf{h} = \int_X \mathbf{r} \times \mathbf{v} dm$. The mass integral for a spacecraft bus's angular momentum about point A is,

$$\begin{aligned}
 \mathbf{h}_A^B &= \int_B (\mathbf{r}_{B/A} + \boldsymbol{\rho}) \times [\mathbf{v}_A + \boldsymbol{\omega}_{B/N} \times (\mathbf{r}_{B/A} + \boldsymbol{\rho})] dm \\
 &= \int_B (\mathbf{r}_{B/A} + \boldsymbol{\rho}) dm \times \mathbf{v}_A + \int_B (\mathbf{r}_{B/A} + \boldsymbol{\rho}) \times [\boldsymbol{\omega}_{B/N} \times (\mathbf{r}_{B/A} + \boldsymbol{\rho})] dm \\
 &= \int_B \mathbf{r}_{B/A} dm \times \mathbf{v}_A + \int_B \boldsymbol{\rho} dm \times \mathbf{v}_A + \int_B \boldsymbol{\rho} \times (\boldsymbol{\omega}_{B/N} \times \boldsymbol{\rho}) dm \\
 &\quad + \int_B \mathbf{r}_{B/A} \times (\boldsymbol{\omega}_{B/N} \times \mathbf{r}_{B/A}) dm + \int_B \boldsymbol{\rho} \times (\boldsymbol{\omega}_{B/N} \times \mathbf{r}_{B/A}) dm \\
 &\quad + \int_B \mathbf{r}_{B/A} \times (\boldsymbol{\omega}_{B/N} \times \boldsymbol{\rho}) dm
 \end{aligned} \tag{A.4}$$

The position vector $\mathbf{r}_{B/A}$ can only be pulled out of the mass integral in Eq. (A.4) if it does not depend on the position of the differential masses, ρ . For example, fuel slosh or flexible appendages of the spacecraft bus may cause the center of mass position to be variable with respect to the spacecraft body B, for which the mass integral is defined.¹ Therefore, if the center of mass of the spacecraft is assumed to be fixed in body B the spacecraft angular momentum with respect to point A is

$$\begin{aligned}\mathbf{h}_A^B &= \int_B \mathbf{r}_{B/A} dm \times \mathbf{v}_A + \int_B \rho \times (\boldsymbol{\omega}_{B/N} \times \rho) dm \\ &\quad + \int_B \mathbf{r}_{B/A} \times (\boldsymbol{\omega}_{B/N} \times \mathbf{r}_{B/A}) dm \\ &= (\mathbf{J}_B^B + \mathbf{J}_A^B) \cdot \boldsymbol{\omega}_{B/N} + m_B \mathbf{r}_{B/A} \times \mathbf{v}_A\end{aligned}\quad (\text{A.5})$$

where the terms that are multiplied by $\int_B \rho dm = 0$ by the center of mass definition in Eq. (A.3) and the inertias \mathbf{J}_B^B and \mathbf{J}_A^B are

$$\begin{aligned}\mathbf{J}_B^B &= \int_B (\rho \cdot \rho \mathbb{1} - \rho \rho) dm \\ \mathbf{J}_A^B &= \int_B (\mathbf{r}_{B/A} \cdot \mathbf{r}_{B/A} \mathbb{1} - \mathbf{r}_{B/A} \mathbf{r}_{B/A}) dm\end{aligned}\quad (\text{A.6})$$

are found through the vector dyadic identity for any vectors \mathbf{a} , \mathbf{b} , and \mathbf{c} as

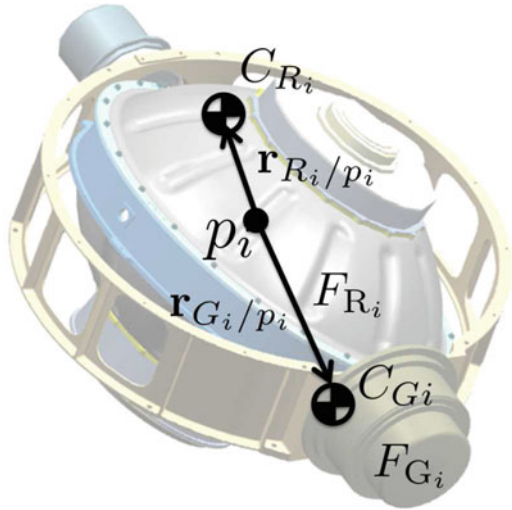
$$\mathbf{a} \times (\mathbf{b} \times \mathbf{a}) = (\mathbf{a} \cdot \mathbf{a} \mathbb{1} - \mathbf{a} \mathbf{a}) \cdot \mathbf{b} \quad (\text{A.7})$$

where $\mathbb{1}$ is known as the unit dyadic. The term \mathbf{J}_A^B is the parallel-axis inertia associated with the translation of the spacecraft center of mass from point A.

A word of caution in deriving angular momentum from mass integrals is to realize the contribution associated with each moment arm and velocity. In the case of Eqs. (A.5) and (A.6), the spacecraft center of mass and all of its particles translate with inertial velocities \mathbf{v}_A and its gyroscopic velocity component $\boldsymbol{\omega}_{B/N} \times (\mathbf{r}_{B/A} + \rho)$. This is not exactly the case for multiple components that are attached together, seen in Sects. A.4.2 and A.4.3.

¹Note that the coupled integral terms that contain the differential mass element vectors, ρ and the offset vectors are nonzero if the spacecraft bus has flexible appendage. These flexible effects are typically approximated by a summation of a finite number of modes for ρ .

Fig. A.3 A single CMG with center of mass offsets



A.4.2 CMG Gimbal Angular Momentum

Consider a single SGCMG as shown in Fig. A.3. We would like to derive the angular momentum of just the CMG gimbal neglecting its rotor for the moment. This is without any loss to the accuracy of the derivation because in the end, angular momenta are vectors and therefore can be added. The angular momentum of a single, SGCMG gimbal with respect to point A, is

$$\begin{aligned}
 \mathbf{h}_A^{G_i} &= \int_{G_i} (\mathbf{r}_{p_i/A} + \boldsymbol{\rho}) \times (\mathbf{v}_A + \boldsymbol{\omega}_{B/N} \times \mathbf{r}_{p_i/A}) dm \\
 &\quad + \int_{G_i} (\mathbf{r}_{G_i/p_i} + \boldsymbol{\rho}) \times [(\boldsymbol{\omega}_{B/N} + \boldsymbol{\omega}_{G_i/B}) \times (\mathbf{r}_{p_i/G_i} + \boldsymbol{\rho})] dm \\
 &= \int_{G_i} \mathbf{r}_{p_i/A} dm \times \mathbf{v}_A + \int_{G_i} \mathbf{r}_{p_i/A} \times (\boldsymbol{\omega}_{B/N} \times \mathbf{r}_{p_i/A}) dm \\
 &\quad + \int_{G_i} \boldsymbol{\rho} \times [(\boldsymbol{\omega}_{B/N} + \boldsymbol{\omega}_{G_i/B}) \times \boldsymbol{\rho}] dm \\
 &\quad + \int_{G_i} \mathbf{r}_{G_i/p_i} \times [(\boldsymbol{\omega}_{B/N} + \boldsymbol{\omega}_{G_i/B}) \times \mathbf{r}_{G_i/p_i}] dm \\
 &\quad + \int_{G_i} \mathbf{r}_{G_i/p_i} \times [(\boldsymbol{\omega}_{B/N} + \boldsymbol{\omega}_{G_i/B}) \times \boldsymbol{\rho}] dm \\
 &\quad + \int_{G_i} \boldsymbol{\rho} \times [(\boldsymbol{\omega}_{B/N} + \boldsymbol{\omega}_{G_i/B}) \times \mathbf{r}_{G_i/p_i}] dm \tag{A.8}
 \end{aligned}$$

For our discussed system, there are multiple moving parts. Therefore, you must use caution when deriving the angular momentum. In Eq. (A.8), it is understood that first, the spacecraft bus has fixed within its reference frame the vector $\mathbf{r}_{p_i/A}$ to the nominal position of the CMG center of mass, p_i . This vector is only the moment arm for velocities of the components with respect to the inertial frame, neglecting the additional velocities of the gimbal about its own axis. The first term on the RHS of Eq. (A.8) is the angular momentum associated with this moment arm and the i th CMG gimbal mass with respect to point A. In addition, to this angular momentum, the contribution of the CMG gimbal-centric angular momentum needs to be incorporated. This contribution is taken with respect to $\mathbf{r}_{p_i/A}$.

If we assume in Eq. (A.8) that the center of mass of the gimbal is at point $\mathbf{r}_{p_i/A}$, then the equation of CMG gimbal angular momentum reduces to

$$\begin{aligned}\mathbf{h}_A^{G_i} &= \int_{G_i} \mathbf{r}_{p_i/A} dm \times \mathbf{v}_A + \int_{G_i} \mathbf{r}_{p_i/A} \times (\boldsymbol{\omega}_{B/N} \times \mathbf{r}_{p_i/A}) dm \\ &\quad + \int_{G_i} \boldsymbol{\rho} \times [(\boldsymbol{\omega}_{B/N} + \boldsymbol{\omega}_{G_i/B}) \times \boldsymbol{\rho}] dm \\ &= \mathbf{J}_A^{G_i} \cdot \boldsymbol{\omega}_{B/N} + \mathbf{J}_{G_i}^{G_i} \cdot (\boldsymbol{\omega}_{B/N} + \boldsymbol{\omega}_{G_i/B}) + m_{G_i} \mathbf{r}_{p_i/A} \times \mathbf{v}_A\end{aligned}\quad (A.9)$$

where

$$\begin{aligned}\mathbf{J}_A^{G_i} &= m_{G_i} [\mathbf{r}_{p_i/A} \cdot \mathbf{r}_{p_i/A} \mathbb{1} - \mathbf{r}_{p_i/A} \mathbf{r}_{p_i/A}] \\ \mathbf{J}_{G_i}^{G_i} &= \int_{G_i} (\boldsymbol{\rho} \cdot \boldsymbol{\rho} \mathbb{1} - \boldsymbol{\rho} \boldsymbol{\rho}) dm\end{aligned}\quad (A.10)$$

In practice, CMG vendors tend to balance their gimbals in such a way that they are inherently stiff, their gimbal center of mass offset is small, and can be approximated as a particle along the gimbal axis, thus providing no variable inertia. If one wishes to use this particle assumption and even relax the assumption that the particle is along the gimbal axis, then they can construct an additional angular momentum perturbation induced to the system by the rotation of a particle imbalance as

$$\begin{aligned}\mathbf{h}_A^{G_{p_i}} &= m_{G_i} \mathbf{r}_{p_i/A} \times \mathbf{v}_A + (\mathbf{r}_{p_i/A} \cdot \mathbf{r}_{p_i/A} \mathbb{1} - \mathbf{r}_{p_i/A} \mathbf{r}_{p_i/A}) \cdot \boldsymbol{\omega}_{B/N} \\ &\quad + m_{G_i} (\mathbf{r}_{G_i/p_i} \cdot \mathbf{r}_{G_i/p_i} \mathbb{1} - \mathbf{r}_{p_i/G_i} \mathbf{r}_{p_i/G_i}) \cdot (\boldsymbol{\omega}_{B/N} + \boldsymbol{\omega}_{G_i/B})\end{aligned}\quad (A.11)$$

Equation (A.11) is found from taking the angular momentum over a single particle mass from Eq. (A.9), reducing the integral to an algebraic equation. Note that gimbal imbalances are typically small, terms associated with spacecraft angular velocity are typically much smaller than that for gimbal angular velocity. Therefore, if we desire to only keep the dominant terms of Eq. (A.11) we get,

$$\mathbf{h}_A^{G_{p_i}} \approx m_{G_i} (\mathbf{r}_{G_i/p_i} \cdot \mathbf{r}_{G_i/p_i} \mathbb{1} - \mathbf{r}_{p_i/G_i} \mathbf{r}_{p_i/G_i}) \cdot \boldsymbol{\omega}_{G_i/B}\quad (A.12)$$

A.4.3 CMG Rotor Angular Momentum

The CMG rotor angular momentum is found analogous to the CMG gimbal angular momentum as

$$\begin{aligned}
 \mathbf{h}_A^{R_i} &= \int_{R_i} (\mathbf{r}_{p_i/A} + \boldsymbol{\rho}) \times (\mathbf{v}_A + \boldsymbol{\omega}_{B/N} \times \mathbf{r}_{p_i/A}) dm \\
 &\quad + \int_{R_i} (\mathbf{r}_{R_i/p_i} + \boldsymbol{\rho}) \times [(\boldsymbol{\omega}_{B/N} + \boldsymbol{\omega}_{G_i/B} + \boldsymbol{\omega}_{R_i/G_i}) \times (\mathbf{r}_{p_i/R_i} + \boldsymbol{\rho})] dm \\
 &= \int_{R_i} \mathbf{r}_{p_i/A} dm \times \mathbf{v}_A + \int_{G_i} \mathbf{r}_{p_i/A} \times (\boldsymbol{\omega}_{B/N} \times \mathbf{r}_{p_i/A}) dm \\
 &\quad + \int_{R_i} \boldsymbol{\rho} \times [(\boldsymbol{\omega}_{B/N} + \boldsymbol{\omega}_{G_i/B} + \boldsymbol{\omega}_{R_i/G_i}) \times \mathbf{r}_{p_i/A}] dm \\
 &\quad + \int_{R_i} \boldsymbol{\rho} \times [(\boldsymbol{\omega}_{B/N} + \boldsymbol{\omega}_{G_i/B} + \boldsymbol{\omega}_{R_i/G_i}) \times \boldsymbol{\rho}] dm \\
 &\quad + \int_{R_i} \mathbf{r}_{R_i/p_i} \times [(\boldsymbol{\omega}_{B/N} + \boldsymbol{\omega}_{G_i/B} + \boldsymbol{\omega}_{R_i/G_i}) \times \mathbf{r}_{R_i/p_i}] dm \\
 &\quad + \int_{R_i} \mathbf{r}_{R_i/p_i} \times [(\boldsymbol{\omega}_{B/N} + \boldsymbol{\omega}_{G_i/B} + \boldsymbol{\omega}_{R_i/G_i}) \times \boldsymbol{\rho}] dm \\
 &\quad + \int_{R_i} \boldsymbol{\rho} \times [(\boldsymbol{\omega}_{B/N} + \boldsymbol{\omega}_{G_i/B} + \boldsymbol{\omega}_{R_i/G_i}) \times \mathbf{r}_{R_i/p_i}] dm
 \end{aligned} \tag{A.13}$$

Again, if we assume in Eq. (A.13) that the center of mass is at point p_i , then the equation of CMG gimbal angular momentum reduces to

$$\begin{aligned}
 \mathbf{h}_A^{R_i} &= \int_{R_i} \mathbf{r}_{p_i/A} dm \times \mathbf{v}_A + \int_{R_i} \mathbf{r}_{p_i/A} \times (\boldsymbol{\omega}_{B/N} \times \mathbf{r}_{p_i/A}) dm \\
 &\quad + \int_{R_i} \boldsymbol{\rho} \times [(\boldsymbol{\omega}_{B/N} + \boldsymbol{\omega}_{G_i/B} + \boldsymbol{\omega}_{R_i/G_i}) \times \boldsymbol{\rho}] dm \\
 &= \mathbf{J}_A^{R_i} \cdot \boldsymbol{\omega}_{B/N} + \mathbf{J}_{R_i}^{R_i} \cdot (\boldsymbol{\omega}_{B/N} + \boldsymbol{\omega}_{G_i/B} + \boldsymbol{\omega}_{R_i/G_i}) + m_{R_i} \mathbf{r}_{p_i/A} \times \mathbf{v}_A
 \end{aligned} \tag{A.14}$$

where

$$\begin{aligned}
 \mathbf{J}_A^{R_i} &= m_{R_i} [\mathbf{r}_{p_i/A} \cdot \mathbf{r}_{p_i/A} \mathbb{1} - \mathbf{r}_{p_i/A} \mathbf{r}_{p_i/A}] \\
 \mathbf{J}_{R_i}^{R_i} &= \int_{R_i} (\boldsymbol{\rho} \cdot \boldsymbol{\rho} \mathbb{1} - \boldsymbol{\rho} \boldsymbol{\rho}) dm
 \end{aligned} \tag{A.15}$$

In practice, CMG vendors tend to statically and dynamically balance their rotors in such a way that they are inherently stiff and precision aligned, their rotor center

of mass offset (i.e., eccentricity) is small, and can be approximated as a particle along the rotor axis. However, these imbalances are a main source of jitter on the spacecraft and are more prevalent than gimbal imbalances since the rotor velocities are of a much higher magnitude.

Therefore, if one wishes to use this particle assumption, they can construct an additional angular momentum perturbation induced to the system by the rotation of a particle imbalance as

$$\begin{aligned} \mathbf{h}_A^{R_{pi}} = & m_{R_i} \mathbf{r}_{p_i/A} \times \mathbf{v}_A + (\mathbf{r}_{p_i/A} \cdot \mathbf{r}_{p_i/A} \mathbb{1} - \mathbf{r}_{p_i/A} \mathbf{r}_{p_i/A}) \cdot \boldsymbol{\omega}_{B/N} \\ & + m_{R_i} (\mathbf{r}_{R_i/p_i} \cdot \mathbf{r}_{R_i/p_i} \mathbb{1} - \mathbf{r}_{p_i/R_i} \mathbf{r}_{p_i/R_i}) \cdot (\boldsymbol{\omega}_{B/N} + \boldsymbol{\omega}_{G_i/B} + \boldsymbol{\omega}_{R_i/G_i}) \end{aligned} \quad (A.16)$$

Choosing to keep only the dominant terms in Eq. (A.16), we arrive at

$$\mathbf{h}_A^{R_{pi}} \approx m_{R,p_i} (\mathbf{r}_{R_i/p_i} \cdot \mathbf{r}_{R_i/p_i} \mathbb{1} - \mathbf{r}_{p_i/R_i} \mathbf{r}_{p_i/R_i}) \cdot \boldsymbol{\omega}_{R_i/G_i} \quad (A.17)$$

The total system angular momentum about point A is found through the summation of all component angular momenta and their general imbalance terms from Eqs. (A.5)–(A.11) and (A.13)–(A.16) as

$$\begin{aligned} \mathbf{h}_A^S = & \mathbf{h}_A^B + \sum_{i=1}^n (\mathbf{h}_A^{G_i} + \mathbf{h}_A^{R_i} + \mathbf{h}_A^{G_{pi}} + \mathbf{h}_A^{R_{pi}}) \\ = & \left[\mathbf{J}_A^B + \mathbf{J}_B^B + \sum_{i=1}^n (\mathbf{J}_A^{G_i} + \mathbf{J}_A^{R_i} + \mathbf{J}_{G_i}^{G_i} + \mathbf{J}_{R_i}^{R_i} + \mathbf{J}_A^{G_{pi}} + \mathbf{J}_A^{R_{pi}}) \right] \cdot \boldsymbol{\omega}_{B/N} \\ & + \left[m_B \mathbf{r}_{B/A} + \sum_{i=1}^n (m_{G_i} \mathbf{r}_{p_i/A} + m_{R_i} \mathbf{r}_{R_i/A} + m_{G,p_i} \mathbf{r}_{G_i/p_i} + m_{R,p_i} \mathbf{r}_{R_i/p_i}) \right] \times \mathbf{v}_A \\ & + \left[\sum_{i=1}^n (\mathbf{J}_{G_i}^{G_i} + \mathbf{J}_{R_i}^{R_i}) + m_{G,p_i} (\mathbf{r}_{G_i/p_i} \cdot \mathbf{r}_{G_i/p_i} \mathbb{1} - \mathbf{r}_{p_i/G_i} \mathbf{r}_{p_i/G_i}) \right] \cdot \boldsymbol{\omega}_{G_i/B} \\ & + m_{R,p_i} (\mathbf{r}_{R_i/p_i} \cdot \mathbf{r}_{R_i/p_i} \mathbb{1} - \mathbf{r}_{p_i/R_i} \mathbf{r}_{p_i/R_i}) \cdot \boldsymbol{\omega}_{G_i/B} \\ & + \left[\sum_{i=1}^n \mathbf{J}_{R_i}^{R_i} + m_{R,p_i} (\mathbf{r}_{R_i/p_i} \cdot \mathbf{r}_{R_i/p_i} \mathbb{1} - \mathbf{r}_{p_i/R_i} \mathbf{r}_{p_i/R_i}) \right] \cdot \boldsymbol{\omega}_{R_i/G_i} \end{aligned} \quad (A.18)$$

With the point A being chosen as the spacecraft n -CMG system center of mass, we have from the definition of the center of mass

$$\left[m_B \mathbf{r}_{B/A} + \sum_{i=1}^n (m_{G_i} \mathbf{r}_{p_i/A} + m_{R_i} \mathbf{r}_{R_i/A} + m_{G,p_i} \mathbf{r}_{G_i/p_i} + m_{R,p_i} \mathbf{r}_{R_i/p_i}) \right] = 0 \quad (A.19)$$

Therefore, Eq. (A.18) can be represented more compactly when taken about the system center of mass as

$$\mathbf{H} = \left(\mathbf{J}_s + \sum_{i=1}^n \mathbf{J}_{gri} \right) \cdot \boldsymbol{\omega}^{B/N} + \left(\sum_{i=1}^n \mathbf{J}_{gri} \right) \cdot \boldsymbol{\omega}^{G_i/B} + \left(\sum_{i=1}^n \mathbf{J}_{r_i} \right) \cdot \boldsymbol{\omega}^{R_i/G_i} \quad (\text{A.20})$$

where \mathbf{J}_{gri} and \mathbf{J}_{r_i} are the gimbal-rotor assembly and rotor inertias about the CMG system center of mass (formally point p_i).

The total angular momentum for a single CMG is

$$\mathbf{h}_i = \mathbf{J}_{gri} \cdot \boldsymbol{\omega}^{B/N} + \mathbf{J}_{gri} \cdot \boldsymbol{\omega}^{G_i/B} + \mathbf{J}_{r_i} \cdot \boldsymbol{\omega}^{R_i/G_i} \quad (\text{A.21})$$

Equation (A.21) can be rewritten with respect to the orthogonal coordinate basis embedded in the i th CMG frame, $\{\hat{\mathbf{s}}_i, \hat{\mathbf{o}}_i, \hat{\mathbf{g}}_i\}$ corresponding to the i th CMG rotor spin vector, gyroscopic torque vector, and gimbal vectors, respectively. Equation (A.21) becomes

$$\mathbf{h}_i = \mathbf{J}_{gri} \cdot \boldsymbol{\omega}^{B/N} + \mathbf{J}_{gri} \cdot \hat{\mathbf{g}}_i \dot{\delta}_i + \mathbf{J}_{r_i} \cdot \hat{\mathbf{s}}_i \Omega_{r,i} \quad (\text{A.22})$$

where

$$\begin{aligned} \boldsymbol{\omega}^{G_i/B} &= \hat{\mathbf{g}}_i \dot{\delta}_i \\ \boldsymbol{\omega}^{R_i/G_i} &= \hat{\mathbf{s}}_i \Omega_{r,i} \end{aligned} \quad (\text{A.23})$$

A.4.4 Spacecraft and Actuator Equations of Motion

Before we derive the equation of motion we will use the following assumptions

1. The spacecraft body center of mass is fixed in the spacecraft body frame.
2. The gimbal and rotor center of mass are fixed in the spacecraft body frame.
3. The gimbal and rotor centers of mass coincide at the origin of their corresponding CMG body, point p_i , which will also be assumed to be where the rotor and gimbal axes intersect.
4. The rotor spin axis is always orthogonal to the gimbal axis.

The relevance for these assumptions in order are:

1. The perturbations from low frequency disturbances such as fuel slosh or flexible appendages are assumed to be designed for early in the spacecraft and mission design and not a direct function of how the CMG is designed and therefore are not the subject of this appendix.
2. The rotor eccentricity (imbalance) effects are typically designed to be negligible when combined with passive isolation for the majority of high precision pointing spacecraft.

3. Most CMG are designed so that there are no changes in the center of mass of the spacecraft body with rotation of the gimbals, which is a harder constraint to design for than a variation in inertia along the gimbal axis (i.e., counter masses can be added to adjust the gimbal center of mass position but not necessarily the inertia).

The first step to finding the actuator dynamics is to take the inertial time derivative of Eq. (A.22)

$$\begin{aligned} \frac{^N\mathbf{d}\mathbf{h}_i}{dt} &= \mathbf{J}_{gr_i} \cdot \frac{^B\mathbf{d}\boldsymbol{\omega}^{B/N}}{dt} + [\boldsymbol{\omega}^{B/N} \times (\mathbf{J}_{gr_i} \cdot \boldsymbol{\omega}^{B/N})] \\ &\quad + \mathbf{J}_{gr_i} \cdot \hat{\mathbf{g}}_i \ddot{\delta}_i + \mathbf{J}_{gr_i} \cdot (\boldsymbol{\omega}^{B/N} \times \hat{\mathbf{g}}_i) \dot{\delta}_i \\ &\quad + \mathbf{J}_{r_i} \cdot \hat{\mathbf{s}}_i \dot{\Omega}_{r_i} + \mathbf{J}_{r_i} \cdot (\boldsymbol{\omega}^{B/N} + \dot{\delta}_i \hat{\mathbf{g}}_i) \times \hat{\mathbf{s}}_i \Omega_{r,i} \end{aligned} \quad (\text{A.24})$$

To find the torque of the i th CMG gimbal, we assume that the gimbal motor shaft is infinitely stiff and perfectly aligned and then must only offset torque along its gimbal axis. Therefore, the gimbal torque is

$$\begin{aligned} \frac{^N\mathbf{d}\mathbf{h}_i}{dt} \cdot \hat{\mathbf{g}}_i &= \tau_{g,i} \\ &= \left(\mathbf{J}_{gr_i} \cdot \frac{^B\mathbf{d}\boldsymbol{\omega}^{B/N}}{dt} \right) \cdot \hat{\mathbf{g}}_i + [\boldsymbol{\omega}^{B/N} \times (\mathbf{J}_{gr_i} \cdot \boldsymbol{\omega}^{B/N})] \cdot \hat{\mathbf{g}}_i \\ &\quad + (\mathbf{J}_{gr_i} \cdot \hat{\mathbf{g}}_i) \cdot \hat{\mathbf{g}}_i \ddot{\delta}_i + [\mathbf{J}_{r_i} \cdot (\boldsymbol{\omega}^{B/N} \times \Omega_{r,i} \hat{\mathbf{s}}_i)] \cdot \hat{\mathbf{g}}_i \end{aligned} \quad (\text{A.25})$$

Similarly, we hold the infinite stiffness and perfect alignment assumptions for the i th CMG rotor to arrive at

$$\begin{aligned} \frac{^N\mathbf{d}\mathbf{h}_i}{dt} \cdot \hat{\mathbf{s}}_i &= \tau_{r,i} \\ &= \left(\mathbf{J}_{gr_i} \cdot \frac{^B\mathbf{d}\boldsymbol{\omega}^{B/N}}{dt} \right) \cdot \hat{\mathbf{s}}_i + [\boldsymbol{\omega}^{B/N} \times (\mathbf{J}_{gr_i} \cdot \boldsymbol{\omega}^{B/N})] \cdot \hat{\mathbf{s}}_i \\ &\quad + \mathbf{J}_{gr_i} \cdot (\boldsymbol{\omega}^{B/N} \times \dot{\delta}_i \hat{\mathbf{g}}_i) \cdot \hat{\mathbf{s}}_i \\ &\quad + (\mathbf{J}_{r_i} \cdot \hat{\mathbf{s}}_i) \cdot \hat{\mathbf{s}}_i \dot{\Omega}_{r_i} \end{aligned} \quad (\text{A.26})$$

With the scalar triple product identity,

$$\mathbf{A} \cdot (\mathbf{B} \times \mathbf{C}) = \mathbf{B} \cdot (\mathbf{C} \times \mathbf{A})$$

and the designation of $(\mathbf{J}_{r_i} \cdot \hat{\mathbf{s}}_i) \cdot \hat{\mathbf{s}}_i = J_{r,i}$ and $(\mathbf{J}_{gr_i} \cdot \hat{\mathbf{g}}_i) \cdot \hat{\mathbf{g}}_i = J_{gr,i}$ as the effective inertias of the rotor about its own spin axis and the gimbal about its own axis,

Eqs. (A.25) and (A.26) are

$$\begin{aligned}\tau_{g,i} = & J_{gr,i} \ddot{\delta}_i + \left(\mathbf{J}_{gr_i} \cdot \frac{^B d\boldsymbol{\omega}^{B/N}}{dt} \right) \cdot \hat{\mathbf{g}}_i + [\boldsymbol{\omega}^{B/N} \times (\mathbf{J}_{gr_i} \cdot \boldsymbol{\omega}^{B/N})] \cdot \hat{\mathbf{g}}_i \\ & + (\mathbf{J}_{r_i} \cdot \boldsymbol{\omega}^{B/N}) \cdot \hat{\mathbf{o}}_i \Omega_{r,i}\end{aligned}\quad (\text{A.27})$$

$$\begin{aligned}\tau_{r,i} = & J_{r,i} \dot{\Omega}_{r_i} + \left(\mathbf{J}_{gr_i} \cdot \frac{^B d\boldsymbol{\omega}^{B/N}}{dt} \right) \cdot \hat{\mathbf{s}}_i + [\boldsymbol{\omega}^{B/N} \times (\mathbf{J}_{gr_i} \cdot \boldsymbol{\omega}^{B/N})] \cdot \hat{\mathbf{s}}_i \\ & + \mathbf{J}_{gr_i} \cdot \boldsymbol{\omega}^{B/N} \cdot \hat{\mathbf{o}}_i \dot{\delta}_i\end{aligned}\quad (\text{A.28})$$

Equations (A.27) and (A.28) can be thought of directly as the input torque to the motors of the CMG gimbals and rotors from their motor electronics. Therefore, if we include friction, we can assume that the actuator equations of motion are

$$\begin{aligned}J_{gr,i} \ddot{\delta}_i = & \tau_{g,i} - \tau_{gf,i} - \left(\mathbf{J}_{gr_i} \cdot \frac{^B d\boldsymbol{\omega}^{B/N}}{dt} \right) \cdot \hat{\mathbf{g}}_i \\ & - [\boldsymbol{\omega}^{B/N} \times (\mathbf{J}_{gr_i} \cdot \boldsymbol{\omega}^{B/N})] \cdot \hat{\mathbf{g}}_i - (\mathbf{J}_{r_i} \cdot \boldsymbol{\omega}^{B/N}) \cdot \hat{\mathbf{o}}_i \Omega_{r,i}\end{aligned}\quad (\text{A.29})$$

$$\begin{aligned}J_{r,i} \dot{\Omega}_{r_i} = & \tau_{r,i} - \tau_{rf,i} - \left(\mathbf{J}_{gr_i} \cdot \frac{^B d\boldsymbol{\omega}^{B/N}}{dt} \right) \cdot \hat{\mathbf{s}}_i \\ & - [\boldsymbol{\omega}^{B/N} \times (\mathbf{J}_{gr_i} \cdot \boldsymbol{\omega}^{B/N})] \cdot \hat{\mathbf{s}}_i - (\mathbf{J}_{gr_i} \cdot \boldsymbol{\omega}^{B/N}) \cdot \hat{\mathbf{o}}_i \dot{\delta}_i\end{aligned}\quad (\text{A.30})$$

where $\tau_{gf,i}$ and $\tau_{rf,i}$ are the assumed internal friction torques of the i th CMG gimbal and rotor. Therefore the total equations of motion for a spacecraft containing an array of n CMGs is

$$\begin{aligned}& \left(\mathbf{J}_s + \sum_{i=1}^n \mathbf{J}_{gr_i} \right) \cdot \frac{^B d\boldsymbol{\omega}^{B/N}}{dt} \\ & = -\boldsymbol{\omega}^{B/N} \times \left[\left(\mathbf{J}_s + \sum_{i=1}^n \mathbf{J}_{gr_i} \right) \right] \cdot \boldsymbol{\omega}^{B/N} \\ & - \boldsymbol{\omega}^{B/N} \times \sum_{i=1}^n \left(\mathbf{J}_{gr_i} \cdot \hat{\mathbf{g}}_i \dot{\delta}_i + \mathbf{J}_{r_i} \Omega_{r,i} \right) \\ & - \sum_{i=1}^n \left(\mathbf{J}_{gr_i} \ddot{\delta}_i \hat{\mathbf{g}}_i + \mathbf{J}_{r_i} \dot{\Omega}_{r_i} \hat{\mathbf{s}}_i + \mathbf{J}_{r_i} \cdot \hat{\mathbf{o}}_i \dot{\delta}_i \Omega_{r,i} \right)\end{aligned}$$

$$-\sum_{i=1}^n \left[(\mathbf{J}_{gr_i} \cdot \boldsymbol{\omega}^{B/N}) \cdot \hat{\mathbf{o}}_i \dot{\delta}_i + (\mathbf{J}_{r_i} \cdot \boldsymbol{\omega}^{B/N}) \cdot \hat{\mathbf{o}}_i \Omega_{r,i} \right] + \tau_{ext} \quad (A.31)$$

where τ_{ext} is the external torque,

$$\begin{aligned} J_{gr,i} \ddot{\delta}_i = & \tau_{g,i} - \tau_{gf,i} - \left(\mathbf{J}_{gr_i} \cdot \frac{B d\boldsymbol{\omega}^{B/N}}{dt} \right) \cdot \hat{\mathbf{g}}_i \\ & - [\boldsymbol{\omega}^{B/N} \times (\mathbf{J}_{gr_i} \cdot \boldsymbol{\omega}^{B/N})] \cdot \hat{\mathbf{g}}_i - \mathbf{J}_{r_i} \cdot \boldsymbol{\omega}^{B/N} \cdot \hat{\mathbf{o}}_i \Omega_{r,i} \end{aligned} \quad (A.32)$$

and

$$\begin{aligned} J_{r,i} \dot{\Omega}_{r_i} = & \tau_{r,i} - \tau_{rf,i} - \left(\mathbf{J}_{gr_i} \cdot \frac{B d\boldsymbol{\omega}^{B/N}}{dt} \right) \cdot \hat{\mathbf{s}}_i \\ & - [\boldsymbol{\omega}^{B/N} \times (\mathbf{J}_{gr_i} \cdot \boldsymbol{\omega}^{B/N})] \cdot \hat{\mathbf{s}}_i \\ & + (\mathbf{J}_{gr_i} \cdot \boldsymbol{\omega}^{B/N}) \cdot \hat{\mathbf{o}}_i \dot{\delta}_i \end{aligned} \quad (A.33)$$

Note that the Eqs. (A.31)–(A.33) must be solved simultaneously so that angular momentum is conserved in the presence of internal friction. Internal friction and the additional torques act against the gimbal and rotor motors of the i th CMG provide a gimbal and rotor acceleration result different from the command. This difference typically shows up as an error for the inner-loop control schemes to track the desired gimbal acceleration, rate, and angle for the gimbal and the desired rotor acceleration and rate for the rotor. However, no matter how well the inner-loop controller is designed, there are physical limits on the how fast or close it can reach the desired gimbal and rotor states and therefore, only the resultant gimbal and rotor states can be fed back into the spacecraft equations of motion in Eqs. (A.29) and (A.30).

Of particular interest are the most dominant torques associated with the equations of motion in Eqs. (A.31)–(A.33). If we reduce Eqs. (A.31)–(A.33), keeping only the dominant terms from the conditions $|\Omega_{r,i}| >> |\dot{\delta}| >> \|\boldsymbol{\omega}^{B/N}\|$, we arrive at

$$\begin{aligned} & \left(\mathbf{J}_s + \sum_{i=1}^n \mathbf{J}_{gr_i} \right) \cdot \frac{B d\boldsymbol{\omega}^{B/N}}{dt} \\ & = - \left[\boldsymbol{\omega}^{B/N} \times \left(\mathbf{J}_s + \sum_{i=1}^n \mathbf{J}_{gr_i} \right) \right] \cdot \boldsymbol{\omega}^{B/N} \\ & \quad - \boldsymbol{\omega}^{B/N} \times \sum_{i=1}^n (\mathbf{J}_{r_i} \Omega_{r,i} \hat{\mathbf{s}}_i) \\ & \quad - \sum_{i=1}^n \left(\mathbf{J}_{r_i} \dot{\Omega}_{r_i} \hat{\mathbf{s}}_i + \mathbf{J}_{r_i} \cdot \hat{\mathbf{o}}_i \dot{\Omega}_{r,i} \right) + \tau_{ext} \end{aligned} \quad (A.34)$$

$$J_{gr,i}\ddot{\delta}_i = \tau_{g,i} - \tau_{gf,i} - (\mathbf{J}_{r_i} \cdot \boldsymbol{\omega}^{B/N}) \cdot \hat{\mathbf{o}}_i \Omega_{r,i} \quad (A.35)$$

$$J_{r,i}\dot{\Omega}_{r,i} = -\tau_{r,i} - \tau_{rf,i} \quad (A.36)$$

The contribution $(\mathbf{J}_{r_i} \cdot \boldsymbol{\omega}^{B/N}) \cdot \hat{\mathbf{o}}_i \Omega_{r,i}$ is known as precession back-drive torque (see Chap. 3) and is typically the largest torque besides internal friction of the gimbal bearings, that the gimbal motor must offset.

A.5 Summary

This appendix complements the dynamics chapter and provides the reader with the generic vector dyadic formulation of the equation of motion as well as their physical significance for a spacecraft hosting an array of n CMGs. It has provided in example the mass integral derivation of a generic set of the equations of motion for a spacecraft containing an array of CMGs. With this derivation, the reader should be able to consider the proper assumptions to reduce the equations of motion.

Appendix B

Stability Analysis of Momentum-Based Attitude Control Systems

Much of the literature assumes that a spacecraft's attitude controller and steering algorithm can be designed separately. The combined performance of the attitude controller and steering algorithm is typically not considered. It is beneficial to understand the implications of using a steering algorithm that is inexact (e.g., uses dirty inverses) on the attitude and angular rate stability of the entire spacecraft system.

This appendix reviews nonlinear stability analysis for some typical nonlinear attitude controllers used for general satellite attitude control along with the stability analysis of a spacecraft hosting CMGs. Two types of attitude maneuvers are considered for analysis, rest-to-rest maneuvers and attitude and angular velocity tracking. It behooves the reader and provides context to have some familiarity with Lyapunov theory and with the simplified equations of motion for a spacecraft hosting CMGs shown in Chap. 4.

B.1 Lyapunov Analysis

Lyapunov stability analysis can offer insight into the stability or even instability of equilibria of nonlinear systems but relies on the candidate Lyapunov function chosen for analysis. Moreover, its use is more of an art than an exact science and may yield conservative results, producing sufficient, though typically not necessary, conditions for stability. Despite these drawbacks, the chief value of Lyapunov methods for us is that they provide a mean to assess the impact of control algorithms on the stability of the attitude control system. The stability analysis of spacecraft hosting CMGs is quite involved since the steering algorithm provides the torque needed for attitude control and this torque may not be always achievable due to singularities and/or motor constraints. Lyapunov stability is defined by:

For a continuous-time system with of a state $x(t) \in \mathcal{D} \subseteq \mathbb{R}^n$ and $f : \mathcal{D} \rightarrow \mathbb{R}^n$,

$$\dot{x} = f(x(t)), \quad x(0) = x_0$$

with equilibrium, x_e where $\dot{x} = f(x_e) = 0$, the equilibrium x_e is:

1. Lyapunov stable, and if for every $\epsilon > 0$, there exists a $\delta > 0$ such that, if $\|x_0 - x_e\| < \delta$, then for all $t \geq 0$, $\|x(t) - x_e\| \leq \epsilon$
2. Asymptotically stable, if it is Lyapunov stable and there exists a $\delta > 0$ such that, if $\|x_0 - x_e\| < \delta$ then $\lim_{t \rightarrow \infty} \|x(t) - x_e\| = 0$
3. Exponentially stable, if it is asymptotically stable and there exists a $\delta > 0$ such that, if $\|x_0 - x_e\| < \delta$, then $\|x(t) - x_e\| \leq a\|x_e - x_0\|e^{-bt}$ for $a, b > 0$ and $t \geq 0$

Basically, Lyapunov stability is a form of solution boundedness. For a Lyapunov stable equilibrium, the maximum deviation of the solution from the equilibrium decreases if the initial condition perturbation decreases.

To assess stability, Lyapunov's second (direct) method is typically used. To use Lyapunov's direct method, a candidate Lyapunov function, V , is defined. The function V is a scalar function of the system's states. Note, the function V which is actually a functional or a scalar function of a function (e.g., $x(t)$). A candidate Lyapunov function $V(x)$ must satisfy the following properties

1. Continuously differentiable
2. Positive definite, $V(x) > 0 \forall x \in \mathcal{D}/\{0\}$
3. $V(0) = 0$

where $\mathcal{D}/\{0\}$ is the domain of x without the equilibrium, $x = 0$ the stability of which is studied. If also, $\dot{V}(x) = \frac{d}{dt}V(x(t)) \leq 0$, the Lyapunov function is said to be stable in the sense of Lyapunov. Note that due to legacy terminology, $V(x)$ is said to be positive definite rather than nonnegative. This is likely due to the fact that many of the past Lyapunov functions were of quadratic type and derived for linear systems: they were of the form $V(x) = x^T Px$ and said to be positive definite if symmetric matrix P were positive definite, i.e., $v^T Pv > 0$ for any $v \neq 0$.

In addition to the conditions needed for Lyapunov's direct method, if the Lyapunov function derivative along system trajectories is negative definite, i.e., $\dot{V}(x) = \frac{d}{dt}V(x(t)) < 0$, for all $x \in \mathbb{R}$, then the equilibrium can be shown to be globally asymptotically stable. That is, Lyapunov stable and the response to any initial condition asymptotically converges to the equilibrium.

The above Lyapunov analysis results only guarantee that the solution converges to zero as time goes to infinity. The transient performance of the system is not characterized from this analysis. Special conditions do exist in Lyapunov analysis which lead to exponential or even finite-time convergence results but, in general, typical results from Lyapunov analysis only guarantee asymptotic convergence of trajectories to the equilibrium. Therefore, transient performance is typically checked through simulations.

In addition to the ability of Lyapunov analysis to assess the stability and instability of known nonlinear dynamical systems, it can also be used for control synthesis. The control synthesis starts with a nonlinear differential equation describing the error dynamics based on the equations of motion,

$$\dot{x} = f(x, u) \quad (\text{B.1})$$

where x is the error state vector and u is the control vector. Systems that are described by dynamic equations such as in Eq. (B.1) that are not an explicit function of time are referred to as autonomous systems. We will concentrate on autonomous systems for the remainder of this appendix, noting that a different set of Lyapunov stability results exist for non-autonomous case which can be exploited for attitude control problems with time-dependent dynamics (e.g., magnetic attitude control and attitude mode switching).

Now consider a candidate Lyapunov function $V(x)$ and its time derivative along the trajectories of Eq. (B.1)

$$\dot{V} = \left(\frac{\partial V}{\partial x} \right)^T \dot{x} = \left(\frac{\partial V}{\partial x} \right)^T f(x, u) \quad (\text{B.2})$$

The control u may be used to stabilize the equilibrium at the origin, by making $\dot{V} \leq 0$. Therefore, control synthesis through Lyapunov analysis uses the control to produce

$$\left(\frac{\partial V}{\partial x} \right)^T f(x, u) \leq 0 \quad (\text{B.3})$$

For an autonomous system, to determine if an equilibrium is globally asymptotically stable when $\dot{V} \leq 0$ and not $\dot{V} < 0$, Lasalle's Invariance principle can be used. The Lasalle's Invariance principle is as follows:

Let $\Omega \subset \mathcal{D}$ be a compact set that is positively invariant for trajectories of $\dot{x} = f(x)$, i.e., trajectories that start in Ω stay in Ω . Let $V(x) : \mathcal{D} \rightarrow \mathbb{R}$ be a continuously differentiable function such that $\dot{V}(x) \leq 0$ on Ω . Let E be the set of all points in Ω such that $\dot{V}(x) = 0$. Let M be the largest invariant set in E . Then every solution starting in Ω approaches M as $t \rightarrow \infty$. When the set M is a single point $x_e = 0$ and $\Omega = \mathcal{D} = \mathbb{R}^n$ then x_e is a globally asymptotic equilibrium.

To apply this principle to an attitude control problem, note that the set $E = \{(\omega, e) : \omega \equiv 0\}$ and for points in E it follows from Equation (B.12) that $u = 0$ and from Equation (B.13) that $e = 0$. Hence $M = \{x_e\}$ and x_e is asymptotically stable.

We will next discuss typical candidate Lyapunov functions used in the literature to analyze attitude control stability and do so for two important cases/control objectives: rest-to-rest or attitude regulation and attitude and angular velocity tracking.

B.2 Rest-to-Rest Attitude Control

Representing the attitude error by an error quaternion $[e_1 \ e_2 \ e_3 \ e_4]^T = [e \ e_4]^T$ is a common approach. It provides global representation for attitude, leads to bilinear kinematic differential equations, and benefits from the absence of singularities. A candidate Lyapunov function for rest-to-rest attitude control, assuming the target equilibrium is at $e = 0, e_4 = 1$, is

$$V = \frac{1}{2}\omega^T J \omega + e^T e + (1 - e_4)^2 \quad (\text{B.4})$$

where e is the vector elements of the error quaternion, e.g., such a quaternion may represent the error in alignment between the body and inertial reference frames, e_4 is its scalar element, ω is the spacecraft angular velocity vector, and J is the spacecraft inertia matrix both expressed in body coordinates. The time derivative of V in Eq. (B.4), gives

$$\dot{V} = \omega^T J \dot{\omega} + 2e^T \dot{e} - 2(1 - e_4)\dot{e}_4 \quad (\text{B.5})$$

The kinetic and kinematic differential equations associated with the rotation motion of the spacecraft are

$$\begin{aligned} \dot{\omega} &= -J^{-1}(\omega^\times J \omega - u) \\ \dot{e} &= \frac{1}{2}e^\times \omega + \frac{1}{2}e_4 \omega \\ \dot{e}_4 &= -\frac{1}{2}e^T \omega \end{aligned} \quad (\text{B.6})$$

Substitution of the dynamics equations in Eqs. (B.6) into (B.5) provides

$$\begin{aligned} \dot{V} &= -\omega^T(\omega^\times J \omega - u) + 2e^T \left(\frac{1}{2}e^\times \omega + \frac{1}{2}e_4 \right) \\ &\quad - 2(1 - e_4) \left(-\frac{1}{2}e^T \omega \right) \\ &= \omega^T u + e^T \omega \end{aligned} \quad (\text{B.7})$$

Let the control law be defined by

$$u = -Ke - C\omega \quad (\text{B.8})$$

where K and C are positive definite symmetric gain matrices. The control law in Eq. (B.8) is of the proportional-derivative type. So, its gains K and C can be

tuned intuitively and/or through analysis of the linearized system. The Lyapunov derivative is found from substituting Eqs. (B.8) into (B.7):

$$\dot{V} = -\omega^T C \omega + e^T (K - I_{3 \times 3}) \omega \quad (\text{B.9})$$

If $K = I_{3 \times 3}$ then

$$\dot{V} = -\omega^T C \omega \leq 0 \quad (\text{B.10})$$

Note that \dot{V} in Eq. (B.10) is only negative semi-definite and it does not depend on e . Further analysis exploits the Lasalle's Invariance principle and can be used to demonstrate almost global asymptotic stability with Eq. (B.8) when $K = I_{3 \times 3}$. The controlled Lyapunov system in Eqs. (B.4) through (B.10) is “almost” globally asymptotically stable for Lasalle’s theorem because a perturbation from the quaternion initial condition $e = 0$ and $e_4 = 1$ may result to an unstable transition to the unstable quaternion $e = 0$ and $e_4 = -1$ and therefore global asymptotic stability is not guaranteed for all quaternion initial conditions. This deviation from the stable equilibrium $e = 0$ and $e_4 = 1$ to the unstable equilibrium $e = 0$, and $e_4 = -1$ is known as quaternion unwinding which is typically surpassed by the augmentation of discontinuous switch or logic variable. Note that local asymptotic stability may also be confirmed using eigenvalue analysis, including for other choices $K \neq I$. Asymptotic stability and estimates of domain of attraction can be obtained via simulations.

Another popular choice of a candidate Lyapunov function for a rest-to-rest attitude maneuver is

$$V = \frac{1}{2} \omega^T K^{-1} J \omega + e^T e + (1 - e_4)^2 \quad (\text{B.11})$$

where $K = K^T > 0$. The time derivative in Eq. (B.11) along system trajectories gives

$$\begin{aligned} \dot{V} &= -\omega^T K^{-1} (\omega^\times J \omega - u) + 2e^T \left(\frac{1}{2} e^\times \omega + \frac{1}{2} e_4 \right) \\ &\quad - 2(1 - e_4) \left(-\frac{1}{2} e^T \omega \right) \\ &= \omega^T K^{-1} u + e^T \omega - \omega^T K^{-1} \omega^\times J \omega \end{aligned} \quad (\text{B.12})$$

and with the eigenaxis control law

$$u = -Ke - C\omega + \omega^\times J\omega \quad (\text{B.13})$$

for positive definite symmetric gain matrices K and C provides

$$\dot{V} = -\omega^T K^{-1} C \omega \quad (\text{B.14})$$

The term $\omega^\times J \omega$ is added to the controller to cancel out components of torque away from the eigenaxis of the maneuver, thereby making the maneuver purely an eigenaxis maneuver. Also, \dot{V} in Eq. (B.14) is negative semi-definite which is not enough to demonstrate asymptotic stability. In fact, for Eqs. (B.13) and (B.14), almost global asymptotic stability can be shown through the application of Lasalle's Invariance principle. The reasons for almost global, i.e., domain of attraction excludes a set of measure zero² rather than global stability have to do with quaternions providing a double cover of the set of all attitudes. For instance, neither Eqs. (B.8) nor (B.13) can avoid $e = 0$, $e_4 = -1$, $\omega = 0$ as another (unstable) equilibrium where $u = 0$ and $V = 0$. Discontinuous control laws such as

$$u = -Ke(\text{sign}(e_4)) - C\omega + \omega^\times J \omega \quad (\text{B.15})$$

have been proposed to address some of the challenges of quaternion stabilization.

Note, that this controller provides no torque when at zero angular velocity and an attitude error angle along the eigenaxis of π if $\text{sign}(0) = 0$. Therefore, $e_4 = \cos(\frac{\pi}{2})$ or the set of error quaternions with an error angle of π are additional equilibria for this controller. More specifically, if the spacecraft goes to rest, i.e., $\omega = 0$ when $e_4 = 0$, then the controller $u = 0$ and it remains at the incorrect attitude for all time. To avoid such a case, the sign function can be replaced by a band of two switching points rather than a single switching point at $e_4 = 0$. This band or region is known as a hysteresis region and it is typically designed considering the amplitude of noise and error from the measurement of attitude. Both the sign and hysteresis region make the controller discontinuous. Discontinuous controllers pose problems of chattering, and care must also be exercised in their synthesis.

Use of rotation matrices (or the Lie group $\text{SO}(3)$, i.e., the Lie group for direction cosine matrices) has also been pursued in place of quaternions for attitude control since they provide a unique parameterization of attitude and lead to almost globally asymptotically stabilizing feedback laws. However, $\text{SO}(3)$ based attitude controllers have their own drawbacks, such as slow convergence if starting close to or at the three unstable of the four possible closed-loop error equilibria.

In summary, for attitude control there is no free lunch. No matter what the parameterization one chooses, no “smooth time-invariant” attitude controller can globally asymptotically stabilize attitude, which is a consequence of Brockett’s Theorem.

²A set measure of zero corresponds to a set consisting of a finite number of points of a set that contain no area or volume.

B.3 Attitude and Angular Velocity Tracking Control

The problem of attitude and angular rate tracking is illustrated in Fig. B.1 for satellite-based Earth imaging and considers the tracking of both the attitude and angular velocity, versus just reaching a reference attitude with zero angular velocity, such as is done in rest-to-rest control.

Therefore, the Lyapunov function must include the error in angular velocity and in attitude. A candidate Lyapunov function for attitude tracking stability analysis is

$$V = \frac{1}{2} \omega_e^T K^{-1} J \omega_e + e^T e + (1 - e_4)^2 \quad (\text{B.16})$$

where $\omega_e = \omega - \omega_d$ is the angular velocity error and ω_d is the desired angular velocity which is assumed to be continuously differentiable and bounded. The time derivative of the Lyapunov function in Eq. (B.16) along the trajectories of the system is

$$\begin{aligned} \dot{V} &= -\omega_e^T K^{-1} (\omega^\times J \omega + J \dot{\omega}_d - u) \\ &\quad + 2e^T \left(\frac{1}{2} e^\times \omega_e + \frac{1}{2} e_4 \omega \right) - 2(1 - e_4) \left(-\frac{1}{2} e^T \omega_e \right) \\ &= \omega_e^T K^{-1} u + e^T \omega_e - \omega_e^T K^{-1} J \dot{\omega}_d \end{aligned} \quad (\text{B.17})$$

Note, that the angular velocity used for the kinematic equations of motion in Eq. (B.6) is now ω_e rather than ω . The angular velocities ω_e and ω happen to be with respect to the same reference frame and because they are both represented in

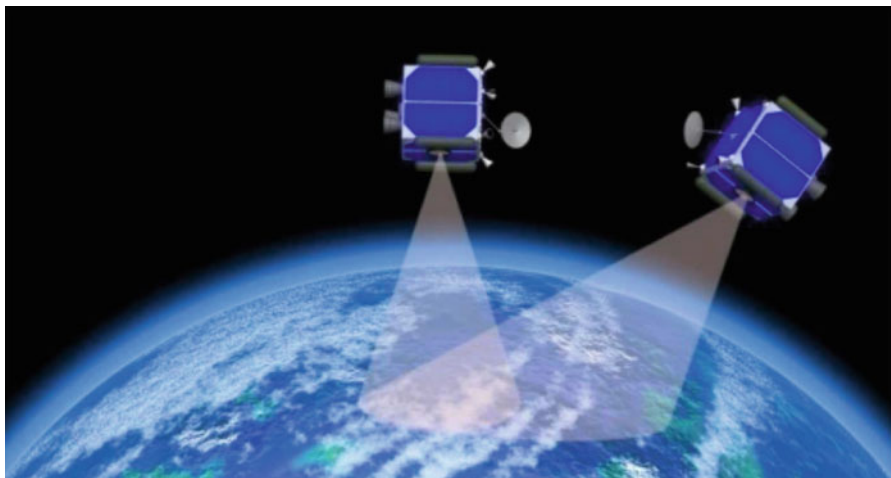


Fig. B.1 Satellite earth imaging

the same coordinate system (i.e., body coordinates), $\omega_e = \omega - \omega_d$ can be used in place of ω when angular rate tracking is desired. A suitable control law that achieves asymptotic tracking based on Eq. (B.17) is of the form

$$u = -Ke - C\omega_e + \omega^\times J\omega + J\dot{\omega}_d \quad (\text{B.18})$$

and

$$\dot{V} = -\omega_e^T K^{-1} C \omega_e \quad (\text{B.19})$$

Note that \dot{V} in Eq. (B.19) is negative semi-definite and Lasalle's Invariance principle for autonomous systems has to be used to show that the controller in Eq. (B.18) achieves asymptotic stability.

B.4 Steering Algorithm Effects on Attitude Regulation and Tracking

The stability of a steering algorithm for satellite attitude control depends on the objective and type of steering algorithm. Singularity-escape, singularity-avoidance, and escape methods add torque error and therefore are destabilizers by nature (i.e., they push the spacecraft away from an equilibrium trajectory). Singularity-avoidance laws and limited-momentum algorithms are typically array-geometry dependent and may sacrifice available angular momentum and torque authority for predictable behavior. Also, many of the steering algorithms in all three of the categories in Chap. 7 can encounter a gimbal lock singularity, which may be stable for angular rate but not for attitude. In other words, a spacecraft whose array is in gimbal lock might rotate in a so-called simple spin (see Chap. 4), in the absence of external torques.

In general, spacecraft controllers may be of the linear proportional derivative or higher order linear type so these nonlinear controls approaches may offer little practical value, but they allow the steering algorithm to be incorporated in a nonlinear analysis of stability with the nonlinear system dynamics. The analysis begins with the Lyapunov candidate function in Eq. (B.11) for eigenaxis attitude regulation

$$V = \frac{1}{2}\omega^T K^{-1} J \omega + e^T e + (1 - e_4)^2$$

and its time derivative along the system trajectories of the form

$$\dot{V} = \omega^T K^{-1} u + e^T \omega + \omega^T K^{-1} \omega^\times J \omega$$

The only difference here is that the steering algorithm may introduce some error in u , i.e., $u = \bar{u} - \tau_e - \omega^\times h_e$ where \bar{u} is the requested control torque, and the torque error from singularity escape may occur for every singularity encounter or remain a constant at gimbal lock (see Chap. 5).

The term \bar{u} is the nominal control torque [i.e., the one that would be used to asymptotically stabilize the system in Eq. (B.12)] and the terms τ_e and $\omega^\times h_e$ are the torque error, and the gyroscopic torque component of the angular momentum error.

Substituting u into Eq. (B.12) leads to

$$\begin{aligned}\dot{V} = & \omega^T K^{-1} (-Ke - C\omega + \omega^\times J\omega - \tau_e - \omega^\times h_e) \\ & + e^T \omega + \omega^T K^{-1} \omega^\times J\omega\end{aligned}\quad (\text{B.20})$$

leading to

$$\dot{V} = -\omega^T K^{-1} C\omega + \omega^T K^{-1} (-\tau_e - \omega^\times h_e) + \omega^T K^{-1} \omega^\times J\omega \quad (\text{B.21})$$

With the assumption that $K = kI_{3 \times 3}$, it follows that

$$\omega^T K^{-1} \omega^\times J\omega = \omega^T K^{-1} \omega^\times h_e = 0$$

Thus

$$\dot{V} \leq -ck\|\omega\|^2 + k\|\omega\|\|\tau_e\| \quad (\text{B.22})$$

where c is the smallest eigenvalue of C . The result in Eq. (B.22) does not provide us much information so we must consider the possible conditions from the majority of steering algorithms (see Chap. 7).

The majority of steering algorithms, except for the case of gimbal lock, result in an instantaneous burst of torque error to escape singularity. If the torque error after singularity escape is very small, i.e., $\|\tau\| \approx \epsilon$ where ϵ is a small number.

$$\dot{V} \leq -ck\|\omega\|^2 + k\|\omega\|\|\epsilon\| \quad (\text{B.23})$$

Both terms in Eq. (B.23) are functions of k and the two-norm of the angular velocity. As velocity decreases, both terms approach zero, but the goal is to have the negative term in Eq. (B.23) dominate. This can be accomplished by making c large as is evident through the completion of the squares

$$\dot{V} \leq -ck \left(\|\omega\| - \frac{\epsilon}{2c} \right)^2 + k \frac{\epsilon^2}{4c} \quad (\text{B.24})$$

The expression in Eq. (B.24) depends on ϵ and hence on the steering algorithm performance. To guarantee $\dot{V} \leq 0$, a large derivative gain may be required, which in effect may cause the spacecraft to never reach the correct attitude and the response

be over damped. Also, “dirty” steering algorithms typically have a torque error that decays exponentially and therefore may be small but always persist. The best result one can get with such a steering algorithm is uniformly ultimate boundedness (UUB) with error converging to a ball that can be made smaller with the increase in the gain c . There appears to be no proof of attitude stabilization possible for this choice of Lyapunov function and attitude controller combination. In particular, a SGCMG array may end up in gimbal lock at nonzero angular velocity which will leave the spacecraft tumbling and therefore, unstable in attitude.

B.5 Summary

Some nonlinear Lyapunov stability analyses for spacecraft attitude control with momentum control systems were performed here to provide the reader understanding of the asymptotic performance behavior of some typical attitude controllers and their combinations with “dirty” inverse steering algorithms. The conclusion from this chapter is that accurate attitude control performance cannot be obtained without taking into account the choice of steering algorithm unless the chosen steering algorithm delivers torque exactly. In the absence of actuator and state constraints and the possibility of gimbal-lock, the magnitude of error from a steering algorithm can be bounded. However, any unpredictable behavior from a steering algorithm or injection of error for singularity escape is troublesome to represent through Lyapunov analysis because singularities are encountered on the fly while performing attitude maneuvers.

Index

A

A2100 (satellite), 10
Acceleration, 18
Agile Satellite, 66
Air Bearing, 210
Angular Momentum
 CMG array, 78
 conservation, 6
 gyrostat, 67
 momentum device, 66
 of docked spacecraft, 25
 spacecraft, 66
Angular Velocity Vector
 rotor, 66
 spacecraft, 66
APT (satellite), 21
Assembly, On-Orbit, 26
Asteroid Redirect Mission, 27
Asteroids, 11, 13, 27
Astronaut Maneuvering Unit, 13
ATK, 11, 24

Attitude

 control, 5, 17, 18, 21, 102
 actuators, 5, 6
 feed forward, 27
 subsystem architecture, 16–18
 definition, 61
 parameterization
 defined, 61
 Euler Angles, 97, 98
 for coordinate-system transformations,
 62
 Gibbs vector, 98
 Rodrigues parameters, 98
 sensors, 5

Automotive Applications, 13
Automotive Applications, 30

B

Ball Aerospace, 1, 3, 10
Bandwidth, 188–191
Base Rate Effect, 22, 31, 47, 80
Basis Vector
 definition, 57
Bearings, 20, 24, 45, 47, 51, 53, 88, 90
 effect of span on stiffness, 84
 impact on coordinates, 63
Bilsat, 13
Blue Canyon Technologies, 90, 91
Boeing, 10, 11
Boeing 702 (spacecraft), 10
Boeing 702 (spacecraft), 17
Brennan, Louis, 30

C

Clarke, Arthur C., 15
Clyde Space, 91
CMG array
 3/4-CMG box array, 143
 6 GAMS, 148
 collinear arrays, 139
 dynamic array, 145
 energy storage, 151
 four-CMG pyramid array, 144
 Langley Six-Pac, 147
 roof, 139
 scissor pairs, 138, 168
 VSCMG array, 149

Coelostat Telescope, 11, 28

ConOps, 18, 20

Conte Di Savoia (ship), 31

Coordinate System

- common spacecraft, 10, 62

- distinguished from reference frame, 61

- indication of, in matrix notation, 58, 62, 67

- momentum device, 63

- array example, 65

- CMG, 63

- CMG pyramid array beta angle, 64

- CMG roof array beta angle, 64

- RWA, 63

Cornell University, 4

CubeSats, 13

D

DARPA, 24

- Phoenix program, 24

Deep Space Industries, 13

DigitalGlobe, 1, 2

direction cosine matrices, 97

Direction Cosine Matrix

- use in attitude control, 61

Disturbance Torques, 18, 20

Double Gimbal CMGs, 19

Double-Gimbal CMG, 20, 45

Dual-Spin Spacecraft, 10, 15, 65, 71

Dyadic

- coordinate systems, 58

- example, 58

- notation, 57

Dyadics

- common operations, 60

Dynamic Balance, 51, 68,

- 72, 77

E

EADS, 13

eigenaxis maneuver, 238

Equations of Motion, 80

Equilibria

- calculation of, 70

- gyrostat with CMGs, 73

- relative, of gyrostat, 67

- relative, of rigid body, 68

- stabilization of, 68–71

- superspin effect, 71

Euler's Theorem, 73

Explorer (spacecraft), 8, 70

F

Failure, 18, 20, 24

first mass moments, 220

Flexible Dynamics, 8, 84

- augmented inertia, 88

- compliant rotor/gimbal behavior, 45, 84

Flexible Structure, 190, 201

Fluid Dynamics, 8

Frame of Reference, 5

Friction, 53, 188, 189, 192, 201, 208

G

Gears, 45, 47, 53, 73, 77, 88, 191

General Dynamics, 11

GeoEye, 2

Geosynchronous Satellites, 15, 18

global asymptotic stability, 238

Goddard Space Flight Center, 24

Goodrich Corporation, 4

Google Earth, 1

Gyroscope

- Back-Torque, 47

- Precession, 42

Gyrostat

- definition, 65

H

Health Monitoring, 24

Honeybee Robotics, 4, 90

Honeywell International, 3, 6, 21, 24, 28

Hubble Space telescope, 24

Hughes, 10, 15

Hughes 601 (spacecraft), 10, 16, 18

Hughes Aircraft, 8

I

Ikonos, 2

Imaging, 18

In Situ Resource Utilization, 27

Induced Vibration, 51, 77, 91

Inertia Matrix, 66

- introduced, 61

International Space Station, 1, 13, 19, 31

ITAR, 13

ITT Excelis, 24

J

Jackscrews, 16

Jacobian, 54, 101, 157

- CMG array, 83

- DGCMG array, 83
RWA array, 82
VSCMG array, 83
- Jacobian (matrix)
defined, 82
- Jerk, 18
due to gimbal acceleration, 77
spacecraft kinematics, 76
- Jitter, 28
- K**
Kennedy Space Center, 19
- L**
Launch Vehicle, 21, 128
Lit Motors, 13, 31
Lockheed Martin, 10, 11
Lyapunov stability, 233
- M**
Magnetic Torque Coils, 8
Mars, 27
Maryland Aerospace Incorporated, 91
Materials Science, 28
Matrix
example, 58
Miniature Momentum Control System, 4, 21, 23
Mir, 13, 19
Mir Space Station, 1
Modeling, 91
Momentum Bias, 16, 17
momentum capability
CMG, 135
DGCMG, 19
RWA, 134
Momentum Conrol Assembly, 24
Momentum Control System, 5, 8, 18, 24
Momentum Storage, 18
Momentum Wheel, 16
Momentum Wheels, 10
Momentum-Bias Satellite, 65, 72
Moore-Penrose Pseudoinverse, 69
Motor Torque Constant, 82
Motors, 24, 63, 65, 71, 73, 77, 80, 82, 84, 90–92, 193
- N**
NASA, 1, 12, 25
Nautical Applications, 13, 31
- Northrop Grumman, 11
null motion
singularity avoidance, 159
- O**
Operationally Responsive Space, 21, 22, 24
Optus, 16
Orbital Sciences, 10
Orbview, 2
ortho-skew array, 134
Output Axis, 65
Output Torque
of a motor, 82
Output-Torque Ripple, 51, 77, 91
- P**
Payload, 1, 11, 16, 28
role in attitude control, 61
Phonesat (spacecraft), 90
Planet Labs, 13
Planetary Resources Inc., 13
Power
Heat, 196
Holding Speed, 188
Motor, 197, 199
Reaction Wheel, 44
Tradeoffs, 50
- Q**
Quaternion
as attitude parameterization, 61
QuickBird, 2
- R**
RCA, 10
RCA Astronautics, 15
Reaction Wheel, 17, 42
Reference Frame
body fixed, 61
definition, 61
distinguished from coordinate system, 61
inertial, 61
Newtonian, 61
Relativity
as irrelevant for rigid-body motion, 61
Requirements, 18, 19, 24, 26
RESTORE (spacecraft), 25
Robotics, 11, 27

- Rotor Balance
 dynamic, 66
 static, 66
- RWA array, 17, 18, 28
 failure response, 71
 four-RWA pyramid array, 135
- S**
- Satellite Servicing, 11, 24
- Scissored Pair, 28, 31
- Seakeeper Gyro, 13
- Seakeeper Inc., 31
- Simulation, 201
- Sinclair Interplanetary, 91
- singular surfaces, 123
 external, 126, 144, 153
 internal, 125, 144, 153
- singular values, 95, 161
- Singularities, 10
 VSCMG array, 83
- singularities
 coordinate, 96
 degenerate hyperbolic, 111, 114
 designations, 141
 DGC MG gimbal lock, 105
 elliptic, 115
 external, 115
 geometric, 99
 hyperbolic, 112, 165
 non-degenerate hyperbolic, 112
- singularities definition matrix, 110
- Singularity Measure, 84
- singularity measure, 161
- singularity parameter, 161
- singularity projection matrix, 110
- Sizing
 gimbal motion as negligible, 80
 impact of base rate, 80
 impact of length scale, 21
 introduced, 20
 of momentum system to achieve slew
 kinematics, 76
 overview, 6
- Skylab, 1, 13, 19
- Slew, 18
 eigenaxis, 74
 rate versine, 75
 versine
 definition, 74
 timing, 75
 trig function, 74
- Slewing
 Acceleration Limited, 38
- Angle vs. Time, 36, 40
 Eigenaxis, 35
- Slip Rings, 90
- Small Satellites, 21, 90
- Solar Max (spacecraft), 24
- Space Shuttle, 24
- Space Systems Loral, 10, 24
- SpaceX, 13
- Sperry Gyroscope Company, 28
- spinup, 129
- Stability, 9, 10, 16, 17, 30, 191, 192
- Static Balance, 51, 77
- Stationkeeping, 18
- steering algorithms, 157
 AMAPS, 178
 Blended Inverse, 160
 FSL, 179
 GISL, 165
 GSR Inverse, 163
 HSL, 177
 local gradient methods, 166
 Moore-Penrose, 160
 pseudoinverse methods, 159
 singularity avoidance algorithms, 158
 singularity avoidance and escape
 algorithms, 158
 singularity direction avoidance, 162
 singularity escape algorithms, 158, 161
 SR Inverse, 161
- Surrey Satellite Technology Ltd., 13
- Syncom, 2, 8, 10, 15, 70
- T**
- Tachometer, 53
- Tacsat-2 (satellite), 24
- TACSAT-5, 21
- Tensor
 notation, 57
- Thales/Alenia, 13
- Thrusters, 5, 6, 8, 18
- Torque Amplification, 46, 48
- tracking control, 239
- Trade Studies, 18–21, 24, 54
- Trains, 30
- Transformations, 206
- Transport Theorem, 67, 80
- Tribology, 28
- U**
- University of Florida, 4, 90

V

Vector

- common operations, 60
- coordinate systems, 58
- example, 58
- notation, 57
- representation as a matrix, 59

Vectrix

- definition, 59

Vibration, 28, 51, 202, 208

- isolation, 22, 24

Violet (satellite), 4, 21, 22

Vivisat, 12, 24

W

Wolseley Tool and Motor Car Company

- 30

Worldview 3, 18

Worldview I, 1, 2

Z

Zarya Module, 19

Zero-Momentum Satellite, 10, 17, 66

Zero-Propellant Maneuver, 20